UNIVERSIDADE FEDERAL DO AMAZONAS

INSTITUTO DE CIÊNCIAS EXATAS

PROGRAMA DE PÓS-GRADUAÇÃO EM QUÍMICA

Tese de Doutorado

INVESTIGAÇÃO DAS PROPRIEDADES VIBRACIONAIS, ESTRUTURAIS E ELETRÔNICAS ATRAVÉS DE CÁLCULOS DFT E ESTUDOS DE DOCKING MOLECULAR DE ALCALOIDES ISOLADOS DE PLANTAS DA FLORA AMAZÔNICA: UMA ABORDAGEM TEÓRICA PARA MOLÉCULAS BIOATIVAS

RENYER ALVES COSTA

MANAUS

2018

Ficha Catalográfica

Ficha catalográfica elaborada automaticamente de acordo com os dados fornecidos pelo(a) autor(a).

Costa, Renyer
C837i Investigação das propriedades vibracionais, estruturais e eletrônicas através de cálculos DFT e estudos de docking molecular de alcaloides isolados de plantas da flora amazônica: uma abordagem teórica para moléculas bioativas / Renyer Costa. 2018
120 f.: il. color; 31 cm.

Orientador: Kelson Mota
Coorientador: Maria Lúcia Belém Pinheiro
Tese (Doutorado em Química) - Universidade Federal do Amazonas.

1. Alcaloides. 2. Dft. 3. Docking. 4. Toposiomerase. I. Mota, Kelson II. Universidade Federal do Amazonas III. Título

UNIVERSIDADE FEDERAL DO AMAZONAS
INSTITUTO DE CIÊNCIAS EXATAS
PROGRAMA DE PÓS-GRADUAÇÃO EM QUÍMICA

Investigação das propriedades vibracionais, estruturais e eletrônicas através de cálculos DFT e estudos de docking molecular de alcaloides isolados de plantas da flora amazônica: uma abordagem teórica para moléculas bioativas

Tese apresentada ao Programa de Pós-Graduação em Química da Universidade Federal do Amazonas, como requisito para obtenção de título de Doutor em Química, área de concentração Química Teórica.

Aluno: Renyer Alves Costa
Orientador: Kelson Mota Teixeira de Oliveira
Coorientador: Maria Lúcia Belém Pinheiro

MANAUS
2018

Agradecimentos

À Deus pai criador do universo, que com sua inteligência suprema me guiou rumo à conclusão deste trabalho

À minha mãe Maria Arlete Alves de Matos que dedicou 21 anos de sua vida à minha criação, educação, ajudando a tornar-me o ser humano que sou hoje. Sem a sua presença em minha vida, tudo e até mesmo este trabalho seria impossível.

Ao curso de Pós-Graduação em Química da Universidade Federal do Amazonas, que oferece oportunidade para a formação e aperfeiçoamento na área de química, fornecendo subsídios essenciais para desenvolvimento de pesquisa acadêmica.

Ao CNPq e Capes, pela concessão da bolsa de doutorado, sem a qual não seria possível a dedicação exclusiva para a realização deste trabalho.

Ao meu orientador Kelson Mota T. Oliveira, pelo apoio, amizade, paciência, conselhos e pela ajuda no meu desenvolvimento como profissional e ser humano. Gostaria de ressaltar a sua enorme paciência com o meu primeiro artigo que demorou cerca de 1 ano para ser aceito, mesmo depois de 5 rejeições nunca desanimou e sempre confiou no meu trabalho.

À coorientadora do projeto, professora Maria Lúcia Belém Pinheiro, pelo total apoio, amizade e confiança em minha pessoa. Gostaria de salientar que sem os seus conselhos, dificilmente estaria desenvolvendo este trabalho na área de química teórica.

Aos colaboradores do projeto, professor Emmanoel Vilaça Costa e professora Rita Nunommura, pelo fornecimento dos dados espectrais acerca dos alcaloides liriodenina, annomontina, *N*-hidroxiannomontina, cantinona e 7-metoxi-cantinona para a realização dos estudos teóricos.

Ao professor Andersson Barison da Universidade Federal do Paraná, pela realização dos espectros de RMN dos alcaloides strictosidina e stricnobrasilina essenciais para a publicação dos dois artigos.

Ao Kahlil Salomé pela paciência e realização dos espectros RMN do alcaloide strictosidina.

Ao Julio Rodolfo pelos ensinamentos valiosos e ajuda no uso do software gaussian (de fundamental importância para o desenvolvimento do meu trabalho).

Ao professor (e colega) Alexandre Alecrim da Universidade Federal do Amazonas-Humaitá, pela ajuda com o manuseamento do software gaussian e pelos ensinamentos à cerca da técnica de docking molecular.

Ao companheiro de laboratório Noam Gadelha, pela ajuda e acolhimento à minha chegada ao laboratório de química teórica, além do apoio inicial ao manuseamento do software gaussian.

Aos companheiros de laboratório Adjane Sampaio, Raquel Costabile, Earle Silva, Diego Valois e Guilherme Braule (vulgo Guilherme Brownie) pelo companheirismo e amizade.

Aos amigos da pós-graduação que sempre me apoiaram e me ajudaram: Rayanne Araújo, Marcos, Fagnaldo, Jessica Gualberto, Jaqueline Bezerra e Josiana Moreira Mar.

À minha namorada, companheira e amiga Andriele Oliveira. Seu apoio foi fundamental nessa jornada.

Abstract

The alkaloids constitute a class of metabolites with great biological activity and o great importance in human history. Among the several classes, the idole and oxoaporphine type alkaloids are worth mentioning. About 1000 of these types alkaloids have already been isolated from plants, however theoretical studies that justify their activities providing new data of their structural, spectroscopic and quantum properties lack in the literature. Based on this premise, the present study investigated the alkaloids strictosidine, stricnobrasiline, 12-hydroxy-10,11-dimethoxystricnobrasiline, liriodenine, cantinone and 7-methoxy-cantinone through a theoretical approach by DFT calculations using the hybrid electronic correlation function B3LYP and the 6-31 G (d), 6-311G (2d, p) and 6-311G ++ (2d, p) basis set. Theoretical geometric optimization data were compared with X-ray spectroscopy data of similar structures in the literature presenting similar values. In addition calculations of Natural Bond Orbitals (NBOs), HOMO and LUMO orbitals and electrostatic potential maps were performed. Theoretical spectra of UV-Vis revealed to be quite similar to the experimental spectra being possible to signal the electronic transitions. Based on the maps of electrostatic potential and the theoretical spectra of IV (by stretches N-H and O-H) it was possible to predict the formation of hydrogen bonds that influences de physic-chemical properties. Molecular docking calculations against human DNA-Topoisomerase II enzyme complexes and *Candida albicans* dihydropholate reductase were carried out in order to perform the described activities in literature.

Resumo

Os alcaloides constituem uma classe de metabólitos com grande atividade biológica e de grande importância na história humana. Dentre as diversas classes merecem destaque os alcaloides indólicos e aporfínicos. Cerca de 1000 tipos de alcaloides dessas classes já foram isolados, entretanto estudos teóricos que justifiquem as suas atividades e forneçam novos dados acerca das suas propriedades estruturais, espectroscópicas e quânticas são escassos na literatura. Partindo desta premissa o presente estudo investigou os alcaloides strictosidina, stricnobrasilina, 12-hidroxi-10,11-dimetoxiestricnobrasilina, liriodenina, cantinona e 7-metoxi-cantinona através de uma abordagem teórica por cálculos DFT usando o funcional híbrido de correlação eletrônica B3LYP e as bases 6-31 G(d), 6-311G(2d,p) e 6-311G++(2d,p). Dados teóricos de otimização geométrica foram comparados com dados de espectroscopia de raio-X de estruturas similares existentes na literatura apresentando valores similares. Em adição cálculos de Orbitais Naturais de ligação (Natural Bond Orbitals-NBOs), orbitais HOMO e LUMO e mapas de potencial eletrostático foram realizados. Espectros teóricos de UV-Vis revelaram-se bastante similares aos espectros experimentais sendo possível o assinalamento das transições eletrônicas. Baseados nos mapas de potencial eletrostático e nos espectros teóricos de IV (por estiramentos N-H e O-H) foi possível prever a formação de ligações de hidrogênio. Cálculos de docking molecular frente os complexos enzimáticos DNA-Topoisomerase II humana e Diidrofalato redutase de *Cândida albicans* foram realizados no intuito de justificar as atividades previamente descritas na literatura.

Lista de figuras

Sumário

1. Introdução

O uso de plantas no tratamento e na cura de enfermidades é tão antigo que supõem se o início próximo a origem da espécie humana. Os primeiros registros de estudos científicos sobre plantas medicinais resultaram no isolamento de alguns princípios ativos que se consagraram como princípios ativos eficazes e que ainda hoje são bastante empregados na clínica médica, a exemplo dos alcaloides morfina (1), quinina (2) e papaverina (3) (Fig 1) (Pinto, 1995; Armikia & Heirinch, 2014). Ainda hoje, principalmente nos países de terceiro mundo, plantas medicinais são comercializadas em feiras livres, mercados populares em virtude de suas propriedades, fato atribuído as seus metabólitos secundários que são alvo de pesquisas até hoje.

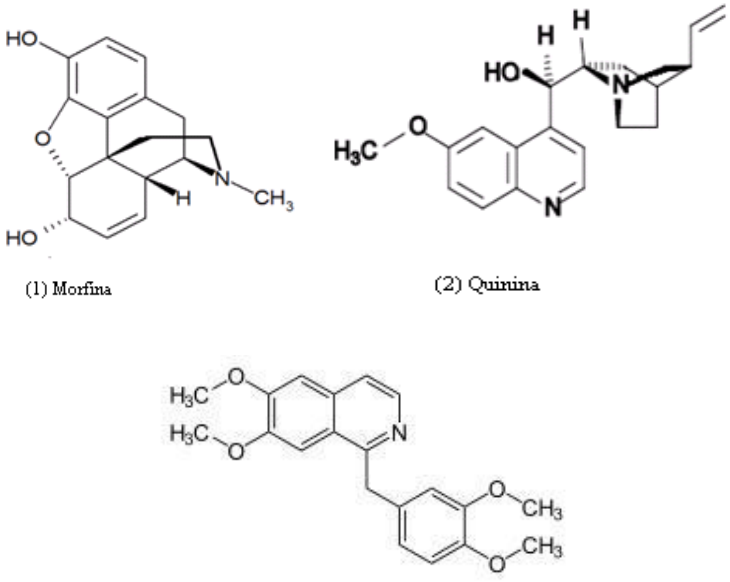

Fig 1. Alcaloides Morfina, Quinina e Papaverina

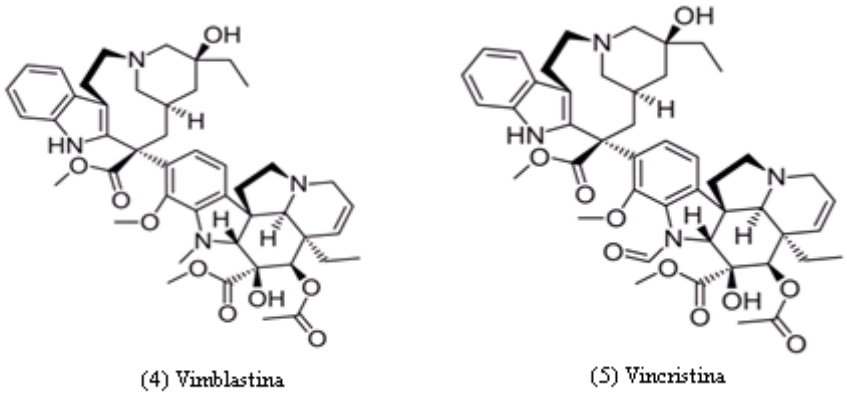

Fig 2. Alcaloides Vimblastina e Vincristina

Segundo Newman (Newman, 2003), medicamentos derivados de produtos naturais são capazes de tratar aproximadamente 80% das enfermidades humanas categorizadas, incluindo as indicadas como antibacterianas, anticoagulantes, antiparasitárias, imunossupresoras e anticancerígenas. E é dentro desse âmbito que os alcaloides, por sua história e atividade biológica chamam atenção. Entre eles estão os alcaloides vincristina (Oncovin®) e a vimblastina (Velban®) isolados de *Catharantus roseus* (Brandão, 2010) que inibem a polimerização das proteínas do fuso mitótico parando a divisão celular na metáfase usada e são amplamente no tratamento de diferentes linfomas, berberina, importante antimicrobiano, reserpina um importante antidepressivo, o vasodilatador vincamina e a efedrina com seu efeito terapêutico contra asma (Armikia & Heirinch, 2014; Fattorusso & Scafadi, 2008) (Fig 3).

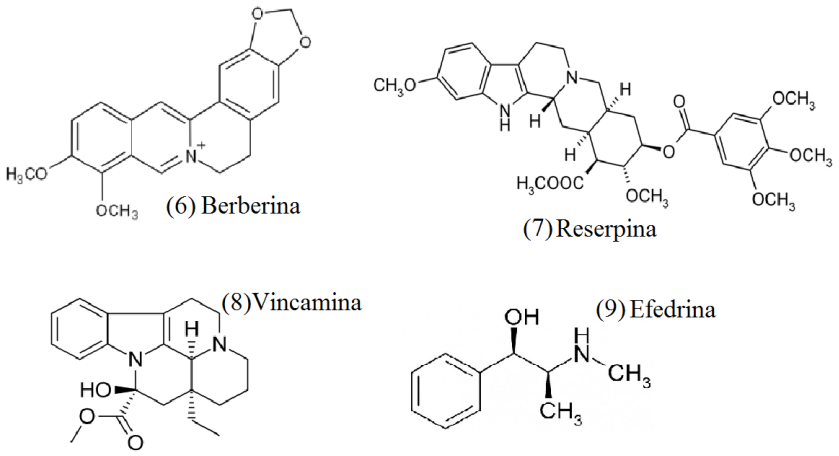

Fig 3. Alcaloides Berberina (6), Reserpina (7), Vincamina (8) e Efedrina (9).

Em virtude de tais caraterísticas e propriedades, o estudo sobre alcaloides ainda é um vasto campo a ser explorado tento em vista a quantidade de tais moléculas que já foram isoladas mas com propriedades estruturais, químicas e farmacêuticas ainda desconhecidas. E é dentro desse âmbito que se insere a química teórica. Através do emprego de cálculos teóricos aliados a dados experimentais, como RMN, UV, IV e EM, a química teórica surge como uma ferramenta que vem a somar os estudos acerca de tais moléculas com o intuito de explicar fenômenos que experimentalmente são difíceis detectar, sendo explicados apenas por dedução. O emprego de ferramentas matemáticas e modelos quânticos teóricos como DFT e Hartree-Fock e softwares avançados como Gaussian torna possível o estudo de propriedades estruturais difíceis de ser obter experimentalmente, como distancia entre átomos, ângulos diedros, orbitais HOMO e LUMO, mapas de potencial eletrostático, propriedades reativas, propriedades óticas não lineares, análise conformacional e etc. A possibilidade de realização de simulações de reações químicas e biológicas, mecanismos de interação enzima-substrato e simulação de dados espectrais obtidos experimentalmente, faz com que a química teórica se torne uma ferramenta poderosa no estudo de metabólitos secundários. Pesquisas têm surgido nesse âmbito, entretanto, no que concerne aos alcaloides, tal campo ainda é muito pouco explorado. Diante de tais premissas, este trabalho tem o objetivo de avaliar teoricamente

alcaloides oriundos de plantas da Amazônia, com o intuito de contribuir para o estudo estrutural e espectroscópico destas substancias e entender seu funcionamento em sistemas biológicos.

2. Alcaloides - um breve resumo

O conceito de alcaloides existente é ainda um pouco vago sendo caracterizados como uma classe de moléculas derivadas de aminoácidos e que possuem nitrogênio básico em sua estrutura, sendo consideradas para alguns autores consideram como uma classe especial de aminas. Presentes em diversas espécies sejam plantas, anfíbios, fungos e até algumas espécies de formigas e borboletas, os alcaloides sempre chamaram a atenção do homem por suas atividades biológicas. Dentre eles podemos citar o ópio, usado desde 400 a.C. Galeno prescrevia tal planta para dores de cabeça, epilepsia, asma, cólicas e até mesmo para estados melancólicos, sendo vulgarizado por Paracelsus, no século XVI, como analgésico (Barreiro, 2001).Em 1804 Friederich Sertüner isolou o principal componente da papoula, o alcaloide morfina, batizado em homenagem ao deus grego Morfeu. Esta substancia, com estrutura química particular, tornou-se o mais poderoso e potente analgésico conhecido em 1853 (Fattorusso & Scafadi, 2008). No entanto sua estrutura só foi determinada em 1923 por Robert Robinson e colaboradores. Embora reconhecida como poderoso analgésico, a morfina provoca tolerância, fenômeno que se manifesta pela necessidade de utilizar doses progressivamente maiores para se obter os mesmos resultados, provocando dependência física causando síndromes de abstinência havendo a necessidade de obtenção de novas estruturas como as 4-fenil-piperidinas (Barreiro, 2001).

A imensa flora da América do Sul permitiu a descoberta de importantes alcaloides com importantes funções terapêuticas, como a lobelina, presente em *Lobelia nicotinaefolia*,

utilizadas por tribos indígenas que fumavam suas folhas para aliviar os sintomas da asma (Fattorusso & Taglialatela-Scafadi, 2008). As culturas americanas, especialmente a Inca, Asteca, Maia, Olmeca e Tolteca consignaram à civilização moderna a quina, a ipecacuanha, a coca e muitas outras drogas de valor terapêutico, cujos princípios ativos são alcaloides (Pinto, 1995). A quinina, um dos principais componentes da casca de *Chinchona officialis* conhecida há muito tempo pelos ameríndios como anti-térmico, foi isolado em Paris em 1820 pelos químicos franceses Pierre Joseph Pelletier (1788-1842) e Joseph Bienaimé Caventou (1795-1877) e por apresentar eficácia contra a malária, originou os fármacos antimaláricos como a cloroquina e a mefloquina (Barreiro,1990; Armikia, & Heirinch,2014). O gênero *Strychnos* em virtude da sua toxicidade, esta atribuída aos alcaloides indólicos presentes, por muitos anos chamou a atenção do homem europeu em virtude do seu emprego no preparo de venenos de origem vegetal usando em flechas e zarabatas (curares) pelos nativos da Amazônia. Em virtude de suas propriedades tóxicas, o curare foi usado pelos índios tanto na caça quanto na guerra (Biocca, 1954) o que despertou o interesse dos pesquisadores pelo seu incrível poder paralisante e aplicabilidade medicinal. Várias espécies de *Strychnos* estão envolvidas na elaboração do curare como por exemplo: *S. amazonica*, *S. castelnaeana*, *S. panamensis*, *S. solimoesana*, *S. subcordata*, *S. tomentasa*, *S. trinervis* e *S. toxifera* (Bisset, 1992).

A partir de 1935 alcaloides curare foram introduzidos na medicina, tendo seu primeiro uso para o tratamento terapêutico de choques elétricos. O alcaloide isoquinolínico (+) tubocurarina, isolado de *Chodendron tomentosum* (Menispermaceae), teve seu uso em processos cirúrgicos devido suas atividade anestésica e relaxante neuromuscular desde 1942 (Bennett, 1968). Seguindo os estudos de *Strychnos*, muitos outros alcaloides usados na medicina foram sintetisados com estruturas muito proximas a dos alcaloides naturais como atracurium (Tracrium®), derivado da (+) tubocurarina e o alcuronium, derivado da C-

toxiferina (Ohiri, 1983 ; Lee, 2003) (Fig3). Muitas pesquisas atuais em *Strychnos* têm se voltado para este a aplicabilidade medicinal, revelando estruturas de alcaloides indólicos com significativa ação antimitótica, antimicrobiana, amebicida, hipotensiva e antipalúdicas (Phillipe, 2004; Caron, 1988).

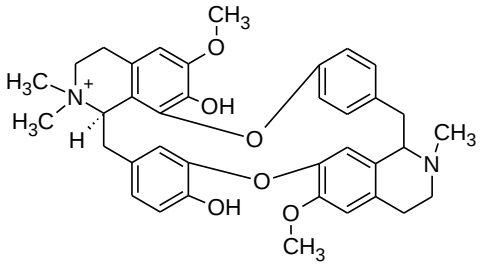

9

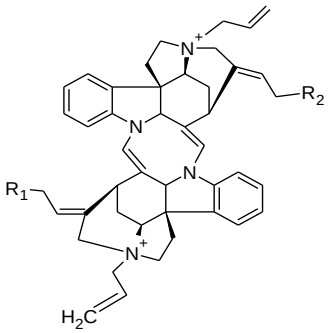

10

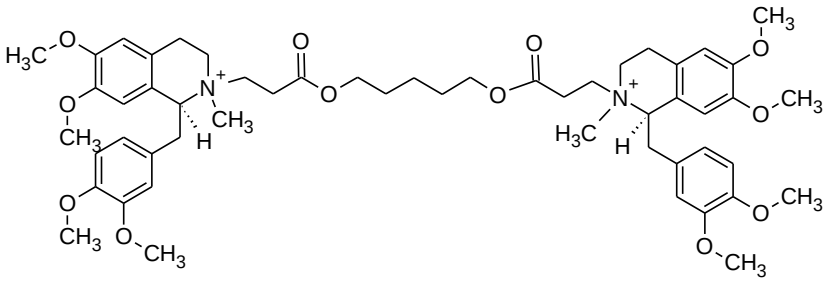

11

Fig 4. Alcaloides curare usado como medicamentos (+) tubocurarina (9), alcuronium (10) e atracurium (11)

Outro conhecido alcaloide por sua importância na medicina é a camptotecina (**12**), isolado de uma árvore ornamental chinesa, *Camptotheca acuminata* Decne. (Cornaceae) (Fattorusso & Scafadi, 2008), que devido a sua citotoxicidade, deu origem aos conhecidos fármacos irinotecan (**13**) e topotecan (**14**) que atuam inibindo a enzima topoisomerase I (Fig 5). As topoisomerases (I e II), por serem enzimas essenciais ubíquas que gerenciam a topologia do DNA durante processos celulares como replicação, transcrição, resultam em atraentes alvos para drogas contra o câncer. Inibidores de topoisomerases agem principalmente na etapa

intermediária da clivagem, e a fita permanece clivada por períodos de tempo praticamente indetectáveis.

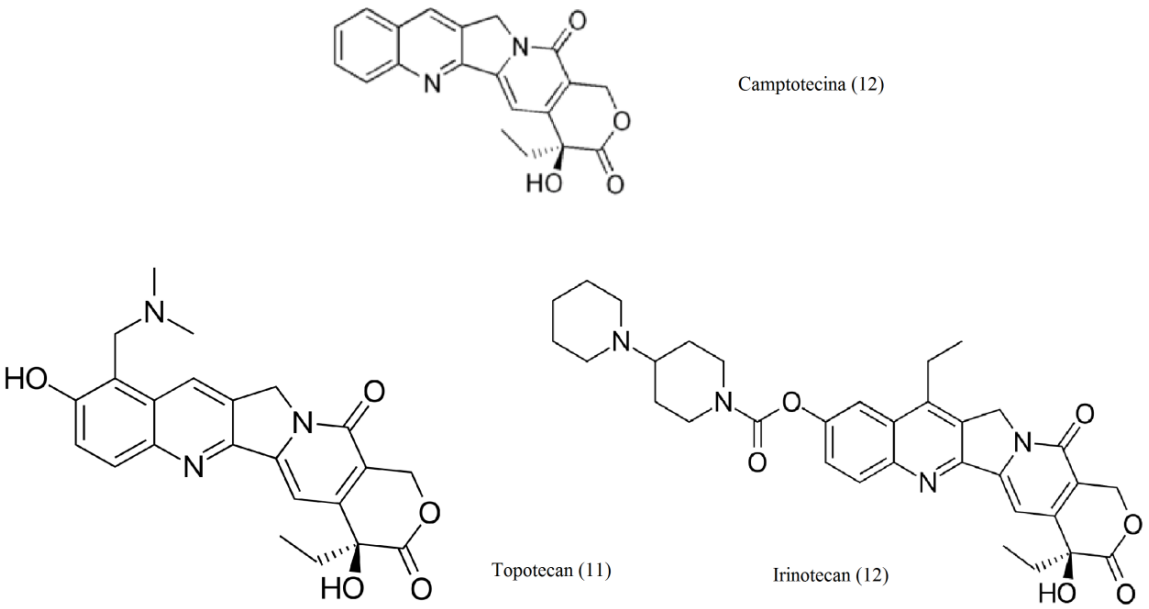

Fig 5. Alcaloide camptotecina (12) e seus derivados, Topotecan (13) e Irinotecan (14)

Ainda no mesmo âmbito do combate ao câncer merece destaque o Paclitaxel (15) (Figura 6), um complexo alcaloide diterpenóide de classe dos taxanos que ocorre no gênero Taxus, vulgarmente conhecido como teixo (Barreiro, 1990; Armikia & Heirinch, 2014). Esta família de diterpenoides tem sido conhecida por sua toxicidade, bem como por outras atividades biológicas. O primeiro estudo químico dos metabólitos do teixo remonta a meados do século XIX, quando uma mistura de taxanos foi obtida pelo farmacêutico alemão Lucas H. em 1856 (Fattorusso & Scafadi, 2008). Entre as drogas antineoplásicas que interferem nos os microtúbulos, o paclitaxel exibe um mecanismo de ação exclusivo (Brandão, 2010). Paclitaxel se liga à proteína tubulina dos microtúbulos e os fixa no lugar. O complexo resultante microtúbulo/paclitaxel não pode ser desfeito, deslocando o equilíbrio entre tubulina solúvel e

microtúbulos para a montagem, reduzindo a concentração crítica de tubulina necessária para a montagem de microtúbulos.

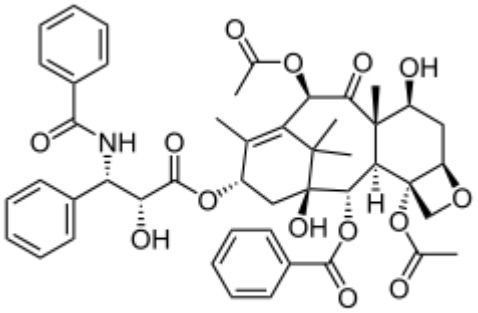

(15) Paclitaxel

Figura 6. Pseudo alcaloide Paclitaxel usando para o tratamento de diversos linfomas

2.3. Classificação dos alcaloides

Os alcaloides apresentam uma grande variedade estrutural e na origem biológica, consequentemente muitos sistemas de classificação de alcaloides são conhecidos. Entretanto baseado no aspecto químicas podemos ter a seguinte divisão (Fig7):

- Alcaloides atípicos não heterocíclicos, chamados comumente de proto-acalóides ou aminas biológicas
- Alcaloides heterocíclicos que são divididos em 8 grupos: pirrolidineos, piridínicos, quinolínicos, isoquinolínicos, aporfínicos, indólicos, imidazólicos e purínicos

Usando o senso geral, tais substâncias podem apresentar átomos de nitrogênio primário (ex. mescalina), secundário (ex. efedrina) terciário (ex. atropina, acagerina e stricnobrasilina) e quaternário (tubocurarina) e tais características estruturais afetam diretamente nas propriedades dos alcaloides, inferindo nos métodos de isolamento, propriedades biológicas e processos de semi síntese além de atividades biológicas.

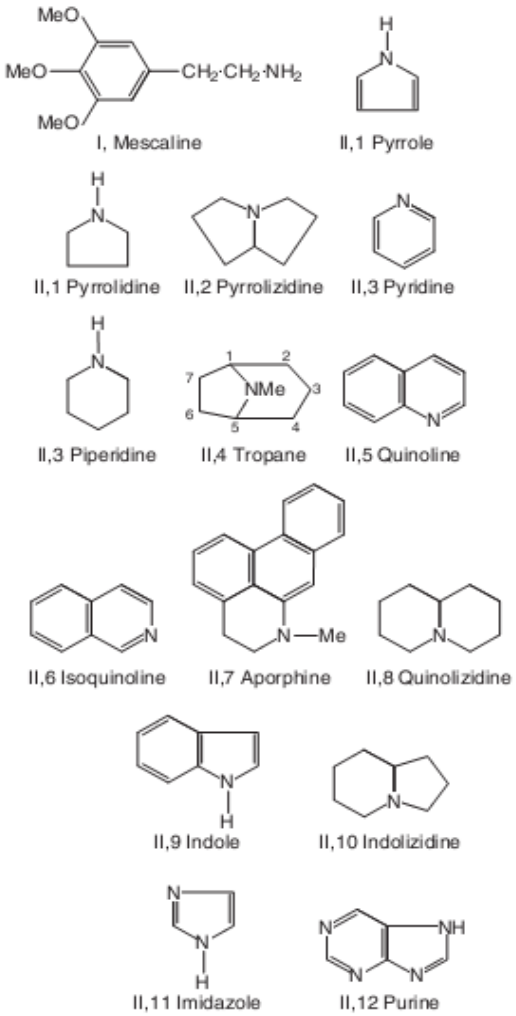

Fig 7. Esqueleto básico de alcaloides encontrados em plantas. I-proto-alcaloides e II-alcaloides heterocíclicos

Diante de tais prerrogativas, os alcaloides se consolidaram na história da humanidade, revelando grande importância, em virtude de suas variadas atividades biológicas e aplicabilidade medicinal desde tempos primórdios. Tal gama de propriedades está intimamente ligada a sua diversidade estrutural, porém ainda superficial para algumas classes. Entretanto o estudo de metabólitos secundários, principalmente de alcaloides tem se restringido apenas a identificação estrutural e avaliação do potencial biológico, sem no entanto estudar os aspectos estruturais, reacionais e quânticos que influenciam nas

propriedades químico-físicas, espectroscópicas e farmacológicas de tais moléculas. Diante disso, a química teórica como uma poderosa ferramenta no auxílio de interpretação de resultados experimentais, na avaliação de fenômenos nos quais as técnicas experimentais não podem ser diretamente utilizadas, na espectroscopia de Infra-vermelho (IR), no UV -VIS, RMN e etc (Haslett, 2000;. Ladeira, 2001; Oliveira 2000; Duarte 2001, Costa, 2017a; Costa, 2017b; Costa, 2017c; Costa 2016). Dentro desse âmbito ganha destaque a Teoria do Funcional de Densidade, que em inglês *Density Functional Theory*, DFT, que através descrição da energia eletrônica e das propriedades moleculares a partir de uma quantidade observável, a densidade eletrônica, permite uma comunicação mais objetiva e eficiente entre teóricos e experimentais (Duarte, 2001).

De acordo com Kohn et al (Kohn, 1996), *DFT é uma linguagem conveniente e universal para a teoria de estrutura eletrônica, a qual ajuda substancialmente a unificar a química orgânica, a inorgânica, química de superfície e a ciência dos materiais.*

2.4. Estudo teórico de moléculas e método DFT

O desenvolvimento da química teórica nos últimos 30 anos, aliado ao avanço dos computadores, têm tornado os métodos teóricos uma ferramenta indispensável na pesquisa química. Cálculos teóricos permitem prever a energia envolvida em alguns processos químicos com apenas alguns décimos de $kcal.mol^{-1}$. Calcular com precisão a geometria e estabelecer a superfície de energia potencial de moléculas, determinar estados de transição, intermediários e a descrição do caminho de reações com determinado grau de precisão são possibilidades atuais dos modelos teóricos. No ponto de vista tecnológico, a possibilidade de se obter informações a cerca de um fenômeno químico ao nível molecular, tem permitido desenvolver áreas como a de fármacos, estabelecer estratégias para aumentar a especificidade

e desempenho de catalisadores e compreender mecanismos impossíveis de serem estudados experimentalmente (Abreu, 2004).

O estudo teórico de algumas propriedades de interesse em sistemas químicos, nos leva invariavelmente ao problema da correlação eletrônica. Provavelmente esta é uma das principais vantagens da Teoria do Funcional de Densidade, DFT, uma vez que a correlação eletrônica é tratada intrinsecamente dentro do formalismo da teoria. De um modo geral a metodologia quântica mais utilizada, a função de onda Hartree-Fock, não é a metodologia mais apropriada, pois não leva em conta a correlação eletrônica, sendo necessários métodos pós-HF (Duarte, 2001; Abreu, 2004). Mesmo assim tal artifício teórico ainda é desvantajoso em virtude do custo computacional, impossibilitando a aplicabilidade desses sistemas para um grande conjunto de átomos. Para tratar de tais sistemas a DFT tem sido largamente utilizada (Szabo, 1989; Lizarga, 2013; Costa, 2017a; Costa 2017b; Costa 2017c; Costa, 2016) além de apresentar baixo custo computacional.

A teoria do funcional de densidade tem se mostrado extremamente eficiente quando comparada a outras metodologias, muitos são os trabalhos a serem citados onde a DFT se apresenta como uma alternativa muito eficaz, em que cálculos ab initio convencionais não puderam ser realizados (Platts, 2001). O fato de a densidade eletrônica do sistema ser uma propriedade observável do sistema, torna a DFT especial. Além disso, a DFT possui o menor custo computacional, o que a coloca como preferência em relação aos demais níveis de teoria ao passo que o número do conjunto de bases orbitalar N pode ser otimizada para uma relação N^3 ou melhor (Abreu, 2004).

Tem sido demonstrado que a DFT prediz a estrutura eletrônica e frequências vibracionais harmônicas com precisão substancialmente maior que nos resultados obtidos via método de Hartree-Fock e são compatíveis com os obtidos em cálculos envolvendo teoria de perturbação de segunda ordem MP2 (teoria de perturbação de Moller-Plesset de segunda ordem-MP2).

Além da descrição de frequências vibracionais, abordagem DFT tem sido explorada para a descrição de técnicas como ressonância magnética nuclear e ressonância eletrônica paramagnética, fornecendo resultados satisfatórios que contribuem para confirmação dos dados experimentais quando existem (Sievänen, 2010).

2.5. Cálculos de docking molecular e correlação com atividades biológicas

Docking molecular, ou ancoragem molecular, ou acoplamento molecular, é uma ferramenta chave para predizer a melhor orientação de ajuste de um ligante em uma proteína e de fundamental interesse dentro da química medicinal. Essa abordagem permite caracterizar o comportamento de pequenas moléculas no sítio de ligação das proteínas alvo, assim como, elucidar as interações moleculares. O processo de *docking* envolve dois passos: (1) predição da conformação, posição, orientação do ligante dentro dos sítios e (2) avaliação da afinidade de ligação. O *docking* também pode ser utilizado para realizar triagem virtual de grandes bibliotecas de compostos, classificar resultados e propor hipóteses estruturais de como ligantes ligam-se aos alvos, que é de extrema importância para a otimização de *leads* (Meng et al.,2011).

As associações entre moléculas biologicamente relevantes, como proteínas, ácidos nucléicos, carboidratos e lipídios, desempenham um papel central na transdução de sinal. Além disso, a orientação relativa dos dois parceiros de interação pode afetar o tipo de sinal produzido (por exemplo, agonismo vs antagonismo). Portanto, o docking é útil para prever a intensidade e o tipo de sinal produzido. O docking é um dos métodos mais frequentemente utilizados na concepção de fármacos baseados na estrutura, devido à sua capacidade para prever a conformação de ligação de uma molécula pequena ao sítio/alvo apropriado em uma proteína ou macromolécula. A caracterização do comportamento de ligação desempenha um

papel importante no desenho racional de fármacos, bem como para elucidar processos bioquímicos fundamentais (Morris et al, 2008).

Pode-se pensar em docking molecular como um problema de “chave-fechadura”, no qual se quer encontrar a orientação relativa correta da “chave” que abrirá a “fechadura”, que no caso está travada pela orientação espacial do sítio da enzima. Aqui, a proteína (enzima) pode ser pensada como a “trava” e o ligante pode ser pensado como uma “chave”. A ancoragem molecular pode ser definida como um problema de otimização, que descreveria a orientação “melhor ajustada” de um ligante que se liga a uma proteína particular de interesse. No entanto, como tanto o ligante quanto a proteína são flexíveis, uma analogia de “mão-de-luva” é mais apropriada do que “chave-fechadura”. Durante o curso do processo de acoplamento, o ligante e a proteína ajustam sua conformação para alcançar um "melhor ajuste" geral e esse tipo de ajuste conformacional, que resulta na ligação global, é referido como "ajuste induzido". A pesquisa de ancoragem molecular concentra-se em simular computacionalmente o processo de reconhecimento molecular, e o “melhor ajuste” conformacional entre a molécula de interesse e o sítio ativo da enzima. O objetivo é obter uma conformação otimizada para a proteína e o ligante, além da orientação relativa entre a proteína e o ligante, de modo que a energia livre do sistema geral seja minimizada.

2.5.1 O mecanismo do docking

Para executar um cálculo de varredura de docking, o primeiro requisito é uma estrutura da proteína de interesse. Normalmente, a estrutura já foi pré-determinada por meio de alguma técnica experimental, como cristalografia de raios X ou espectroscopia de RMN, mas também pode derivar da construção de modelagem de homologia. Esta estrutura de proteína presente em um banco de dados, juntamente com ligantes potenciais, servem como entradas para um cálculo chamado de *padronização* (Meng et al, 2011). O sucesso de um ensaio de acoplamento depende de dois componentes: o algoritmo de busca e a função de pontuação

(scoring function). Uma variedade de estratégias de busca conformacionais é aplicada ao ligante ao receptor. Esses incluem:

- Buscas torsionais sistemáticas ou estocásticas sobre ligações rotativas
- Simulações de dinâmica molecular
- Algoritmos genéticos para "desenvolver" novas conformações de baixa energia onde a pontuação de cada pose (conformação de docagem) atua como a função de adequação usada para selecionar indivíduos para a próxima iteração.

De um modo geral, independente do algoritmo empregado, a maioria dos programas de docking em uso analisa todo o espaço conformacional do ligante (ligante flexível), onde tentam modelar um receptor de proteína flexível. Cada "snapshot" do par é referido como uma pose. Um programa amplamente usado para cálculos de interação de moléculas e sítios ativos de enzimas alvo, inclusive nos artigos que serão apresentados a seguir, é o AutodockVina. O cálculo de encaixe no AutoDockVina (ADV) consiste em vários passos sequenciais. Cada passo envolve uma perturbação aleatória da conformação seguida por uma otimização (usando o algoritmo de Broyden-Fletcher-Goldfarb-Shanno, que é um método quase-Newton eficiente) e uma seleção em que o passo é aceito ou não (Trott & Olson, 2010). Cada otimização local envolve muitas “avaliações” da função de pontuação, bem como derivados nas coordenadas de posição-orientação-torção. O número de avaliações em uma otimização local é guiado por convergência.

Uma interação de ligação entre uma de molécula pequena e uma enzima pode resultar na ativação ou inibição da mesma. Se a proteína é um receptor, a ligação com o ligante pode resultar em agonismo ou antagonismo. O docking molecular é mais comumente usado no campo do design de fármacos (*drug design*) - onde a maioria das drogas são pequenas moléculas orgânicas, tendo os seguinte usos:

- O docking combinado com uma função de pontuação pode ser usado para rastrear rapidamente grandes bancos de dados de potenciais medicamentos in silico para identificar moléculas que provavelmente se ligam a proteínas alvo de interesse (ver triagem virtual).
- Otimização local - o acoplamento pode ser usado para prever em onde e em qual orientação relativa um ligante se liga a uma proteína (também referida como o modo de ligação ou pose). Esta informação pode por sua vez ser usada para projetar análogos mais potentes e seletivos.
- Biorremediação - A ancoragem de ligantes de proteína também pode ser usada para prever poluentes que podem ser degradados por enzimas

3. Justificativa

Diante da grande importância dos alcaloides, novos estudos acerca de tais moléculas necessitam ser realizados, principalmente os relativos aos aspectos estruturais, espectroscópicos e biológicos. Devido a dificuldade de se obter informações através de métodos experimentais o seguinte trabalho consistiu em realizar estudos teóricos em nível DFT e cálculos de docking molecular com o intuito de fornecer novas informações a cerca das propriedades estruturais, espectroscópicas e reacionais dos alcaloides isolados.

4. Objetivos

4.1. Objetivos gerais

- Realizar estudos teóricos estruturais de alcaloides oriundos de plantas nativas da Amazônia combinando dados espectroscópicos experimentais e cálculos DFT, visando testar sua atividade frente a precursores de doenças específicas.

4.2. Objetivos específicos

- Realizar cálculos á nível de teoria DFT usando as funções 6-31G(d), 6-311G(2d,p) e 6-311++G(2d,p) e funcional de troca de correlação B3LYP, com o intuito de reproduzir os dados experimentais fornecendo assim novas informações à cerca dos alcaloides strictosidina, stricnobrasilina, 12 hidroxi-10,11-dimetoxistricnobrasilina, liriodenina, cantinona e 7-metoxi-cantinona.

- Realizar estudos de docking molecular com DNA-Topoisomerase II humana e enzimas de *Candida albicnas* a fim de avaliar a atividade antitumoral e antimicrobiana dos alcaloides estudados.

5. Metodologia

5.1. Fundamentação teórica da metodologia

5.1.1 Método Hartree-Fock

Os métodos de cálculo da estrutura electrónica da matéria (átomos,moléculas e sólidos) baseiam-se, em geral, no conceito de orbitais, de elétrons independentes, que se movem num campo médio. A teoria pressupõe que os elétrons se movem independentemente uns dos outros no campo do(s) núcleo(s), considerado(s) fixo(s) (aproximação de Born-Oppenheimer), e num campo médio, das interações com os outros elétrons. A estrutura

electrónica é descrita em termos de um conjunto de orbitais ocupadas e orbitais não ocupadas (orbitais virtuais), as quais são funções mono eletrónicas. As energias das orbitais são representadas em diagramas de níveis, que podem ser ocupados por um ou dois eletrons, neste caso, de spins opostos (Alcácer, 2007).

Nos métodos de Hartree-Fock (HF), ainda os mais usados, define-se uma função de onda polieletrônica, Ψ para os estados estacionários que pode ser calculada, em princípio, pela resolução da equação de Schrödinger não relativista:

$$H\Psi = E\Psi \quad (1)$$

Sendo H o hamiltoniano que contém os termos de energia cinética dos elétrons, a atração entre os elétrons e o(s) núcleo(s), as interações entre os vários elétrons e, no caso de moléculas, a repulsão entre os núcleos.

A teoria do funcional da densidade, que usa a densidade eletrônica como variável fundamental (em vez da função de onda), é a base de uma nova classe de métodos de cálculo da estrutura electrónica, em plena expansão e com grandes potencialidades. Em ambos os casos, existe a noção de orbitais mono eletrônicos embora na teoria DFT elas sejam ainda mais irreais do que na teoria de HF (Alcácer, 2007).

A natureza da teoria de HF implica o uso de métodos interativos, sendo por isso uma teoria do campo autocoerente (self consistent field, SCF). É também uma teoria aproximada que se baseia no método variacional (Abreu, 2004). Isso implica que a energia total do sistema pode escrever-se sob a forma de uma função de um conjunto de parâmetros variacionais, λ,podendo a energia total do estado fundamental ser calculada como o mínimo do funcional, E[Ψ(λ)], ou seja, E0 = min E[Ψ(λ)].

A equação de Schrödinger para este hamiltoniano pode ser resolvida na aproximação de Born-Oppenheimer (se M=1, é o caso do átomo de hidrogénio), dando soluções ψi(r). Se considerarmos também coordenadas de spin, podemos definir funções χi (x) nas coordenadas

de espaço e spin, x, como os produtos das orbitais espaciais ψi(r) pelas componentes de spin σi(ω) = α ou β, da forma

$$\chi_i(X) = \Psi(r)\sigma_i(\omega) \text{ (2)}$$

devendo usar-se o termo orbitais-spin para as χi(x) e o termo orbitais para as ψi(r). As funções χi(x) satisfazem as equações de valores próprios

$$h\chi(X) = \varepsilon_i \chi_i(x)(\text{ (3)}$$

com a interpretação de que o elétron ocupa a orbital-spin χi, de energia εi. Se ignorarmos as interações elétron-elétron, podemos imaginar um sistema de N elétrons independentes com o hamiltoniano:

$$H = \sum_{i=1}^{N} h(i) \text{ (4)}$$

e a respectiva equação de Schrödinger:

$$H\Psi = E\Psi \text{ (5)}$$

que se reduz a um conjunto de N equações iguais a (3), sendo Ψ o produto

$$\Psi(x_1, x_2, \ldots\ldots\ldots x_n) = \chi_a(X_1)\chi_b(X_2) \ldots\ldots X_n(X_n) \text{ (6)}$$

e

$$E = \varepsilon_a + \varepsilon_b + .. + \varepsilon_n (7)$$

como facilmente se pode verificar, atendendo a que as funções de onda têm sempre uma dependência temporal da forma $\chi_{(X,t)} = \chi(X)e^{i(\frac{E}{\hbar})}$.

A função de onda de um sistema com N elétrons será então uma sobreposição (combinação linear) de todas as possíveis permutações de pares de elétrons, com a con-dição de que em cada troca de dois elétrons a função de onda muda de sinal, isto é $\Psi(x_1, x_2, \ldots\ldots x_k \ldots\ldots) = -\Psi(\ldots., x_k, \ldots\ldots x_2, x_1)$ Um modo de obter funções de onda anti-simétricas consiste em construir o chamado determinante de Slater, que é da forma

$$\Psi = \frac{1}{\sqrt{N!}}\begin{bmatrix} Xa\ (X1) & \cdots & Xn(X1) \\ \vdots & \ddots & \vdots \\ Xa(Xn) & \cdots & Xn(Xn) \end{bmatrix}$$

e que é hábito escrever abreviadamente de qualquer das formas seguintes,

$$\Psi = \frac{1}{\sqrt{N!}}|\chi_a(X1), \chi_b \ldots\ldots \chi_n(Xn)| \equiv |\chi_a(X1)\chi_b(X2) \ldots\ldots \chi_n(Xn)| \ (8)$$

Consideremos um sistema de dois elétrons como o átomo de hélio.

O respectivo determinante de Slater é

$$\Psi = \frac{1}{\sqrt{2}}\begin{vmatrix} \chi_a(X1) & X_b(X1) \\ \chi_a(X2) & \chi_b(X2) \end{vmatrix} = \frac{1}{\sqrt{2}}|\chi_a(X1)\chi_b(X2) - \chi_b(X1)\chi_b(X2) \ (9)$$

O princípio de exclusão de Pauli segue diretamente quando tentamos ocupar a mesma orbital-spin com os dois elétrons:

$$\Psi = \frac{1}{\sqrt{N!}} = [\chi_a(X1)\chi_a(X2) - \chi_a(X1)\chi_a(X2)] \ (10)$$

Uma forma de função de onda para um sistema de N eletrons independentes apropriada ao hamiltoniano $H = \sum_i^N h(i)$pode ser portanto, um determinante de Slater. Consideremos então que a função de onda é um determinante de Slater e procuremos uma expressão para o valor expectável da energia. Para o estado fundamental, seria

$$(E_0) = (\Psi_0|H|\Psi_0) = \int \Psi_0 H \Psi_0 dr \ (11)$$

$$He = -\sum_1^N \frac{1}{2}\nabla_1^2 - \sum_i^N \sum_A^N \frac{Za}{|ri - R_A|} + \sum_i^N \sum_{k>i}^N \frac{Za}{|rk - k_I|} = T + Vne + Vee \ (12)$$

em que dτ é o elemento de volume nas coordenadas de espaço e spin de todos os elétron. Analisando o hamiltoniano (12) vê-se que contém operadores envolvendo um só elétron como o operador da função de e operadores envolvendo dois elétrons. Podemos escrever

$$He = -\sum_1^N h(i) + \sum_i^N \sum_{k>i}^N \frac{1}{|rk - k_I|} = H^{mono} + Vee \ (13)$$

em que H^{mono} é a soma de operadores mono electrónicos $h(i)$,o índice superior mono significa operador mono eletrônico. Vee é o operador que representa as interações elétron-elétron — é uma soma de operadores de dois elétron. Conclui-se assim, que é possível escrever o hamiltoniano para um sistema de N elétrons e M núcleos como a soma de operadores de Fock:

$$H = \sum_{i=1}^{N} f(i)$$

sendo as orbitais-spin χa(x), as soluções das equações de Hartree-Fock da forma:

$$f\ \chi_a = \varepsilon_a \chi_a \qquad a = 1{,}2 \ldots \ldots \ldots n$$

Convém, nesta altura, distinguir se a molécula ou o átomo tem todas as camadas completas ou não. Se tiver camadas incompletas é necessário usar a versão não restrita do método de Hartree-Fock (UHF, de unrestricted Hartree-Fock), segundo a qual a energia deve ser calculada considerando todas as orbitais-spin ocupadas (com um único elétron).Se a molécula ou o átomo tiverem todas as camadas completas, o estado é singuleto e as orbitais (espaciais) estão ocupadas com dois elétrons de spins opostos. Neste caso pode usar-se a versão restrita do método de Hartree-Fock (RHF, de restricted Hartree-Fock). A energia na versão não restrita é então:

$$E_{HUF} = \sum_{a=1}^{OSOC} haa + \frac{1}{2}\sum_{a,b=1}^{OSOC}(Jab - Kab) \quad (14)$$

Quando o sistema tem só camadas completamente preenchidas (closed shell), pode usar-se o método de Hartree-Fock restrito (RHF) que implica o uso de orbitais (espaciais) duplamente ocupados. Nesse caso:

$$E_{RHF} = 2\sum_{a=1}^{odoc} haa + \sum_{a,b=1}^{odoc}(2Jab - Kab) \quad (15)$$

Para efeitos de cálculo computacional convém usar notação matricial. Pode ver-se que a expressão (15) se pode escrever em notação matricial sob a forma (F − εS)C = 0, ou:

$$FC = \varepsilon\, SC \quad (16)$$

em que C é a matriz cujas colunas são as orbitais moleculares de coeficientes $\mathbf{c}^a = \{c_p^a\}$, F e S são respectivamente as matrizes de Fock e de sobreposição de componentes F_{pq} e S_{pq}. A forma (16) não é, no entanto, muito conveniente, por não ter a forma simples de uma equação de valores próprios (a base de C não é ortogonal). Então transformar a equação (16) numa equação da forma:

$$F'C' = \varepsilon C' \quad (17)$$

5.1.2 Teoria do funcional de densidade

A partir da função de onda Ψ é possível calcular várias propriedades moleculares. Em particular, é possível calcular mapas de distribuição da densidade electrónica. De fato os postulados da mecânica quântica estabelecem que, embora a função de onda não tenha significado físico, pode definir-se uma quantidade física, a densidade eletrónica, ρ, que tem um valor definido, ρ(r), em cada ponto de coordenadas r e que, na teoria das orbitais pode ser associada às orbitais moleculares (Szabo, 1989), sendo:

$$\rho(r) = ni|\Psi\_i\,(r)|^2 \quad (18)$$

Onde

$$\rho(r) = \sum_i^{OC} ni\,|\Psi\_i\,(r)|^2 \quad (19)$$

$$\int \rho(r)dr = N \quad (20)$$

a densidade eletrônica no ponto de coordenadas r está associada ao orbital molecular ψi(r) supostamente ocupada por ni elétrons. A densidade eletrônica total será o somatório estendido a todas as orbitais ocupadas. A integração da função densidade electrónica para todo o espaço da molécula dá o número total de elétrons. Muita atenção tem sido dada a densidade eletrônica nos últimos anos e mapas de densidade eletrônica estão disponíveis em vários lugares. Para um átomo no seu estado fundamental, a densidade decresce monoliticamente do núcleo de modo exponencial por partes. Para moléculas, em uma

primeira análise, as densidades eletrônicas soam como uma superposição das densidades eletrônicas atômicas. Uma análise mais específica (experimental ou teórica), “acúmulos” de densidade eletrônica são observados nas regiões de ligações.

A tentativa de usar a densidade eletrônica como uma variável surgiu antes dos anos de 1900. Porém somente em 1964, com a publicação de dois teoremas por Hohenberg e Kohn, que o uso da densidade eletrônica como variável básica foi rigorosamente legitimado. Eles forneceram os fundamentos da teoria do funcional de densidade moderna DFT e mostraram que os modelos baseados no funcional de energia TFD devem ser vistos como uma aproximação de uma teoria exata (Duarte, 2001). Os dois teoremas mostram que existe um funcional de energia exato da densidade eletrônica E[ρ] e um princípio variacional exato para este funcional, semelhante a :

$$\delta\{E_{TDF}[\rho] - \mu N(\rho)\} = 0 \quad (21)$$

Em 1965, Kohn e Sham (Kohn & Shan, 1965) propuseram uma forma de contornar o problema de se encontrar o funcional de energia exato (o método KS). Desde a publicação destes dois artigos, a DFT tem atraído cada vez mais a atenção da comunidade científica e, atualmente, ela é largamente usada para se estudar sistemas cada vez mais complexos. No entanto, sabemos que ainda é um grande desafio interpretar e transmitir as informações, geradas pelos cálculos teóricos, numa linguagem capaz de ser facilmente compreendida por um químico experimental. Em relação a este último ponto, a Teoria do Funcional de Densidade apresenta uma grande vantagem. A descrição da energia eletrônica e das propriedades moleculares a partir de uma quantidade observável, a densidade eletrônica, permite uma comunicação mais objetiva entre teóricos e experimentais. Vale ressaltar que a Teoria do Funcional de Densidade, em seu formalismo, levanta o véu sobre importantes aspectos da química que ainda eram vistos à luz do empirismo. Conceitos como potencial

químico, μ, maciez, dureza e índice de reatividade formalmente definidos a partir da DFT abrem uma nova perspectiva na compreensão dos fenômenos químicos.

5.1.2.1 Modelo de Thomas-Fermi

Para um melhor entendimento da teoria do funcional de densidade e suas implicações, principalmente no que tange ao uso da densidade eletrônica ρ em cálculos de sistemas de multielétrons, é preciso voltar no tempo e compreender o trabalho de Thomas e Fermi, mas conhecido como modelo Thomas-Fermi.

O modelo Thomas-Fermi (TF), com o nome de Llewellyn Thomas e Enrico Fermi, é uma teoria da mecânica quântica para a estrutura eletrônica de sistemas de muitos corpos desenvolvidos semi classicamente logo após a introdução da equação de Schrödinger. Ela está separada da teoria da função de onda como sendo formulada apenas em termos da densidade eletrônica e, como tal, é vista como um precursor da moderna teoria funcional da densidade. O modelo TF está correto apenas no limite de uma carga nuclear infinita. O uso da aproximação para sistemas realistas produz previsões quantitativas pobres, não reproduzindo algumas características gerais da densidade, como a estrutura da casca em átomos e oscilações de Friedel em sólidos (variações no valor experimental da densidade eletrônica em semicondutores e metais). No entanto, encontrou aplicações modernas em muitos campos através da capacidade de extrair analiticamente tendências qualitativas e com a facilidade com que o modelo pode ser resolvido.

A premissa do modelo de Thomas-Fermi consiste o considerar o sistema multieletrônico (uma molécula, uma superfície metálica ou grupamento qualquer de átomos) como um gás de Fermi (gás composto por partículas que chamadas férmions que não interagem entre si, onde o férmion é qualquer partícula que obedecem ao princípio da exclusão de Pauli) sujeito a energia potencial resultante dos todos os núcleos (Parr & Yang, 1989). Então para um

pequeno elemento de volume ΔV, considerando o átomo em seu estado fundamental, podemos definir um volume de espaço de momento esférico até o momento Fermi p_f para a partícula da seguinte forma

$$V_f = \frac{4}{3}\pi {p_f}^3(\vec{r}) \text{ (22)}$$

onde $\vec{r}$ é um ponto em ΔV. O correspondente volume de fase para o conjunto de partículas do sistema considerado é

$$\Delta V_{ph} = V_f \Delta V = \frac{4}{3}\pi {p_f}^3(\vec{r})\Delta V \text{ (23)}$$

Os elétrons que ocupam o espaço ΔV_{Ph} estão distribuídos uniformemente em dois elétrons por h^3 do volume considerado, onde h é a constante de Planck. Então o numero de elétrons pode ser descrito como

$$\Delta N_{ph} = \frac{2}{h^3}\Delta V_{ph} = \frac{8\pi}{3h^3}{p_f}^3(\vec{r})\Delta V \text{ (24)}$$

O número de elétrons em ΔV é definido como produto da densidade eletrônica, (ρ) ou $(\vec{n})$, pelo volume do sistema

$$\Delta N = n(\vec{r})\Delta V \text{ (25)}$$

Aplicando na equação 24 temos que $(\vec{n})$ é

$$\overrightarrow{(n)} = \frac{8\pi}{3h^3}{p_f}^3(\vec{r}) \text{ (26)}$$

A fração de elétrons em $\vec{r}$ que possuem momento entre p e $p + dp$, ou seja, variando infinitesimalmente p, pode ser avaliado da seguinte forma

$$F_{\vec{r}}(p)dp = \frac{(d\vec{n}/dp)}{2\vec{n}} = \frac{(dV_f/dp)}{\vec{n}} = \frac{4\pi p^2 dp}{\frac{4}{3}\pi {p_f}^3(\vec{r})} \quad \text{por elétron (27)}$$

Usando a expressão clássica da energia cinética de uma partícula, tomando a massa do elétron, variando em *dp*, podemos obter a densidade de energia cinética de uma fração de um volume de elétrons

$$t(\vec{r}) = \int_o^{pf} \frac{p}{2m_e} n(\overrightarrow{r}) F_{\vec{r}}(p)dp \qquad (28)$$

Substituindo as (26) e (27) e tendo que o momento de Fermi é dando por $p_f = \sqrt{2mE_F}$ (onde $E_F = \frac{h^2}{2m\pi^2}(\frac{3\pi^2 N}{V})^{\frac{2}{3}}$) definimos a energia cinética por volume, ou a densidade de energia cinética

$$t(\vec{r}) = C_F\,[n(\overrightarrow{r})]^{\frac{5}{3}} \text{ (29)}$$

Integrando a energia cinética por unidade de volume $t(\vec{r})$por todo o espaço (d^3r) obtêm-se a energia cinética total dos elétrons que não interagem (férmions que não interagem)

$$T = \int t(\vec{r})\, d^3r \text{ , } C_F = \frac{3}{10}(3\pi^3)^{2/3} = 2.871 \text{ (30)}$$

Substituindo a equação (29) obtemos a expressão para energia cinética para elétrons (férmions) no modelo Thomas-Fermi

$$T = C_F \int [n(\vec{r})]^{5/3}\, d^3r \text{ (31)}$$

onde o limite $\Delta V \to 0$, com $n(\vec{r}) = \Delta N/\Delta V$ finito, foi tomada para dar uma integração em vez de um somatório. A expressão (31) é o famoso funcional de energia cinética de Thomas-Fermi, que Thomas e Fermi ousaram aplicar aos elétrons nos átomos em sistemas complexos.

A expressão (31) realiza a aproximação da energia cinética em termos da densidade eletrônica $n(\vec{r})$, também representada por $\rho(r)$, e partindo desta definição é possível montar um funcional da energia em termos da densidade eletrônica. A energia total é dado pela soma da energia cinética e energias potenciais

$$E_{[\rho]} = T + U_{eN} + U_{ee} \text{(32)}$$

Onde

$$U_{eN} = \int \rho(r)\, V_N(\vec{r}) d^3r \text{ (33)}$$

(33) é a energia potencial devido à atração que o núcleo carregado positivamente exerce sobre os elétrons

$$U_{ee} = \frac{1}{2}\iint \frac{\rho(r1)\rho(r2)}{\vec{r_1}-\vec{r_2}} d^3r_1 d^3r_2 \quad (34)$$

Substituindo as expressões (31), (34) e (33) na expressão (34) temos a descrição da energia total em termos de $\rho(r)$

$$E_{TF[\rho]} = C_F \int [n(\vec{r})]^{5/3}\, d^3r + \int \rho(r)\, V_N(\vec{r}) d^3r + \frac{1}{2}\iint \frac{\rho(r1)\rho(r2)}{\vec{r_1}-\vec{r_2}} d^3r_1 d^3r_2 \quad (35)$$

A teoria de Thomas-Fermi sofre de muitas deficiências, provavelmente o defeito mais sério é que ela não prevê a ligação entre átomos [Parr & Yang, 1989], então moléculas e sólidos não podem se formar nesta teoria. A principal fonte de erro vem da aproximação da energia cinética de forma tão grosseira, seguida pelos erros na energia de troca e pela completa negligência da correlação de elétrons. A energia cinética representa uma porção substancial da energia total de um sistema e, portanto, mesmo pequenos erros se mostram desastrosos. Outra desvantagem é a descrição simplificada das interações elétron-elétron, que são tratadas classicamente e, portanto, não levam em conta fenômenos quânticos como a interação de troca. A precisão da equação de Thomas-Fermi é limitada porque a expressão resultante para a energia cinética é apenas aproximada, além de não representar a energia de troca de um átomo como uma conclusão do princípio de Pauli. Um termo para a energia de troca foi adicionado por Dirac em 1928. No entanto, a teoria de Thomas-Fermi-Dirac permaneceu bastante imprecisa para a maioria das aplicações. O problema com a modelagem imprecisa da energia cinética no modelo de Thomas-Fermi, bem como outros funcionais de densidade implementados posteriormente, é contornado anos depois na teoria do funcional de densidade de Kohn-Sham com um sistema fictício de elétrons não interagentes cuja expressão de energia cinética é conhecida.

5.1.2.2 Teoremas Hohemberg-Kohn

Embora a teoria funcional da densidade tenha suas raízes no modelo de Thomas-Fermi para a estrutura eletrônica de materiais, a DFT foi primeiramente colocada em uma base teórica sólida por Walter Kohn e Pierre Hohenberg (1964) no contexto dos dois teoremas de Hohenberg-Kohn (H-K) (Kohn & Sham, 1965). Os teoremas originais de H-K foram desenvolvidos apenas para estados fundamentais não-degenerados na ausência de um campo magnético, embora tenham sido generalizados desde então para abranger estes. O primeiro teorema de H-K demonstra que as propriedades do estado fundamental de um sistema de muitos elétrons são determinadas unicamente por uma densidade de elétrons que depende apenas de três coordenadas espaciais.

Para entendermos o primeiro teorema, é preciso lembrar que para o hamiltoniano da equação de Schrödinger, $\widehat{H} = \sum_{i=1}^{N}(-\frac{1}{2}\nabla_i^2 + \sum_{i=1}^{N} v(\vec{r_i}) + \sum_{i<j}^{N} \frac{1}{r_{ij}}$, ambas a energia no estado fundamental e a função de onda do estado fundamental são determinadas pela minimização do funcional de energia

$$E[\psi] = \frac{\langle \psi \,|\, \hat{H} \,|\, \psi \rangle}{\langle \psi | \psi \rangle}, \text{ onde } \langle \psi | \hat{H} | \psi \rangle = \int \psi^* \hat{H} \psi dx \quad (36)$$

Significando que cada medida de energia fornece um autovalor de $\widehat{H}$ onde temos que $E[\psi] \geq E_0$, ou seja, a energia mínima será maior que a verdadeira energia do estado fundamental. Introduzindo o conceito de densidade eletrônica, em um sistema com *N*-elétrons o potencial externo $v(r)$ consertam o hamiltoniano, sendo assim *N* e $v(r)$ determinam todas as propriedades do estado fundamental. Isso não deve ser espantoso pois, $v(r)$ define todo o frame nuclear para uma molécula, que junto com o número de elétrons determina todas as propriedades eletrônicas. No entanto, no lugar de *N* e $v(r)$, o primeiro teorema de Hohenberg-Kohn legitimiza o uso da densidade eletrônica $\rho(r)$ (ou $n(\vec{r})$) como uma variável básica afirmando (Parr & Yang, 1989):

"*O potencial externo $v(r)$ é determinado, dentro de uma constante trivial aditiva, pela densidade eletrônica $\rho(r)$."*

O que tem como consequência fundamental a definição da densidade eletronica ρ, que determina o número de elétrons com $\rho(r)$ determinando o estado fundamental da função de onda ψ e todas as demais propriedades do sistema. Em suma dois valores diferentes de $v(r)$ e ψ não fornecem o mesmo ρ para seus estados fundamentais. Assim podemos expressar a equação (35) em dependência de $v(r)$ em termos de ρ da seguinte maneira

$$E_v[\rho] = T_{[\rho]} + V_{ne}[\rho] + V_{ee}[\rho]$$

$$E_v[\rho] = \int \rho(r)v(r)dr \ + F_{HK}[\rho] \quad (37)$$

Onde

$$F_{HK}[\rho] = T[\rho] + V_{ee}[\rho] \ (38)$$

O termo $V_{ee}[\rho]$ referente ao potencial de repulsão elétron-elétron tem como componentes

$$V_{ee}[\rho] = \ J[\rho] + \ termo\ não\ clássico \ (39)$$

$J[\rho]$ refere-se a repulsão clássica dado por $J[\rho] = \frac{1}{2}\iint \frac{1}{r_{12}}\rho(r_1)\rho(r_2)dr_1dr_2$ e o termo não clássico refere-se à uma quantidade muito importante, que ante então era desconsiderada no modelo Thomas-Fermi, a energia de troca e correlação.

O Primeiro teorema H-K estabeleceu a base para reduzir o problema de muitos corpos de N elétrons com coordenadas espaciais $3N$ para três coordenadas espaciais, através do uso de funções da densidade eletrônica, além de determinar que a densidade eletrônica, por determinar N e v pode determinar todas as propriedades do sistema no seu estado fundamental deste modo, a energia cinética, potencial e energia total do sistema podem ser obtidas como um funcional de densidade (Szabo &Ostlund, 1989). Este teorema foi estendido ao domínio dependente do tempo para desenvolver a teoria do funcional da densidade dependente do

tempo (TDDFT), que pode ser usada para descrever estados excitados (Parr & Yang, 1989). O segundo teorema de H-K define uma energia funcional para o sistema e prova que a densidade eletrônica correta do estado fundamental minimiza essa energia funcional. Baseia-se no princípio variacional da energia e tem como enunciado:

"*Para uma tentativa de densidade eletrônica* $\check{\rho}(r)$*, onde* $\check{\rho}(r) \geq 0$ *e* $\int \check{\rho}(r)dr = N$ *,a energia total do sistema será sempre maior ou igual a energia exata do sistema, ou seja* $E_0 \leq E_v[\check{\rho}]$*"*

Onde $E_v[\check{\rho}]$ é o funcional de energia da equação (37).

Essa análise é análoga ao princípio variacional aplicado para funções de onda. Isto promove uma justificativa para o principio variacional para o modelo Thomas-Fermi onde $E_{TF[\rho]}$ é uma aproximação de $E_v[\rho]$. De acordo com o primeiro teorema $\check{\rho}(r)$, determina seu próprio $\check{v}(r)$, $\check{H}$ e função de onda $\check{\psi}$. A função de onda por sua vez pode ser usada como uma função tentativa para um sistema com potencial externo v. De acordo com a assertiva do segundo teorema tem-se

$$E_0 = E_v[\rho] = F_{HK}[\rho] + \int \rho(r)v(r)dr \leq E_v[\check{\rho}] = F_{HK}[\widetilde{\rho}] + \int \check{\rho}(r)v(r)dr \quad (40)$$

Em um trabalho que mais tarde lhes valeu o prêmio Nobel de química, o teorema de H-K foi aplicado por Walter Kohn e Lu Jeu Sham para produzir a *teoria do funcional de densidade de Kohn-Sham* (KS DFT) (Parr & Yang, 1989). Dentro desse quadro, o intratável problema de muitos corpos de elétrons interagentes em um potencial externo estático é reduzido a um problema tratável de elétrons não-interativos movendo-se em um potencial efetivo. O potencial efetivo inclui o potencial externo e os efeitos das interações de Coulomb entre os elétrons, por exemplo, as interações de troca e correlação. Modelar as duas últimas interações torna-se a dificuldade dentro da KS DFT. A aproximação mais simples é a aproximação de densidade local (LDA), que é baseada na energia de troca exata para um gás de elétrons uniforme, que pode ser obtido do modelo de Thomas-Fermi e de ajustes na energia de

correlação para um gás de elétrons uniforme (Parr & Yang, 1989; Szabo & Outlund, 1989). Sistemas não interagentes são relativamente fáceis de resolver, além disso, a funcional de energia cinética de tal sistema é conhecida exatamente.

5.1.2.3 Equações Kohn-Sham

Para um sistema de muitos elétrons o estado fundamental de energia pode ser obtido a partir do mínimo da energia do funcional

$$E[\rho] = \int \rho(r)v(r)dr + F[\rho] \quad (41)$$

onde

$$F[\rho] = T[\rho] + V_{ee}[\rho] \quad (42)$$

A densidade do estado fundamental é a densidade que minimiza $E[\rho]$, partindo do pressuposto que o número de elétrons por unidade de volume é a densidade eletrônica

$$N = N[\rho(r)] = \int \rho(r)dr \quad (43)$$

Podemos inserir essa condição pelo método de Lagrange, onde a densidade eletrônica do estado fundamental deve satisfazer o seguinte princípio variacional

$$\delta\{E[\rho] - \mu[\int \rho(r)dr - N] = 0 \quad (44)$$

onde

$$\mu = \frac{\delta E[\rho]}{\delta p(r)} = v(r) + \frac{\delta F[\rho]}{\delta \rho(r)} \quad (45)$$

μ é o multiplicador de Lagrange e se refere ao potencial químico

A estrutura do funcional tem como base o modelo de Thomas-Fermi, no entanto o modelo de Thomas-Fermi consiste em uma aproximação das formas da energia cinética $T[\rho]$ e potencial de repulsão eletrônica V_{ee}, entretanto o a aproximação bruta deste modelo impõe muitas limitações ao mesmo. Kohn e Sham propuseram a introdução de orbitais no funcional de energia cinética, de modo que o mesmo pudesse ser computado de modo simples mas com

uma boa acurácia, deixando uma pequena correção residual que é tratada separadamente (Parr & Yang, 1989). O próximo passo dessa análise simplificada do principio de Kohn-Sham é entender como a introdução de orbitais foi realizada e obter o funcional de energia para assim expressão a base da teoria do funcional de densidade (DFT- density functional theory). É conveniente começar com a exata formula da energia cinética para o estado fundamental

$$T_s = \sum_i^N n_i \left\langle \psi_i \middle| -\frac{1}{2}\nabla^2 \middle| \psi_i \right\rangle (46)$$

onde ψ_i não é uma função de onda mas sim o spin orbital e n_i os números de ocupação (número partículas que ocupam um determinado estado quântico de acordo com o segundo princípio da quantização), onde de acordo com o princípio de Pauli, $0 \leq n_i \leq 1$. Segundo os princípios dos teoremas de Hohenberg-Kohn, T é um funcional da densidade eletrônica total que é dada por

$$\rho(r) = \sum_I^N n_i \sum_s |\psi_i(r,s)|^2 (47)$$

Para um sistema interativo, existem infinitos termos para as equações (46) e (47), entretanto Kohn e Sham mostraram um termo que poderia resolver o problema de forma bem simples, assumindo $n_i = 1$ para *N* orbitais, a representação da energia cinética se torna válida para a função de onda determinante que descreve elétrons não interativos, onde se tem

$$T_s[\rho] = \sum_i^N \left\langle \psi_i \middle| -\frac{1}{2}\nabla^2 \middle| \psi_i \right\rangle (48)$$

onde

$$\rho(r) = \sum_i^N \sum_s |\psi_i(r,s)|^2 (49)$$

válido para a função de onda determinante que descreve elétrons não interativos

$$\Psi = \frac{1}{\sqrt{N!}} \det[\psi_1 \psi_2 \psi_3 \ldots . \psi_N] (50)$$

onde $$T_S[\rho] = \left\langle \Psi \middle| \sum_i^N (-\frac{1}{2}\nabla^2) \middle| \Psi \right\rangle = \sum_i^N \left\langle \psi_i \middle| -\frac{1}{2}\nabla^2 \middle| \psi_i \right\rangle (51)$$

onde $\psi_i$se refere aos N estados referentes aos autovalores da função de onda. Entretanto a energia cinética definida $T_s[\rho]$ continua não sendo o exato funcional da energia cinética que foi idealizado no modelo Thomas-Fermi. Outro problema que surge diante das equações (48) e (49) é que para uma dada densidade $\rho(r)$ como poderíamos ter uma única decomposição em termos de orbitais de modo a fornecer um único valor de $T_S[\rho]$? Diante disso Kohn e Sham propuseram que $T[\rho]$ fosse o funcional de cinética puro e exato de um sistema em que os elétrons não interagissem como referência, a teoria resultante acaba por ser de forma de partículas independentes (Alcácer, 2007; Parr & Yang, 1989; Kohn & Sham, 1965). Para isso é necessário invocar o funcional $F[\rho]$ (42) de modo

$$F[\rho] = T_s[\rho] + J[\rho] + E_{xc}[\rho] \quad (52)$$

onde

$$E_{xc} = T[\rho] - T_S + V_{ee}[\rho] - J[\rho] \quad (53)$$

O funcional $E_{xc}[\rho]$ desse modo reflete a diferença entre $T[\rho]$ e T_S, refletindo a diferença entre o termo calculado e o termo puro (que se refere ao estado fundamental). Aplicando tal premissa na equação (45) temos a seguinte conclusão

$$\mu = \mathrm{v_{eff}}(r) + \frac{\delta T_s[\rho]}{\delta \rho(r)} \quad (54)$$

onde $\mathrm{v_{eff}}(r)$ é o potencial efetivo de Kohn-Sham, que é definido por

$$\mathrm{v_{eff}} = v(r) + \frac{\delta J[\rho]}{\delta \rho(r)} + \frac{\delta E_{xc}[\rho]}{\delta \rho(r)} = v(r) + \int \frac{\rho(r')}{|r-r'|} dr' + v_{xc}(r) \quad (55)$$

onde v_{xc} é o potencial de troca de correlação e é dado por

$$v_{xc}(r) = \frac{\delta E_{xc}[\rho]}{\delta \rho(r)} \quad (56)$$

O potencial efetivo possui uma densidade eletrônica que satisfaz a equação (54) pela simples relação de *N*-elétrons

$$\left[-\frac{1}{2}\nabla^2 + \mathrm{v_{eff}}\right]\psi_i = \varepsilon_i \psi_i \quad (57)$$

onde

$$\rho(r) = \sum_i^N \sum_s |\psi_i(r,s)|^2 (58)$$

Esse conjunto de equações trabalham de forma auto-consistente, onde a partir de uma ρ tentativa é obtido um v_{eff} (55) que aplicado nas euqações (57) e (58) geram uma nova $\rho(r)$, onde um valor ideal que satisfaça as condições (valores que convergem) são utilizados na equação (41) computando-se assim a energia total mínima do sistema em questão. Todas essas equações de Kohn-Sham são a base da teoria do funcional de densidade, ou, Density functional theory (DFT) (Duarte, 2001). O ultimo aspecto que suma importância da aplicação da teoria do funcional de densidade em cálculos de sistemas multieletrônicos é o uso de funcionais de troca e de correlação $E_{xc}[\rho]$ expressos nas equações (52), (53), (55) e (56). Existem inúmeros funcionais de troca de correlação, no entanto o mais usado ultimamente em modelagem molecular é o funcional híbrido B3LYP, (3 parâmetros de Axel Becke e mais três outros parâmetros de C.Lee, Weitao Yang e Robert Parr)

$$E_{xc}^{B3LYP} = E_{xc}^{LDA} + a_0(E_X^{HF} - E_X^{LDA}) + a_X(E_X^{GGA} - E_X^{LDA}) + a_c(E_C^{GGA} - E_C^{LDA})$$

onde a_0=0.20, a_X=0.72 e a_c=0.81, E_X^{HF} é o funcional de troca e correlação de Hartree-Fock, E_X^{GGA} é o funcional de troca de Axel Becke (Kohn & Becke, 1996) e E_C^{GGA} é o funcional de correlação eletrônica de C.Lee, Weitao Yang e Robert Parr (Parr & Yang, 1989; Kohn & Becke, 1996).

5.2. Metodologia computacional

Os cálculos quânticos foram realizados em PC INTEL Quadcore ™ PC (8 GB RAM) usando plataforma Debian LINUX (versão 5.0) e o software Gaussian 09 [Frisch, 2009]. Os cálculos de otimização geométrica foram realizados a nível DFT usando funcional B3LYP e a função de base 6-311G (2d,p) para os alcaloides stricnobrasilina, 12-hidroxi-10,11-dimetoxistricnobrasilina, liriodenina, cantinona e 7-metoxi-cantinona. Para o estudo do

strictosidina especificamente, foram empregadas funções de base 6-31G(d) e 6-311++G (2d,p). As geometrias obtidas foram submetidas a cálculos de escaneamento de energia potencial de superfície, que consistiram na variação de ângulos diedros para a obtenção de pontos mínimos de energia (confôrmeros), os quais foram submetidos a cálculos padrão de otimização e análise vibracional analítica usando algoritmo de Berny. Os espectros UV-Vis teóricos foram calculados usando as respectivas bases para cada alcaloide a nível TD-DFT. Os cálculos NBO (Natural Bond Orbitals) e de NLO (Non Linear Optics) foram realizados nas mesmas bases. Às atribuições das bandas IV-FT obtidas experimentalmente foram realizadas através do da opção de animação oferecida pelo software Gaussian, o qual possibilita a apresentação visual dos modos vibracionais, e pelo cálculo do potencial de distribuição de energia provido pelo software VEDA4 [Jamroz, 2004].

Cálculos de dockagem molecular foram realizados por meio do software AutoDock Vina, que utiliza uma função de pontuação (*scoring function*) atômica geral, que consiste em etapas sequenciais por meio perturbação randômica da conformação das moléculas seguida de uma otimização local (através do algorítimo de Broyden-Fletcher-Golfarb-Shanno) [Nocedal & Wright, 1999], onde cada otimização, em termos de energia livre de gibbs, é pontuada ou não. As otimizações são guiadas pelo critério de convergência. As estruturas 3D das enzimas-alvo foram obtidas do repositório internacional Protein Data Bank (PDB), disponível na internet. Para o estudo de interação com o complexo enzimático topoisomerase II-DNA, foi utilizada a estrutura cristalina com a identificação 4G0U. Para a interação com as enzimas dihidro-folatoredutase e protease aspártica de *Candida albicans* foram utilizadas as estruturas cristalinas 4HOE e 1ZAP, respectivamente. O protocolo de cálculo consistiu na definição do espaço de docagem (*grid Box*), o qual foi definido (para cada enzima) como o a região que compreende o sítio ativo e os aminoácidos envolvidos. A validação do *grid Box* consistiu na retirada do ligante original e acoplando-o, ou docando-o, novamente a estrutura usando o grid

Box definido. A comparação entre a estrutura docada e a estrutura cristalizada foi realizada mediante o calculo de desvio quadrático médio (RMSD). Valores de RMSD abaixo de 2 foram considerados suficientes para validar cada *grid Box*.

6. Resultados

O estudo teórico dos alcaloides, stricnobrasilina, 12 hidroxi-10,11-dimetoxi-stricnobrasilina, liriodenina, cantinona e 9-metoxi-cantinona usando a metodologia DFT resultaram em quatro publicações, que foram lançadas segundo o tipo e a similaridade estrutural das moléculas em estudo. De modo geral o estudo das moléculas alvo constituiu de uma abordagem teórica (cálculos de otimização geométrica, HOMO-LUMO, descritores de reatividade, cálculos NBO e NLO, simulação de espectros UV, IV e análise de docking molecular) somada a comparação a dados experimentais (espectros experimentais UV e IV, dados de cristalografia de raios-x e testes biológicos), com o intuito de buscar novas informações a cerca das estruturas e partir destas novas informações tentar compreender as propriedades físicas, químicas e biológicas das mesmas. Cada molécula apresenta peculiaridades e em alguns artigos alguns tipos de cálculos específicos foram realizados, como cálculos de scan, com o objetivo de realizar estudos conformacionais com o intuito de identificar confôrmeros estáveis, cálculos NLO (non linear opitcs) com o objetivo de estudar efeitos óticos não lineares que moléculas podem apresentar frente à incidência de um feixe de laser e formações de dímeros. O critério usado para a escolha das enzimas na análise de docking molecular foi unicamente os resultados das atividades biológicas in vitro registradas na literatura e comentada nos artigos a seguir. Informações suplementares dos artigos publicados se encontram na seção “Anexos”.

6.1. Investigação das propriedades químico-quânticas e análise de docking molecular com DNA topoisomerase II de acaloides β-carbolinicos isolados de *Simaba guianensis:* um estudo experimental e teórico

O presente artigo, publicado no prestigiado periódico Structural chemistry, constituiu no estudo das propriedades vibracionais, estruturais e quânticas dos alcaoides 9-metoxi-cantin-6-ona (cantinona) (I) e ácido 7-metoxi (9-H-β-carbolin-1-il)-Z-prop-2-enoico (7-metóxi-cantinona) (II) usando o funcional de troca de correlação B3LYP usando base de cálculo 6-311G (2d,p). O dados de otimização geométrica de ambas as estruturas foram comparadas com dados de cristalografia de raios-x para uma estrutura similar da literatura e um estudo conformacional para o alcaloide (II) foi realizado, promovendo uma boa compreensão acerca da estabilidade conformacional da molécula. Em adição, cálculos de NBO (Natural Bond Orbitals), cálculos de orbitais HOMO-LUMO, gaps de energia, mapas de potencial eletrostático e cálculos NLO foram realizados no mesmo nível teórico. Cálculos de espectro UV foram comparados com os espectros experimentais, permitindo com que as bandas fossem assinaladas. Os estudos vibracionais mostraram que, para o alcaloide II ligações de hidrogênio intramoleculares das conformações e ligações de hidrogênio intermolecular da forma dimérica influenciam de sobremaneira os espectros vibracionais. Cálculos de docking molecular com DNA topoisomerase II revelaram energias de ligação de -8.4 e -9.6 kcal/mol para II e I respectivamente, enquanto que para a amsacrina, molécula usada como padrão por ser um inibidor natural da topoisomerase II, apresentou um valor de ligação de -9.9 kcal/mol, mostrando uma boa docagem do alcaloide I, justificando resultados da literatura. Informações suplementares deste artigo se encontram na seção “ANEXO 1”.

Struct Chem (2018) 29:299–314
DOI 10.1007/s11224-017-1029-5

ORIGINAL RESEARCH

Quantum chemical properties investigation and molecular docking analysis with DNA topoisomerase II of β-carboline indole alkaloids from *Simaba guianensis*: a combined experimental and theoretical DFT study

Renyer A. Costa[1] · Kelson M. T. Oliveira[1] · Rita de Cássia Saraiva Nunomura[1] · Earle Silva A. Junior[2] · Maria Lucia B. Pinheiro[1] · Emmanoel V. Costa[1] · Andersson Barison[3]

Received: 23 May 2017 / Accepted: 22 August 2017 / Published online: 12 September 2017

Abstract A theoretical and experimental DFT study of the vibrational, structural, and quantum properties of 9-methoxy-canthin-6-one (I) and 7-methoxy-(9H-β-carbolin-1-il)-(Z)-prop-2-enoic acid (II) alkaloids is presented using B3LYP exchange-correlation functional with 6-311G(2d,p) basis set. The theoretical geometry optimization data of both structures were compared with the X-ray data for a similar structure in the associated literature and a conformational study is presented for (II), providing a good comprehension of its conformers' stability. In addition, natural bond orbitals (NBOs), HOMO-LUMO energy gap, mapped molecular electrostatic potential surface (MEPS) calculations, and first- and second-order hyperpolarizabilities were also performed at the same calculation level. The calculated UV spectra agreed well with the measured experimental data, with transitions assigned. Calculated HOMO/LUMO energy gaps revealed the excitation energy of the structures, justifying their stability and kinetics reaction. IR studies showed that for structure II the intramolecular hydrogen bond of the conformations and the intermolecular hydrogen bonds of the dimeric form influence the results and also revealed several characteristic vibrations for both structures. Molecular docking studies with DNA topoisomerase II-DNA complex showed binding free energies of − 8.4 and − 9.6 kcal/mol for II and I, respectively, while for amsacrine, used for the treatment of leukemia, the binding free energy ΔG presented a value of − 9.9 kcal/mol, showing a good binding affinity of alkaloid I.

Keywords β-carboline alkaloids · UV-vis · FT-IR · DFT · Hyperpolarizability · DNA topoisomerase II · Molecular docking

Introduction

Indole alkaloids constitute a wide range of chemical structures that possesses many biological activities like antiplasmodial [1, 2], cytotoxic [3–5], antibacterial [6], antifungal [7, 8], antimalarial [9], anti-inflammatory [10], and antidiabetic [11] playing a very important role in the natural products field. A common class of this group is the β-carboline indole alkaloids that possess a common tricyclic pyrido indole ring structure [12–15], whereas the partially or completely saturated ones are known as dihydrocarbolines and tetrahydrocarbolines, respectively. The β-carboline alkaloids were originally isolated from *Peganum harmala* (Zygophillaceae, Syrian Rue), which is being used as a traditional herbal drug and abortifacient in the Middle East and North Africa [16]. In the Amazon basin,

Electronic supplementary material The online version of this article (https://doi.org/10.1007/s11224-017-1029-5) contains supplementary material, which is available to authorized users.

✉ Renyer A. Costa
renyer.costa@gmail.com

✉ Kelson M. T. Oliveira
kelsonmota@ufam.edu.br

[1] Department of Chemistry, Federal University of Amazonas (DQ-UFAM), Manaus, Amazonas 69077-000, Brazil

[2] Federal Institute of Science and Technology of Amazonas (IFAM), Manaus, Amazonas 69020-120, Brazil

[3] NMR Laboratory, Department of Chemistry, Federal University of Paraná, Curitiba, Paraná 80060-000, Brazil

plants containing these alkaloids were widely used as hallucinogenic drinks or snuffs and numerous reports also disclosed that β-carboline alkaloids were extensively presented in extracts from the leaves, barks, and roots of a great variety of plants [17–20]. An example are *Simaba* plants, which have been outstanding for being a promising source of β-carboline alkaloids over the years [20–24] and for have many pharmacological properties such as cytotoxic, antitumor, antimalarial, antiviral, and antimicrobial [17]. As a matter of fact, β-carboline alkaloids of canthin-6-one and harmane type are chemical markers of *Simaba* genus plants and they have been related to the biological activities of these plants; however, despite the structural elucidation and pharmacological properties investigations of these alkaloids being very common in the literature, investigations of their structural, reactive, spectroscopic, and quantum properties are still lacking in the literature. In this context, theoretical quantum models such as DFT and advanced software make theoretical chemistry a powerful tool for the study of the properties of plants' secondary metabolites [25, 26]. The alkaloids 9-methoxycanthin-6-one and 7-methoxy-(9H-β-carbolin-1-il)-(Z)-prop-2-enoic acid (Fig. 1.), isolated from *Simaba guianensis* by one of our authors [22], are cases of structures that did not have their properties fully investigated yet.

From this premise, this work discusses 9-methoxycanthin-6-one and 7-methoxy-(9H-β-carbolin-1-il)-(Z)-prop-2-enoic acid from a theoretical view (geometry optimization, natural bond orbitals (NBO), and molecular electrostatic potential map surface (MEPS) calculations) based on experimental data (NMR, UV, FTIR), providing a more complete description of their structure and spectral behavior. To the best of our knowledge, no theoretical molecular modeling study that discusses the structural geometry and conformations was previously presented, and a detailed description of the spectroscopic behavior of these compounds with the help of quantum chemical DFT calculations along with NBO and non-linear optical (NLO) properties has not been performed yet. In view of the cytotoxic potential registered by Kardono et al. [3] for these two compounds, molecular docking studies were also performed with DNA topoisomerase II, for being an essential nuclear enzyme which manages the topology of DNA during cellular processes such as replication, transcription, recombination, and chromatin remodeling, resulting in an attractive drug target against cancer.

Methodologies

The alkaloids 9-methoxycanthin-6-one and 7-methoxy-(9H-β-carbolin-1-il)-(Z)-prop-2-enoic acid have been isolated from *S. guianensis ecaudata* (Cronquist) collected on a period of rainfall at the Adolpho Ducke Forest Reserve, located on the AM-010 highway, 23 km from Manaus City, in the state of Amazonas. The isolation methodology and spectroscopic data obtainment were described in previous works [22]. The theoretical quantum chemical calculations were performed using the Gaussian 09 D.01 Program [27] on Debian LINUX (5.0 version) platform on an INTEL Quadcore™ PC. The DFT approach was used for the calculations using the 6-311G(2d,p) basis sets and the B3LYP functional. Potential energy surfaces were scanned for structures using relaxed dihedral angle scan coordinates, and all minima geometries were fully optimized by the force gradient method using Berny's algorithm and standard analytical harmonic vibrational analysis (no imaginary frequencies or negative eigenvalues were found). The theoretical IR spectra were obtained from the DFT intensities in combination with the calculated vibrational wavenumbers uniformly scaled by a factor of 0.98. The UV spectra were calculated using the TD-B3LYP-FC functional and 6-311G(2d,p) basis set in methanol using the PCM model. The NBO values were obtained with the NBO 3.1 program, as implemented in the GAUSSIAN 09 package at the same basis set. The assignments of the calculated IR wavenumbers are aided by the animation option of GAUSSVIEW 5.0 program, which gives a visual presentation of the vibrational modes [28]. The potential energy distribution (PED) was calculated with the help of the VEDA4 software package [29].

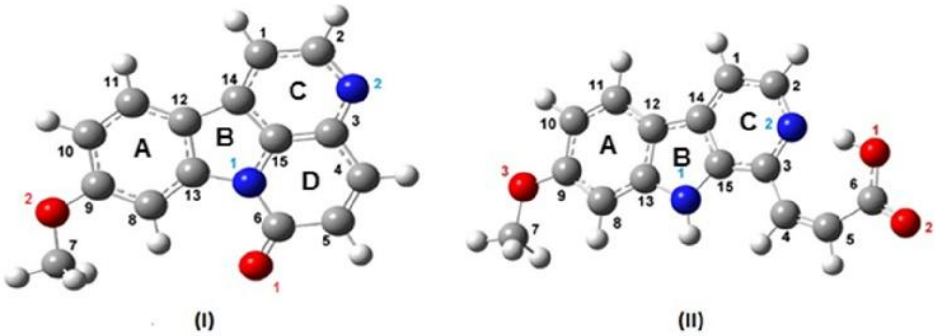

Fig. 1 Optimized structures of 9-methoxycanthin-6-one (I) and 7-methoxy-(9H-β-carbolin-1-il)-(Z)-prop-2-enoic acid (II)

Results and discussions

Geometry optimization

The theoretical geometry optimization data of the studied molecules, which were calculated using the B3LYP/6-311G(2d,p) approach, were compared with X-ray data for 5-methoxycanthin-6-one [30], due to the structural similarity (Table S1 in the "supplementary material" section). The two compounds show significant polarities being 9-methoxycanthin-6-one soluble in chloroform, ethyl acetate, and methanol, while 7-methoxy-(9H-β-carbolin-1-il)-(Z)-prop-2-enoic acid is soluble in acetonitrile and water, with theoretical dipole moments of 1.94 and 10.21 D, respectively. The structures showed stable conformations and good structural cohesion with C1 symmetry and energy values of − 837.81 and − 914.26 a.u., respectively.

9-Methoxycanthin-6-one presents a planar structure that shows slight distortions in its rings. Concerning to the bond lengths, the benzene ring shows certain uniformity revealing values around ~ 1.39 A°. In the B ring, N1-C13 and N1-C15 bonds are slightly distorted because the N1 atom is attached to the C6 atom that presents a positive partial charge, since it is a carbonyl group, shortening the N1-C6 connection, making the pentacyclic ring non-uniform. C and D rings reveal certain uniformity showing similar bond length values, except for N1-C15, C6-N1, N2-C2, and N2-C3 bonds. Relative to the bond angles values, the entire structure shows distortions: Ring A presented angles with values of 121.225° (C8-C9-C10), 120.899° (C9-C10-C11), 119.405° (C10-C11-C12), and 116.758° (C13-C8-C9); Ring B showed values of 111.354° (N1-C15-C14), 105.52° (C15-C14-C12), 107.24° (C14-C12-C13), and 108.42° (C12-C13-N1); Ring C showed values of 115.433° (C1-C14-C15), 120.094° (C15-C3-N2), 117.092° (C3-N2-C2), 125.718° (N2-C2-N1), and 117.828° (C2-C1-C14); and Ring D showed values of 115.689° (C15-C3-C4), 120.035° (C3-C4-C5), 124.287° (C4-C5-C6), and 121.783° (C6-N1-C15).

For 7-methoxy-(9H-β-carbolin-1-il)-(Z)-prop-2-enoic acid, the most stable conformation presents a planar structure with small distortions in its rings, similar to those of 9-methoxycanthin-6-one (see Figs. 1 and 2). Concerning to the bond lengths, the benzene ring presented a certain uniformity with values of 1.391 Å (C8-C9), 1.413 Å (C9-C10), 1.380 Å (C10-C11), 1.401 Å (C11-C12), and 1.411 Å (C12-C13), showing a variance of 0.071 Å (Table S1). The five-membered ring showed slight distortions, but compared to the bonds of the five-membered ring of 9-methoxycanthin-6-one molecule, the distortions are less significative because the N1 atom is not attached to a C6=O group, presenting the bond length values 1.383 Å (N1-C13), 1.391 Å (N1-C15), 1.411 Å (C12-C13), 1.418 Å (C14-C15), and 1.440 Å (C12-C14). The C ring presented slight distortions with bond length values 1.387 Å (C2-N2), 1.336 Å (C2-N2), 1.399 Å (C14-C15), and 1.392 Å (C14-C1). Relative to the bond angle values, the entire structure presents a certain uniformity compared to 9-methoxycanthin-6-one structure; in fact due to the absence of ring D, cohesion to the indole moiety was thus provided (see Table S1). Guided by the possibility of formation of conformers, by the rotation around C3-C4 axis, a scan calculation has been performed which consisted of 60 steps varying by 6° (totalizing a 360° turn) the angle between the β-carboline moiety and –C4HC5HC6O2O1 H planes (Fig. 2). From the results, it is notable that conformer A is the most stable followed by conformer D with energy values of − 573,710.00 and − 573,703.44 kcal/mol, respectively, presenting ΔE of 7 kcal (A → D). The non-planar conformations showed the highest energies with emphasis on conformations B (− 573,699.88 kcal/mol), C (− 573,700.1 kcal/mol), and E (− 573,695.5 kcal/mol), that show ΔE values of 11 kcal (A → B), 10 kcal (A → C), and 14 kcal (A → E). It is important to report that the conformations A and D presented different dipole moment values, 10.2 and 3.7 D, respectively, showing that conformational changes influence the polarity of a molecule, because when a certain axis is rotated the dipole vectors change their direction being possible that they add or cancel to each other providing a new dipole resultant vector.

Electrostatic potential maps

The MEPS is a helpful tool for predicting sites and relative reactivity towards electrophilic and nucleophilic attacks, studies of biological recognition, and for predicting hydrogen bonding interactions and interactions between the same molecules (forming clusters and crystal structures) or other molecules. MEPS consists in a plot of electrostatic potential mapped onto the constant electron density surface where negative electrostatic potential corresponds to a region that attracts the proton due to the high electron density (and is colored in shades of red); the positive electrostatic potential corresponds to repulsion of the proton in regions where low electron density exists and the nuclear charge is partially deshielded (and is colored in shades of blue). Potential increases in the order red < yellow < green < blue (Fig. 3).

9-Methoxycanthin-6-one (I) shows polarized regions with positive potentials over H2 (0.0155 a.u.), H1 (0.0265 a.u.), H11 (0.0260 a.u.), H10 (0.0166 a.u.), H4 (0.0178 a.u.), and H5 (0.0157 a.u.) atoms and negative potentials over O1 (− 0.0461 a.u.), N2 (− 0.0401 a.u.), and O2 (− 0.0202 a.u.); being the lone pair of N2 not incorporated into the aromatic π system. The MEPS of 7-methoxy-(9H-β-carbolin-1-il)-(Z)-prop-2-enoic acid (II) shows polarized regions with positive potentials over CH_3 (0.0334 a.u.) and over the hydrogen atoms H9 (0.0745 a.u.), H10 (0.0201 a.u.), H11 (0.0293 a.u.), H12 (0.0291 a.u.), and H1 (0.0213 a.u.). Negative potentials were observed over O1 (− 0.0664 a.u.), O2 (− 0.0741 a.u.), and O3

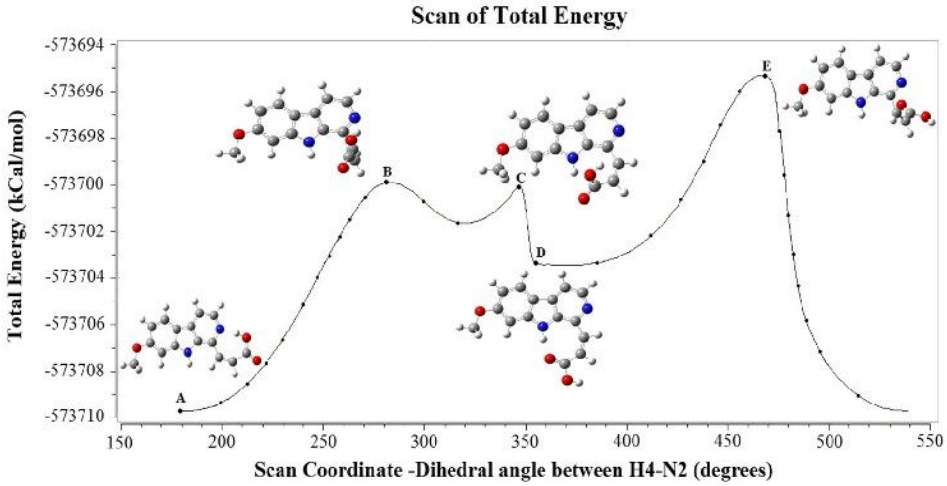

Fig. 2 Potential surface energy scan calculation for structure II

(− 0.0118 a.u.) atoms. The potential over the rings A, B, and C presented good electronic density distribution with values − 0.0032, 0.0060, and − 0.0031 a.u., respectively, which indicates a resonant system with distributed electron density. Guided by the opposite charges of the MEPS calculated for II, it was possible to infer the formation of intramolecular hydrogen bonds between N2—H-O1 and N1-H—O2 which occur in the conformers A and D (Fig. 2), respectively; however, like 9-methoxycanthin-6-one, the lone pair of N2 atom is not incorporated into the aromatic π system, which makes the hydrogen bond N2—H-O1 more stable than N1-H—O2 because the transfer of charge is more effective, making conformer A more stable.

HOMO and LUMO analysis

The energy gap between the HOMO (highest occupied molecular orbital) and LUMO (lowest unoccupied molecular orbital) is very important for determining the electrical properties, kinetic stability, and chemical reactivity descriptors, such as hardness and softness, of a molecule. The concept of hardness (η) and softness is related to a compound's reactivity and is a property that measures the extent of chemical reactivity to which the addition of a charge stabilizes the system. The chemical potential (μ) provides a global reactivity index and is related to charge transfer from a system of higher chemical potential to one of lower chemical potential. Electronegativity (χ) is the power to attract electrons which is equal to the negative of the chemical potential. All these properties are defined as follows [31, 32]:

$$\eta = \frac{1}{2}\left(\frac{\partial_2 E}{\partial N_2}\right)V_{(r)} = \frac{1}{2}\left(\frac{\partial_\mu}{\partial N}\right)V_{(r)}$$

$$\mu = \left(\frac{\partial E}{\partial N}\right) \quad V_{(r)}$$

$$\chi = -\mu = -\left(\frac{\partial E}{\partial N}\right) V_{(r)}$$

Where, E and $V_{(r)}$ are the electronic energy and the external potential of an N-electron, respectively. According to the Janak theorem [33] and Perdew et al. [34] for closed-shell molecules, these global chemical reactivity descriptors can be simplified and defined as follows:

$$\eta = \frac{(I-A)}{2}$$

$$\mu = \frac{-(I+A)}{2}$$

$$\chi = \frac{(I+A)}{2}$$

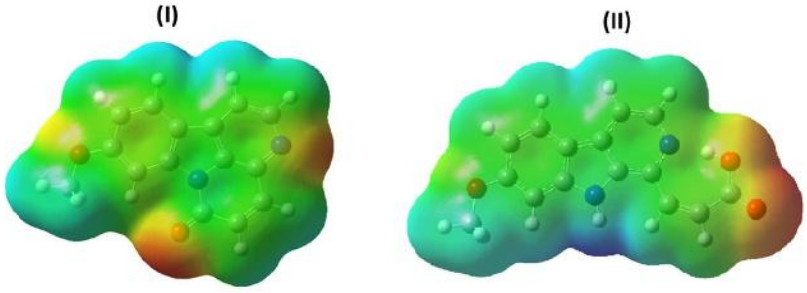

Fig. 3 Calculated molecular electrostatic potential maps for 9-methoxycanthin-6-one (I) and 7-methoxy-(9H-β-carbolin-1-il)-(Z)-prop-2-enoic acid (II) at DFT B3LYP/6-311G(2d,p)

Where, I is the ionization potential and A is the electron affinity of the molecule. The ionization energy and electron affinity are obtained from the HOMO and LUMO energies as $I = -E_{HOMO}$ and $A = -E_{LUMO}$. In terms of chemical hardness, a large HOMO-LUMO gap indicates a hard molecule and is related to more stable molecules, whereas a small gap indicates a soft molecule and is related to a more reactive molecule.

Another important descriptor is the electrophilicity index (ω), a global maximum reactivity index that is related to chemical hardness and chemical potential. The electrophilicity index measures the global electrophilic nature of a molecule and was proposed by Parr et al. [35] as a measure of energy lowering due to charge transfer. The electrophilicity index is defined as follows:

$$\omega = \left(\frac{\mu^2}{2\eta}\right)$$

This parameter permits the classification of organic molecules as strong, $\omega > 1.5$ eV, moderate, $0.8 < \omega < 1.5$ eV, and marginal electrophiles, $\omega < 0.8$ eV [36]. However, when the molecule bears more than one functional group with opposite electrical charges, its nucleophilic character cannot be straightforwardly associated with the inverse of the electrophilicity. Thus, the nucleophilicity index (N) appears as a different descriptor which gives more information about nucleophilicity and is defined [36, 37]:

$$N = E_{HOMO} - E_{HOMO\ (TCE)}$$

Where, tetracyanoethylene (TCE) is taken as reference. All these properties were calculated for the *S. guianensis* β-carboline alkaloids at B3LYP/6-311G(2d,p) basis sets using the above equations and their values are shown in Table 1. As seen in Fig. 4, the calculated HOMO for I is located in the β-carboline moiety and the LUMO is located in the entire structure; for II, both HOMO and LUMO are located in the entire structure. Structure I has a HOMO-LUMO gap value slightly smaller than that calculated for II ($\Delta E = 0.10$ eV) revealing I to be slightly more reactive; however, the variation is not too significant and does not influence directly the hardness, electronegativity (χ), electrophilicity index (ω), and chemical potential (μ) values, thus justifying their similar values (see Table 1). Comparing these parameters to the calculated ones for other known natural occurring structures [25, 26, 38–41], these two molecules can be classified as soft molecules.

UV-vis analysis

The electronic spectra of 9-methoxycanthin-6-one (I) and 7-methoxy-(9H-β-carbolin-1-il)-(Z)-prop-2-enoic acid (II) in methanol solution phase were compared to the calculated spectra at time-dependent density functional using B3LYP-611G(2d,p) basis set in methanol (PCM model) (Fig. 5). The experimental spectrum of structure I presented bands at 208, 272, 311, 353, and 380 nm that were assigned to the sum of the $n \rightarrow \pi^*$ and $\pi \rightarrow \pi^*$ transitions characteristic of canthin-6-one alkaloids [42]. The theoretical spectrum presented an intense electronic transition of 5.76 eV at 215.1 nm (oscillator strength $f = 0.8587$) with major contributions from H-6 → L (16%), H-2 → L + 1 (31%), H-1 → L + 3 (14%), and H → L + 3 (21%), being equivalent to the experimental band at 208 nm. The calculations also showed intense electronic transitions at 268.35 (4.620 eV), 300.73 (4.123 eV), 347.54 (3.56 eV), and 383.19 nm (3.23 eV) that are equivalent to the experimental bands 272, 311, 353, and 380 nm, respectively. These four calculated absorption wavelengths correspond to the contributions of the electronic transitions from H → L + 1 (82%) for 268 nm, H-2 → L (87%) for 300.7 nm, H-1 → L (94%) for 347.5 nm, and H → L (96%) for 383.19 nm. The experimental spectrum of structure II presented bands at 244, 302, and 350 nm characteristic of harman alkaloid transitions [43]. The theoretical spectrum revealed an intense electronic transition of 5.33 eV at 232.6 nm (oscillator strength $f = 0.4205$) with major contributions from H-1 → L + 2 (28.8%), H-6 → L (27.9%), and H → L + 2 (16%) being equivalent to the experimental band at 244 nm. The calculations also presented intense electronic transitions at 287.58 nm (4.311 eV) and 374.07 nm (3.314 eV) that are equivalent to the experimental bands at 302 and 350 nm, respectively. These two calculated absorption wavelengths corresponded to the contributions of the electronic transitions from H-2 → L (71%) for 287 nm and H-1 → L (89%) for 374 nm (see Figure S1 in "supplementary material").

IR analysis

Figures 6 and 7 show the superimposition of the experimental and theoretical IR spectra of 9-methoxycanthin-6-one (I) and 7-methoxy-(9H-β-carbolin-1-il)-(Z)-prop-2-enoic acid (II) alkaloids. The assignment of the experimental bands to the normal modes of vibration was made using the optimized structures with the lowest potential energy (Fig. 1). A total of 90 normal vibrations modes were obtained for 7-methoxy-(9H-β-carbolin-1-il)-(Z)-prop-2-enoic acid and 81 vibration modes were obtained for 9-methoxycanthin-6-one but were compared with the experimental spectrum only the modes between 400 and 4000 cm^{-1} in both cases (see Tables 2 and 3).

The experimental IR spectrum of 9-methoxycanthin-6-one showed bands in the 3200–2500, 1700–1000, and 980–400 cm^{-1} regions. The bands between 3200 and 2500 cm^{-1} were assigned to aromatic C-H stretching vibration modes (bands at 3117 and 3100 cm^{-1}) and CH_3 stretching modes (bands at 3063, 3011, and 2834 cm^{-1}). Bands between 1700 and 1000 cm^{-1} were assigned to C=O stretching vibration

Table 1 Calculated energy parameters for the studied β-carboline indole alkaloids from *Simaba guianensis*

Parameters	7-Methoxy-(9H-β-carbolin-1-il)-(Z)-prop-2-enoic acid	9-Methoxycanthin-6-one
Energy (a.u.)	−914.27	−837.81
Dipole moment (debye)	10.21	1.94
E_{HOMO} (eV)	−6.32	−6.22
E_{LUMO} (eV)	−2.35	−2.35
$E_{HOMO\text{-}LUMO}$ (eV)	3.97	3.87
E_{HOMO-1} (eV)	−6.45	−6.43
E_{LUMO+1} (eV)	−1.15	−0.99
$E_{(HOMO-1)-(LUMO+1)}$ (eV)	5.30	5.45
Hardness (η)	1.98	1.94
Chemical potential (μ)	−4.34	−4.29
Electronegativity (χ)	4.34	4.29
Electrophilicity index (ω)	4.76	4.74
Nucleophilicity index (N)	4.68	4.78

(band at 1667 cm^{-1} that corresponds to calculated theoretical scaled wavenumber 1701 cm^{-1}), C=C stretching vibrations (bands at 1634, 1562, 1493, 1451, 1421, and 1332 cm^{-1} that correspond to the theoretical scaled wavenumbers 1627, 1565, 1493, 1454, 1424, and 1343 cm^{-1}), N=C stretching vibrations (bands at 1332 and 1249 cm^{-1} that corresponds to the scaled theoretical wavenumbers 1343 and 1250 cm^{-1}), and H-C=C bend vibration modes (bands at 1223, 1108, and 1058 cm^{-1} that correspond to the theoretical scaled wavenumbers 1225, 1105, and 1055 cm^{-1}). Bands between 1000 and 400 cm^{-1} are mostly related to torsions (distortions between dihedral angles) of OCNC, HCCC, CNCC, CCCC, HCCN, and HCNC types and out of plane vibration modes of HCCH, HCCC, and CCCC types.

The assignment of the experimental bands of 7-methoxy-(9H-β-carbolin-1-il)-(Z)-prop-2-enoic acid in the 3500–2900 cm^{-1} region infers that bands at 3460-3390 (broad band) and 2855 cm^{-1} correspond to H—N2 stretching of D conformer (that presents N1-H–O2 hydrogen bond) and H—O stretching of A conformer (that presents N2—HO1 hydrogen bond) with theoretical scaled wavenumber values of 3430 and 2920 cm^{-1}, respectively. Guided by the opposite charges of conformer A presented in the calculated electrostatic potential map (Fig. 3), we inferred the formation of a dimer as seen in Fig. 8 that showed two bands (scaled) in this region, 3347.26 cm^{-1} (H—N1 + H—O stretching) and 2862.56 cm^{-1} (H—O stretching), indicating that the intermolecular hydrogen bond N1-H1—O2 contributes to the experimental bands in this region (see Fig. 7). The experimental band at 1734 cm^{-1} was related to C=O stretching vibration mode that

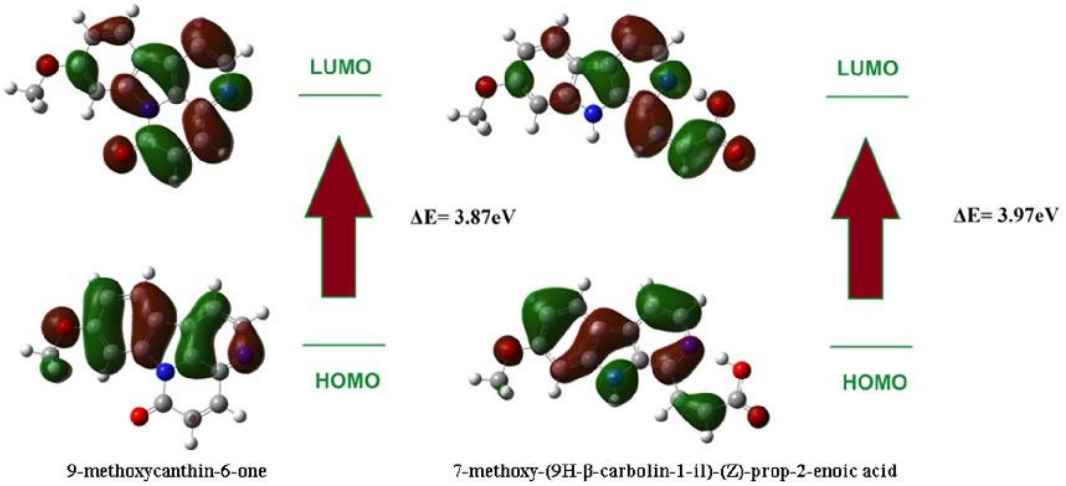

Fig. 4 Calculated frontier molecular orbitals for 9-methoxycanthin-6-one (I) and 7-methoxy-(9H-β-carbolin-1-il)-(Z)-prop-2-enoic acid (II) at DFT–B3LYP/6-311G(2d,p) basis set level

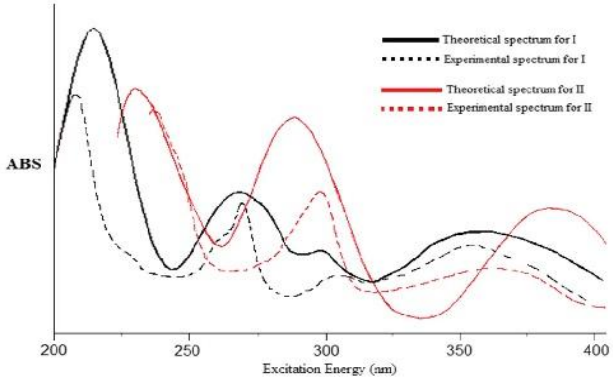

Fig. 5 Comparison between experimental and theoretical at B3LYP 6-311G(2d,p) UV spectra in methanol (PCM model) of 9-methoxycanthin-6-one (I) and 7-methoxy-(9H-β-carbolin-1-il)-(Z)-prop-2-enoic acid (II)

corresponds to the scaled theoretical wavenumber 1763 cm^{-1} of conformer D and 1749 cm^{-1} of conformer A, showing that the C=O stretching of form A is closest to the experimental data. For the dimer, the C=O stretching vibration occurs at 1717 cm^{-1} revealing that the intermolecular interaction of the proposed dimer is plausible. Bands between 1700 and 1000 cm^{-1} were related to C=C stretching vibration modes (experimental bands at 1673, 1634, 1611, 1459, 1374, 1332 and 1276 cm^{-1} that were assigned to C4=C5, C14=C1, C10=C11, C12=C13, C9=C10 and C1=C2 stretching vibrations), N=C stretching vibrations (assigned to the experimental bands at 1611, 1387, 1332, 1175 and 1099 cm^{-1}), CH_3 wagging mode (assigned to the experimental band at 1430 cm^{-1}), O-C stretching modes (assigned to the experimental bands at 1309, 1276, and 1175 cm^{-1}), and H-C = C bend vibrations (assigned to the bands at 1387, 1309, 1225 and 1175 cm^{-1}). Bands between 1000 and 400 cm^{-1} are mostly related to torsions (distortions between dihedral angles) of OCCC, HCCO, HOCC, CCCC, HCCN, HCNC, and HCCC types and out of plane modes of HCCH, HCCC, NCCC, CCCC, and CCOO types.

NBO analysis

NBO analysis describes the Lewis-like molecular bonding pattern of electron pairs (or of individual electrons in the open-shell case) in optimally compact form. NBOs determine the localized Natural Lewis Structure (NLS) representation of the wave function, while the remaining "non-Lewis"-type NBOs complete the span of the basis and describe the residual "delocalization effects" by the second-order perturbation energies E(2) [donor (i) → acceptor (j)] that involve the most important delocalizations and are given by [44–47]:

$$E^2 = \Delta_{ij} = q_i \frac{F_{ij\,2}}{\varepsilon_i - \varepsilon_j}$$

Thus, NBOs provide a valence bond-type description of the wave function, closely linked to classical Lewis structure concepts and is a helpful tool for understanding the delocalization of electron density [48–50]. The NBO analysis of the two structures revealed strong π → π* and n → π* hyperconjugative intramolecular interactions formed by orbital overlaps between C==C bondings and C==C antibondings and between N and O lone pairs (LP) and C==C and C-C antibondings, leading to an intramolecular electron density delocalization causing stabilization of the molecular systems (see Tables S2 and S3 in "supplementary material"). For 9-methoxycanthin-6-one, the second-order perturbation energy analysis shows that the greater E^2 values are the π → π* hyperconjugations C2-N2 → C14-C1 (11.89 kcal/mol), C2-N2 → C15-C3 (21.82 kcal/mol), C5-C4 → C6-O (22.44 kcal/mol), C9-C8 → C13-C12 (25.41 kcal/mol), C13-C12 → C14-C1 (23.12 kcal/mol), C14-C1 → C15-C3 (20.19 kcal/mol), C14-C1 → C2-N2 (27.21 kcal/mol), and C15-C3 → C14-C1 (18.35 kcal/mol). For 7-methoxy-(9H-β-carbolin-1-il)-(Z)-prop-2-enoic, the strongest hyperconjugative intramolecular interactions are the π → π* conjugations C10-C11 → C9-C8 (22.40 kcal/mol), C10-C11 → C13-C12 (14.98 kcal/mol), C9-C8 → C10-C11 (13.48 kcal/mol), C9-C8 → C13-C12 (23.75 kcal/mol), C13-C12 → C10-C11 (21.58 kcal/mol), C14-C15 → N2-C3 (30.21 kcal/mol), C1-C2 → C14-C15 (20.85 kcal/mol), N2-C3 → C1-C2 (23.43 kcal/mol), C4-C5 → N2-C3(15.20 kcal/mol), and C4-C5 → C6-O1 (13.37 kcal/mol).

σ → σ* type hyperconjugative intramolecular interactions also occur in both structures and contribute to the stabilization of the systems, deserving prominence the interactions C1-C2 → C12-C14 (6.26 kcal/mol), C2-H2 → N2-C3 (5.58 kcal/mol), C4-H4 → C6-C5 (5.37 kcal/mol), C9-C8 → C13-N1 (6.17 kcal/mol), C11-C10 → C12-C14 (5.13 kcal/mol), C13-C12 → C14-C1 (5.40 kcal/mol), C14-C15 → C11-C12 (5.40 kcal/mol), and C14-C15 → C15-C3 (5.54 kcal/mol) for 9-methoxycanthin-6-one and C4-H4 → C5-C6 (7.21 kcal/mol), C5-H5 → C3-C4 (8.54 kcal/mol), C9-C8 → C13-N1 (5.60 kcal/mol), C13-C12 → C14-C1 (5.47 kcal/mol), C1-C2 → C12-C14 (5.62 kcal/mol), and C2-H3 → N2-C3 (6.06 kcal/mol) for 7-methoxy-(9H-β-carbolin-1-il)-(Z)-prop-2-enoic acid. The hydrogen bond C6-O1H—N2 that gives stability for the conformer A of 7-methoxy-(9H-β-carbolin-1-il)-(Z)-prop-2-enoic acid (II) is justified by the strong hyperconjugative interaction N2 → H-O1 (LP → σ*, 58.98 kcal/mol) (Fig. 2 and Table S3). For

Table 2 Experimental and calculated wavenumbers (cm^{-1}) and assignments for 9-methoxycanthin-6-one

IR solid	B3LYP 6-311 (2d,p)			PED
	Calculated unscaled	Calculated scaled	IR intensity	
	3248.98	3184.00	5.24	STRE C8-H8 (99%)
	3204.67	3140.58	2.89	STRE C5-H5 (90%)
	3197.13	3133.19	6.71	STRE C11-H11(12%) + STRE C10-H10 (87%)
	3186.54	3122.81	12.98	STRE C1-H1 (94%)
3117	3179.14	3115.56	4.58	STRE C4-H4 (91%)
3100	3175.05	3111.55	3.90	STRE C11-H11 (87%) + STRE C10-H10 (12%)
	3150.55	3087.54	25.55	STRE C2-H2 (95%)
3063	3136.87	3074.13	22.70	STRE C7-H7 (90%)
3011	3074.03	3012.55	28.84	STRE C7-H7 (50%)
2834	3013.77	2953.49	44.46	STRE C7-H7 (90%)
1667	1736.46	1701.73	425.02	STRE O=C6 (74%) + BEND C6-N1-C15 (10%)
1634	1660.84	1627.62	157.04	STRE C5=C4 (13%) + STRE C13-C8 (11%) + STRE C3-C15 (26%)
1608	1647.65	1614.70	124.21	STRE C13-C8 (25%) + STRE C11-C12 (11%)
	1617.00	1584.66	5.98	STRE N2=C2 (10%) + STRE C1=C14 (17%) + STRE C14=C15 (15%)
	1609.51	1577.32	4.33	STRE C11=C12 (17%) + STRE C9=C10 (24%) + BEND C13-C8=C9 (10%)
1562	1597.04	1565.10	32.60	STRE C5=C4 (29%) + STRE C1=C14 (23%)
1493	1524.04	1493.56	104.95	STRE C8=C9 (13%) + BEND C8=C9-C10 (10%)
–	1506.96	1476.82	13.47	BEND H-C7-H (73%) + TORS H-C7-O-C9 (20%)
–	1495.24	1465.34	8.72	BEND H-C7-H (74%) + TORS H-C7-O-C9 (17%)
	1493.58	1463.71	23.13	STRE N2=C3 (13%) + BEND H2-C2=N2 (31%)
1451	1483.61	1453.94	86.85	STRE C10=C11 (15%)
–	1476.05	1446.53	48.04	BEND H8-C8-C13 (13%) + BEND H-C7-H (52%)
1421	1453.83	1424.75	76.61	STRE C10=C11 (14%) + STRE C13=C8 (10%) + BEND H10-C10=C11 (10%) + BEND H1-C1=C2 (11%)
1391	1419.52	1391.13	15.93	BEND H2-C2=N2 (19%) + BEND H5-C5=C4 (28%) + BEND H4-C4=C5 (20%)
1332	1371.41	1343.98	35.60	STRE C8=C9 (16%) + STRE N1=C15 (15%)
–	1350.32	1323.31	61.96	STRE C12-C14 (23%) + BEND H1-C1=C2 (15%)
	1332.98	1306.32	16.50	STRE N2=C2 (11%) + STRE C11=C12 (10%) + STRE N2=C3 (12%)
–	1328.95	1302.37	70.27	BEND C13-C8=C9 (15%)
1275	1301.20	1275.18	120.14	STRE C13-C8 (10%) + BEND H11-C11=C10 (19%) + BEND H8-C8-C13 (14%)
	1286.99	1261.25	90.44	STRE N2=C2 (15%) + STRE N1-C6 (11%)
1249	1275.82	1250.30	50.00	STRE N2=C2 (22%) + STRE N2-C3 (10%) + BEND H2-C2=N2 (25%) + BEND H5-C5=C4 (11%)
1223	1249.65	1224.66	93.99	STRE O-C9 (12%) + BEND H8-C8=C13 (19%)
1189	1212.37	1188.12	2.24	BEND H-C7-H (12%) + TORS H-C7-O-C9 (48%)
	1183.97	1160.29	12.19	STRE C10=C11 (11%) + BEND H11-C11=C10 (11%) + BEND H10-C10=C11 (11%) + BEND H5-C5=C4 (11%)
1152	1171.58	1148.15	1.07	BEND H-C7-H (28%) + TORS H-C7-O-C9 (72%)
	1170.74	1147.33	83.27	BEND H10-C10=C11 (13%) + BEND H4-C4=C5 (10%)
1108	1128.29	1105.72	18,35	BEND H11-C11=C10 (15%) + BEND H10-C10=C11 (14%)
	1108.55	1086.38	19.11	BEND C13-C8=C9 (10%) + BEND H5-C5=C4 (10%) + BEND H4-C4=C5 (14%) + BEND C2-N2=C3 (10%)
1058	1077.21	1055.67	20.21	BEND H1-C1=C2 (26%) + BEND C2-N2=C3 (10%) + BEND C14=C15-C3 (14%)
	1053.24	1032.18	50.96	STRE O-C7 (63%)
–	1010.54	990.33	0.10	TORS H5-C5=C4-C3 (29%) + TORS H4-C4=C5-C6 (43%) + TORS C5=C4-C3-C15 (17%)
–	1009.16	988.98	0.20	STRE C14= C15 (10%) + BEND C13-C8=C9 (13%) + BEND N2=C3-C15 (10%)
975	993.11	973.25	1.82	BEND C1-C14=C15 (14%) + BEND C9-C10=C11 (10%)

Table 2 (continued)

IR solid	B3LYP 6-311 (2d,p)			PED
	Calculated unscaled	Calculated scaled	IR intensity	
	972.73	953.28	0.37	TORS H1-C1=C2-N2 (20%) + TORS H2-C2-N2=C3 (66%)
–	951.38	932.35	0.08	TORS H11-C11=C10-C9 + (49%) TORS H10-C10=C11-C12 (37%)
916	937.38	918.63	11.00	STRE C4-C3 (11%) + BEND C12-C14=C15 (13%)
–	886.22	868.50	24.94	TORS H8-C8-C13-N1 (82%)
844	867.40	850.05	39.23	TORS H5-C5=C4-C3 (31%) + TORS H4-C4=C5-C6 (13%) + TORS C1-C4-C15-C12 (10%) + OUT O=C6-N1-C5 (10%)
834	852.76	835.70	23.20	STRE C8=C9 (14%) + STRE C9-C10 (10%)
–	847.20	830.26	4.89	TORS H1-C1=C2-N2 (28%) + TORS H5-C5=C4-C3 (12%) + TORS H4-C4=C5-C6 (11%) + OUT O=C6-N1-C5 (10%)
815	832.36	815.71	42.72	TORS H11-C11=C10-C9 (24%) + TORS H10-C10=C11-C12 (33%) + TORS H1-C1=C2-N2 (20%) + OUT O-C9-C10 =C8 (10%)
788	816.76	800.42	0.43	TORS C2-N2=C3-C15 (17%) + OUT O=C6-N1-C5 (18%)
–	769.99	754.59	034	TORS C13-C8=C9-C10 (22%) + TORS C8=C9-C10=C11 (18%) + TORS C9-C10=C11-C12 (29%)
–	768.85	753.47	0.15	BEND N1-C15-C3 (10%) + BEND C2-N2=C3 (10%) + BEND C6-N1-C15 (12%)
–	712.05	697.81	0.28	TORS H5-C5=C4-C3 (16%) + OUT O=C6-N1-C5 (22%)
694	710.01	695.81	3.40	STRE C9-C10 (12%) + BEND C10-C11-C12 (13%) + BEND C9-C10=C11 (20%)
–	697.40	683.45	3.18	BEND C2-N2=C3 (14%) + BEND C8=C9-C10 (16%)
–	649.59	636.60	2.58	TORS C13-C8=C9-C10 (11%) + TORS C8=C9-C10=C11 (22%) + TORS C9-C10=C11-C12 (18%) + OUT O-C9-C10=C8 (21%)
619	630.47	617.86	11.94	BEND O=C6-C5 (13%) + BEND C4-C3=N2 (13%)
–	626.21	613.69	0.01	TORS C2-N2=C3-C15 (35%) + TORS C1-C4-C15-C12 (12%) + OUT C12-C14-C1 =C15 (11%)
–	568.32	556.95	1.31	BEND C5=C4-C3 (22%) + BEND O=C6-C5 (23%) + BEND O-C9-C10 (15%)
547	558.21	547.05	33.17	BEND C1-C14=C15 (10%) + BEND N1-C15-C3 (13%)
–	557.49	546.34	2.33	TORS C14=C15-C3-N2 (19%) + OUT O=C6-N1-C5 (15%) + OUT C4-C3-C15=N2 (12%)
–	535.49	524.78	1.15	STRE C14=C15 (12%) + STRE C4-C3 (11%) + BEND O-C9-C10 (14%)
–	478.56	468.99	9.35	BEND N2=3-C15 (16%) + BEND C7-O-C9 (22%)
–	457.64	448.49	0.65	STRE N1-C15 (11%) + BEND O-C9-C10 (13%)
445	456.82	447.68	5.38	TORS H11-C11=C10-C9 (10%) + TORS C13-C8=C9-C10 (14%) + TORS C11-C12-C14=C14 (17%) + TORS C9-C10=C11-C12 (15%) + OUT O-C9-C10=C8 (17%)
–	431.94	423.30	0.04	TORS C5=C4-C3-C15 (20%) + TORS C13-C8=C9-C10 (14%) + OUT N1-C15=C14-C3 (16%)
–	410.33	402.12	4.84	STRE N1-C6 (14%) + BEND O=C6-C5 (17%) + BEND C10-C11-C12 (13%)

the dimer, the second-order perturbation energy analysis shows an intermolecular LP → σ* hyperconjugation that stabilizes the dimeric form O6 → N1-H (2.41 kcal/mol), where O6 atom acts as an electron donor, justifying the experimental data.

Molecular docking study

Guided by the characteristic cytotoxicity of β-carboline alkaloids, molecular docking calculations were performed on AutoDock Vina [51] with DNA topoisomerase II-DNA complex due to the fact that a wide variety of molecules used for the treatment of human cancers (antineoplastics) such as lung, ovarian, brain, breast, adrenocortical, testicular cancers, and Hodgkin and non-Hodgkin lymphomas are eukaryotic topo II inhibitors. The docking calculation in AutoDock Vina (ATDV) consists of a number of sequential steps. Each step involves a random perturbation of the conformation followed by a local optimization (using the Broyden-Fletcher-Goldfarb-Shanno algorithm [52] which is an efficient quasi-Newton method) and a selection in which the step is accepted or not. Each local optimization involves many

Table 3 Experimental and calculated wavenumbers (cm^{-1}) and assignment for 7-methoxy-(9H-β-carbolin-1-il)-(Z)-prop-2-enoic acid

IR solid	B3LYP 6-311 (2d,p)			PED
	Calculated unscaled	Calculated scaled	IR intensity	
	3673.57	3600.10	48.26	STRE N1-H1 (100%)
3460	3471.92 (conformer D)	3430.78	949.82	STRE N1-H1 (100%)
3390	3405.58 (dimer)	3337.46	2233.46	STRE O1-H (70%) + STRE N1-H1 (25%)
–	3206.00	3141.88	4.58	STRE C8-H8 (99%)
–	3199.01	3135.03	5.37	STRE C10-H10 (88%) + STRE C11-H11 (11%)
–	3193.94	3130.06	9.70	STRE C1-H1 (89%) + STRE C11-H11 (10%)
	3177.61	3114.06	5.34	STRE C5-H5 (95%)+
–	3175.75	3112.24	3.57	STRE C10-H10 (11%) + STRE C11-H11 (88%)
–	3167.46	3104.11	12.33	STRE C1-H1 (10%) + STRE C2-H2 (90%)
3078	3137.03	3074.29	20.05	STRE C7-H7 (92%)
3063	3128.60	3066.03	11.47	STRE C7-H7 (95%)
–	3064.67	3003.38	34.20	STRE C7-H (50%) + STRE C7-H (50%)
–	3006.70	2946.57	48.76	STRE C-H (46%) + STRE C-H (46%)
2925	2977.05	2920.12	1727.19	STRE O-H (99%)
2855	2921.02 (dimer)	2862.56	1697.15	STRE O-H (99%)
1734	1785.55	1749.84	454.54	STRE C=O (75%) + BEND H-O1-C6 (14%)
	1799.26 (conformer D)	1763.27	616.26	STRE C=O (79%)
	1751.09 (dimer)	1717.57	949.42	STRE C=O (75%) + BEND H-O1-C6 (14%)
1673	1664.48	1631.19	116.26	STRE C5=C4 (43%)
1634	1660.27	1627.06	295.91	STRE C5=C4 (14%) + C14=C1 (10%)
–	1629.47	1596.88	31.44	STRE C1=C2 (11%) + STRE C14=C1 (10%)
1611	1606.18	1574.06	75.27	STRE N2=C2 (15%) + STRE C14=C1 (10%)
–	1598.29	1566.32	22.57	STRE C11=C12 (13%) + STRE C13=C8 (10%) + STRE C9=C10 (11%)
1493	1544.86	1513.96	126.33	BEND H-O1-C6 (45%)
–	1543.00	1512.14	9.86	BEND H-O1-C6 (17%)
–	1508.98	1478.80	10.02	BEND H-C7-H (50%)
–	1503.19	1473.13	66.79	BEND H2-C2-N2 (11%)
	1495.05	1465.15	8.53	WAGG H-C7-H (76%)
1459	1487.89	1458.13	67.73	STRE C10=C11 (15%) + BEND H2-C2=N2 (16%)
1430	1478.00	1448.44	7.69	Wagg. H-C7-H (46%)
–	1453.75	1424.68	15.03	BEND H-C4=C5 (32%) + BEND H5-C5-C6 (10%)
1387	1442.91	1414.05	80.11	STRE N1=C15 (32%) + BEND H1-C1-C2 (11%) + BEND H4-C4=C5 (19%) + BEND H5-C5-C6 (13%)
1374	1385.56	1357.85	6.09	STRE C8=C9 (12%) + STRE C9=C10 (14%) + BEND H1-N1-C15 (16%)
1332	1359.15	1331.97	48.12	STRE C12=C13 (10%) + STRE N1=C13 (13%) + BEND H2-C2=N2 (13%)
–	1354.05	1326.97	39.22	STRE C14=C12 (21%) + BEND H10-C10=C11 (16%) + BEND H1-C1=C2 (11%) + BEND H11-C11=C10 (11%)
1309	1344.24	1317.36	104.51	STRE O-C6 (13%) + BEND H4-C4 = C5 (10%) + BEND H5-C5-C6 (31%)
–	1322.25	1295.81	124.76	STRE N2=C2 (13%) + STRE C15=C14 (11%)
1276	1292.57	1266.72	188.55	STRE C9=C10 (11%) + STRE O-C9 (15%) + BEND H1-N1-C15 (13%)
–	1288.33	1262.56	64.83	STRE N2=C2 (16%) + STRE OH-C6 (15%) + STRE C4-C3 (10%) + BEND H2-C2=N2 (11%)
–	1266.68	1241.35	47.60	STRE N1-C15 (22%) + BEND H8-C8=C9 (11%)
1225	1239.90	1215.10	37.70	BEND H11-C11=C10 (13%)
	1225.60	1201.09	3.77	STRE O-C6 (13%) + BEND H5-C5-C6 (4%)
–	1219.08	1194.70	138.76	TORS H-C7-O3-C9 (36%)
1175	1188.53	1164.76	136.99	STRE N1=C13 (14%) + STRE O-C9 (11%) + BEND H8-C8=C9 (21%)
1152	1173.28	1149.81	1.10	BEND H-C7-H (28%) + TORS H-C7-O3-C9 (36%)
–	1149.30	1126.31	96.69	STRE C10-C11 (17%) + BEND H10-C10-C11 (38%) + BEND H11-C11-C10 (11%)
1099	1112.97	1090.71	45.00	STRE C1=C2 (25%) + STRE N2=C2(10%) + BEND H1-C1=C2 (31%)
1057	1089.88	1067.82	18.98	
	1051.21	1030.19	36.16	STRE C9=C10 (14%) + STRE O-CH3 (16%)
1031	1008.20	988.04	0.33	TORS H10-C10=C9-C8 + TORS H5-C5-C6-O1 + TORS O1-C6-C5=C4 (11%)
–	968.04	948.68	8.41	STRE C8=C9 (14%) + STRE C9=C10 (12%) + STRE N1-C13 (12%) + BEND C9=C10-C11 (19%)
–	964.67	945.38	1.00	TORS H1-C1-C2-N2 (21%) + TORS H2-C2-N2=C3 (63%)
–	951.35	932.32	0.26	TORS H10-C10-C9-C8 (32%) + TORS H11-C11-C10-C9 (51%) + TORS C10-C11 =C9-C8 (13%)
919	942.39	923.54	37.38	TORS H-O-C5-C6 (81%)

Table 3 (continued)

IR solid	B3LYP 6-311 (2d,p)			PED
	Calculated unscaled	Calculated scaled	IR intensity	
	924.33	905.84	1.07	STRE OH-C6 (14%) + STRE C4-C3 (15%) + STRE C6-C5 (13%)
887	894.51	876.62	8.01	STRE N1-C15 (14%) + BEND C1-C2-N2 (22%) + BEND C2-N2-C3 (13%)
–	877.55	860.00	5.00	STRE OH-C6 (15%) + STRE C6-C5 (10%)
842	851.36	834.33	38.01	TORS H1-C1-C2-N2 (15%) + TORS H4-C4=C5-C6 (17%) + TORS H2-C2-N2=C3 (10%) + OUT C5-C6=O2-O1 (12%) + OUT C12-C14-C1 =C15 (14%)
–	840.35	823.54	9.19	TORS H1-C1=C2-N2 (18%) + TORS H4-C4=C5-C6 (21%) + OUT C5-C6-OOH (23%)
814	832.08	815.44	72.64	OUT H8-C8-C9-C10 (22%) + TORS H11-C11-C10=C9 (16%) + OUT N1-C15=C14–C3) (24%)
–	818.78	802.40	5.64	TORS H10-C10=C9-C8 (18%) + OUT H8-C8-C9-C10 (26%) + TORS H1-C1=C2-N2 (13%)
–	802.52	786.47	1.77	STRE C6-C5 (12%) + BEND O=C6-O (16%) + BEND C5=C4-C3 (17%) + BEND O1-C6-C5 (11%)
–	800.20	784.20	3.69	TORS H1-C1=C2-N2 (11%) + OUT C5-C6-OOH (12%) + OUT N1-C8=C14 -C3 (18%)
–	787.85	772.09	5.36	STRE C11==C12 (11%) + BEND C11=C12-C13 (16%)
753	757.47	742.32	1.92	TORS H11-C11-C10=C9 (23%) + TORS C12-C13=C11-C10 (12%) + OUT C14-C13=C11 -C13 (13%)
727	707.04	692.90	0.65	TORS H5-C5-C6-O (16%) + TORS C6-C5=C4-C3 (17%) + OUT C5-C6-O2 =O1 (16%)
–	682.96	669.30	6.96	BEND C1-C2-N2 (14%) + BEND C2-N2=C3 (22%) + BEND C9=C10-C11 (11%)
–	672.71	659.26	2.07	BEND C13=C8-C9 (23%) + BEND C14-C12=C11 (15%)
626	645.50	632.59	2.70	TORS H10-C10-C9-C8 (25%) + TORS C12-C11=C9-C8 (11%) + OUT O3-C9=C10-C8 (33%)
–	615.43	603.12	0.29	TORS C14-C1=C2-N2 (16%) + TORS C14-C1=C2-N2 (23%) + TORS C3-C15 =N2-C2 (26%)
–	607.55	595.40	3.00	STRE C6-C5 (15%) + BEND O=C6-O (40%)
–	573.30	561.83	29.51	BEND O=C6-O (10%) + BEND C11=C12-C13 (12%) + BEND C9=C10-C11 (31%) + BEND C7-O3C9 (10%)
547	558.85	547.67	43.29	BEND C13=C8-C9 (11%)
	551.43	540.40	2.08	BEND C15-C12=C11 (12%) + BEND O1-C6-C5 (12%)
–	538.15	527.39	0.44	TORS C14-C1=C2-N2 (20%) + OUT C4-C3-C15=N2 (21%)
453	474.94	465.44	1.82	BEND O3-C9=C10 (20%) + BEND C7-O3-C9 (37%)
–	447.77	438.81	8.86	TORS H11-C11-C10-C9 (10%) + TORS C9-C8=C13-C12 (17%) + TORS C12-C13=C11-C10 (26%)
–	420.50	412.09	4.17	BEND C13=C8-C9 (20%)
–	408.02	399.86	4.11	TORS C9-C8=C13-C12 (14%) + OUT N1-C8=C13 -C12 (12%)

The results are referred to conformer A; however, the wavenumber values corresponding to conformation D and to the dimer form are highlighted in parentheses. Theoretical wavenumbers between 1600 and 400 cm^{-1} did not present significative differences between the structures

"evaluations" of the scoring function as well as its derivatives in the position-orientation-torsion coordinates. The number of evaluations in a local optimization is guided by convergence [51, 52]. X-ray crystal structure of human DNA topoisomerase II beta complexed with DNA and amsacrine (PDB ID: 4G0U) [53] was obtained from the Protein Data Bank web site (http://www.rcsb.org/pdb/). Amsacrine and water molecules were removed, Gasteiger charges were assigned, and the macromolecule was saved in PDBQT file format using ATDV. A grid box size of 20 × 20 × 20 Å centered at the site of DNA cleavage of topo II-DNA complex was selected. The docking protocol was tested by removing the co-crystallized inhibitor amsacrine from the protein and then docking it at the same site (Fig. 9).

The superimposition of the structures showed RMSD = 0.987; RMSD values up to 2 Å are considered reliable for a docking protocol. Free energy of binding (ΔG) analysis demonstrated that molecules I and II (Fig. 10) docked with ΔG values of − 9.6 and − 8.4 kcal/mol, respectively, while the known inhibitor amsacrine docked with ΔG − 9.9 kcal/mol. Binding modes analysis demonstrated that the two structures docked at the site of DNA cleavage between the base pairing similar to amsacrine in topo II-DNA complex (Fig. 10). Structure I (Fig. 11a) binds at the site of the substrate by non-covalent π-π interactions. Rings A, B, and C interact with DG 13 base, ring C interacts with DC 8 and DT 9 base, and ring D interacts with DG 13 and DA 12 bases. Structure II (Fig. 11b) binds at the site

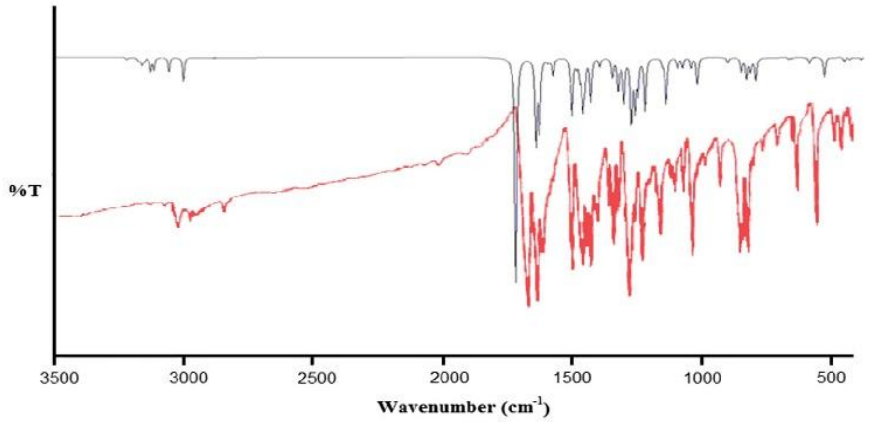

Fig. 6 Theoretical (black line) and recorded (red line) IR spectra of 9-methoxycanthin-6-one

of the substrate by alkyl-π (CH_3 with DT9 base), π-π (Ring A with DG 13 base and C4═C5 with DA 12 base) and OH-alkyl (O1H group with Ala 521) interactions. It is important to note that 9-methoxycanthin-6-one (I) binds at the DNA-topoisomerase II complex with both upstream and downstream base pairs thus interacting more efficiently than 7-methoxy-(9H-β-carbolin-1-il)-(Z)-prop-2-enoic acid (II), justifying the ΔG values. These results may justify the fact that structure I presents a higher cytotoxic activity than II, as showed by Kadorno et al. [3].

NLO analysis

Non-linear effects arise from the interactions of electromagnetic fields in various media to produce new fields altered in phase, frequency, amplitude, or other propagation characteristics from the incident fields [54, 55]. When light passes through any molecular medium, the oscillating electric field of the incident light induces an electronic polarization of the molecules comprising the medium. In ordinary materials, this electronic displacement (polarization) is directly proportional to the strength of the electric field (intensity of the light). In a non-linear material, the induced polarization is a non-linear function of the applied field. Non-linear optics is used either to shift the optical frequency of the available fields or to remodel their spatiotemporal characteristics; the example here is the second harmonic generation (SHG), essentially a frequency-doubling process: two waves, each of frequency ω, simultaneously superimpose constructively, the resulting wave excites an electron from the ground state to a virtual excited state, on relaxation, one wave of frequency 2ω is emitted with half the wavelength of the initial photons. Such materials can be used to double or triple the frequency of laser light and are of considerable interest for the high-speed processing of data, which is essential for numerous modern technologies and due to its relation with SHG effect, the calculation of the first hyperpolarizability is essential on the molecular scale.

The total static dipole moment μ, the mean polarizability α, the anisotropy of the polarizability $\Delta\alpha$, and the mean first hyperpolarizability β_0 using x, y, and z components are defined as:

Dipole moment

$$\mu = \left(\mu_x^2 + \mu_y^2 + \mu_z^2\right)^{1/2}$$

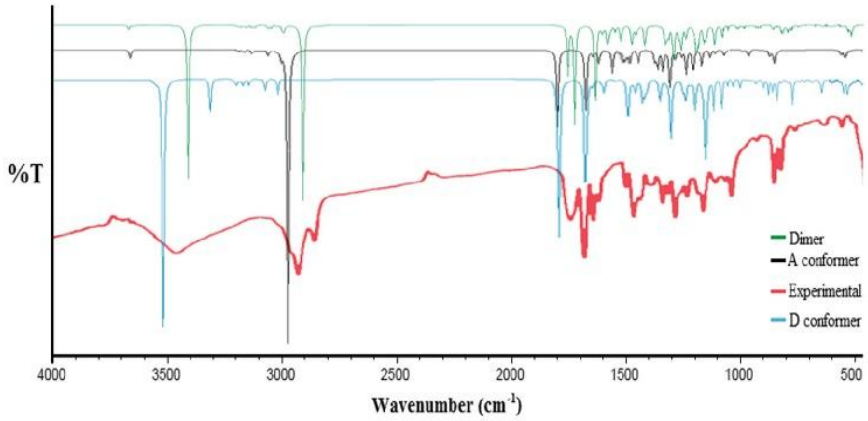

Fig. 7 Theoretical IR of dimer (green line), A conformer (black line), D conformer (blue line), and experimental (red line) IR spectra of 7-methoxy-(9H-β-carbolin-1-il)-(Z)-prop-2-enoic acid

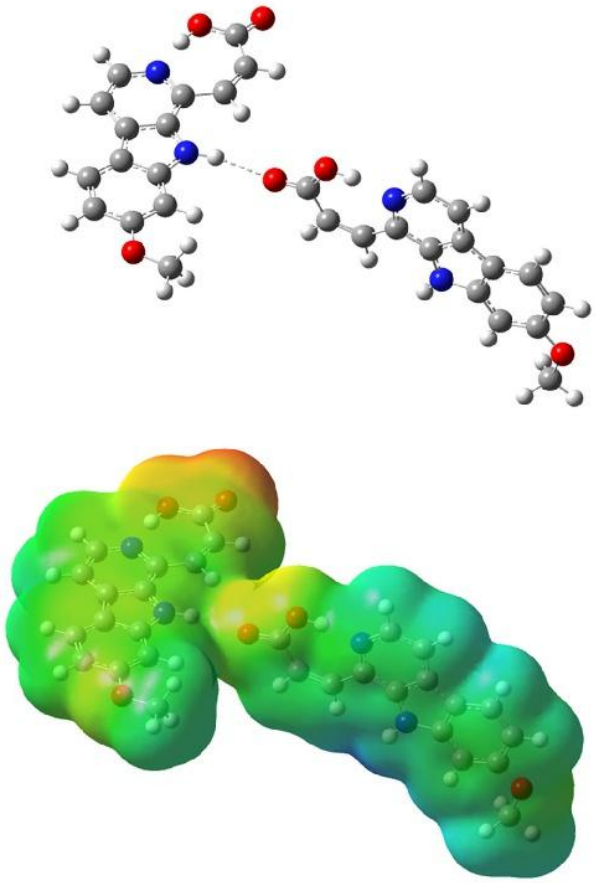

Fig. 8 Proposed dimer for 7-methoxy-(9H-β-carbolin-1-il)-(Z)-prop-2-enoic acid

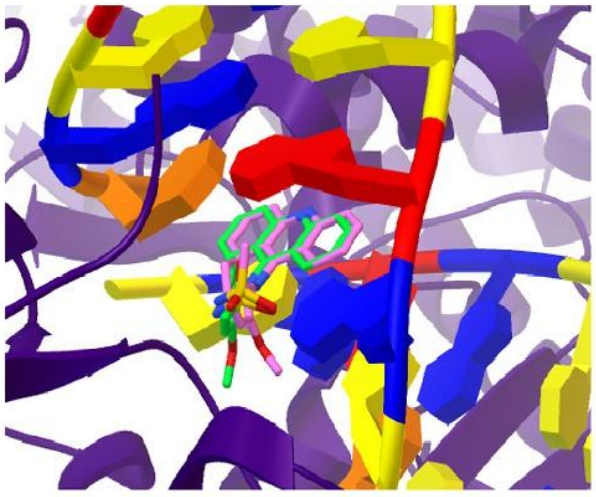

Fig. 9 Superimposition of the docked (pink) and co-crystallized (green) structure of amsacrine into the DNA cleavage site of DNA topoisomerase II

Static polarizability

$$\alpha_0 = \left(\alpha_{xx} + \alpha_{yy} + \alpha_{zz}\right)/3$$

Total polarizability

$$\Delta\alpha = 2^{-1/2}\left[\left(\alpha_{xx}-\alpha_{yy}\right)^2 + \left(\alpha_{yy}-\alpha_{zz}\right)^2 + \left(\alpha_{zz}-\alpha_{xx}\right)^2 + 6\alpha_{xz}^2 + 6\alpha_{xy}^2 + 6\alpha_{yz}^2\right]^{1/2}$$

First-order hyperpolarizability is

$$\beta = \left(\beta_x^2 + \beta_y^2 + \beta_z^2\right)^{1/2}$$

Where,

$$\beta_x = \left(\beta_{xxx} + \beta_{xyy} + \beta_{xzz}\right)$$
$$\beta_y = \left(\beta_{yyy} + \beta_{yzz} + \beta_{yxx}\right)$$
$$\beta_z = \left(\beta_{zzz} + \beta_{zxx} + \beta_{zyy}\right)$$

Since the values of polarizabilities of the Gaussian output are reported in atomic units (a.u.), the calculated values have been converted into electrostatic units (esu) (for α: 1 a.u. = 0.1482 × 10^{-24} esu; for β: 1 a.u. = 8.639 × 10^{-33} esu) (see Tables S4 and S5). The DFT theory at the B3LYP/6-311G(2d,p) level has been used to predict dipole moments, polarizability, and first-order hyperpolarizability for 7-methoxy-(9H-β-carbolin-1-il)-(Z)-prop-2-enoic acid and 9-methoxy-canthin-6-one. As seen in Table S4, the highest value dipole component for 7-methoxy-(9H-β-carbolin-1-il)-(Z)-prop-2-enoic is the μ_x = 10.2 *D* and the total dipole moment is μ_{total} = 10.3 *D*. The calculated mean polarizability α_0 and anisotropy of polarizability $\Delta\alpha_{total}$ are 3.23 × 10^{-23} and 36.01 × 10^{-24} esu, respectively. The calculated values of first-order hyperpolarizability β is 19.37 × 10^{-30} esu, 96 times greater than β of urea (~ 0.2 × 10^{-30} esu) [56], which indicates that 7-methoxy-(9H-β-carbolin-1-il)-(Z)-prop-2-enoic acid is a potential candidate for non-linear optical applications. For 9-methoxy-canthin-6-one (Table S5), the highest value dipole component is the μ_y = − 1.5 *D* and the total dipole moment is μ_{total} = 1.94 *D*. The calculated mean polarizability α_0 and anisotropy of polarizability $\Delta\alpha_{total}$ are 3.24 × 10^{-23} and 27.00 × 10^{-24} esu, respectively. The calculated value of first-order hyperpolarizability β is 12.8 × 10^{-30} esu, which is 64 times greater than β of urea.

Conclusion

9-Methoxycanthin-6-one and 7-methoxy-(9H-β-carbolin-1-il)-(Z)-prop-2-enoic acid, which were isolated from

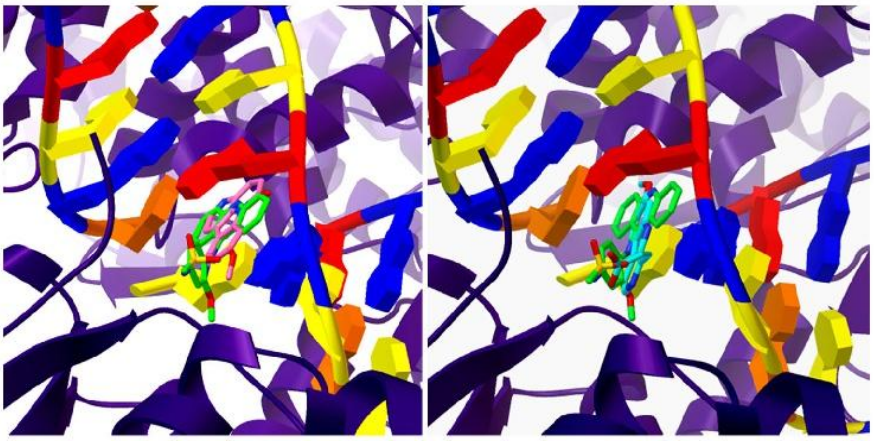

Fig. 10 Superimposition of the docked 9-methoxycanthin-6-one (pink) and 7-methoxy-(9H-β-carbolin-1-il)-(Z)-prop-2-enoic acid (ciano) structure with co-crystallized amsacrine (green)

S. guianensis, were comprehensively characterized with their spectral behavior and quantum properties described. The interatomic distances and angles proved to be plausible compared to the X-ray data for similar structure. The conformational analysis of 7-methoxy-(9H-β-carbolin-1-il)-(Z)-prop-2-enoic acid showed that conformation A is the most stable rotamer while the non-planar conformations showed the highest energies which was justified by the presence of the hydrogen bond O1H—N2 that gives high stability for the conformer A with hyperconjugative interaction N2 → H-O1 (LP → σ*) of 58.98 kcal/mol in NBO calculations. The HOMO-LUMO gap value of 9-methoxycanthin-6-one was slightly smaller than that calculated for 7-methoxy-(9H-β-carbolin-1-il)-(Z)-prop-2-enoic acid, showing that 9-methoxycanthin-6-one is slightly more reactive. The small HOMO-LUMO energy gaps calculated for both structures are directly related to their amount of chemical hardness, electrophilicity, nucleophilicity index, and electronegativity, which lead to classifying them as soft molecules when compared to other structures in the associated literature. The electronic spectra of the structures showed consistency with the experimental spectra, with bands assigned to a sum of $n \rightarrow \pi^*$ and $\pi \rightarrow \pi^*$ transistions and a bathochromic shift of structure II spectrum in relation to I was also registered. The comparative IR studies showed that for structure II the intramolecular hydrogen bonds of the conformations and the intermolecular hydrogen bonds of the dimeric form influence the results (making them the closest to the experimental ones) and also revealed several characteristic vibrations for both structures that may be used as a diagnostic tool for other β-carboline-type alkaloids, simplifying their identification and structural characterization. NLO analysis revealed that the first-order hyperpolarizability β of II is 96 times greater than β of urea, while for structure I the calculated β is 64 times greater than β of urea, indicating that these two molecules are potential candidates for non-linear optical applications. The molecular docking results revealed good

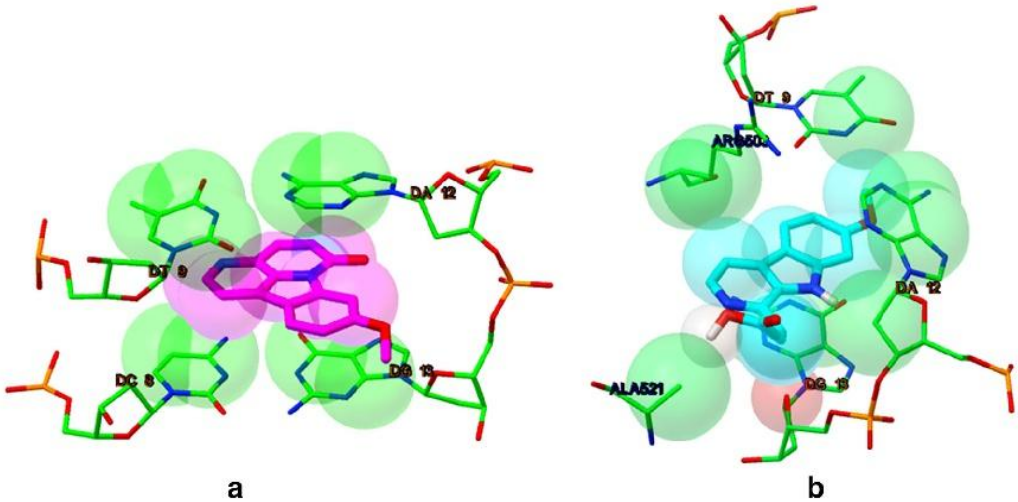

Fig. 11 Ligand-protein interaction of 9-methoxycanthin-6-one (**a**) and 7-methoxy-(9H-β-carbolin-1-il)-(Z)-prop-2-enoic acid (**b**) with topo II-DNA complex

interactions of 9-methoxycanthin-6-one with the DNA-topoisomerase II complex, similar to those of amsacrine, while 7-methoxy-(9H-β-carbolin-1-il)-(Z)-prop-2-enoic acid interacts less efficiently justifying the ΔG values, complementing the literature results.

Acknowledgements The authors thank Dr. Elaine H.T. Oliveira of Federal University of Amazonas for the spelling support, and Capes and FINEP for the financial support.

Compliance with ethical standards

Conflict of interest The authors declare that they have no conflict of interest.

References

1. Frédérich M, Hayette MP, Tits M, DeMol P, Angenot L (1999) In vitro activities of Strychnos alkaloids and extracts against Plasmodium falciparum. Antimicrob Agents Chemother 43:2328–2331
2. Rasoanaivo P, Ratsimamanga-Urverg S, Milijaona R, et al. (1994) In vitro and in vivo chloroquine-potentiating action of Strychnos myrtoides alkaloids against chloroquine-resistant strains of Plasmodium malaria. Plant Med 60:13–16
3. Kardono LB, Angerhofer CK, Tsauri S, Padmawinata K, Pezzuto JM, Kinghorn AD (1991) Cytotoxic and antimalarial constituents of the roots of *Eurycoma longifolia*. J Nat Prod 54:1360–1367
4. Rivero-Cruz JF, Lezutekong R, Lobo-Echeverri T, Ito A, Mi Q, Chai HB, Soejarto DD, Cordell GA, Pezzuto JM, Swanson SM, Morelli I, Kinghorn AD (2005) Cytotoxic constituents of the twigs of Simarouba glauca collected from a plot in southern Florida. Phytother Res 19:136–140
5. Kuo PC, Shi LS, Damu AG, Su CR, Huang C-H, Ke C-H, Wu J-B, Lin A-J, Bastow KF, Lee K-H, Wu T-S (2003) Cytotoxic and antimalarial β-carboline alkaloids from the roots of *Eurycoma longifolia*. J. Nat Prod 66:1324–1327
6. Caron C, Hoizey MJ, Olivier LLM, et al. (1988) Antimicrobial and antifungal activities of quasi-dimeric and related alkaloids. Plant Med 54:409–412
7. Quetin-Leclercq J, Favel A, Balansard G, Regli P, Angenot L (1995) Screening for in vitro antifungal activities of some indole alkaloids. Planta Med 61:475–477
8. Singh U, Sarma B, Mishra P, Ray A (2000) Antifungal activity of venenatine, an indole alkaloid isolated from *Alstonia venenata*. Folia Microbiol 45:173–176
9. Frederich M, Tits M, Angenot L (2008) Potential antimalarial activity of indole alkaloids. Trans R Soc Trop Med Hyg 102:11–19
10. Laine AE, Lood C, Koskinen AMP (2014) Pharmacological importance of optically active Tetrahydro-β-carbolines and synthetic approaches to create the C1 stereocenter. Molecules 19(2014):1544–1567. https://doi.org/10.3390/molecules19021544
11. Sasaki T, Li W, Higai K, Koike K (2015) Canthinone alkaloids are novel protein tyrosine phosphatase 1B inhibitors. Bio Med Chem Lett 25:1979–1981
12. Abrimovitch RA, Spencer ID (1964) The carbolines. Adv Heterocycl Chem 3:79
13. Allen JRF, Holmstedt B (1980) The simple β-carboline alkaloids. Phytochemistry 19:1573
14. Dias A, Varela AP, Miguel MG, Macanita AL, Becker RSJ (1992) β-carboline photosensitizers. 1: photophysics, kinetics, and excited-state equilibrium in organic solvents, and theoretical calculations. Phys Chem 96:10290–10296
15. Carmona C, Galan M, Angulo G, Munoz MA, Guardado P, Balon M (2002) Electronic spectra and photophysics of δ-carboline (5H-pyrido[3,2-b]indole). Chem Phys 276:155–165
16. Mahmoudian M, Jalilpour H, Salehian P (2002) Toxicity of *Peganum harmala*: review and a case report. Iran J Pharmacol Ther 1:1
17. Cao R, Peng W, Wang Z, Xu A (2007) β-carboline alkaloids: biochemical and pharmacological functions. Curr Med Chem 14:479–500
18. Lounasmaa M, Tolvanen A (2000) Simple indole alkaloids and those with a nonrearranged monoterpenoid unit. Nat Prod Rep 17:175–191
19. Fo ER, Fernandes JB, Vieira PC, Silva MFDGF (1992) Canthin-6-one alkaloids from *Picrolema granatesis*. Phytochemistry 31:2499–2501
20. Barbosa LF, Braz-Filho R, Vieira IJC (2010) Chemical constituents of plants from the genus *Simaba* (Simaroubaceae). Chem Biodivers 8:2163–2178
21. Saraiva RCG, Pinto AC, Nunomura SM, Pohlit AM (2006) Triterpenos e alcaloide tipo cantinona dos galhos de *Simaba polyphylla* (Cavalcante) W.W. Thomas (Simaroubaceae). Quim Nova 29:264–268
22. Nunomura RCS, Pinto AC, Nunomura SM, Pohlit AM, Fernandes Amaral AC (2012) Chemical constituents from stems of *Simaba guianensis* subesp. *ecaudata* (Cronquist). Quim Nova 35:2153–2158
23. Barbosa LF, Braz-Filho R, Vieira IJC (2011) Chemical constituents of plants from the genus *Simaba* (Simaroubaceae). Chem Biodivers 8:2163–2177
24. Arisawa M, Kinghorn AD, Cordell GA, Farnswort NR (1983) Alkaloids constituents of Simaba multiflora. J Nat Prod 46:222–225
25. Costa RA, Pinheiro MLB, Oliveira KMT, Barison A, Salomé KS, Iank JR, Silva NG, Cabral TS, Costa EV (2016) Structural, vibrational, and electronic properties of the glucoalkaloid strictosidine: a combined experimental and theoretical study. J Chem ID 1752429. https://doi.org/10.1155/2016/1752429
26. Costa RA, Pitt PO, Pinheiro MLB, Oliveira KMT, Barison A, Salomé KS, Costa EV (2017) Spectroscopic investigation, vibrational assignments, HOMO-LUMO, NBO, MEP analysis and molecular docking studies of oxoaporphine alkaloid liriodenine. Spectrochim Acta A 174:94–104
27. Frisch MJ, Trucks GW, Schlegel HB, Scuseria GE, Robb MA, Cheeseman JR, Scalmani G, Barone V, Mennucci B, Petersson GA, Nakatsuji H, Caricato M, Li X, Hratchian HP, Izmaylov AF, Bloino J, Zheng G, Sonnenberg JL, Hada M, Ehara M, Toyota K, Fukuda R, Hasegawa J, Ishida M, Nakajima T, Honda Y, Kitao O, Nakai H, Vreven T, Montgomery Jr JA, Peralta JE, Ogliaro F, Bearpark M, Heyd JJ, Brothers E, Kudin KN, Staroverov VN, Kobayashi R, Normand J, Raghavachari K, Rendell A, Burant JC, Iyengar SS, Tomasi J, Cossi M, Rega N, Millam JM, Klene M, Knox JE, Cross JB, Bakken V, Adamo C, Jaramillo J, Gomperts R, Stratmann RE, Yazyev O, Austin AJ, Cammi R, Pomelli C, Ochterski JW, Martin RL, Morokuma K, Zakrzewski VG, Voth GA, Salvador P, Dannenberg JJ, Dapprich S, Daniels AD, Farkas Ö, Foresman JB, Ortiz JV, Cioslowski J, Fox DJ (2009) Gaussian 09. Gaussian, Inc., Wallingford,
28. Dennington R, Keith T, Millam J (2009) Gaussian version 5. Semichem. Inc., Shawnee Missions, Kansas
29. Jamroz M (2004) Vibrational energy distribution analysis. VEDA 4 Computer Program, Poland,
30. Donkwe SMM, Happi EN, Wansi JD, Lenta BN, Devkota KP, Neumann B, Stammler HG, Sewald N (2012) Oxidative burst

inhibitory and cytotoxic activity of constituents of the fruits of *Odyendyea gabonensis*. Planta Med 78:1949–1956
31. Parr R, Pearson G (1983) Absolute hardness: companion parameter to absolute electronegativity. J Am Chem Soc 105:7512–7516
32. Parr R, Yang W (1989) Functional theory of atoms and molecules. Oxford University Press, New York,
33. Janak JF (1978). Phys Rev B 18:7165
34. Perdew JP, Parr RG, Levy M, Balduz JL (1982). Phys Rev Lett 49: 1691
35. Parr R, Szentpaly L, Liu S (1999) Electrophilicity index. J Am Chem Soc 121:1922–1924
36. Domingo LR, Pérez P (2011) The nucleophilicity N index in organic chemistry. Org Biomol Chem 9:7168–7175
37. Domingo LR, Chamorro E, Perez P (2008) Understanding the reactivity of captodative ethylenes in polar cyclo addition reactions. A Theoretical Study. J Org Chem 73:4615–4624
38. Glossman-Mitnik D (2013) A comparison of the chemical reactivity of naringenin calculated with the M06 family of density functional. Chem Cent J 7:155
39. Costa RA, Pinheiro MLB, Oliveira KMT, Costa EV (2017) Vibrational, structural and electronic properties investigations by DFT calculations and molecular docking studies with DNA topoisomerase II of strychnobrasiline type alkaloids: a theoretical approach for potentially bioactive molecules. J Mol Struct 1145:254–267
40. Gomes SAP, Flores N, Hernández AP, Piñón M, Glossman-Mitnik D (2010) Computational molecular characterization of the flavonoid rutin. Chem Cent J 4:12. https://doi.org/10.1186/1752-153X-4-12
41. Al-Mazaideh GM, Ababneh TS, Abu-Shandi KH, Jamhour RMAQ, Salman HJA, Al-Msiedeen AM, Khalil SM (2016) DFT calculations of Mesembryanthemum nodiflorum compounds as corrosion inhibitors of aluminum. Phys Sci Int J 12:1–7
42. Abdullah N, Ismail I, Hassan NH, Basherudin N (2016) 9-methoxycanthin-6-one production in elicited roots culture of *Eurycoma longifolia*. AIP Conf Proc. https://doi.org/10.1063/1.4966733
43. Pereira CAM, Rodrigues TR, Yariwake J (2014) Quantification of harman alkaloids in sour passion fruit and seeds by a novel dual SBSE-LC/Flu (stir bar sorptive extraction-liquid chromatography with fluorescense detector) method. J Braz Chem Soc 25:1472–1483
44. Carlson BC, Keller JM (1957) Orthogonalization procedures and the localization of Wannier functions. Phys Rev 105:102–103
45. Weinhold F, Carpenter JE (1988) Analysis of the geometry of the hydroxymethyl radical by the 'different hybrids for different spins' natural bond orbital procedure. J Mol Struct (THEOCHEM) 169: 41–62
46. Reed AE, Weinstock RB, Weinhold F (1985) Natural population analysis. J Chem Phys 83:735–739. http://dx.doi.org/10.1063/1.449486
47. Davidson ER (1976) Reduced density matrices in quantum chemistry. Academic Press, New York,
48. Mulliken RS (1955) Electronic population analysis on LCAO-MO molecular wave functions. J Chem Phys 23:1833–1841. http://dx.doi.org/10.1063/1.1740588
49. Reed AE, Weinhold F (1983) Natural bond orbital analysis of near-Hartree-Fock water dimer. J Chem Phys 78:4066–4073
50. Badenhoop JK, Weinhold F (1997) Natural bond orbital analysis of steric interactions. J Chem Phys 107:5406–5421
51. Trott O, Olson AJ (2010) Software news and update AutoDock Vina: improving the speed and accuracy of docking with a new scoring function, efficient optimization, and multithreading. J Comput Chem 31:455–461
52. Nocedal J, Wright SJ (1999) Numerical optimization, Springer series in operations research. Springer Verlag, Berlin,
53. Wu CC, Li YC, Wang YR, Li TK, Chan NL (2013) On the structural basis and design guidelines for type II topoisomerase-targeting anticancer drugs. Nucleic Acids Res 41:10630–10640
54. Kleinman D (1962) Nonlinear dielectric polarization in optical media. J Phys Rev 126:1977–1979
55. Arivuoli D (2001) Fundamentals of nonlinear optical materials. Pramana J Phys 57:871883
56. Geskin VM, Lambert C, Bredás JL (2003) Origin of high second- and third-order nonlinear optical response in ammonio/borato diphenylpolyene zwitterions: the remarkable role of polarized aromatic groups. J Am Chem Soc 15:15651–15658

6.2. Investigação das propriedades vibracionais, estruturais e eletrônicas e estudos de docking molecular com DNA topoisomerase II de alcaloides do tipo stricnobrasilina: uma abordagem teórica para moléculas bioativas

O presente artigo, publicado no periódico Journal of Molecular structure, de grande impacto na química teórica, consistiu em um estudo teórico e experimental através de uma abordagem DFT que se caracterizou pela avaliação das propriedades estruturais, vibracionais e eletrônicas usando o funcional de troca e correlação B3LYP e base de cálculo 6-311G (2d,p) dos alcaloides stricnobrasilina (I) e 12-hidroxi-10,11 dimetoxi stricnobrasilina (II). O interesse do estudo teórico acerca desses acaloides surgiu devido à complexidade estrutural apresentada pelas duas estruturas, somado ao fato de haver na literatura testes de citotoxicidade *in vitro* referentes ao alcaloide I, o que despertou o interesse a cerca do potencial farmacológico do alcaloide II. No presente trabalho dados de otimização geométrica foram comparados com dados de cristalografia de raio-x para uma estrutura similar, se mostrando bem próximos. Cálculos de orbitais HOMO-LUMO mostraram que à presença de substituintes no anel benzênico influenciam nas propriedades quânticas, as quais estão intimamente ligadas às propriedades biológicas. Cálculos de Mapas de potencial eletrostático, Orbitais naturais de ligação (Natural Bond Orbitals- NBOs) e NLO (Non Linear Optics) também foram realizados, com o intuito de avaliar as propriedades químico-quânticas das duas estruturas. Cálculos vibracionais se mostraram bem próximos dos valores obtidos através dos espectros IV, para ambas as moléculas e análise de docking molecular evidenciou um possível efeito antitumoral para a estrutura II, em virtude da boa docagem com o complexo DNA-topoisomerase II.

Journal of Molecular Structure 1145 (2017) 254–267

Contents lists available at ScienceDirect

Journal of Molecular Structure

journal homepage: http://www.elsevier.com/locate/molstruc

Vibrational, structural and electronic properties investigation by DFT calculations and molecular docking studies with DNA topoisomerase II of strychnobrasiline type alkaloids: A theoretical approach for potentially bioactive molecules

Renyer A. Costa*, Kelson M.T. Oliveira**, Emmanoel Vilaça Costa, Maria L.B. Pinheiro

Department of Chemistry, Federal University of Amazonas, Av General Rodrigo Otávio nº 3000, Coroado, Manaus, Amazonas, Brazil

ARTICLE INFO

Article history:
Received 25 February 2017
Received in revised form
16 May 2017
Accepted 17 May 2017
Available online 18 May 2017

Keywords:
Strychnobrasiline
DNA topoisomerase II
DFT
FTIR
Molecular docking

ABSTRACT

A combined experimental and theoretical DFT study of the structural, vibrational and electronic properties of strychnobrasiline and 12-hydroxy-10,11-dimethoxystrychnobrasiline is presented using the Becke three-parameter Lee-Yang-Parr function (B3LYP) and 6-311G(2d,p) basis set. The theoretical geometry optimization data were compared with the X-ray data for a similar structure in the associated literature, showing close values. The calculated HOMO-LUMO gap values showed that the presence of substituents in the benzene ring influences the quantum properties which are directly related to the reactive properties. Theoretical UV spectra agreed well with the measured experimental data, with bands assigned. In addition, Natural Bond Orbitals (NBOs), Mapped molecular electrostatic potential surface (MEPS) and NLO calculations were also performed at the same theory level. The theoretical vibrational analysis revealed several characteristic vibrations that may be used as a diagnostic tool for other strychnobrasiline type alkaloids, simplifying their identification and structural characterization. Molecular docking calculations with DNA Topoisomerase II-DNA complex showed binding free energies values of −8.0 and −9.5 kcal/mol for strychnobrasiline and 12-hydroxy-10,11-dimethoxystrychnobrasiline respectively, while for amsacrine, used for the treatment of leukemia, the binding free energy ΔG presented a value of −10.0 kcal/mol, suggesting that strychnobrasiline derivative alkaloids might exhibit an antineoplastic activity.

1. Introduction

Indole alkaloids are a diverse class of natural products, comprising over 2000 members and especially recognized for their use in clinical medicine. These natural products possess a range of chemical structures and a wealth of biological activities like antiplasmodial [1,2] cytotoxic [3], antibacterial [4], antifungal [5], spasmodic [6], hypotensive [7] and anti-inflammatory [8], playing a very important role in the natural products field. As a matter of fact, a large number of naturally occurring molecules playing important roles in biochemistry are constituted by an indole nucleus (e.g., tryptophan, tryptamine, serotonin and melatonin) and owing to the versatile binding properties of these structural units, they are abundantly found in drugs with different therapeutic applications [8–10] and constitute privileged molecular scaffolds in drug discovery [11,12].

In this context the *Strychnos* plants are an important source of indole monoterpene alkaloids being very attractive for pharmacological and chemical studies. Because of their toxicity, many of these species have been used as arrow poisons by American natives, however in Africa and in Asia, *Strychnos* genus is important due to its reputation as a remedy against snakebites and poisonings, stomach, abdominal and intestinal complaints (as well as in the treatment of worms and parasites) and malaria [13]. Over the years many *Strychnos* indole alkaloids have been isolated and identified with their pharmacological properties reported, however, combined theoretical and experimental investigations of their structural, reactive, spectroscopic and quantum properties and molecular docking studies still lack in the literature. The alkaloids

* Corresponding author.
** Corresponding author.
E-mail addresses: renyer.costa@gmail.com (R.A. Costa), kelsonmota@ufam.edu.br (K.M.T. Oliveira), lbelem@ufam.edu.br (M.L.B. Pinheiro).

http://dx.doi.org/10.1016/j.molstruc.2017.05.087
0022-2860/

strychnobrasiline (I), isolated 5 times [14–17], and 12-hydroxy-10,11-dimethoxystrychnobrasiline (II) (Fig. 1.), isolated only once in 2002 by one of our authors [18], are structures that did not have their properties fully investigated yet. Strychnobrasiline and its derivates (called strychnobrasiline type alkaloids) belong to a small group of indole alkaloids called indoline alkaloids (due to the presence of the single bond C2–C7) and have been little studied in the literature. This work analyses these two alkaloids from a theoretical view (geometry optimization, NBO, theoretical IR, UV gaps and MEPS calculations) using density functional theory (DFT) approach, comparing the obtained calculated data with the experimental ones, providing a more complete description of the vibrational, structural and quantum properties of these structures. To the best of our knowledge no theoretical molecular modeling study that discusses the geometrical parameters and conformational stability was previously presented and a detailed description of the spectroscopic (FT-IR and UV–Vis) behavior with the help of quantum (DFT) calculations along with NBO, MEPS and HOMO-LUMO calculations has not been performed yet for these alkaloids. In view of the antineoplastic potential registered in the PASS (prediction of activity spectra) molecular docking studies were also performed with DNA topoisomerase II, for being an essential ubiquitous nuclear enzyme which manage the topology of DNA during cellular processes such as replication, transcription, recombination and chromatin remodeling, resulting in an attractive drug target against cancer.

2. Methodologies

Strycnobrasiline (I) and 12-Hydroxy-10,11dimethoxy-strychnobrasiline (II) have been isolated from *Strychnos mattogrossensis*, collected in the Igarapé Grande located on the right bank of the Amazon river near Careiro county (voucher specimen 142.800, deposited in the herbarium of the National Research Institute of Amazonas-INPA). The isolation methodologies, the spectroscopic identification (NMR H1, C13, HMBC, HSQC and ESI-MS analysis), the Ultra-violet (UV) and FT-IR (Fourier transform infrared) spectroscopic data obtainment, recorded in KBr pellet technique (solid phase), were described in previous works [15,18]. The theoretical quantum chemical calculations were performed using the Gaussian 09 W Program on the Debian LINUX (5.0 version) platform on an INTEL QuadcoreTM PC (8 GB RAM) [19]. The DFT approach using the 6-311G(2d,p) basis set and the B3LYP functional was applied in all optimization procedures. Potential energy surfaces were scanned using relaxed dihedral angle scan coordinates and all minima geometries (conformers A and B of both molecules) were fully optimized by the force gradient method using Berny's algorithm and standard analytical harmonic vibrational analysis (no imaginary frequencies or negative eigenvalues were found). The UV spectra were calculated for the lowest energy structures using the TD-B3LYP-FC functional and 6-311G (2d,p) basis set in methanol by the polarizable continuum model. The NBO values were obtained with NBO 3.1, as implemented in the GAUSSIAN 09 package using the same theory level. The assignments of the calculated IR wavenumbers are aided by the animation option of GAUSSVIEW 5.0 program, which gives a visual presentation of the vibrational modes [20]. The potential energy distribution (PED) was calculated with the help of VEDA4 software package [21].

3. Results and discussions

3.1. Geometry optimization

The theoretical geometry optimization results of the studied molecules (Figs. 2 and 3), which were calculated at B3LYP/6-311G(2d,p) basis set, were compared with X-ray data for 14-hydroxistrychnobrasiline [22] (Table 1), due to the fact that crystallographic data are not available yet for them. I and II shows significant polarities being soluble in chloroform, ethyl acetate and methanol. The two structures showed C1 symmetry with stable conformations showing energy electronic values of −1189.47 and −1493.80 a.u. respectively.

In structure I the calculated bond lengths values (Table 1) indicated distortions in the five-membered ring, showing distinct values for all bonds: 1.48 Å (N1–C2), 1.42 Å (N1–C13), 1.39 Å (C13–C8), 1.52 Å (C7–C8) and 1.58 Å (C7–C2). C Ring, the interconnected nine-membered ring with conformation that remind a boat (N4, C5, C6, C7, C3, C14, C15, C20, C21) shows small distortions: 1.54 Å (C7–C6), 1.43 Å (C6–C5), 1.48 Å (C5–N2), 1.42 Å (N2–C21) and 1.33 Å (C21–C20). D ring shows very similar bond lengths (~1.54 Å) except for C3–C14 (1.50 Å) and C2–C7 (1.57 Å) bonds. E ring shows certain uniformity (~1.54 Å) except for C19–O (1.44 Å) and C17–O (1.42 Å) bonds and the benzene ring presented close values of bond lengths (~1.39). Concerning to the bond angles, the entire structure present distortions (except ring A) especially the C ring due to the transanular interaction between N4 and C3 (distance of 2.50 Å) with angles: 111.38° (C7–C6–C5), 112.51° (C6–C5–N4), 123.05° (N4–C21–C20). Relative to the molecular conformation, the five-membered ring shows an envelope

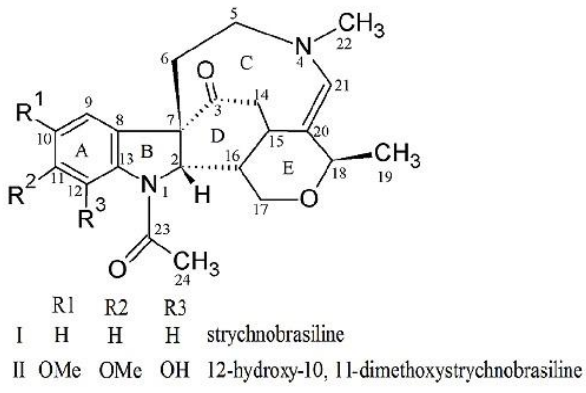

Fig. 1. Planar molecular structure of the studied strychnobrasiline indoline alkaloids.

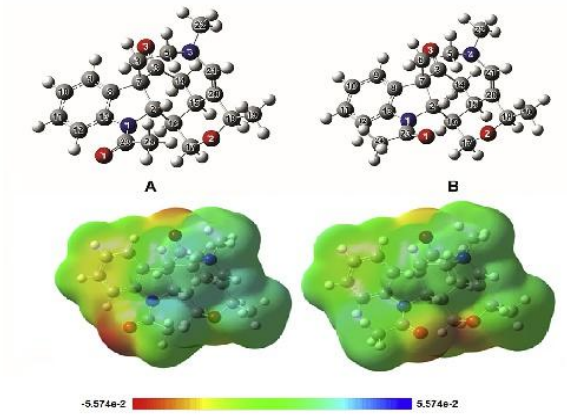

Fig. 2. Calculated conformers and Meps for strychnobrasiline (I).

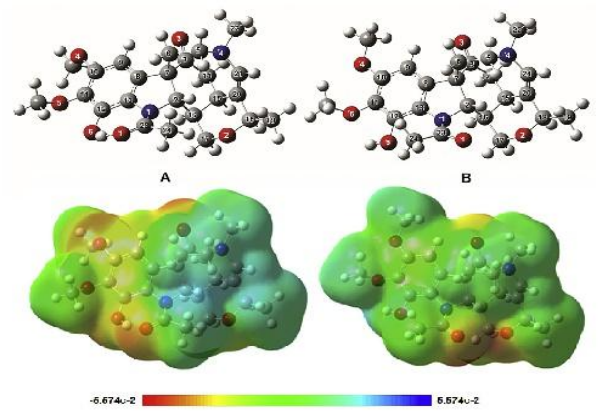

Fig. 3. Calculated conformers and Meps for 12-hydroxy-10, 11-dimethoxystrychnobrasiline (II).

conformation with C2 atom having an angle of −15.69° with the C13−C8−C7 plane. The N-acetyl group plane presents an angle of −40.15° with the C12−C13−N1 plane and the electron pair of the pyramidal N1 atom is in axial position (*cis*-relationship) with C17 atom. The non flat design of the structure is reflected by the angles between the planes B-D and D-E which are −127.20° and 99.9° respectively. Regarding the orientation of the N-acetyl group, two conformers have been evaluated for I (Fig. 2) and the theoretical data showed free energy of ΔGab = 0.22 kcal/mol indicating that conformer B is the most stable in gas phase. However in chloroform (ε = 4.806), using the polarizable continuum model (PCM), the obtained Gibbs free energy value is ΔGab = −0.17 kcal/mol which reveals that the equilibrium is shifted to conformer A when the dielectric constant of the medium is increased, showing that the solute-solvent electrostatic interactions have great influence on the strychnobrasiline conformers stability. The calculated equilibrium constant ($k = e^{-\Delta G/RT}$) for the conformational interconversion A→ B in chloroform at 298 K is k = 1.33, meaning that two conformers exist in a 57:43 ratio. Experimental analysis based on NMR ^{1}H in deuteriochloroform, suggests a ratio (A/B) of 66:33 [15,16]. The calculated energetic barrier for the rotation is 15 kcal/mol.

Structure II (Table 1) shows the same geometrical aspects of structure I, a non planar strucuture with distortions in their rings however including the benzene ring. Initially due to the interaction between the substituents groups, distortions in the benzene ring are observed, C8−C9 (1.38 Å), C9−C10 (1.39 Å), C10−C11 (1.40 Å), C11−C12 (1.41 Å) and C12−C13 (1.40 Å). The five-membered tryptophan ring showed distinct values for all connections: 1.49 Å (N1−C2), 1.42 Å (N1−C13), 1.38 Å (C13−C8), 1.53 Å (C7−C8) and 1.58 Å (C7−C2). C, D and E rings bond lengths showed very close values to structure I, due to the presence of heteroatoms and double bonds. Concerning to the bond angles the entire structure presents angles distortions (including benzene ring), with attention to C ring (with a transanular interaction between N4 and C3, 2.48 Å) that presented the angles values: 117.38° (C7−C6−C5), 112.92° (C6−C5−N4), 113.14° (C5−N4−C21) and 124.02° (N4−C21−C20). The five-membered ring shows an envelope conformation with C2 atom having an angle of −18.26° with the C13−C8−C7 plane. The benzene ring showed dihedral angles values of 4.97° (C9−C8−C13−C12), 3.42° (C10−C11−C12−C13) and −5.88° (C11−C12−C13−C8), thus indicating a non planarity thereof. The N-acetyl group plane shows an angle of −55.36° with the C12−C13−N1 plane, more pronounced than the strychnobrasiline value due to the interaction between acetyl and hydroxyl (C12−OH) group. Concerning to the planes between B, C and D rings, the angles values between them are similar to those of structure I. Likewise I, two conformers have been evaluated (Fig. 3) and the theoretical data showed that conformer A is the most stable in both gas phase (ΔGab = 1.82 kcal/mol) and chloroform (ΔGab = 2.68 kcal/mol) due to the hydrogen bond C12−O6H−−O=C23 which gives great stability to this conformation. The calculated equilibrium constant for the conformational interconversion A → B in chloroform at 298 K is k = 93.88, meaning that two conformers exist in a 98.42:1.58 ratio. The calculated energetic barrier for the rotation is 24 kcal/mol.

Table 1
Calculated geometrical parameters for strychnobrasiline (I) and 12-hydroxy-10, 11-dimethoxystrychnobrasiline (II).

Parameter	Structure I	Structure II	Experimental [22]
Bond length			
N1−C2	1.489	1.503	1.49
C3−C7	1.548	1.554	1.52
C3−C14	1.505	1.512	1.51
C3−O	1.216	1.209	1.23
C2−C16	1.542	1.551	1.50
N4−C5	1.482	1.469	1.53
N4−C21	1.429	1.422	1.46
C5−C6	1.540	1.524	1.58
C6−C7	1.549	1.574	1.54
C7−C8	1.525	1.516	1.52
C8−C9	1.386	1.382	1.38
C9−C10	1.395	1.394	1.42
C10−C11	1.390	1.498	1.40
C11−C12	1.394	1.410	1.37
C12−C13	1.391	1.399	1.42
C13−N1	1.417	1.418	1.40
N1−C23	1.384	1.381	1.38
C23−O	1.220	1.223	1.22
C14−C15	1.522	1.525	1.53
C15−C16	1.544	1.549	1.56
C16−C17	1.539	1.533	1.53
C17−O	1.423	1.423	1.46
C18−O	1.442	1.439	1.46
C18−C19	1.516	1.516	1.52
C18−C20	1.517	1.519	1.53
C20−C21	1.332	1.333	1.36
C21−N4	1.429	1.422	1.46
N4−C22	1.457	1.457	1.48
Bond angle			
N1−C2−C16	111.663	113.975	113.4
N1−C2−C7	103.585	103.116	103.4
N1−C13−C8	109.922	110.763	110.5
N1−C23−O	120.572	121.652	122.2
C7−C3−C14	119.450	117.997	119.0
C3−C14−C15	114.900	114.611	113.2
C14−C15−C16	111.343	109.122	–
C15−C16−C2	110.057	113.318	109.3
C7−C2−C16	115.336	116.765	116.8
C7−C6−C5	111.342	117.385	110.1
C6−C5−N4	112.522	112.924	107.5
C5−N4−C21	112.331	113.139	106.5
N4−C21−C20	123.130	124.023	117.6
C21−C20−C15	126.594	127.375	–
C21−C20−C18	122.776	122.121	118.3
C16−C15−C20	107.382	111.379	106.8
C15−C20−C18	109.454	110.370	110.5
C20−C18−O	106.012	107.377	106.6
C17−O−C18	115.345	113.135	112.6
C8−C9−C10	119.269	118.691	119.9
C9−C10−C11	120.190	120.792	117.5
C10−C11−C12	120.951	120.816	123.6
C11−C12−C13	118.479	117.358	118.3
C12−C13−C8	120.786	121.403	119.4

Table 2
Calculated energy values for strychnobralisine (I) and 12-Hidroxy-10,11-dimethoxy-strychnobrasiline (II) using B3LYP/6-311G (2d, p) basis set.

Parameters	I	II
Energy (a.u.)	−1189.4706	−1493.8254
E_{HOMO} (eV)	−5.9571	−5.6738
E_{LUMO} (eV)	−0.6196	−0.6525
$E_{HOMO-LUMO}$ (eV)	5.3375	5.0213
E_{HOMO-1} (eV)	−6.2975	−5.8442
E_{LUMO+1} (eV)	−0.4974	−0.3075
$E_{(HOMO-1)-(LUMO+1)}$ (eV)	5.8001	5.5367
Hardness (η)	2.6687	2.5106
Chemical potential (μ)	−3.2883	−3.1632
Electronegativity (χ)	3.288	3.1632
Electrophilicity index (ω)	2.04	1.99
Nucleophilicity index (*N*)	5.143	5.426

3.2. Electrostatic potential maps

The Molecular Electrostatic Potential Surface (MEPS) is a plot of electrostatic potential mapped onto the constant electron density surface. The MEPS has been used primarily for predicting sites and relative reactivity towards electrophilic attack, in studies of biological recognition and hydrogen bonding interactions. The negative electrostatic potential corresponds to an attraction of the proton by the concentrated electron density in the molecule (and is colored in shades of red), the positive electrostatic potential corresponds to repulsion of the proton by atomic nuclei in regions where low electron density exists and the nuclear charge is incompletely shielded (and is colored in shades of blue). Potential increases in the order red < yellow < green < blue (Figs. 2 and 3).

The MEPS for strychnobrasiline (I) (Fig. 2) indicates regions with positive potentials over methyl group in position 22 (0.0117 a.u.), over H10 (0.0132 a.u.), H11(0.0170), H12 (0.0236 a.u.), H15 (0.0165 a.u.), H16 (0.0129 a.u.), αH17 (0.0117 a.u.) and αH18 (0.0134 a.u.) atoms. Regions with negative potentials were located over aromatic ring (−0.0174 a.u.), O1 (−0.0552 a.u.), O2 (−0.0231 a.u.) and O3 (−0.0453 a.u.). The calculated MEPS for 12-Hidroxy-10,11-dimethoxy-strychnobrasiline (II) (Fig. 3) indicates regions with positive potentials over H5α (0.0242 a.u.), H5β(0.0205 a.u.), H21 (0.0249a.u), H18(0.0242 a.u.) and H15(0.0258 a.u.) atoms. Regions with negative potentials were located over aromatic ring (−0.0240 a.u.), over O1 (−0.0435 a.u.), O2 (−0.0176 a.u.), O3 (−0.0467 a.u.), O4 (−0.0430 a.u.), O5 (−0.486 a.u.) and O6 (−0.0528a.u.).

It is important to note that N-acetyl group acts as an electron withdrawing group thus increasing the delocalization of the electron density over the benzene ring. However the benzene ring of structure II has an electrostatic potential area more negative than structure I, due to the fact that the substituents on positions 10, 11 and 12 acts as electron density donors (see Table 6).

Table 3
Experimental and calculated wavenumbers (cm^{-1}) and assignments for I.

IR solid	B3LYP 6-311G(2d,p)			PED >5%
	Calculated Wavenumber	Scaled calculated wavenumber	Intensity	
3080	3146.23	3083.30	7.69	Stre C2–H2 (11%) + Stre C14–H14 (11%) + Stre C17–H17 (20%) + Stre C24–H24 (38%)
3068	3134.63	3071.93	3.75	Stre C2–H2 (23%) Stre C14–H14(21%) Stre C17–H177 assym.(38%) + Stre C24–H24 (26%)
3060	3115.42	3053.11	19.69	Stre C19–H19 assym. (80%)
3040	3106.69	3044.55	16.60	Stre assym. C22–H22 (47%) + Stre assym. C18–H18 (15%) + Stre assym. C5–H5 (15%) + Stre C6–H6 (18%)
3028	3098.09	3036.12	13.47	Stre C14–H14 (10%) + Stre assym. C6–H6 (30%) + Stre C22–H22 (10%)
3007	3068.10	3006.73	17.24	Stre C21–H21 (44%) + Stre C22–H22 (27%)
3001	3065.20	3003.89	61.26	Stre C6–H6 (10%) + Stre C22–H22(49%) + Stre C21–H21 (34%)
2950	3014.19	2954.21	93.91	Stre C5–H5 (24%) + Stre C16–H16 (11%)
2930	2986.94	2927.20	40.65	Stre C14–H14 (35%) + Stre C15–H15 (50%)
2890	2953.50	2894.43	72.14	Stre C17–H17 (68%)
2888	2950.67	2891.49	116.17	Stre symm.C22–H22 (86%)
2875	2938.12	2879.35	34.89	Stre C18–H18 (56%)
1690	1735.57	1700.85	143.16	Stre O3=C3 (91%)
1688	1722.61	1688.15	269.61	Stre O1=C23 (67%) + Stre C20=C21 (30%)
1685	1721.13	1686.70	28.26	Stre O1=C23 (23%) + Stre C21=C20 (53%)
1600	1635.39	1602.68	11.83	Stre C9=C10(44%) + Stre C12=C13 (10%) + Bend C10–C11–C12(10%)
1592	1628.65	1596.07	10.75	Stre C8=C9 (17%) + Stre C10=C9 (19%) Stre C8=C13 (29%) + Bend H10–C10=C9 (14%)
1470	1513.09	1482.82	92.64	Stre C8=C13 (10%) + Bend H11–C11–C12 (25%) + Bend H12–C12–C113 (22%)
1468	1507.17	1477.02	3.24	Sciss. H19–C19–H 19 (30%) + Tors H22–C22–N4–C5 (11%)
1399	1427.27	1398.72	6.12	Bend H21–C21–C20 (14%) + Bend H15–C15–C14 (22%)
1318	1346.36	1319.43	33.43	Bend H18–C19–O2(44%) + Twist H17–C17–H17
1280	1311.58	1285.34	80.02	Stre N1–C23 (15%)+ Tors H2–C2–N1 (21%) + Bend H12–C12–C13 (22%) + Bend H15–C15–H15 (15%)
1235	1262.13	1236.88	29.73	Tors H16–C16–C15–C14 (22%) + Tors H 15-C15-C16-C2 (26%)
1187	1210.74	1186.52	52.16	Stre assym. C8–C3–C14 (20%)
1100	1127.31	1104.76	11.38	Distortions in aromatic ring (breathing)
1052	1075.84	1054.32	19.68	Bend H19–C19–C18 (10%) + Tors H19–C19–C18–O2 (14%) + Tors H18–C18–C20–C15 (10%)
866	881.43	863.80	4.10	Tors H10–C10–C9–H9 (41%) + Tors H12–C12–C13–N1 (39%)
849	870.50	853.09	3.13	Out aromatic ring
755	765.86	750.54	16.75	Out H10–C10–C11–H11 (28%) + Out H11–C11–C12–H12 (28%)
690	711.59	697.35	6.07	Aromatic ring torsion + Ring D breathing
600	612.93	600.67	0.89	Tors H6–C6–C5–N4 (13%)
590	601.86	589.82	14.13	Out C24–C23–O1–N1
587	596.10	584.17	25.47	Bend O1–C24–C23 (31%)
529	538.48	527.71	11.87	Out C3–O2–C14–C3 (18%)
500	521.98	511.54	6.05	Tors H21–C21–C20–C18 (40%) + Bend C22–N4–C21 (12%)
480	489.76	479.96	7.23	Rings Breathing
450	460.79	451.57	3.02	Tors C9=C10=C11=C12 (10%)
RMSD	42.88	5.06		

Table 4
Experimental and calculated wavenumbers (cm^{-1}) and assignments for II.

IR solid	B3LYP 6-311G(2d,p)			PED >5%
	Calculated Wavenumber	Scaled calculated wavenumber	Intensity	
3520	3592.42(A3)	3513.01	112.5	Stre OH (100%)
3400	3469.23(A2)	3400.01	141.32	Stre OH (100%)
3170	3238.12(A1)	3171.23	636.8	Stre OH (100%)
3100	3165.36	3102.05	4,78	Stre C2–H2 (90%) + Stre assim. C24–H24 (10%)
3068	3151.74	3088.70	3,9	Stre assym.C24–H24 (91%)
3065	3123.38	3060.91	31.63	Stre assym. C–H methoxy group (73%)
3060	3122.87	3060.36	20,09	Stre symm. C–H methoxy group (67%)
3050	3112.31	3050.06	6,18	Stre assym C24–H24 (74%)
3040	3110.74	3048.52	14,26	Stre assym C19–H19 (98%)
2990	3108.15	3045.98	16,36	Stre assym. C22–H22 (93%)
2988	3068.76	3007.38	10,93	Stre C22–H22 (75%)
2986	3057.83	2996.67	73.99	Stre C21–H21 (91%)
2980	3051.42	2990.39	21,91	Stre assym. C5–H5 (94%)
2975	3042.95	2982.09	3,42	Stre symm. C19–H19 (90%)
2966	3031.45	2970.82	33,13	Stre C16–H16 (95%)
2960	3017.76	2957.40	64,06	Stre symm. Methoxy group (86%)
2946	3008.46	2948.29	72,76	Stre C14–H14 (59%) +Stre C15–H15 (17%) + Stre Methoxy groups (13%)
2938	3008.20	2948,36	28,17	Stre symm. Methoxy groups (80%)
2925	2994.07	2934.18	50.15	Stre C15–H15 (80%)
2920	2977.24	2917.69	41.99	Stre C17–H17 (90%)
2868	2952.22	2893.17	112.62	Stre symm. C22–H22 (93%)
1660	1744.55	1709.65	134.10	Stre C3=O (91%)
1630	1663.01	1628.74	285.19	Stre C23=O
1600	1640.18	1607.37	84.42	Stre aromatic C9=C8 (11%) + Bend O–H (26%) + Stre C23=O (12%)
1585	1620.99	1588.57	46.66	Stre C9=C8 (30%) + Stre C10=C11 (33%)
1468	1501.03	1471.00	17,37	Sciss C24–H24 (47%)
1460.2	1492.24	1462.39	15,13	Wagg. C22–H22 (32%)+ Tors H22–C22–N4–C5 (31%)+ Sciss C6–H6 (14%)
1460	1491.89	1462.05	32,08	Wagg. CH methoxy group (14%) + Sciss. CH methoxy group (27%)
1458.3	1488.78	1459.00	3,91	Sciss. CH methoxy group (31%)+ Tors HCOC (10%)
1458	1488.00	1458.24	3,89	Sciss. C19–H19 (27%) + Wagg (21%) C24–H24
1456	1487.67	1457.91	37,04	Bend C19–H19 (13%) + Bend C5–H5 (18%) + Bend CH methoxy (18%)
1450	1487.17	1457.42	23,34	Sciss. C6–H6 (56%) + Sciss CH methoxy (10%)
	1486.18	1456.45	4,07	Bend C24–H24 (30%) +Bend C17–H17(15%) + Bend C19–H19 (10%)
1440	1476.67	1447.13	17,42	Bend O6–H(28%) +Wagg. CH methoxyl groups (35%)
1430	1463.85	1434.57	156,21	Stre C12–O (10%) + Wagg. C–H methoxyl group (15%) + Bend C24–H24 (13%)
1428	1459.01	1429.82	9,69	Wagg C19–H19 (49%) +Sciss. C14–H14
1426	1457.03	1427.88	5,47	Sciss. C14–H14 (50%)
1412	1438.96	1410.18	97,84	Stre N1–C23 (26%) + Bend H2–C2–N1(19%)
1351	1416.77	1388.43	232,05	Bend O–H (30%)+ Stre C=C aromatic (15%)
1350	1408.35	1380.18	14,26	Bend H2–C2–C16(14%) + Tors H16–C16–C17–O (10%) + Tors H17–C17–O–C18 (13%)
1348	1391.95	1364.11	26,96	Bend H5–C5–N4(20%) + Tors H17–C17–O–C18(12%) + Tors H5–C5–N–C22 (12%)
1330	1357.30	1330.15	51,78	Stre O6–C12 (11%) +Bend H2–C2–N1 (17%) + entire Aromatic ring Vibration
1320	1341.62	1314.78	102,15	Bend HCN (21%) + Stre C23–N1 (10%)
1300	1323.48	1297.01	23,29	Tors H2–C2–N1–C23 (27%)
1280	1299.83	1273.83	66,65	Stre C9=C10 (15%) + Stre C11=C12(12%) +Stre C13=C8 (10%)
1228	1261.78	1236.54	88,09	Stre C9=C10(10%)+ Stre O–C11 (27%) +Bend C11=C12=C13(10%)
1200	1228.43	1203.86	23,57	Bend H14–C14–C3 (28%)Tors H15–C15–C14–C3 (12%)
1100	1119.37	1096.98	65,18	Distortions Entire structure
1060	1092.63	1070.77	22,98	Stre N4–C22(13%)
1020	1044.47	1023.58	17,71	Stre N4–C5(12%) Stre N4–C21(13%)
1000	1033.62	1012.94	99,64	Stre O–C26(46%)
980	1005.81	985.69	19,03	Stre O–C25(23%)
975	990.94	971.12	15,53	Stre C6–C5 (17%) Stre C2–C7(11%) Stre C14–C15(15%)
960	984.40	964.71	25,62	Distortins entire strucuture
953	974.35	954.86	5,99	Distortions Entire structure
930	954.01	934.92	15,62	Distortions Entire structure
920	952.63	933.57	11,64	Stre C23–C24(16%)
880	900.53	882.51	42,37	Tors H14–C14–C15–C16 (62%)
868	893.15	875.28	26,56	Out C7=C2=C16=C17(10%)
857	881.66	864.02	11,17	Distortions Entire Strucuture
836	857.47	840.32	12,18	Distortions Entire Structure
810	836.99	820.25	7,49	Stre C23–C24(10%)
795	819.19	802.80	5,43	Stre O–C18 (10%)
790	798.58	782.60	5,06	Out C9=C10=C11=C12 (17%) + Out C10=C11=C12=C13 (22%) + Out H9–C10–C11–C12 (11%)
648	659.50	646.31	10,09	Bend O=C23–C24 (12%)
621.3	641.76	628.92	7,98	Tors H9–C9–C10–C11(20%)
620	633.49	620.82	1,97	Distortions entire structure
523	539.90	529.10	23,37	Bend O=C23C24 (15%)Tors H–O–C12–C13(19%)
500	517.36	507.01	72,89	Tors H–O–C12–C13 (50%)
480	494.49	484.60	4,26	Distortions Entire structure
RMSD	47.11	10.25		

3.3. HOMO and LUMO analysis

The energy gap between the HOMO (Highest Occupied Molecular Orbital) and LUMO (Lowest Unoccupied Molecular Orbital) is very important for determining the electrical properties, kinetic stability, optical polarizability and chemical reactivity descriptors, such as hardness and softness, of a molecule. The concept of hardness (η) is related to a compound's reactivity and is a property that measures the extent of chemical reactivity to which the addition of a charge stabilizes the system. The chemical potential (μ) provides a global reactivity index and is related to charge transfer from a system of higher chemical potential to one of lower chemical potential. Electronegativity (χ) is the power to attract electrons which is equal to the negative of the chemical potential. All these properties are defined as follows [23,24]:

$$\eta = \frac{(I - A)}{2}$$

$$\mu = \frac{-(I + A)}{2}$$

$$\chi = \frac{(I + A)}{2}$$

where A is the electron affinity and I is the ionization potential of the molecule. The ionization energy and electron affinity are obtained from the HOMO and LUMO energies as $I = -E_{HOMO}$ and $A = -E_{LUMO}$. In terms of chemical hardness, a large HOMO-LUMO gap indicates a hard molecule and is related to more stable molecules, whereas a small gap indicates a soft molecule and is related to a more reactive molecule.

Another important descriptor is the electrophilicity index (ω), a global reactivity index that is related to chemical hardness and chemical potential. The electrophilicity index measures the global electrophilic nature of a molecule and was proposed by Parr et al. [25] as a measure of energy lowering due to charge transfer. The electrophilicity index is defined as follows:

$$\omega = \left(\frac{\mu^2}{2\eta}\right)$$

This parameter permits the classification of organic molecules as strong, ω > 1.5 eV, moderate, 0.8 < ω < 1.5 eV and marginal electrophiles, ω < 0.8 eV. On the other hand, a good correlation with the inverse of the electrophilicity (1/ω) can be made, thus molecules located at the bottom of the electrophilicity scale classified as marginal electrophiles corresponds as good nucleophiles [26]. However, when the molecule bears more than one functional group with opposite electrical charge, its nucleophilic character cannot be straightforwardly associated with the inverse of the electrophilicity. Thus the nucleophilicity index (N) appears as a different descriptor which gives more information about nucleophilicity and is defined [27]:

$$N = E_{HOMO} - E_{HOMO(TCE)}$$

where tetracyanoethylene (TCE) is taken as reference. All these properties were calculated using these equations for the indoline alkaloids through B3LYP/6-311G (2d,p) basis set and their values are shown in Table 2.

As seen in Fig. 4 the calculated HOMO and LUMO orbitals comprise the indoline portion and part of the monoterpene moiety in both structures, however II has a HOMO-LUMO gap slightly

Table 5
Selected second-order perturbation energies of I.

Donor orbital (i)	Type	Acceptor orbital (j)	Type	$E^{(2)}$ (kcal/mol)
C10–C9	π	C11–C12	π*	22.88
C10–C9	π	C8–C13	π*	21.56
C11–C12	π	C10–C9	π*	18.86
C11–C12	π	C8–C13	π*	21.79
C9–C8	σ	C8–C7	σ*	4.14
C9–H9	σ	C8–C13	σ*	5.36
C8–C13	σ	C13–C12	σ*	5.56
C8–C13	σ	N1–C23	σ*	3.87
C8–C13	π	C11–C12	π*	19.49
C8–C7	σ	C12–C13	σ*	4.18
C12–H12	σ	C13–C8	σ*	4.63
C7–C2	σ	C9–C8	σ*	4.47
C2–N1	σ	C13–C12	σ*	4.13
C14–H14	σ	C15–C16	σ*	4.44
C15–C20	σ	C20–C21	σ*	4.14
C18–C20	σ	N4–C21	σ*	4.85
C17–H17	σ	C18–O2	σ*	4.14
C21–H21	σ	C15–C20	σ*	7.26
C23–C24	σ	C2–N1	σ*	4.12
C24–H24	σ	C23–O1	π*	5.67
N1	LP	C13–C8	π*	24.56
N1	LP	C2–C16	σ*	4.56
N1	LP	C23–O1	π*	59.34
O2	LP	C10–C20	σ*	4.75
O2	LP	C17–H17	σ*	6.27
N4	LP	C3–O3	π*	13.39
N4	LP	C21–H21	σ*	8.53
N4	LP	C22–H22	σ*	6.70
O3	LP	C3	RY	18.87
O3	LP	C3–C8	σ*	21.60
O1	LP	N1–C23	σ*	25.66
O1	LP	C23–C24	σ*	18.50
O1	LP	C23	RY	15.53

Table 6
Selected second-order perturbation energies of II.

Donor orbital (i)	Type	Acceptor orbital (j)	Type	$E^{(2)}$ (kcal/mol)
C10–C11	π	C9–C8	π*	16.63
C10–C11	π	C12–C13	π*	20.41
C11–C12	σ	C13–N1	σ*	5.77
C9–C8	σ	C8–C13	σ*	4.75
N1–C2	σ	C2–C7	σ*	4.05
C9–C8	π	C13–C8	π*	17.96
C9–H9	σ	C8–C13	σ*	5.20
C8–C13	σ	C12–C13	σ*	5.11
C8–C13	σ	C12–O6	σ*	4.02
C12–C13	σ	C8–C13	σ*	6.13
C13–C12	π	C10–C11	π*	17.07
C13–C12	π	C9–C8	π*	22.63
C18–C20	σ	N4–C21	σ*	4.84
C20–C21	σ	C18–O2	σ*	5.24
C6–H6	σ	C7–C2	σ*	4.34
C21–H21	σ	C15–C20	σ*	7.31
C23–C24	σ	C13–N1	σ*	4.81
C25–H25	σ	C23–O1	π*	5.54
O6–H6	σ	C11–C12	σ*	4.60
N1	LP	C13–C12	π*	22.05
N1	LP	C23–O1	π*	57.31
N4	LP	C3–O3	π*	12.61
N4	LP	C22–H22	σ*	6.69
O3	LP	C3–C14	σ*	19.49
O3	LP	C3	RY	18.85
O3	LP	C7–C3	σ*	21.83
O1	LP	C24–C23	σ*	17.66
O1	LP	O6–H6	σ*	23.17
O6	LP	C12–C13	σ*	27.23
O5	LP	C10–C11	π*	6.24
O4	LP	C10–C11	σ*	6.54
C10–C11	π*	C9–C8	π*	241.61
C12–C13	π*	C3–C4	π*	210.84

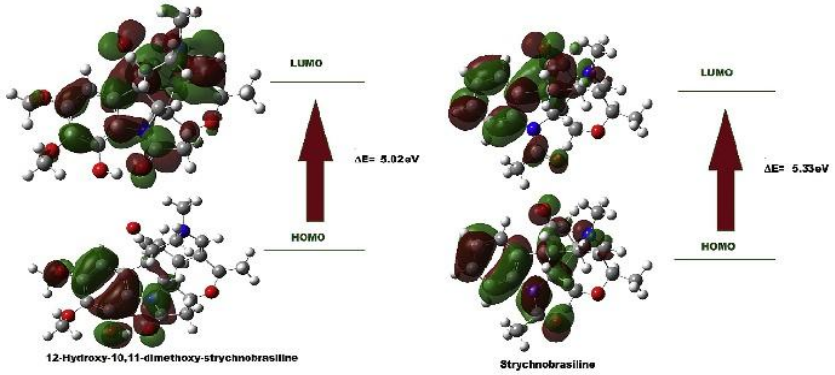

Fig. 4. Frontier molecular orbitals of strychnobrasiline type structures.

smaller than the calculated for structure I (differentiated by 0.28 eV), indicating II to be slightly more reactive. These values influences directly the hardness and the Nucleophilicity index (N) values, revealing II to be softer and more nucleophilic than I, however when these parameters are compared to calculated values for other known natural occurring structures [28–33], I and II present values that classifies them as soft molecules. These results show that the presence of substituents in the benzene ring influences the reactive properties of strychnobrailine type alkaloids as long as these substituents can withdraw or donate electrons to the system.

3.4. UV-VIS analysis

The electronic spectra of the substances in methanol solution were compared to the calculated spectra at time dependent density functional using B3LYP-6311G (2d,p) basis set in methanol (PCM model) as showed in Fig. 5. The experimental spectrum of I revealed bands at 217 and 230–260 nm that were assigned to the sum of the $n \rightarrow \pi^*$ and $\pi \rightarrow \pi^*$ transitions involving the indoline moiety, characteristic of N-acetyl indoline alkaloids [28,34]. The theoretical spectrum presented an intense electronic transition of 6.55 eV at 191.5 nm (oscillator strength f = 0.2865) with major contributions from H-3→L+3 (26%), H-6→L+5 (18%) and H-4→L+2 (50%), being equivalent to the experimental band at 217 nm. The calculations also showed intense electronic transitions at 247.45 nm (5.135 eV) and 257.52 nm (4.813 eV) equivalent to the experimental band at 230–260 nm with contributions from H-1→L (72%) (247.4 nm), H→L (34%) and H→L+1 (43%) (257.52 nm).

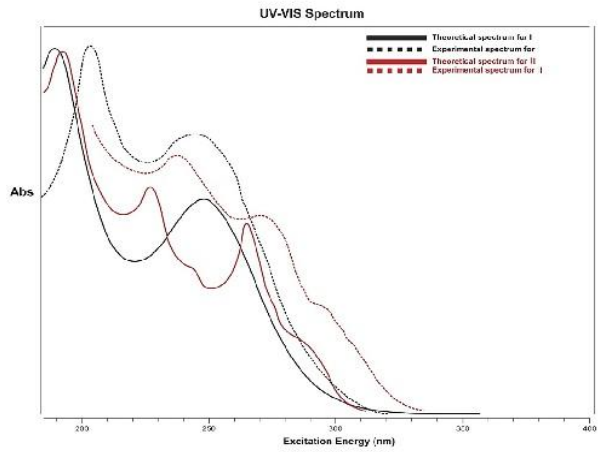

Fig. 5. Comparison between experimental and theoretical at B3LYP 6-311G (2d, p) UV spectra in methanol for strychnobrasiline (I) and 12-hydroxy-10,11dimethoxy strychnobrasiline (II).

The experimental spectrum of II showed bands at 222, 260–270 and 284 nm, characteristic of substituted N-acetyl indoline alkaloids [18,34], revealing a bathochromic shift compared to strychnobrasiline spectrum due to the hyperconjugative $\pi \rightarrow \pi^*$ interactions of the benzene ring with its substituents that act as auxocromic groups (O4, O5 and O6 atoms see Table 6 in NBO section). The theoretical spectrum predicted intense electronic transitions at 222 nm (5.57eV), 254 nm (4.86eV) and 278 nm (4.48eV), showing good agreement with the measured experimental data (Fig. 5). In respect to the electronic transitions the tree maximum calculated absorptions correspond to the major transitions contributions from H-1→L+3 (67%) for 220 nm, H-1→L (33.3%), H→L (16%) and H→L+1 (20%) for 254 nm and H→L (73%) for 278 nm.

3.5. IR analysis

A total of 153 and 180 normal vibration modes were obtained for structures I and II respectively, but only modes between 400 and 4000 cm^{-1} were compared with the experimental spectrum. Fig. 6 shows the experimental and theoretical IR spectra comparison. The differences around can be attributed to the fact that the theoretical DFT calculations were made for the molecules in the gas phase, whereas intermolecular interactions occur experimentally. The assignment of the experimental bands to the normal modes of vibration was made by the calculated potential energy distribution (PED) using the optimized structures with the lowest potential energy at B3LYP/6-311G (2d, p) calculation level (see Tables 3 and 4). In order to investigate the performance of the calculated wavenumbers, the root mean square deviation (RMSD) values between the calculated scaled (scale factor of 0.9802 [35]) and observed wavenumbers were calculated.

The assignment of the experimental bands of structure I (Table 3) show that the wavenumbers between 3100 and 2800 cm^{-1} were related to H–C stretching modes of the aromatic ring (positions 10 and 11), H–C stretching modes of groups 2, 16, 15 and 18, CH_3 stretching modes of groups 19, 22 and 24 and CH_2 stretching vibrations of groups on positions 5, 6, 14 and 17. Bands between 1700 and 1000 were related to C3=O3, C23=O1 and C21=C20 stretching vibrations (assigned to the experimental

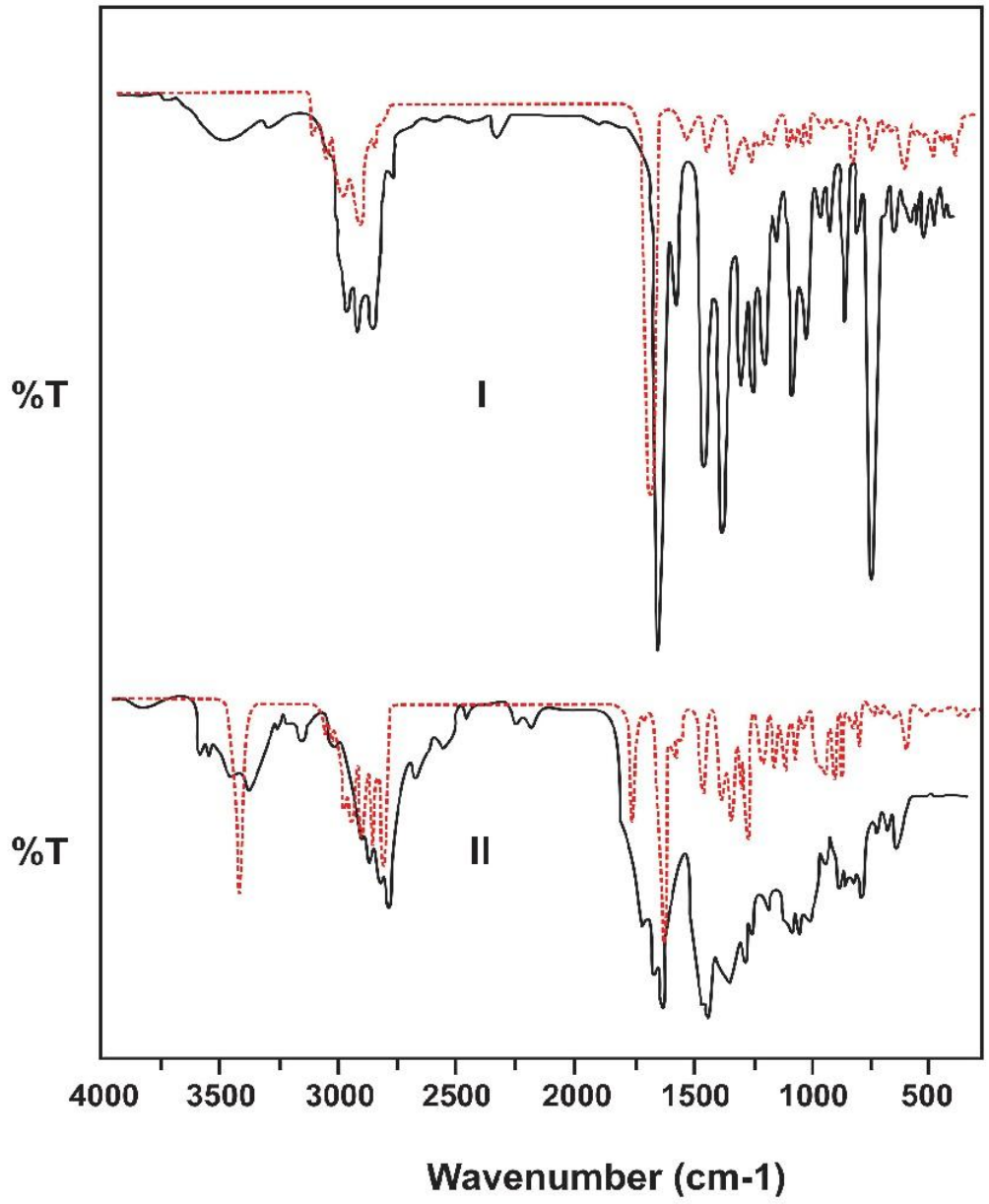

Fig. 6. Theoretical (dashed red line) and recorded FT-IR (black line) spectra of strychnobrasiline (I) and 12-hydroxy-10,11dimethoxystrychnobrasiline (II). (For interpretation of the references to colour in this figure legend, the reader is referred to the web version of this article.)

broad band at 1690/1680 cm^{-1} that corresponds to the calculated scaled wavenumbers 1700 and 1688cm^{-1}), C=C stretching modes of the aromatic ring (bands at 1600 and 1592 cm^{-1} that correspond to the calculated scaled wavenumbers 1602 and 1596 cm^{-1}), H–C=C aromatic ring bend modes (bands at 1470 and 1280 cm^{-1} that correspond to the calculated scaled wavenumbers 1482 and 1285 cm^{-1}), CH_2 scissoring modes (assigned to the experimental band at 1468 cm^{-1}), HCC bend vibration modes (assigned to the band at 1399 cm^{-1} that corresponds to the calculated scaled wavenumber 1398 cm^{-1}), CH_2 twisting mode (assigned to the experimental band at 1318 cm^{-1}), N–C stretching vibration (assigned to the experimental band at 1280 cm^{-1}) and HCCC torsions modes (assigned to the experimental band at 1235 cm^{-1}). Bands between 1000 and 400 cm^{-1} are mostly related to torsions (distortions between dihedral angles) of HCCC, CCCC, HCCN and HCCH type and out of plane modes of HCCH, CCON, COCC type.

The assignment of the experimental bands of structure II (Table 4) shows that bands between 3500 and 2800 cm^{-1} were related to H–O stretching (broad band at 3550/3150cm^{-1}) and H–C stretching modes (bands between 3100 and 2880 cm^{-1}) principally of the methoxy groups and CH_2 groups of C and D rings. Bands between 1700 and 1000 cm^{-1} were related to C3=O3, C23=O1

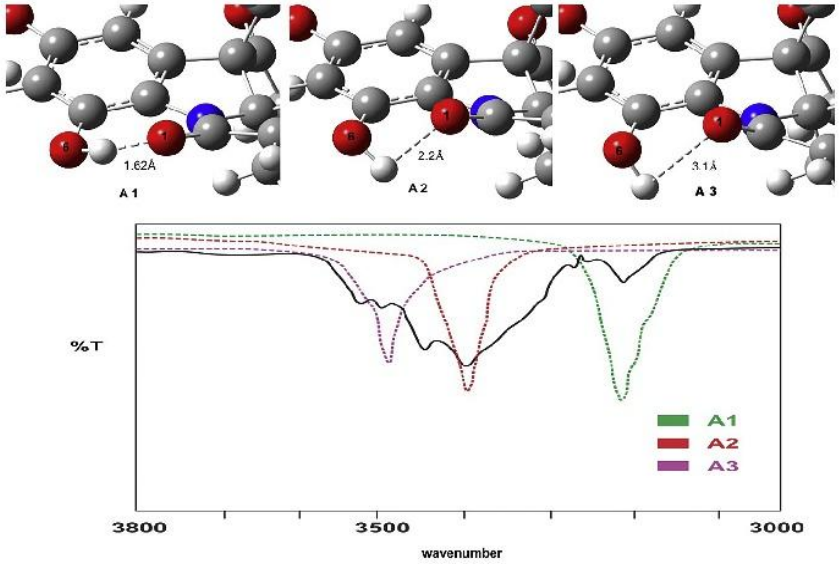

Fig. 7. Comparison between experimental (black line) and theoretical (calculated at different lengths between O6–H and O1) IR bands in the 3800-3000 cm^{-1} region.

and C21=C20 stretching vibration modes (assigned to the bands at 1660 cm^{-1}, 1630 cm^{-1} and 1600 cm^{-1} that correspond to the calculated scaled wavenumbers 1709, 1628and 1607 cm-1), C=C aromatic stretching vibration modes (assigned to the band at 1585 cm^{-1} that corresponds to the calculated scaled wavenumber 1588 cm^{-1}), H–C=C and H–O–C aromatic ring bend vibration modes (assigned to the bands at 1440 and 1351 cm^{-1} that correspond to the calculated scaled wavenumbers 1447 and 1388 cm^{-1}), CH_2 scissoring modes (groups of positions 6, 14, 19, 22, 24 and methoxyl groups assigned to the experimental bands at 1460, 1458, 1428 and 1426 cm^{-1} that correspond to the calculated scaled wavenumbers 1462, 1459, 1429 and 1427 cm^{-1}), CH_2 and CH_3 wagging vibration modes (groups of positions 19, 22, 24 and methoxyl groups assigned to the experimental bands at 1460, 1440, 1430 and 1428 cm^{-1}), H–C bend vibration modes and N–C stretching vibration modes (assigned to the bands at 1412, 1060 and 1020 cm^{-1} that correspond to the calculated scaled wavenumbers at 1410, 1070 and 1023 cm^{-1}). Bands between 1000 and 400 cm^{-1} are mostly related to torsions (distortions between dihedral angles) of HOCC, HCOC, HCCC, CCCC, HCCH and CNCO type and C–C, C–O stretching vibration modes. Concerning to the experimental broad band at 3550/3150 cm^{-1}, assigned to O–H stretching vibration, four bands are displayed, 3175, 3400, 3480 and 3520 cm^{-1}. Theoretical analysis suggest that these dismemberments occur due to the stretching of the hydrogen bond C12–O6H–––O1=C23, as the length of the hydrogen bond varies, the harmonic oscillator frequency of the O–H group changes, producing superimposed shifted bands (downshifted or upshifted) that forms a broad band. Calculated OH wavenumbers at specifics O6H–––O1 lengths (see Fig. 7) presented values close to the experimental ones: 1.62 Å showed O–H stretching vibration at 3171 cm^{-1} (unscaled 3238 cm^{-1}), 2.2 Å showed O–H stretching vibration at 3400 cm^{-1} (unscaled 3469 cm^{-1}) and 3.1 Å showed O–H stretching vibration at 3513 cm^{-1} (unscaled 3592 cm^{-1}).

3.6. NBO analysis

NBO analysis describes the Lewis-like molecular bonding pattern of electron pairs (or of individual electrons in the open-shell case) in optimally compact form. NBOs determine the localized Natural Lewis Structure (NLS) representation of the wave function, while the remaining "non-Lewis"-type NBOs complete the span of the basis and describe the residual "delocalization effects" by the second-order perturbation energies E(2) [donor (i) →acceptor (j)] that involve the most important delocalization and are given by [36–39]:

$$E(2) = \Delta_{ij} = q_i \frac{F_{ij^2}}{\varepsilon_j - \varepsilon_i}$$

Thus, NBOs provide a valence bond-type description of the wave function, closely linked to classical Lewis structure concepts and is a helpful tool for understanding the delocalization of electron density [38,40–42]. The NBO analysis for the title molecules revealed strong hyperconjugative intramolecular interactions of $\pi \rightarrow \pi^*$ and LP→π^* transitions, which are formed by orbital overlaps between C=C bondings and C=C anti-bondings and between N and O lone pairs (LP) and C–C anti-bondings, leading to an intramolecular electronic density transfer causing stabilization of the molecular system in both structures (Tables 5 and 6). For structures I and II the second-order perturbation energies values analysis shows that the greater conjugations values are the $\pi \rightarrow \pi^*$ hyperconjugations of the indoline portion, the LP→π^* hyperconjugations N1→C13–C8, N1→C23–O3 and N4→C3–O3 and the LP→σ^* hyperconjugation O3→C3–C8. $\sigma \rightarrow \sigma^*$ type hyperconjugative intramolecular interactions are predominant in the two structures and contributes to the stabilization of the systems, deserving prominence the interactions C9–H9→C8–C13 (5.36 kcal/mol), C8–C13→C13–C12 (5.56 kcal/mol), C12–C14→C14–C21 (4.14 kcal/mol), C18–C20→N4–C21 (4.85 kcal/mol), C21–H21→C15–C20 (7.26 kcal/mol) for strychnobrasiline and C11–C12→C13–N1 (5.77 kcal/mol), C9–H9→C8–C13 (5.20 kcal/mol), C20–C21→C18–O2 (5.24 kcal/mol), C6–H6→C7–C2 (4.34 kcal/mol), C21–H21→C15–C20 (7.31 kcal/mol), C18–C20→N4–C21 (4.85 kcal/mol), O6–H6→C11–C12 (4.60 kcal/mol) for 12-Hidroxy-10,11-dimethoxystrychnobrasiline. Concerning to the interconnected nine-membered ring (Ring C) the hyperconjugative interaction N4→C3–O3 (LP→π^*) is noteworthy and occur in both structures with values of 13.39 and 12.67 kcal/mol for I and II respectively, thus justifying the transanular interaction between N4 and C3=O (2.50 Å) in experimental results. The hydrogen bond O6H–––O1=C23 that gives stability for the

conformer A of structure II is justified by the strong hyperconjugative interaction O1→H–O6 (LP→σ*, 23.17 kcal/mol) (Fig. 3). Other hyperconjugative interactions that give strong stabilization for both strucutures are noteworthy: C14–H14→C15–C16, C15–C20→C20–C21, C17–H17→C18–O2 and C21–H21→C15–C20. Tables 5 and 6 provide all the significant values of the hyperconjugative interactions given by the second-order perturbation theory.

3.7. NLO analysis

Non-linear effects arise from the interactions of electromagnetic fields in various media to produce new fields altered in phase, frequency, amplitude or other propagation characteristics from the incident fields [43]. When light passes through any molecular medium, the oscillating electric field of the incident light induces an electronic polarization of the molecules comprising the medium. In ordinary materials this electronic displacement (polarization) is directly proportional to the strength of the electric field (intensity of the light). In a nonlinear material, the induced polarization is a nonlinear function of the applied field. NLO activity provides the key functions for frequency shifting, optical modulation, optical switching, optical interconnections and others [44]. The non-linear optical response of an isolated molecule in an electric field can be defined as a Taylor series expansion of the energy of the system in an applied external electric field. Due to the homogeneity and weakness of the external electronic field, this expansion is given below:

$$E = E^o - \mu_\alpha F_\alpha - 1/2\alpha_{\alpha\beta}F_\alpha F_\beta - 1/6\beta_{\alpha\beta\gamma}F_\alpha F_\beta F_\gamma + \ldots\ldots$$

where E^o is the energy of the unperturbed molecules, F_α is the field at the origin, μ_α, $\alpha_{\alpha\beta}$ and $\beta_{\alpha\beta\gamma}$ are the permanent dipole moment, the linear polarizability and the first hyperpolarizability tensor components respectively. In molecules that have an acentric electron distribution, like organic molecules, β values are significant.

The total static dipole moment μ, the mean polarizability, α the anisotropy of the polarizability, $\Delta\alpha$ and the mean first hyperpolarizability, β using x, y and z components are defined as:

Dipole moment

$$\mu = \left(\mu_x^2 + \mu_y^2 + \mu_z^2\right)^{1/2}$$

Static polarizability

$$\alpha_0 = (\alpha_{xx} + \alpha_{yy} + \alpha_{zz})/3$$

Total polarizability

$$\Delta\alpha = 2^{-1/2}\left[(\alpha_{xx} - \alpha_{yy})^2 + (\alpha_{yy} - \alpha_{zz})^2 + (\alpha_{zz} - \alpha_{xx})^2 + 6\alpha_{xz}^2 + 6\alpha_{xy}^2 + 6\alpha_{yz}^2\right]^{1/2}$$

First order hyperpolarizability

$$\beta = \left(\beta_x^2 + \beta_y^2 + \beta_z^2\right)^{1/2}$$

where

$$\beta_x = \left(\beta_{xxx} + \beta_{xyy} + \beta_{xzz}\right)$$

$$\beta_y = \left(\beta_{yyy} + \beta_{yzz} + \beta_{yxx}\right)$$

$$\beta_z = \left(\beta_{zzz} + \beta_{zxx} + \beta_{zyy}\right)$$

Since the values of polarizabilities in Gaussian output are reported in atomic units (a.u.) the calculated values have been converted into electrostatic units (esu) (For α: 1 a.u. = 0.1482×10^{-24} esu; For β: 1 a.u. = 8.639×10^{-33} esu) (See Tables 7 and 8). The DFT approach at B3LYP/6-311G(2d,p) level has been used to predict dipole moments, polarizability and first order hyperpolarizability. Nonlinear optics is used either to shift the optical frequency of the available fields or to remodel their spatio-temporal characteristics, an example here is the second harmonic generation (SHG), this is essentially a frequency-doubling process: two waves, each of frequency ω, simultaneously superimpose constructively. The resulting wave excites an electron from the ground state to a virtual excited state, on relaxation, one wave of frequency 2ω is emitted with half the wavelength of the initial photons. Such materials can be used to double or triple the frequency of a laser light and are of considerable interest for the high-speed data processing, which is essential for numerous modern technologies and due to its relation with SHG effect the calculation of first hyperpolarizability is essential on molecular scale [45]. As seen in Tables 7 and 8 the highest value dipole component for I is the $\mu_z = -4.866$ and the total dipole moment is $\mu_{total} = 4.502D$. For structure II the highest value dipole component is the $\mu_x = -5.92664D$ and the total dipole moment is $\mu_{total} = 6.0824D$. The calculated mean polarizability α_0 and anisotropy of polarizability $\Delta\alpha_{total}$ for I are 2.14×10^{-23} and 24.36×10^{-24} esu respectively while for II these parameters are 4.45×10^{-23} and 20.37×10^{-24} esu respectively. The calculated values of first order hyperpolarizability β for these molecules are 1.88×10^{-30} and 3.421×10^{-30} esu for I and II respectively which concludes that structure II have higher nonlinear value than I, however these values are significantly greater than β of urea (~0.2×10^{-30} esu) [46–48], which indicate that these molecules are potential candidates for nonlinear optical applications.

3.8. Molecular docking study

PASS (prediction of activity spectra) [49] is an online tool that estimates the pharmacological activities of a molecule based on SAR (structure activity relationship) analysis of a data set containing more than 205000 compounds exhibiting more than 3000 kinds of biological activities. It works on the principle that the biological activity of a compound equates to its structure. PASS

Table 7
Dipole moment, polarizability and hyperpolarizability data in gas phase for structure I at B3LYP 6-311G(2d,p).

Dipole, D	Polarizability, a.u.	Hyperpolarizability, a.u.
$\mu_x = -4.8661$	$\alpha_{xx} = 0.0003$	$\beta_{xxx} = 62.2652$
$\mu_y = -0.7588$	$\alpha_{xy} = -4.3281$	$\beta_{xxy} = -0.1148$
$\mu_z = -0.4717$	$\alpha_{yy} = 266.1424$	$\beta_{xyy} = -104.1293$
$\mu_{total} = 4.502$	$\alpha_{xz} = -17.5246$	$\beta_{yyy} = 105.3091$
	$\alpha_{yz} = -0.8564$	$\beta_{xxz} = -144.3697$
	$\alpha_{zz} = 202.222$	$\beta_{xyz} = 58.4057$
	$\alpha_{total} = 2.1372 \times 10^{-23}$esu	$\beta_{yyz} = 0.0010$
	$\Delta\alpha_{total} = 24.3563 \times 10^{-24}$esu	$\beta_{xzz} = -31.0571$
		$\beta_{yzz} = 10.5004$
		$\beta_{zzz} = -26.0655$
		$\beta_{total} = 1.887 \times 10^{-30}$esu

Table 8
Dipole moment, polarizability and hyperpolarizability data in gas phase for structure II at B3LYP 6-311G(2d,p).

Dipole, D	Polarizability, a.u.	Hyperpolarizability, a.u.
$\mu_x = -5.9266$	$\alpha_{xx} = 369.5805$	$\beta_{xxx} = -119.00059$
$\mu_y = -0.32346$	$\alpha_{xy} = -4.58889$	$\beta_{xxy} = -27.68699$
$\mu_z = -1.32916$	$\alpha_{yy} = 300.03212$	$\beta_{xyy} = -248.96981$
$\mu_{total} = 6.08246$	$\alpha_{xz} = -15.08873$	$\beta_{yyy} = 68.00944$
	$\alpha_{yz} = 1.126915$	$\beta_{xxz} = -92.474886$
	$\alpha_{zz} = 231.47619$	$\beta_{xyz} = 42.53393$
	$\alpha_{total} = 4.45136 \times 10^{-23}$esu	$\beta_{yyz} = 102.59022$
	$\Delta\alpha_{total} = 20.3684 \times 10^{-24}$esu	$\beta_{xzz} = -22.5852$
		$\beta_{yzz} = -0.3776321$
		$\beta_{zzz} = -61.98293$
		$\beta_{total} = 3.4212 \times 10^{-30}$esu

prediction tools are constructed using 20000 principal compounds from MDDR database (produced by Accelrys and Prous Science) [50,51]. The database contains over 180000 biologically relevant compounds and is constantly updated. PASS web tool has the ability to predict approximately 3700 pharmacological effects, mechanisms and special toxicities of a molecule including mutagenicity, carcinogenicity, teratogenicity, and embryotoxicity. Average accuracy of prediction is about 95% according to leave-one-out cross validation (LOOCV) estimation and the probabilities, the Pa (probable activity) and Pi (probable inactivity), are values that vary from 0.000 to 1.000, in general Pa+Pi≠1 since these probabilities are calculated independently [51]. The PASS prediction results for the studied alkaloids are listed in Tables 9 and 10.

Among the various predicted properties the following activities deserve attention: antineoplastic, uterine relaxant, CYP17 inhibitor, antiprotozoal, analeptic, dementia treatment and polarization stimulant. From this premise molecular docking calculations were performed on AutoDock-Vina [52] with DNA Topoisomerase II-DNA complex (topo II-DNA) due to the fact that a wide variety of molecules used for the treatment of human cancers (antineoplastics)

Table 9
PASS prediction for the activity spectrum for strychnobrasiline with Pa>0.2

Pa	Pi	Activity name
0.633	0.055	CYP2H substrate
0.462	0.046	Polarization stimulant
0.461	0.047	Respiratory analeptic
0.423	0.049	Analeptic
0.395	0.023	Prostate cancer treatment
0.402	0.051	Dementia treatment
0.384	0.050	CYP17 inhibitor
0.443	0.116	Nicotinic alpha4beta4 receptor agonist
0.376	0.058	P-glycoprotein substrate
0.333	0.039	Uterine relaxant
0.396	0.106	Antineoplastic
0.398	0.108	27-Hydroxycholesterol 7alpha-monooxygenase inhibitor
0.394	0.112	Mannotetraose 2-alpha-N-acetylglucosaminyltransferase inhibitor
0.378	0.121	Anaphylatoxin receptor antagonist
0.275	0.026	Antimycoplasmal
0.313	0.105	5 Hydroxytryptamine release stimulant
0.315	0.117	Analgesic
0.308	0.130	CYP2C19 inducer
0.247	0.074	Xenobiotic-transporting ATPase inhibitor
0.234	0.064	Antineoplastic alkaloid
0.266	0.098	Prostate disorders treatment
0.225	0.059	Antineoplastic (lung cancer)
0.239	0.077	Antiprotozoal
0.208	0.067	Lipocortins synthesis antagonist
0.275	0.145	CYP3A5 substrate
0.223	0.096	Antiinfertility, female
0.314	0.193	Neurotransmitter uptake inhibitor

Table 10
PASS prediction for the activity spectrum for 12-hydroxy-10,11-dimethoxystrychnobrasiline with Pa>0.2.

Pa	Pi	Activity name
0.622	0.040	Antineoplastic
0.623	0.059	CYP2H substrate
0.533	0.031	Respiratory analeptic
0.489	0.033	Analeptic
0.446	0.016	Prostate cancer treatment
0.491	0.085	Nicotinic alpha4beta4 receptor agonist
0.422	0.060	Polarization stimulant
0.378	0.056	P-glycoprotein substrate
0.368	0.073	Dementia treatment
0.328	0.035	Antineoplastic (lung cancer)
0.389	0.114	Mannotetraose 2-alpha-N-acetylglucosaminyltransferase inhibitor
0.317	0.049	Uterine relaxant
0.336	0.071	CYP17 inhibitor
0.295	0.046	Xenobiotic-transporting ATPase inhibitor
0.389	0.150	General pump inhibitor
0.267	0.028	Antimycoplasmal
0.467	0.229	Gluconate 2-dehydrogenase (acceptor) inhibitor
0.321	0.138	Histamine release stimulant
0.282	0.105	Antineoplastic (solid tumors)
0.233	0.065	Antineoplastic alkaloid
0.293	0.144	Caspase 3 stimulant
0.231	0.085	Cardiovascular analeptic

such as lung, ovarian, brain, breast, adrenocortical and testicular cancers, Hodgkin and non-Hodgkin lymphomas are eukaryotic topo II inhibitors. The docking calculation in AutoDock Vina (ADTV) consists in a number of sequential steps. Each step involves a random perturbation of the conformation followed by a local optimization (using the Broyden-Fletcher-Goldfarb-Shanno algorithm [53] which is an efficient quasi-Newton method) and a selection in which the step is accepted or not. Each local optimization involves many "evaluations" of the scoring function as well as its derivatives in the position-orientation-torsion coordinates. The number of evaluations in a local optimization is guided by convergence [52,53]. X-ray crystal structure of human DNA topo II beta complexed with DNA and amsacrine (PDB ID: 4G0U) [54] was

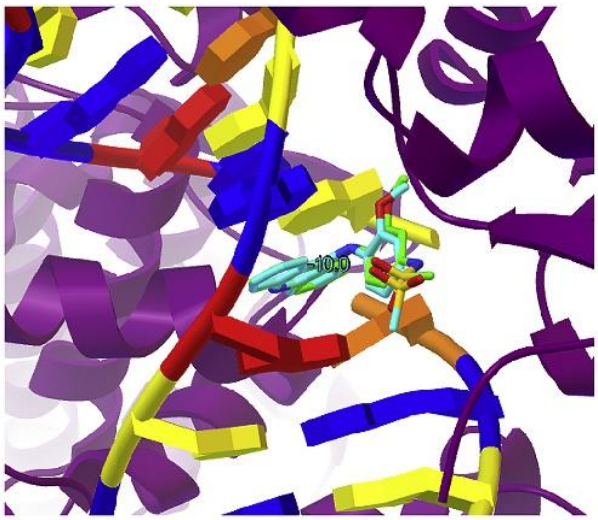

Fig. 8. Superimposition of the docked (ciano) and co-crystallized (green) structure of amsacrine into the DNA cleavage site of DNA topoisomerase II. (For interpretation of the references to colour in this figure legend, the reader is referred to the web version of this article.)

obtained from the Protein Data Bank web site (http://www.rcsb.org/pdb/). Water molecules and amsacrine were removed, Gasteiger charges were assigned and the macromolecule was saved in PDBQT file format using ADTV. A Grid box size of 50 × 50 × 50 Å was centered at the site of DNA cleavage of topo II–DNA complex. The docking protocol was tested by removing the co-crystallized inhibitor from the protein and then docking it at the same site (Fig. 8). The superimposition of the structures showed RMSD = 0.382, RMSD, values up to 2 Å are considered reliable for a docking protocol. Free energy of binding (ΔG) analysis demonstrated that molecules I and II docked with ΔG values of −8.0 and −9.5 kcal/mol respectively while the know inhibitor amsacrine docked with ΔG = −10.0 kcal/mol. Binding modes analysis demonstrated that 12-hydroxy-10,11-dimethoxystrychnobrasiline docked at the site of DNA cleavage between the base pairing similar to amsacrine in topo II-DNA complex while strychnobrasiline docked at the site of DNA cleavage around to the base pairing (Fig. 9a and b). Amsacrine binds more efficiently with the base pairs, because it is a flat structure with benezene rings, conferring a greater anticancer potential, however the indoline group present in both alkaloids promotes a good interaction with topo II-DNA complex and the addition of substituents in the benzene ring enhance such interaction.

Strychnobrasiline (I) binds at the catalytic site of the substrate (Fig. 9c) by weak non-covalent interactions, π-π interactions, alkyl-alkyl interactions and amino-alkyl interactions. Ring A interacts with Pro819 by alkyl-π interaction, Ring C interacts with Met781 by an alkyl-alkyl interaction, Ring D, E and CH_3 (position 23) interact with Met 781 by alkyl-alkyl interactions, CH_3 (24) interacts with base DT 9 by weak alkyl-alkyl interaction and CH_3 (position 19) interacts with Arg 820 by amino-alkyl interaction.12- hydroxy-10,11-dimethoxstrychnobrasiline (II) binds at the catalytic site of the substrate (Fig. 9d) by alkyl-π interactions, alkyl-alkyl interactions, sulfur-alkyl interactions, amino-alkyl interactions and π-π interactions. A Ring and B Ring interacts with base DG 13 and DA 12 by π-π and amino-π interactions, CH_3 (position 24) interacts with Met 782 and Gln 778 by sulfur-alkyl interaction and alkyl-alkyl interaction respectively.

Structure II binds at the topo II-DNA complex by pi-pi interactions between aromatic rings with both upstream and downstream base pairs thus interacting more efficiently than I that binds only laterally with one base pair, justifying the ΔG values. These results suggest that II may have a more significant antineoplastic activity than I. In fact structure I has a very low cytotoxicity against some cancer cells [2,55], however based on molecular docking results, the presence of substituents in the benzene ring might increase the cytotoxicity of these type of molecules revealing a possible anticancer potential for structure II.

4. Conclusion

Strychnobrasiline (I) and 12-hydroxy-10,11dimethoxystrychnobrasiline (II), which were isolated from *Strychnos mattogrossensis*, were comprehensively characterized with their spectral behavior

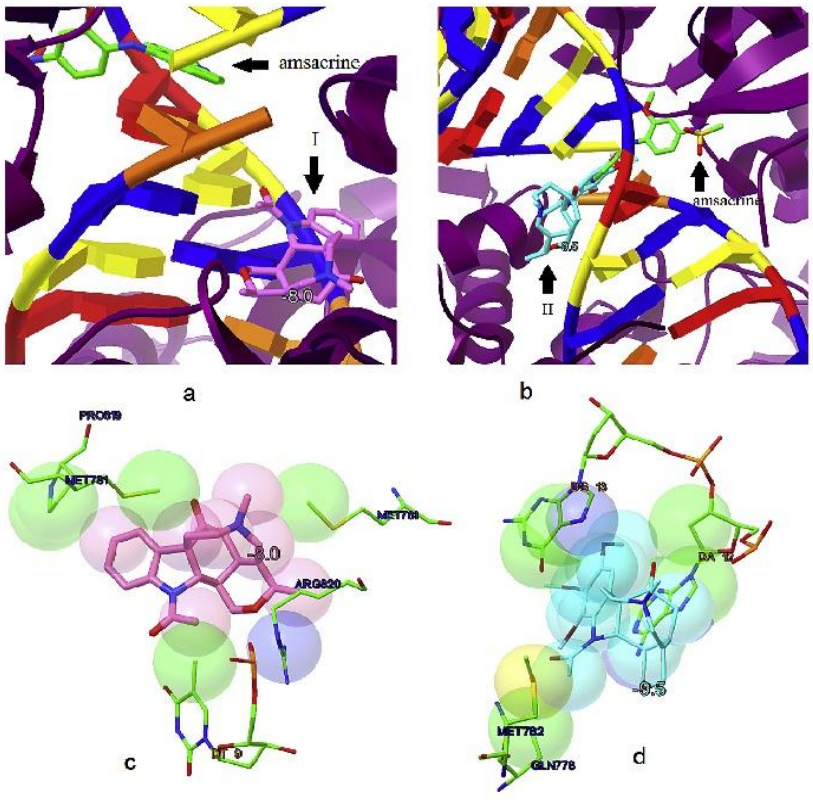

Fig. 9. Binding modes of strychnobrasiline type alkaloids docked to topo II-DNA complex (a) Superimposition of the docked strychnobrasiline (I-pink) and co-crystallized structure of amsacrine (green); (b) Superimposition of the docked 12- hydroxy-10,11-dimethoxstrychnobrasiline (II-ciano) and co-crystallized structure of amsacrine (green); (c)Ligand-protein complex interactions of strychnobrasiline-topo II-DNA complex; (d)Ligand-protein complex interactions of 12-hydroxy-10,11-dimethoxstrychnobrasiline -topo II-DNA complex. The spheres are regions of interaction between the atoms of the ligand and the groups of the topo II-DNA complex site. (For interpretation of the references to colour in this figure legend, the reader is referred to the web version of this article.)

and quantum properties described. The interatomic distances and angles proved to be plausible compared to the X-ray data for a similar molecule. The conformational analysis evaluated two possible conformers for both structures and revealed that conformer B presents the lowest energy for strychnobrasiline in gas phase, however in chloroform the conformer A is the most stable, showing that the solvatation is decisive for the Gibbs free energy of strychnobrasiline conformers. For 12-Hydroxy-10,11dimethoxystrychnobrasiline the conformer A is the most stable in both the gas phase and chloroform medium, due to the hydrogen bond O6—H—O1═C23 (with hyperconjugation energy of 23.17 kcal/mol in NBO calculations). The HOMO-LUMO gap of II is slightly smaller than the calculated for I (~0.28 eV), showing 12-hidroxy-10,11-dimethoxystrycnobrasiline slightly more reactive. However the small HOMO-LUMO gap calculated for both structures are directly related to their reactivity, reflecting their amount of chemical hardness, electrophilicity, nucleophilicity index, and electronegativity, which leads to classify them as soft molecules compared to other structures in the associated literature. The calculated electronic spectra of the structures showed consistency with the experimental spectra, with bands assigned to a sum of $n \rightarrow \pi^*$ and $\pi \rightarrow \pi^*$ transitions of indoline moiety. The UV spectrum of II presented a bathochromic shift in relation to I, justified by hyperconjugative $LP \rightarrow \pi^*$ interactions of the O4, O5 and O6 substituents with benzene ring in NBO calculations. The comparative IR studies revealed several characteristic vibrations that may be used as a diagnostic tool for other strychnobrasiline type alkaloids, simplifying their identification and structural characterization. The calculated hyperpolarizability of structures I and II are 10 and 17 times that of the standard NLO material urea showing that strychnobrasiline type alkaloids are an attractive object for future studies of nonlinear optical properties. The molecular docking results reveal good interactions of 12-hydroxy-10,11-dimethoxstrychnobrasiline with the DNA-Topoisomerase II complex, with ΔG value close to amsacrine, suggesting that strychnobrasiline alkaloids might exhibit antineoplastic properties and require the necessity of carrying out new studies with these structures due to the presented activity spectrum.

Acknowledgments

The authors thank Dr. Elaine H.T. Oliveira from Federal University of Amazonasfor the spelling support, CAPES and Finep for the financial support.

References

[1] M. Frederick, M.P. Hayette, M. Tits, P. De Mol, L. Angenot, In vitro activities of *Strychnos* alkaloids and extracts against *Plasmodium falciparum*, Antimicrob. Agents Chemother. 43 (1999) 2328–2331.
[2] P. Rasoanaivo, S. Ratsimamanga-Urverg, R. Milijaona, In vitro and in vivo chloroquine-potentiating action of *Strychnos myrtoides* alkaloids against chloroquine-resistant strains of *Plasmodium* malaria, Planta Med. 60 (1994) 13–16.
[3] R. Bassleer, M.C. Depauw-Gillet, B. Massart, Effets de trois alkaloides extraits du *Strychnos usambarensis* sur dès cellules cancéreuses en culture, Planta Med. 45 (1982) 123–126.
[4] C. Caron, M.J. Hoizey, L. Le Men-Olivier, Antimicrobial and antifungal activities of quasi-dimeric and related alkaloids, Planta Med. 5 (1988) 409–412.
[5] J. Quetin-Leclercq, A. Favel, G. Balansard, P. Regli, L. Angenot, Screening for in vitro antifungal activities of some indole alkaloids, Planta Med. 61 (1995) 475–477.
[6] C.L.C. deMedeiros, G. Tomas, R. Mukherjee, The source of Ca^{2+} for the spasmolytic actions of longicaudatine, a bisindole alkaloid isolated from *Strychnos trinervis*, Phytother. Res. 5 (1991) 24–28.
[7] V.K. Kapoor, S.K. Sharma, K.K. Chagti, M. Singh, Synthesis and hypotensive activity of diaboline, Indian J. Chem. B Org. Chem. Incl. Med. Chem. 27 (1988) 641–644.
[8] M. Tits, J. Damas, J. Quetin-Leclercq, L. Angenot, From ethnobotanical uses of *Strychnos henningsii* to antiinflammatories, analgesics and antispasmodics, J. Ethnopharmacol. 34 (1991) 261–267.
[9] N. Kaushik, N. Kaushik, P. Attri, N. Kumar, C. Kim, A. Verma, E. Choi, Biomedical importance of indoles, Molecules 18 (2013) 6620–6662.
[10] S. Biswal, U. Sahoo, S. Sethy, H.K.S. Kumar, M. Banerjee, Indole: the molecule of diverse biological activities, Asian J. Pharm. Clin. Res. 5 (2012) 1–6.
[11] M.E. Welsch, S.A. Snyder, B.R. Stockwell, Privileged scaffolds for library design and drug discovery, Curr. Opin. Chem. Biol. 14 (2010) 347–361.
[12] H. Johansson, T.B. Jorgensen, D.E. Gloriam, H. Brauner-Osborne, D.S. Pedersen, 3-substituted 2-phenyl-indoles: privileged structures for medicinal chemistry, RSC Adv. 3 (2013) 945–960.
[13] G. Philippe, L. Angenot, M. Tits, M. Frédérich, About the toxicity of some *Strychnos* species and their alkaloids, Toxicon 44 (2004) 405–416.
[14] I. Iwataki, J. Comin, Studies on argentine plants—XXXI: alkaloids from *Strychnos brasiliensis*, Tetrahedron 27 (1971) 2541–2552.
[15] L. Angenot, M.L.B. Pinheiro, A.F.I. Rocha, P. Poukens-Renwart, J. Quetin-Leclercq, R. Warin, An indolinic alkaloid from *Strychnos mattogrossensis*, Phytochemistry 29 (1999) 2746–2749.
[16] M. Caprasse, L. Angenot, Les Alcaloïdes majoritaires du *Strychnos scheffleri* du zaire, Planta Med. 42 (1983) 364–370.
[17] F.C. Ohiri, R. Verpoorte, A.B. Svendsen, Alkaloids of *Strychnos soubrensis* Hutch. et. Dalz (Loganiaceae), J. Nat. Prod. 43 (1983) 595–597.
[18] M.B. Pinheiro, P. Couceiro, A. Da Rocha, F. Monte, J. Villar, A new strychnobrasiline base of *Strychnos mattogrossensis*, Nat. Prod. Lett. 16 (2002) 229–233.
[19] M.J. Frisch, G.W. Trucks, H.B. Schlegel, G.E. Scuseria, M.A. Robb, J.R. Cheeseman, G. Scalmani, V. Barone, B. Mennucci, G.A. Petersson, H. Nakatsuji, M. Caricato, X. Li, H.P. Hratchian, A.F. Izmaylov, J. Bloino, G. Zheng, J.L. Sonnenberg, M. Hada, M. Ehara, K. Toyota, R. Fukuda, J. Hasegawa, M. Ishida, T. Nakajima, Y. Honda, O. Kitao, H. Nakai, T. Vreven, J.A. Montgomery Jr., J.E. Peralta, F. Ogliaro, M. Bearpark, J.J. Heyd, E. Brothers, K.N. Kudin, V.N. Staroverov, R. Kobayashi, J. Normand, K. Raghavachari, A. Rendell, J.C. Burant, S.S. Iyengar, J. Tomasi, M. Cossi, N. Rega, J.M. Millam, M. Klene, J.E. Knox, J.B. Cross, V. Bakken, C. Adamo, J. Jaramillo, R. Gomperts, R.E. Stratmann, O. Yazyev, A.J. Austin, R. Cammi, C. Pomelli, J.W. Ochterski, R.L. Martin, K. Morokuma, V.G. Zakrzewski, G.A. Voth, P. Salvador, J.J. Dannenberg, S. Dapprich, A.D. Daniels, Ö. Farkas, J.B. Foresman, J.V. Ortiz, J. Cioslowski, D.J. Fox, Gaussian 09, Gaussian, Inc., Wallingford CT, 2009.
[20] R. Dennington, T. Keith, J. Millam, Gaussian Version 5, Semichem. Inc., Shawnee Missions KS, 2009.
[21] M. Jamroz, Vibrational Energy Distribution Analysis, VEDA 4 Computer Program, 2004. Poland.
[22] A. Mostad, K. Lundquist, T. Greibrokk, L. Mitscher, D.T.W. Chu, Crystal and molecular structure of 14-Hydroxy-strychnobrasiline, Acta Chem. Scand. 38 (1984) 381–386.
[23] R. Parr, G. Pearson, Absolute hardness: companion parameter to absolute electronegativity, J. Am. Chem. Soc. 105 (1983) 7512–7516.
[24] R. Parr, Functional Theory of Atoms and Molecules, Oxford University Press, New York, 1989.
[25] R. Parr, L. Szentpaly, S. Liu, Electrophilicity index, J. Am. Chem. Soc. 121 (1999) 1922–1924.
[26] L.R. Domingo, P. Pérez, The nucleophilicity N index in organic chemistry, Org. Biomol. Chem. 9 (2011) 7168–7175.
[27] L.R. Domingo, E. Chamorro, P. Perez, Understanding the reactivity of captodative ethylenes in polar cyclo addition reactions. A theoretical study, J. Org. Chem. 73 (2008) 4615–4624.
[28] R.A. Costa, M.L.B. Pinheiro, K.M.T. Oliveira, A. Barison, K.S. Salomé, J.R. Iank, N.G. Silva, T.S. Cabral, E.V. Costa, Structural, vibrational, and electronic properties of the glucoalkaloid strictosidine: a combined experimental and theoretical study, J. Chem. (2016), http://dx.doi.org/10.1155/2016/1752429. Article ID 1752429.
[29] R.A. Costa, P.O. Pitt, M.L.B. Pinheiro, K.M.T. Oliveira, A. Barison, K.S. Salomé, E.V. Costa, Spectroscopic investigation, vibrational assignments, HOMO-LUMO, NBO, MEP analysis and molecular docking studies of oxoaporphine alkaloid liriodenine, Spectrochim. Acta A 174 (2017) 94–104.
[30] D. Glossman-Mitnik, A comparison of the chemical reactivity of naringenin calculated with the M06 family of density functionals, Chem. Cent. J. 7 (2013) 155.
[31] E.H. Anouar, K. Marakchi, N. Komiha, O.K. Kabbaj, D. Zoubeida, S. Lahmar, Relationship between antioxidant acidity of several flavonols and their molecular properties, Phys. Chem. News 45 (2009) 107–113.
[32] S.A.P. Gomes, N. Flores, A.P. Hernández, M. Piñón, D. Glossman-Mitnik, Computational molecular characterization of the flavonoid rutin, Chem. Cen. J. 4 (2010) 12, http://dx.doi.org/10.1186/1752-153X-4-12.
[33] G.M. Al-Mazaideh, T.S. Ababneh, K.H. Abu-Shandi, R.M.A.Q. Jamhour, H.J.A. Salman, A.M. Al-Msiedeen, S.M. Khalil, DFT Calculations of mesembryanthemum nodiflorum compounds as corrosion inhibitors of aluminum, Phys. Sci. Inter. J. 12 (2016) 1–7.
[34] A.W. Sangster, K.L. Stuart, Ultraviolet spectra of alkaloids, Chem. Rev. 65 (1965) 69–130.
[35] S.G. Andrade, Luísa C.S. Gonçalves, F.E. Jorge, Scaling factors for fundamental vibrational frequencies and zero-point energies obtained from HF, MP2, and DFT/DZP and TZP harmonic frequencies, J. Mol. Struct. THEOCHEM 864 (2008) 20–25.
[36] B.C. Carlson, J.M. Keller, Orthogonalization procedures and the localization of wannier functions, Phys. Rev. 105 (1957) 102–103.

[37] F. Weinhold, J.E. Carpenter, Analysis of the geometry of the hydroxymethyl radical by the 'different hybrids for different spins' natural bond orbital procedure, J. Mol. Struct. (Theochem) 169 (1988) 41–62.
[38] A.E. Reed, R.B. Weinstock, F. Weinhold, Natural populationanalysis, J. Chem. Phys. (1985) 735–739.
[39] E.R. Davidson, Reduced Density Matrices in Quantum Chemistry, Academic Press, New York, 1976.
[40] R.S. Mulliken, Electronic population analysis on LCAO-MO molecular wave functions, J. Chem. Phys. (1955) 1833–1841.
[41] A.E. Reed, F. Weinhold, Natural bond orbital analysis of near-Hartree-Fock water dimer, J. Chem. Phys. 78 (1983) 4066–4073.
[42] J.K. Badenhoop, F. Weinhold, Natural bond orbital analysisof steric interactions, J. Chem. Phys. 14 (107) (1997) 5406–5421.
[43] D. Kleinman, Nonlinear dielectric polarization in optical media, J. Phys. Rev. 126 (1962) 1977–1979.
[44] V.M. Geskin, C. Lambert, J.L. Bredás, Origin of high second- and third-order nonlinear optical response in ammonio/borato diphenylpolyene Zwitterions: the remarkable role of polarized aromatic groups, J. Am. Chem. Soc. 15 (2003) 15651–15658.
[45] D. Arivuoli, Fundamentals of nonlinear optical materials, Pramana J. Phys. 57 (2001) 871–883.
[46] C. Adant, M. Dupuis, J.L. Brédas, Ab initio study of the nonlinear optical properties of urea: electron correlation and dispersion effectsInt, J. Quantum Chem. 29 (1995) 497–507.
[47] M. Ferrero, B. Civalleri, M. Rérat, R. Orlando, R. Dovesi, The calculation of the static first and second susceptibilities of crystalline urea: a comparison of Hartree–Fock and density functional theory results obtained with the periodic coupled perturbed Hartree–Fock/Kohn–Sham scheme, J. Chem. Phys. 131 (2009), http://dx.doi.org/10.1063/1.3267861.
[48] H. Abbas, M.M. Shkir, S. Al Faify, Density functional study of spectroscopy, electronic structure, linear and nonlinear optical properties of L-proline lithium chloride and L-proline lithium bromide monohydrate: for laser applications, Arab. J. Chem. (2015), http://dx.doi.org/10.1016/j.arabjc.2015.02.011.
[49] A. Lagunin, A. Stepanchikova, D. Filimonov, V. Poroikov, PASS: prediction of activity spectra for biologically active substances, Bioinformatics 16 (2000) 747–748.
[50] S. Parasuraman, Prediction of activity spectra for substances, J. Pharm. Pharmacol. 2 (2017) 52–53.
[51] R. Pramely, T.L.S. Raj, Predicition of biological activity spectra of a few phytoconstituents of *Azadirachta indicia*, A. Juss J. Biochem. Tech. 3 (2012) 375–379.
[52] O. Trott, A.J. Olson, Software news and update AutoDock Vina: improving the speed and accuracy of docking with a new scoring function, efficient optimization and multithreading, J. Comput. Chem. 31 (2010) 455–461.
[53] J. Nocedal, S.J. Wright, Numerical Optimization, Springer Series in Operations Research, Springer Verlag, Berlin, 1999.
[54] C.C. Wu, Y.C. Li, Y.R. Wang, T.K. Li, N.L. Chan, On the structural basis and design guidelines for type II topoisomerase-targeting anticancer drugs, Nucleic Acids Res. 41 (2013) 10630–10640.
[55] J. Leclercq, M.C. de Pauw-Gillet, R. Basller, L. Angenot, Screening of cytotoxic activity of *Strychnos* alkaloids, J. Ethnopharmacol. 15 (1986) 305–316.

6.3. Investigação das propriedades espectroscópicas, assinalamento vibracional, análises HOMO-LUMO, NBO, MEP e estudos de docking molecular do alcaloide oxoaporfínico liriodenina

O artigo em questão, publicado no prestigiado período Spectrochimica acta A (Fator de impacto = 2.82), consistiu no estudo das propriedades estruturais, vibracionais e eletrônicas do alcaloide liriodenina. A escolha da realização de um estudo teórico acerca deste alcaloide se deu em virtude de ser uma molécula muito conhecida e de amplo espectro farmacológico no campo da fitoquímica e farmacologia. O estudo abordou a avaliação de: dados de otimização geométrica (até então inexistentes na literatura devido à inexistência de dados de raios-x para tal molécula), que comparados com dados de cristalografia de raios-x de uma estrutura similar apresentaram valores bem aproximados; cálculos de UV-Vis teórico onde foi possível analisar os orbitais envolvidos nas transições eletrônicas; cálculos de orbitais HOMO-LUMO e índices de reatividade; análise de mapas de potencial eletrostático, onde foi possível deduzir a formação de dímeros a partir da observação de regiões com potencial eletrostático oposto; análise de bandas vibracionais, onde foi possível realizar o assinalamento das principais bandas experimentais (obtidas no espectro de IV) e confirmar a formação de dímeros. Estudos de docking molecular realizados com as enzimas diidrofalato redutase e protease aspártica de *Candida albicans* evidenciaram boas energias de ligação do alcaloide liriodenina, com valores de -8.5 e -8.3 kcal/mol respectivamente, justificando dados da literatura. O material suplementar referente a este artigo se encontra na sessão "Anexo 2".

Spectrochimica Acta Part A: Molecular and Biomolecular Spectroscopy 174 (2017) 94–104

Contents lists available at ScienceDirect

Spectrochimica Acta Part A: Molecular and Biomolecular Spectroscopy

journal homepage: www.elsevier.com/locate/saa

Spectroscopic investigation, vibrational assignments, HOMO-LUMO, NBO, MEP analysis and molecular docking studies of oxoaporphine alkaloid liriodenine

Renyer A. Costa [a,*], Priscilla Olliveira Pitt [a], Maria Lucia B. Pinheiro [a], Kelson M.T. Oliveira [a,*], Kahlil Schwanka Salomé [b], Andersson Barison [b], Emmanoel Vilaça Costa [a]

[a] LQTC Laboratory, Department of Chemistry, Federal University of Amazonas, Manaus, Amazonas, Brazil
[b] NMR Laboratory, Department of Chemistry, Federal University of Paraná, Paraná, Curitiba, Brazil

ARTICLE INFO

Article history:
Received 30 July 2016
Received in revised form 10 November 2016
Accepted 12 November 2016
Available online 16 November 2016

Keywords:
Aporphine alkaloid
DFT
Molecular docking
FT-IR
UV-VIS
Hyperpolarizabily

ABSTRACT

A combined experimental and theoretical DFT study of the structural, vibrational and electronic properties of liriodenine is presented using B3LYP function with 6-311G (2d, p) basis set. The theoretical geometry optimization data were compared with the X-ray data for a similar structure in the associated literature, showing similar values. In addition, natural bond orbitals (NBOs), HOMO-LUMO energy gap, mapped molecular Electrostatic Potential (MEP) surface calculation, first and second order hyperpolarizabilities were also performed with the same calculation level. Theoretical UV spectrum agreed well with the measured experimental data, with transitions assigned. The molecular electrostatic potential map shows opposite potentials regions that forms hydrogen bonds that stabilize the dimeric form, which were confirmed by the close values related to the C ═O bond stretching between the dimeric form and the experimental IR spectra (1654 cm^{-1} for the experimental, 1700 cm^{-1} for the dimer form). Calculated HOMO/LUMO gaps shows the excitation energy for Liriodenine, justifying its stability and kinetics reaction. Molecular docking studies with *Candida albicans* dihydrofolate reductase (DHFR) and *Candida albicans* secreted aspartic protease (SAP) showed binding free energies values of −8.5 and −8.3 kcal/mol, suggesting good affinity between the liriodenine and the target macromolecules.

1. Introduction

Liriodenine (Fig. 1) is an oxoaporphine alkaloid that have a wide range of pharmacological activities. Was isolated for the first time from *Liriodedron tulipifera* [1] and was subsequently isolated from plant species of Magnoliaceae, Annonaceae [2,3] Rutaceae, Monimiaceae and Menispermaceae [4]. Biological and pharmacological activities of liriodenine constitute a topic of discussion and evaluation, being fully explored the potential of these compounds as cytotoxic and antitumor agents [5–7], but other biological activities are attributed to this alkaloid which deserve attention the antimicrobial activity against *Staphylococcus aureus, Mycobacterium smegatis, Candida albicans, Aspergilus niger* [8–9] *Cryptococcus neoformans, S. aureus*, the wood rooting fungi *Laetiporus sulphureus, Gloeophyllum traebeu, Fomitopsis pinicola, Lenzites betulina* and *Trametes versicolor*, cardiovascular effects like antiarrhythmic activity [10–12] antiplatelet actions [13] and against Gram-positive bacteria [14]. For more information regarding the importance of liriodenine, a recent review on this subject was published by Chen et al. [15]. However the spectroscopic behavior and quantum chemical aspects of such compound has not been fully evaluated and due to this fact the study of liriodenine alkaloid needs to continue in order to provide new information about the structural, physicochemical, spectral and quantum properties that lacks in the literature, thus increasing the knowledge about the aporphine alkaloids and liriodenine in particular. Within this premises, theoretical quantum models such as DFT and advanced software make the theoretical chemistry a powerful tool for the study of the properties of plants secondary metabolites [16,17].

This work discusses liriodenine from a theoretical view (geometry optimization, NBO, NLO and Meps calculations) based on experimental data (NMR, UV, ESI-IT-MS, FTIR), providing a more complete description of its structure and spectral behavior. To the best of our knowledge no theoretical molecular modeling study that discusses the bond lengths, planar and dihedral angles was previously presented and a detailed description of the spectroscopic behavior of the title compound with the help of quantum chemical DFT calculations along with NLO and NBO properties has not been performed yet. Guided by the related potential activity of liriodenine against *Candida albicans* and by the fact that

* Corresponding authors.
E-mail addresses: renyer.costa@gmail.com (R.A. Costa), kelsonmota@ufam.edu.br (K.M.T. Oliveira).

http://dx.doi.org/10.1016/j.saa.2016.11.018
1386-1425/

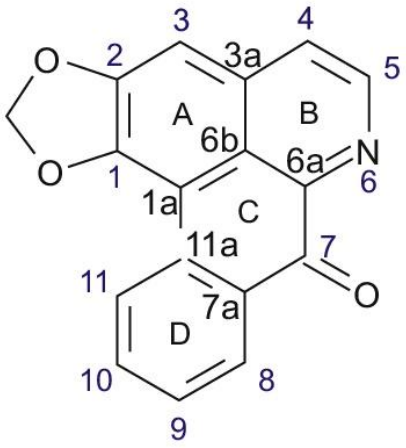

Fig. 1. Oxoaporphine alkaloid liriodenine.

C. albicans is the fifth leading cause of microbial infection in the hospital setting [18], molecular dockings of liriodenine with *Candida albicans* dihydrofolate reductase (DHFR) and with *Candida albicans* secreted aspact protease (SAP) are described due to the fact that the inhibition of these macromolecules, amongst the various targets, be a well established mechanism for drug action [18–20].

2. Experimental Section

2.1. General Procedures

Nuclear magnetic resonance (NMR) spectra were recorded on a Bruker 600 AVANCE spectrometer with 14.0 Tesla magnetons at 295 K in deuteriochloroform containing 0.06% TMS as internal standard. The UV analysis was recorded on a PDA Detector plus Finnigan Surveyor Thermo Scientific in methanol. The FT-IR data were recorded in KBr pellet technique (solid fase) on a Shimadzu IR Prestige-21 spectrophotometer. The ESI-MS data were recorded on LQC fleet ion trap Termo Scientific spectrometer equipped with an electrospray ionization (ESI) ion source on positive mode with the following parameters: capillary voltage at 26 V; spray voltage at 5 kV; tube lens offset at 100 V; capillary temperature at 225 °C; auxiliary gas at 5%; and sheet gas at 12%.

2.2. Plant Material

Barks of *Annona foetida* were collected in Federal University of Amazonas located in Manaus city, Amazonas, Brazil. The specie was identified by Dr. Antonio Carlos Webber from the Biological sciences Institute of Federal University of Amazonas and the voucher specimen of *Annona foetida* was deposited in the Federal University herbarium under code 2360.

2.3. Isolation of Liriodenine

The barks of *Annona foetida* was pulverized and subjected to solvent extraction by maceration in order of increasing polarity, hexane and methanol, with removal at interval of three days. The methanolic extract was solubilized in dichloromethane (DCM) and extracted successively with hydrochloric acid solution 3% v/v (HCl), which yielded two fractions: the acidic aqueous fraction and the fraction in neutral DCM. The acidic aqueous fraction was basified with concentrated ammonium hydroxide (NH_4OH) to pH 12 and extracted with DCM. The alkaloidal fraction was subjected to fractionation by preparative thin layer chromatography (PTLC) with dichloromethane/methanol 9:1 as mobile phase, thus resulting in the isolation of liriodenine and then submitted to NMR (^1H, HMBC, HSQC and COSY), UV, FTIR and ESI-MS analysis (see Table ST1 and Figs. S1, S2, S3 and S4 in Supplementary material).

2.4. Computational Methods

The theoretical quantum chemical calculations were performed on an INTEL Quadcore™ PC (8 GB RAM), with Debian LINUX (5.0 version) platform by the mean Gaussian 03 Program (Revision E.01) [21]. In the optimization geometry routine, the DFT approach was used, with 6-311G (2d, p) basis set and B3LYP functional. Molecular geometries were fully optimized by the force gradient method using Bernys' algorithm, and potential energy surfaces were characterized using standard analytical harmonic vibrational analysis to confirm that the stationary points corresponded to minima of the potential energy surfaces (no imaginary frequencies or negative eigenvalues were found). UV spectra were calculated using TD-B3LYP-FC functional and 6-311G (2d, p) basis set. The NBO and NLO values are obtained with same basis. The assignments of the calculated IR wavenumbers are aided by the animation option of GAUSSVIEW program, which gives a visual presentation of the vibrational modes [22]. The potential energy distribution (PED) was calculated with the help of VEDA4 software package [23].

3. Results

3.1. Geometry Optimization

Liriodenine shows a significant polarity being soluble in chloroform, ethyl acetate and methanol, presenting a dipole moment of 9.46 Debye. The geometry optimization results using B3LYP functional and 6-311G (2d, p) basis set were compared with the X-ray data for a similar structure (—*N*-acetylanonaine) [24] showing a stable conformation with a C1 symmetry revealing a good structural cohesion and an energy value of −933.91 a.u ($-4.0716.10^{-12}$ kJ or $-9.7248.10^{-19}$ kCal).

Initially the bond lengths values indicate uniformity in all structure showing small distortions in the rings. Ring A shows very similar bond lengths, 1.415 Å (C1—C2), 1.42 Å (C3—C3a), 1.43 Å (C3a—C6a), 1.38 Å (C1—C1a) in exception the bond length C2—C3 (1.35 Å) Ring B shows very close bond lengths too, except the distance between N6—C6a (1.33 Å) and N6—C5 (1.33 Å) different in relation to C6a—C6b, C6b—C3a and C4—C5 bonds. Rings C and D shows uniformity with very similar bond lengths and the pentacyclic ring (that contains de dioxomethylene function) shows slight differences, 1.36 Å (O—C1), 1.43, 1.42 (O—CH2—O) and 1.36 Å (O—C2). Concerning the planar angles, which are show similar to the experimental data for —*N*-acetylanonaine, the structure does not show large deformations, especially the angles in the pentacyclic, C and D. A and B rings show slight distortions and the angles C2—C3—C3a (116.60°) and C1—C1a—C6b (114.77°) are noteworthy, because they are slightly smaller in relation to the other angles in A ring.

3.2. Frontier Molecular Orbitals

The highest occupied molecular orbitals (HOMO) and the lowest-lying unoccupied molecular orbitals (LUMO), also called frontier molecular orbitals (FMOs), play an important role in many properties of a compound as well as in quantum chemistry and UV–VIS spectra. The energy gap between the HOMO and LUMO is very important for determining the electrical properties, kinetic stability, optical polarizability and chemical reactivity descriptors, such as hardness and softness, of a molecule. The quantum bonding features of liriodenine are depicted by a plot of the HOMO, HOMO-1, LUMO and LUMO-1 in Fig. 2.

The concept of hardness (η) and softness is related to a compound's reactivity and is a property that measures the extent of chemical reactivity to which the addition of a charge stabilizes the system. The

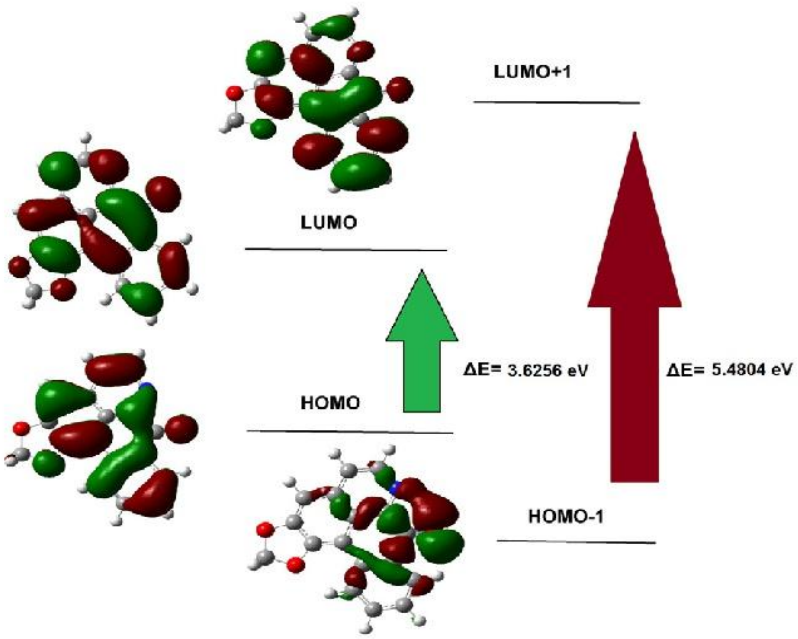

Fig. 2. Frontier molecular orbitals of liriodenine.

chemical potential (μ) provide a global reactivity index and is related to charge transfer from a system of higher chemical potential to one of lower chemical potential. Electronegativity (χ) is the power to attract electrons and is directly related to all the previously mentioned properties. All these properties are defined as follows [25–27]:

$$\eta = \frac{(I-A)}{2}$$

$$\mu = \frac{-(I+A)}{2}$$

$$\chi = \frac{(I+A)}{2}$$

where A is the ionization potential and I is the electron affinity of the molecule. The ionization energy and electron affinity are obtained from the HOMO and LUMO energies as $I = -E_{HOMO}$ and $A = -E_{LUMO}$ according to the Janak theorem [28] and Perdew et al. [29]. In terms of chemical hardness, a large HOMO-LUMO gap indicates a hard molecule and is related to more stable molecules, whereas a small gap indicates a soft molecule and is related to a more reactive molecule. Another important descriptor is the electrophilicity index (ω) [26], that measures the energy lowering due to charge transfer. The electrophilicity index is defined as follows:

$$\omega = \left(\frac{\mu^2}{2\eta}\right)$$

All these properties were calculated using these equations for liriodenine in methanol (PCM model) with B3LYP/6-311G (2d, p) basis sets and the linear correlation relationship correction proposed by Zhan et al. [30], due to the fact that the VIPs values given by the negative DFT HOMO-LUMO energies values (when are used the typical exchange-correlation functionals) are usually smaller than experimental VIPs [30–32]. The values are shown in Table 2. The small value of Hardness (η) (3.29 eV) reflects high polaratizability showing liriodenine as a soft molecule with faster reactions since the electrons are further from the nucleus. The chemical potential (μ) value (−4.807 eV) reveals stability, indicating that liriodenine does not decompose spontaneously. Electronegativity and electrophilicity values of liriodenine indicates that this molecule have a significative attractive electron power. (See Table 1.) (See Table 3.)

3.3. UV Analysis

The electronic spectrum of the substance in methanol solution phase was compared with the calculated spectrum at time dependent density functional using B3LYP-6311G (2d, p) basis set in methanol (PCM model) as showed in Fig. 3. The experimental spectra assigned bands at 212, 268, 376 and 408 nm, consistent with the structure, because liriodenine is a polynuclear heterocyclic compound. The theoretical calculations predict an intense electronic transition of 6.1985 eV with an oscillator strength f = 0.4367 at 200.02 nm, showing good agreement with the measured experimental data (212 nm). The calculations also predict electronic transitions at 273.44 nm (4.528 eV) and at 380.75 (3.25803 eV) which are equivalent to the bands 268 and 376–408 nm, assigned to a sum of $n \rightarrow \pi^*$ and $\pi \rightarrow \pi^*$ transitions of the heterocyclic rings and the carbonyl group. In general, such interactions between n and π electrons cause shifts in the secondary and primary absorption bands of aromatic compounds (extended conjugation). $n \rightarrow \pi^*$ transitions allows the formation of charges, so the n system becomes deficient in electrons while the π^* system acquires an extra electron, causing a separation of charge in the molecule which is stabilized by resonance in π^* orbital, this excited state is called *charge transfer state* and is easily applicable to such system. In respect to the electronic transitions the two maximum calculated absorptions wavelengths corresponding to the contributions from HOMO → LUMO + 4 (25.15%), HOMO-5 → LUMO + 3 (24.5%) and HOMO-4 → LUMO + 3 (9%) for 200.02 nm (212 nm in experimental spectrum) and HOMO → LUMO + 1

Table 1
Calculated geometrical parameters for liriodenine.

Parameter	B3LYP 6-311G (2d, p)	Experimental [23]
Bond length		
C1—C2	1.42	1.39
C1—C1a	1.37	1.37
C2—C3	1.35	1.36
C3—C3a	1.42	1.41
C3a—C4	1.40	–
C4—C5	1.38	–
C5—N6	1.34	–
N6—C6a	1.33	–
C6a—C6b	1.42	–
C6b—C1a	1.44	1.43
C6b—C3a	1.43	1.39
C1a—C11a	1.47	1.48
C11a—C7a	1.42	1.41
C7a—C7	1.48	1.51
C7—C6a	1.49	1.53
C11—C11a	1.40	1.40
C10—C11	1.38	1.38
C9—C10	1.39	1.38
C9—C8	1.38	1.37
C8—C7a	1.39	1.39
Bond angle		
C1—C2—C3	123.06	121.3
C2—C3—C3a	116.60	120.4
C3—C3a—C6b	121.50	119.5
C1—C1a—C6b	114.77	118.5
C4—C5—N6	123.41	109.0
C5—N6—C6a	118.24	118.4
C6b—C1a—C11a	120.04	119.3
C1a—C11a—C7a	119.45	118.6
C11a—C7a—C7	121.93	120.6
C7a—C7—C6a	117.05	121.5
C7—C6a—C6b	120.16	118.6
C1a—C6b—C6a	121.35	119.3
C11—C11a—C7a	117.80	117.2
C10—C11—C11a	121.02	119.6
C9—C10—C11	120.73	120.7
C10—C9—C8	119.12	119.4
C9—C8—C7a	120.91	121.3
C7a—C11a—C11	117.80	120.8
C11a—C11—C10	121.02	123.1
C11—C10—C9	120.73	119.2
C1—O—C	107.70	105.5
O—C—O	107.03	107.7
C2—O—C	107.17	105.3
C1—C2—O	109.68	109.7

(77.23%) for 273.44 nm (268 nm in experimental spectrum) (see Fig. S4).

3.4. Molecular Electrostatic Potential Surface

The molecular electrostatic potential surface (MEPs) for liriodenine molecule in 3D plot is illustrated in Fig. 4. The MEPs is a plot of electrostatic potential mapped onto the constant electron density surface and used primarily for predicting sites and relative reactivity towards electrophilic and nucleophilic attack, in studies of biological recognition and interactions between the same molecules (forming clusters and crystal structures) or other molecules and in the correlation and prediction of a wide range of macroscopic properties [33]. The color code of this molecule map range from −2.258 eV (deepest red) to 2.258 eV (deepest blue), where blue indicates a minimal concentration of electrons and red indicates a high density of electrons.

The MEPs for liriodenine (Fig. 4) indicated regions with positive potentials over hydrogens in dioxo portion (1.0340 eV), in position 3 (0.7619 eV) and position 4 (0.5183 eV). A region with negative potential is located between the carbonyl group and nitrogen atom N6 (−2.2041 eV) and indicate that this site of the molecule tends to join the chemical reactions according to the rest of the molecule. The mep calculation leads to infer a dimer of the molecule, where hydrogen of dioxomethylene portion interacts with carbonyl oxygen and nitrogen forming C—H—O and C—H—N hydrogen bonds, due to the opposite charges (Figs. 4 and 6), similar to —*N*-acetylanonaine alkaloid [23].

3.5. IR Analysis

Fig. 5 shows the experimental and theoretical IV spectra. The differences around can be attributed to the fact that the theoretical DFT calculations were made for the molecule in the gas phase, whereas intermolecular interactions occur in solution. The assignment of the experimental bands to the normal modes of vibration was made using the optimized structure for monomer and for dimer form (Fig. 6) with the lowest potential energy, considering the potential energy distribution (PED) by using the B3LYP/6-311G (2d, p) level. A total of 84 normal vibration modes were obtained but were compared with the experimental spectrum only between 400 and 4000 cm^{-1} (Table 3). The experimental FT-IR spectrum showed bands in the 3000–2800, 1700–1500, 1490–1300, 1300–900 and 900–400 cm^{-1} regions with the following wavenumbers: 3002 2922, 2852, 1654, 1596, 1577, 1485, 1470, 1443, 1422, 1384, 1311, 1262, 1228, 1207, 1165, 1117, 1051, 1017, 964, 911, 872, 779, 752, 725, 690, 670, 609, 570, and 467 cm^{-1}.

The assignment of the experimental bands (Table 3) show that bands 2922 cm^{-1} and 2822 cm^{-1} were related to H—C stretching of the aromatic rings, (principally on positions 4, 5, 9 and 10) and H—C stretching of the oxo-portion respectively. Bands between 1700 and 1000 were related to C ═O streching (1654 cm^{-1} and 1443 cm^{-1}), C ═C stretchings (principally between positions 2–3, 1–1a, 4–5, 7a–8, 11–11a), N ═C stretchings (positions 6–5 and 6–6a), H—C—H (oxo) wagging (1443 cm^{-1}), H—C—H (oxo) twisting (1207 cm^{-1}), and H—C bends (principally in the positions 4, 5, 8 and 11). Bands between 1000 and 400 cm^{-1} are mostly related to torsions (distortions between dihedral angles) of HCCC type (principally on rings B and D), CCCC type (ring D), CNCC and NCCC type (ring B). No significant differences were registered between the monomer and dimer form wavelengths values (Table 3), except the value assigned to the stretching of carbonyl group in position 7 that shows to be closer to the experimental (1654 cm^{-1}) in the dimer (Fig. 6), (1721 cm^{-1} to the monomer and 1700 cm^{-1} to the dimer form), implying that the interaction between the carbonyl and dioxomethylene group is plausible and directly influenced the infrared spectrum by decreasing the stretching frequency oscillator related to C═O bond, causing a reduction in the wavelength. This interaction is justified by NBO energies values (Table 4) and in Mep calculations (Figs. 4 and 6).

3.6. NBO Study

NBO analysis describes the Lewis-like molecular bonding pattern of electron pairs (or of individual electrons in the open-shell case) in

Table 2
Calculated energy values for liriodenine using B3LYP/6-311G (2d, p) basis sets. The values in parenthesis are related to the corrected data using a linear correlation relationship [30].

Parameter	B3LYP/6-311G (2d, p)
Energy (eV)	−25,412.90
Dipole moment	9.46 Debye
E_{HOMO} (eV)	−6.18 (IP = 8.47)
E_{LUMO} (eV)	−2.56 (EA = 1.14)
$E_{HOMO\text{-}LUMO}$ (eV)	3.63
$E_{HOMO\text{-}1}$ (eV)	−6.67
E_{LUMO+1} (eV)	−1.19
$E_{(HOMO\text{-}1)\text{-}(LUMO+1)}$ (eV)	5.48
Hardness (η)	1.81 (3.65)
Chemical potential (μ)	−4.37 (−4.805)
Electronegativity (χ)	4.37 (4.805)
Electrophilicity index (ω)	3.36 (4.42)

Table 3
Experimental and calculated wavenumbers (cm^{-1}) and assignments for Liriodenine.

IR solid	B3LYP 6-311 (2d, p)				PED
	Monomer		Dimer		
	Calculated	IR intensity	Calculated	IR intensity	
–	3244.83	4.44	3245.38	4.67	STRE C11—H11 (99%)
–	3205.71	2.61	3202.36	14.12	STRE C3—H3 (99%)
–	3201.31	16.08	3200.80	4.56	STRE C9—H9 (12%) STRE C8—H8 86
–	3184.95	22.71	3183.33	29.81	STRE C9—H9 (34%) STRE C10—H10 (54%) STRE C8—C H8(12%)
3068	3180.88	31.49	3178.59	34.66	STRE C4—H4 (91%)
3002	3170.09	7.12	3168.53	6.99	STRE C9—H9 (64%) STRE C10—H10 (34%)
2922	3152.73	34.84	3149.44	37.72	STRE C5—H5 (91%)
–	3116.13	23.05	3140.63	128.78	STRE C—H (dioxo) (50%) STRE C—H (dioxo) (50%)-assimetric
2822	3056.80	134.51	3046.39	81.65	STRE C—H (50%) (dioxo) STRE C—H (50%) (dioxo)-simmetric
1654	1721.25	373.07	1700.52	427.38	STRE C7 =O (79%)
1596	1668.11	23.29	1666.99	33.99	STRE C2= C3 (60%)
1577	1634.79	87.12	1634.88	85.20	STRE C11= C10 (17%) STRE C7a= C8 (14%) STRE C9= C8 (16%) STRE C8= C7a (13%)
–	1628.96	16.72	1626.49	18.91	STRE C1= C1a (26%) STRE C4= C5 (11%)
–	1605.50	88.51	1604.18	123.89	STRE C1= C1a (19%) STRE C3a= C4 (17%)
–	1601.88	41.73	1601.07	43.09	STRE C10= C9 (31%)
–	1547.47	0.49	1560.26	2.10	BEND HCH (dioxo) simmetric (79%)
1485	1536.32	1.08	1536.85	1.16	STRE N6= C5 (15%) STRE C4= C3a (13%) BEND HCH (oxo) simmetric (24%)
1470	1519.29	103.95	1520.03	113.72	BEND H11—C11—C11a (38%) BEND H8—C8—C7a (15%)
1470	1460.82	236.74	1461.84	247.33	STRE N6= C6a (10%) STRE C1b= C3a (12%)
1443	1445.68	187.37	1448.90	144.80	STRE C= O (10%) Wagging HCH (dioxo) (53%)
–	1442.95	156.93	1441.66	323.40	STRE C1= C2 (13%) BEND H3—C3a—C4 (13%) BEND H4—C4—C5 (13%) BEND H4—C4—C (512%) BEND H5—C5—N6 (10%)
1422	1421.70	80.57	1422.39	59.01	STRE C1a= C1b (16%) STRE C4= C5 (10%) BEND H4—C4—C5 (11%)
1384	1382.79	34.16	1384.06	52.85	STRE C1b= C6a (12%) STRE C1a = C11a (12%)
–	1336.12	13.46	1336.41	17.42	STRE C11= C11a (10%) STRE C10 = C9 (10%) STRE C8 = C7a (14%)
–	1327.95	41.21	1328.32	70.72	STRE C1b= C3a (20%) STRE N6= C5 (40%)
1311	1318.15	268.17	1317.07	298.21	STRE N6= C6a (16%) STRE C—C7—C7a (19%) BEND H5—C5—N6 (15%)
–	1291.90	46.14	1291.37	36.34	STRE C11= C11a (22%) BEND H11—C11—C11a (15%) BEND H8—C8—C9 (15%)
1262	1275.66	275.62	1277.02	506.18	STRE entire structure
	1243.57	239.79	1248.37	299.60	STRE C1a= C1b (14%) STRE O—C1 (20%)
1228	1227.32	100.16	1227.47	116.54	STRE C7—C7a (10%) STRE C11a= C11 (16%)
–	1211.32	0.001	1221.32	20.59	Twisting H—C—H (oxo) (90%)
1207	1205.65	8.96	1206.66	8.17	STRE C1a—C11a (17%) BEND H3—C3—C3a—C4—H4 (38%)
1165	1189.62	4.87	1188.62	8.02	BEND H11—C11—C10—H10 (30%) BEND H10—C10—C9—H9 (23%) BEND H9—C9—C8—H8 (12%)
–	1139.80	22.14	1139.42	25.41	STRE C4 =C5 (10%) BEND HCC (16%) TORS COCC (78%)
1117	1127.19	2.11	1128.51	4.67	BEND C1= C2= C3 (12%) BEND H4—C4—C5 (10%)
–	1104.60	8.88	1107.92	8.61	STRE C4 =C5 (12%) STRE N6 =C5 (11%)
–	1072.35	90.22	1071.37	11.07	STRE C= C (aromatic ring A) (15%) STRE OC (oxo) (13%)
1051	1065.86	128.72	1058.42	246.50	STRE C =C (ring D) (15%) STRE OC (dioxo) (17%) BEND OC1—C2 (10%)
1017	1031.58	69.32	1030.58	94.76	STRE entire structure
–	1007.55	0.21	1006.29	0.12	TORS H10—C10—C11 (13%) TORS H9—C9—C10 (37%) TORS H8—C8—C9 (30%)

Table 3 (*continued*)

IR solid	B3LYP 6-311 (2d, p)				PED
	Monomer		Dimer		
	Calculated	IR intensity	Calculated	IR intensity	
964	988.91	0.004	990.17	0.05	TORS H4C4═ C5═ N6 (24%) TORS H5C5═ C4═ C3a (63%)
–	983.78	0.78	983.90	0.80	TORS H8C8═ C9═ C10 (43%) TORS H10C10═ C9═ C8 (28%) TORS H11C11═ C11a═ C7a (21%)
–	982.01	199.79	972.49	170.15	STRE OC assimetric (dioxo) (52%) BEND COC (12%)
–	951.22	17.55	950.86	12.29	BEND C9═ C9═ C10 (11%)
911	923.74	49.07	919.53	55.44	BEND COC (dioxo) (16%) BEND C4═ C5═ N6 (15%)
–	902.57	0.31	902.40	0.32	TORS H11C11═10═ C9 (34%) TORS H9C9═ C10═ C11 (25%) TORS H8C8═ C9═10 (11%)
872	893.58	1.57	892.56	0.13	STRE C1b═ C3a (14%) BEND C8═ C9═ C10 (11%)
–	885.21	46.76	885.91	48.03	TORS H3C3C3aC4 (28%) TORS H4C4C5N6 (17%) TORS H5C5N6C6a (13%) TORS C3aC4C5N6 (10%)
–	852.97	7.64	851.44	9.63	TORS H3–C3–C3a–C4 (21%) OUT O═ C7–C6a–C7a (79%)
–	831.97	7.64	828.16	0.911	TORS H3C3C3aC4 (21%) TORS H4C4C5N6 (40%) TORS H5C5N6C6a (11%)
–	808.14	9.37	808.00	5.63	STREC entire structure
779	800.68	21.39	800.7	29.30	TORS H11C11C10C9 (10%) TORS H9C9C8C7a (12%) OUT O═ C7═ C7a (12%)
–	777.72	14.77	777.85	14.65	TORS HCCC (10%) TORS C7═ C6a═ N6═ C5 (10%) TORS CCCC (10%) TORS C6a═ N6═ C5═ C4 (10%) TORS C3═ C3a═ C4═ C5 (12%) OUT C11–C11a–C1a–C1b (10%)
752	767.69	0.203	765.69	1.18	BEND COC (26%) (oxo) BEND O–C–C2 (28%)
–	747.96	15.80	743.65	3.73	OUT O–C1═ C2═ C3 (17%)
725	711.11	10.36	713.82	12.74	TORS C11═ C11a═ C7a═ C7 (12%) OUT OC1C2C1a (14%) OUT O═ C7C6aC7a (10%)
690	686.46	6.646	686.54	8.58	BEND O═ C7–C–7a (25%) BEND C4═ C5═ N6 (11%) BEND C11a–C7a═ C8 (10%)
670	657.52	4.65	657.77	4.20	BEND C7a–C8═ C9 (13%) BEND C11a–C11═10 (30%) BEND C11–C11a–C7a (12%)
–	622.25	0.56	622.72	0.69	TORS C8═ C9═ C10═ C11 (10%) TORS C1a═ C1b═ C3a═ C3 (11%) TORS C11a═ C1a═ C1═ C2 (13%) OUT OC2C1C3 (11%)
609	617.66	17.47	619.58	22.79	BEND C1b═ C3a═ C4 (18%) BEND C6a═ N6═ C5 (13%) BEND O–C2═ C3 (13%)
–	589.00	30.91	589.51	24.60	TORS C7═ C6a═ N6═ C5 (27%) TORS N6═ C5═ C4═ C3a (10%) TORS C6a═ N6═ C5═ C4 (18%) OUT O═ C7–C6a–C1b (10%)
570	584.27	0.44	585.47	2.04	BEND C6aC7C7a (17%) BEND C1C2C3 (13%) BEND C6a–N6═ C5 (13%)
–	530.16	0.01	531.12	0.03	TORS C9C10C11C11a (12%) TORS C3aC4C5N6 (26%) TORS C6aC1bC3aC4 (16%)
467	455.22	1.67	457.17	1.35	OUT OC1–C2═ C3 (10%) OUT O–C2═ C3–C3a (18%) OUTC11aC11═ C10C9(14%)
–	454.33	2.95	454.80	2.67	STRE C7═ C7a (12%) BEND O–C1–C1a (12%)
–	442.41	8.48	443.77	11.87	STRE C3a═ C4 (24%)

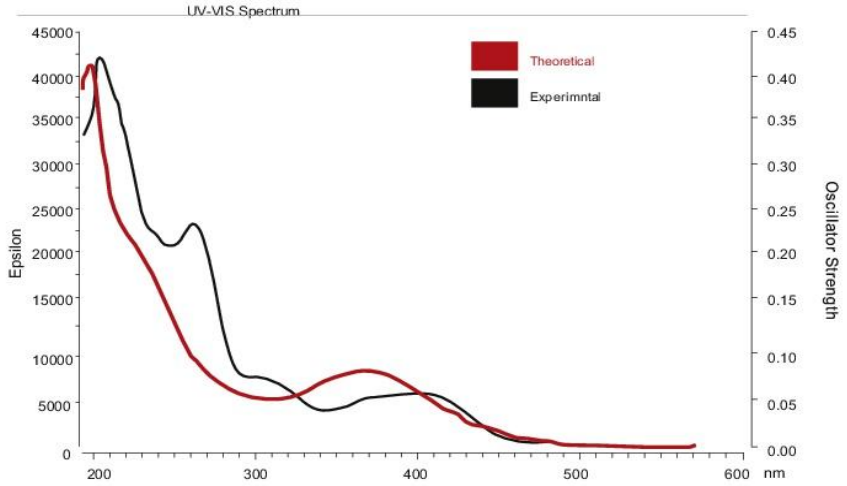

Fig. 3. Comparison between experimental and theoretical B3LYP 6-311G (2d, p) spectra in methanol for liriodenine.

optimally compact form. NBOs determine the localized *Natural Lewis Structure* (NLS) representation of the wave function, while the remaining "non-Lewis"-type NBOs complete the span of the basis and describe the residual "delocalization effects" by the second-order perturbation energies E(2) [donor (i) → acceptor (j)] that involve the most important delocalization and are given by [34–37]:

$$E(2) = \Delta_{ij} = q_i \frac{F_{ij}^2}{\varepsilon_j - \varepsilon_i}$$

Thus, NBOs provide a valence bond-type description of the wave function, closely linked to classical Lewis structure concepts and is a helpful tool for understanding the delocalization of electron density [36,38]. The NBO analysis of liriodenine revealed strong hyperconjugative intramolecular interactions of $\pi \rightarrow \pi^*$ transitions, which are formed by the orbital overlaps between C ═C bondings and C ═C anti-bondings and overlaps between N and O lone pairs (LP) and C ═C anti-bondings, leading to an intramolecular charge transfer causing stabilization of the molecular system (Table 4). The second-order perturbation energies values analysis shows greater conjugation in the rings A, B, C e D, principally by $\pi \rightarrow \pi^*$ interactions as, C1—C1a → C2—C3 (17.44 kcal/mol), C2—C3 → C1—C1a (16.69 kcal/mol), C2—C3 → C1—C1a (16.56 kcal/mol), C1—C1a → C3a—C1b (16.01 kcal/mol), C3a—C1b → N6—C6a (26.83 kcal/mol), N6—C6a → C4—C5 (23.46 kcal/mol), N6—C6a → C7—O (13.93 kcal/mol), C11a—C7a→ C7—O (20.51 kcal/mol), C11—C10→C11a—C7a (20.61 kcal/mol) and by $\pi^* \rightarrow \pi^*$ interactions as, C1—C1a→C11a—C7a (193.56 kcal/mol), N6—C6a →C4—C5 (281.16 kcal/mol), C7a—O → C11a—C7a (173.11 kcal/mol). For the dimer the second-order perturbation energies values analysis also shows $n \rightarrow \sigma^*$ intermolecular conjugations, N6 → C—Hα(oxo) (1.94 kcal/mol) and O(7) → C—Hα(oxo) (1.08 kcal/mol), that stabilizes the dimer form (Fig. 6) where the O(7) and N6 acts as an electron donors and the dioxo group acts as an electron acceptor, justifying previous experimental works [24,39].

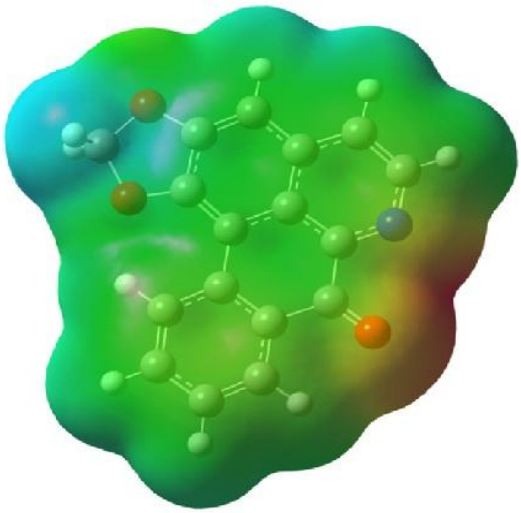

Fig. 4. Molecular electrostatic potential surface of liriodenine calculated at B3LYP/6-311G (2d, p) level.

3.7. NLO Analysis

Non-linear effects arise from the interactions of electromagnetic fields in various media to produce new fields altered in phase, frequency, amplitude or other propagation characteristics from the incident fields [40]. When light passes through any molecular medium, the oscillating electric field of the incident light induces an electronic polarization of the molecules comprising the medium. In ordinary materials this electronic displacement (polarization) is directly proportional to the strength of the electric field (intensity of the light). In a nonlinear material, the induced polarization is a nonlinear function of the applied field. NLO activity provides the key functions for frequency shifting, optical modulation, optical switching, optical interconnections and others [41]. The non-linear optical response of an isolated molecule in an electric field can be defined as a Taylor series expansion of the energy of the system in an applied external electric field. Due to the homogeneity and weakness of the external electronic field, this expansion is given below:

$$E = E^{\circ} - \mu_{\alpha} F_{\alpha} - 1/2 a_{\alpha\beta} F_{\alpha} F_{\beta} - 1/6 \beta_{\alpha\beta\gamma} F_{\alpha} F_{\beta} F_{\gamma} + \ldots\ldots$$

where $E^{o}$is the energy of the unperturbed molecules, F_{α} is the field at the origin, μ_{α} , $\alpha_{\alpha\beta}$ and $\beta_{\alpha\beta\gamma}$ are the permanent dipole moment, the linear polarizability and the first hyperpolarizability tensor components

respectively. In molecules that have an acentric electron distribution, like organic molecules, β values are significant.

The total static dipole moment μ, the mean polarizability α, the anisotropy of the polarizability $\Delta\alpha$ and the mean first hyperpolarizability β_0 using x, y and z components are defined as:

Dipole moment

$$\mu = \left(\mu_x^2+\mu_y^2+\mu_z^2\right)^{1/2}$$

Static polarizability

$$\alpha_0 = (\alpha_{xx} + \alpha_{yy} + \alpha_{zz})/3$$

Total polarizability

$$\Delta\alpha = 2^{-1/2}[(\alpha_{xx}-\alpha_{yy})^2 + (\alpha_{yy}+\alpha_{zz})^2 + (\alpha_{zz}+\alpha_{xx})^2 + 6\alpha_{xz}^2]^{1/2}$$

First order hyperpolarizability is

$$\beta = (\beta_x^2+\beta_y^2+\beta_z^2)^{1/2}$$

where

$$\beta_x = (\beta_{xxx} + \beta_{xyy} + \beta_{xzz})$$

$$\beta_y = (\beta_{yyy} + \beta_{yzz} + \beta_{yxx})$$

$$\beta_z = (\beta_{zzz} + \beta_{zxx} + \beta_{zyy})$$

Since the values of polarizabilities of the Gaussian output are reported in atomic units (a.u.) the calculated values have been converted into electrostatic units (esu) (For α: 1 a.u. = 0.1482×10^{-24} esu; For β:1 a.u. = 8.639×10^{-33} esu). The DFT theory at B3LYP/6-311G (2d, p) level has been used to predict dipole moments, polarizability and first order hyperpolarizability (Table 5). The highest value dipole component is the $\mu_x = -2.74017$ *D* and the total dipole moment is

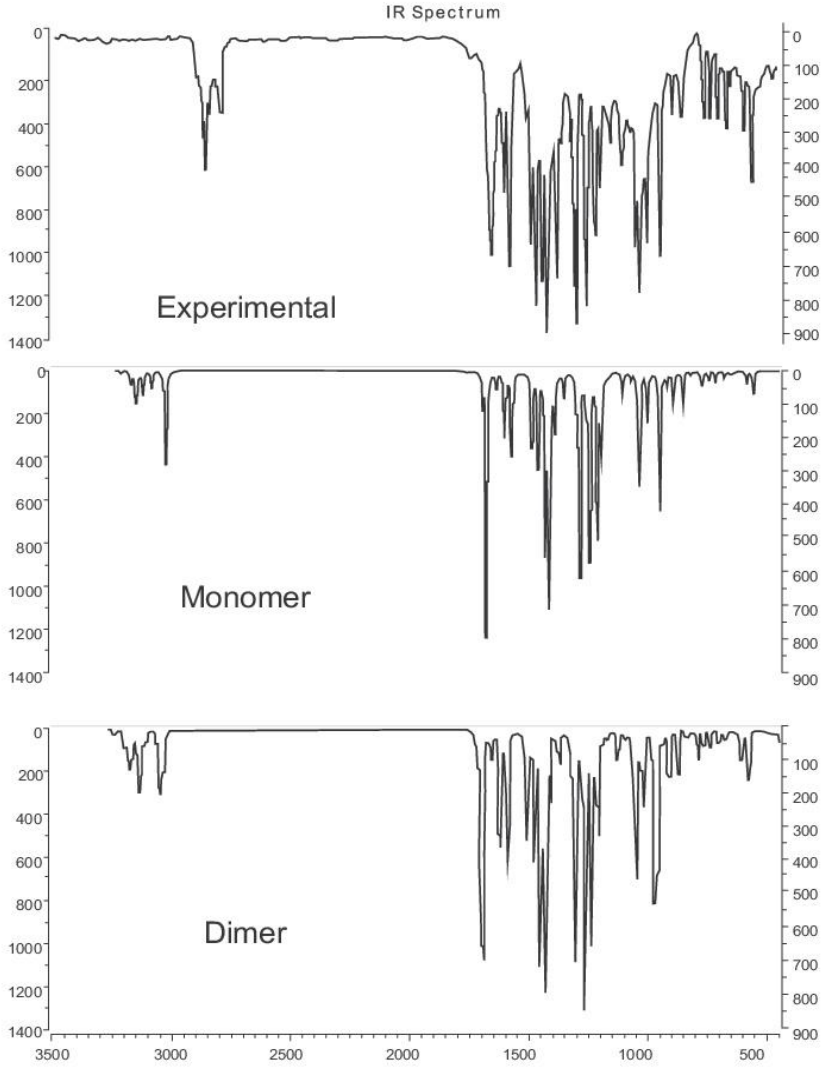

Fig. 5. Experimental (top), theoretical B3LYP 6-311G (2d, p) monomer (middle) and dimer (bottom) IR spectra of liriodenine oxaporphine alkaloid.

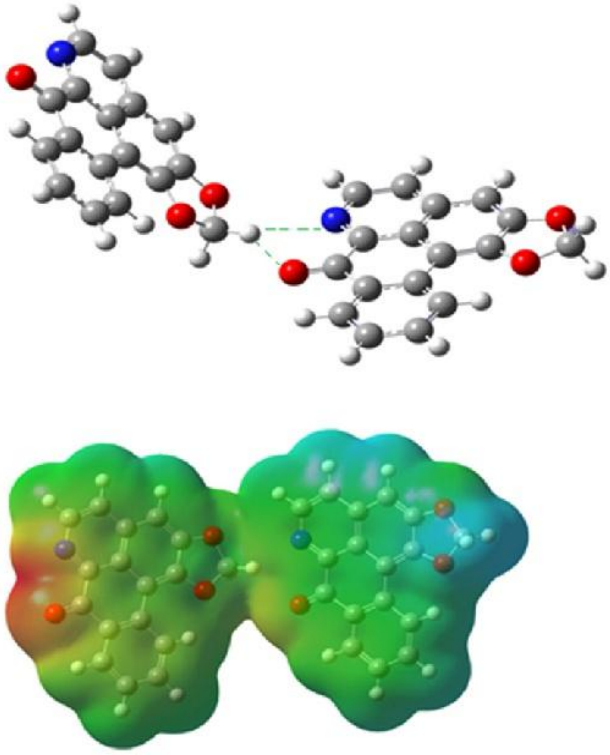

Fig. 6. Geometry optimization (top) and Mep (bottom) of liriodenine dimer.

$\mu_{total} = 3.72362$ *D*. The calculated mean polarizability ($\alpha_{total} = 4.116 \times 10^{-23}$ esu) and first hyperpolarizability ($\beta = 15.182 \times 10^{-30}$ esu) of liriodenine, which is 78 times more than β of urea (0.1947×10^{-30} esu), indicates that this molecule is a potential candidate for non-linear optical applications.

3.8. Molecular Docking Studies

Molecular docking is an efficient tool to get an insight into ligand-receptor interactions and screen molecules for the binding affinities against a particular receptor. Among various activities related to liriodenine we explore the molecule for its inhibition against *Candida albicans* dihydrofolate reductase (DHFR) and *Candida albicans* secreted aspact protease (SAP) due to its significative activity against *Candida albicans*. SAP act as cytolysins in macrophages after phagocytosis of *Candida*, are present in tissue penetration and are also involved in adherence to epithelial cells. DHFR is an enzyme that catalyzes the reduction of dihydrofolate (DHF) to tetradihydrofolate (THF) using NADPH as a cofactor, the loss of DHFR function via inhibition deplets THF pools and causes proteomic instability and cell death, thus the key role played by DHFR makes it a good target for therapeutic antimicrobial and antineoplastic agents. The 3D crystal structures of the enzymes DHFR and SAP were obtained from Protein Data Bank by ID 4HOE and 1ZAP respectively (Fig. 7), the molecular docking calculations were performed on AutoDock-Vina software that uses an united-atom scoring function [42]. The search space were defined to include residues of the related active sites [18–20] within the grid size of 22 Å × 21 Å × 20 Å, water molecules and co-crystallized ligands were removed. The docking calculation in AutoDock Vina consists of a number of sequential steps. Each step involves a random perturbation of the conformation followed by a local optimization (using the Broyden-Fletcher-Goldfarb-Shanno algorithm [42] which is an efficient quasi-Newton method) and a selection in which the step is accepted or not. Each local optimization involves many "evaluations" of the scoring function as well as its derivatives in the position-orientation-torsion coordinates. The number of evaluations in a local optimization is guided by convergence [43–45]. The docking protocol was tested by removing the co-crystallized inhibitor from the protein and then docking it at the same site. To evaluate the quality of docking results, the common way is to

Table 4
Selected second-order perturbation energies of liriodenine.

Donor orbital (i)	Type	Acceptor orbital (j)	Type	$E_{(j)} - E_{(i)}$ a.u.	$E^{(2)}$ (kcal/mol)
C2—C1	σ	C2—C3	σ*	1.31	5.32
C2—C1	σ	C1—C1a	σ*	1.30	5.63
C2—C3	π	C1—C1a	π*	0.31	16.56
C2—C3	π	C3a—C1b	π*	0.31	16.69
C1—C1a	π	C2—C3	π*	0.30	17.44
C1—C1a	π	C3a—C1b	π*	0.30	16.01
C1—C1a	π	C11a—C11	π*	0.31	15.03
C3a—C1b	π	C2—C3	π*	0.27	13.58
C3a—C1b	π	C1—C1b	π*	0.27	15.70
C3a—C1b	π	C4—C5	π*	0.28	16.51
C3a—C1b	π	N6—C6a	π*	0.26	26.83
C4—C5	π	C3a—C1b	π*	0.28	19.80
C4—C5	π	N6—C6a	π*	0.27	17.43
N6—C6a	π	C3a—C1b	π*	0.32	12.10
N6—C6a	π	C4—C5	π*	0.33	23.46
N6—C6a	π	C7—O	π*	0.32	13.93
C11a—C7a	π	C1—C1a	π*	0.27	16.60
C11a—C7a	π	C7—O	π*	0.27	20.51
C11a—C7a	π	C11—C10	π*	0.28	17.27
C11a—C7a	π	C8—C9	π*	0.29	19.57
C11—C10	π	C11a—C7a	π*	0.29	20.61
C11—C10	π	C9—C8	π*	0.29	17.61
C9—C8	π	C11a—C7a	π*	0.28	19.35
C9—C8	π	C11—C10	π*	0.28	20.93
C8—H	π	C11—C7a	π*	1.08	5.39
N9	LP	C1b—C6a	σ*	0.88	11.75
N9	LP	C4—C5	σ*	0.91	9.23
O(7)	LP(1)	C7	RY	1.64	13.66
O(7)	LP(2)	C6a—C7	σ*	0.68	21.19
O(7)	LP(2)	C6—C7	σ*	0.71	18.63
O2'	LP(2)	C2—C3	π*	0.36	27.56
O2'	LP(2)	C—Hβ(oxo)	σ*	0.74	6.84
O2'	LP(2)	C—Hα(oxo)	σ*	0.74	6.84
O1'	LP(2)	C1—C1a	π*	0.36	26.70
O1'	LP(2)	C—Hβ(oxo)	σ*	0.75	6.52
O1'	LP(2)	C—Hα(oxo)	σ*	0.75	6.52
C1—C1a	π*	C11a—C7a	π*	0.01	193.56
N6—C6a	π*	C4—C5	π*	0.01	281.16
N9—C10	π*	C4—C5	π*	0.02	153.66
C7—O	π*	C11a—C7a	π*	0.01	173.11
Dimer					
Monomer 2		Monomer 1			
N6	LP(1)	C—Hα(oxo)	σ*	0.77	1.94
O(7)	LP(2)	C—Hα(oxo)	σ*	0.69	1.08

Table 5
Dipole moment, polarizability and hyperpolarizability data in gas phase for liriodenine at B3LYP 6-311G (2d, p).

Dipole	Polarizability	Hyperpolarizability
$\mu_x = -2.74017$	$\alpha_{xx} = 371.868$	$\beta_{xxx} = 973.0539$
$\mu_y = -2.5213$	$\alpha_{xy} = -4.8282$	$\beta_{xxy} = 153.5538$
$\mu_z = -0.00003$	$\alpha_{yy} = 363.3418$	$\beta_{xyy} = 833.2562$
$\mu_{total} = 3.72362$	$\alpha_{xz} = 0.0000$	$\beta_{yyy} = 0.0000$
	$\alpha_{yz} = 0.0000$	$\beta_{xxz} = -0.0064$
	$\alpha_{zz} = 98.0670$	$\beta_{xyz} = -0.0078$
	$\alpha_{total} = 4.11638 \times 10^{-23}$ esu	$\beta_{yyz} = -0.0043$
	$\Delta\alpha_{total} = 62.642 \times 10^{-24}$ esu	$\beta_{xzz} = -48.8957$
		$\beta_{yzz} = -64.2203$
		$\beta_{zzz} = 0.00021$
		$\beta_{total} = 15.182 \times 10^{-30}$ esu

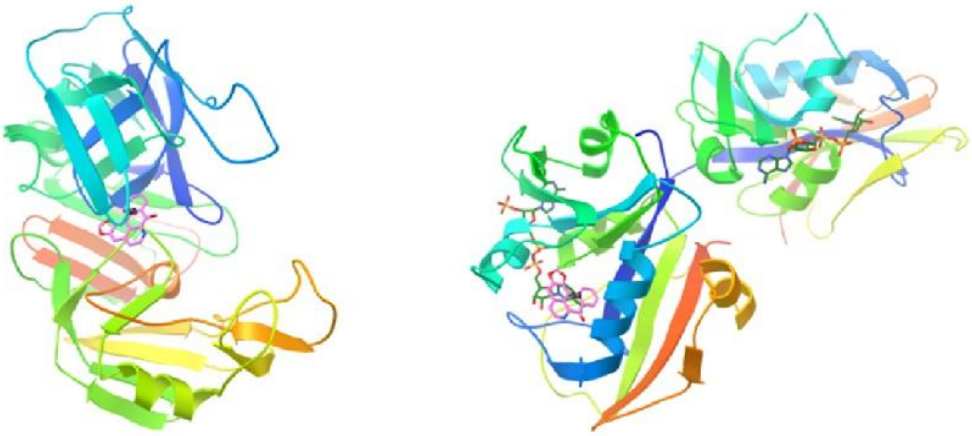

Fig. 7. Liriodenine (pink) complexed with enzymes 1ZAP (left) and 4HOE (right).

calculate the Root Mean Square Deviation (RMSD) between the docked pose and the known crystal structure conformation. RMSD values up to 2 Å are considered reliable for a docking protocol.

For 4HOE the ligand binds at the active site by non-covalent alkyl-π (ring D-NADPH) interaction, alkyl-alkyl interactions (between oxo group-Thr58 and oxo group-Ile 112), $\pi-\pi$ interactions (ring D-Phe36, ring A-Phe36, ring B-Phe36, ring C-Phe36), amino-alkyl interaction (N-Ile33) and by a hydrogen bond between oxygen of the dioxomethylene group and Ile 112, with a total free energy predicted by Autodock (ΔG in kcal/mol) of −8.5 suggesting a good affinity (Fig. 8a), for the native ligand the free energy predicted by Autodock is −8.2 kcal/mol. In 1ZAP the ligand binds at the active site by non-covalent alkyl-π interactions between Ring A-Asp86, RingA-Gly85, Ring B-Gly86, Ring B-Ile305, Ring D-Tyr84 and Ring D-Ile123 with a total free energy predicted by Autodock (ΔG in kcal/mol) of −8.3 suggesting a good affinity too (Fig. 8b), for the native ligand the free energy predicted by Autodock is −8.0 kcal/mol. Is important to explain that the ΔG value provided by Docking calculations is the binding Gibbs free energy of the equilibrium, not the formation. Thus the value of ΔG refers to greater composing enzymes complexed with liriodenine compared to those who not complexing. These calculations justifying in part the already known antimicrobial activity of liriodenine against *Candida albicans*, but other mechanisms may be involved in the biological activity and biological tests as **Surface plasmon resonance** (**SPR**) should be done to validate these results.

SPR is the resonant oscillation of conduction electrons at the interface between a negative and positive permittivity material stimulated by incident light. The resonance condition is established when the frequency of incident photons matches the natural frequency of surface electrons oscillating against the restoring force of positive nuclei. Surface plasmons have been used to enhance the surface sensitivity of several spectroscopic measurements including fluorescence, Raman scattering and second harmonic generation. However, in their simplest form, SPR reflectivity measurements can be used to detect molecular adsorption, such as polymers, DNA or proteins, etc.

4. Conclusions

FT-IR and UV-VIS spectra of the title compound were recorded and studied experimentally and theoretically. The electronic spectrum of the substance shows consistent with the experimental spectrum, with bands assigned to a sum of $n \rightarrow \pi^*$ and $\pi \rightarrow \pi^*$ transitions. The MEP calculation leads to infer a dimer for the molecule, where hydrogen of dioxomethylene portion interacts with carbonyl oxygen and nitrogen

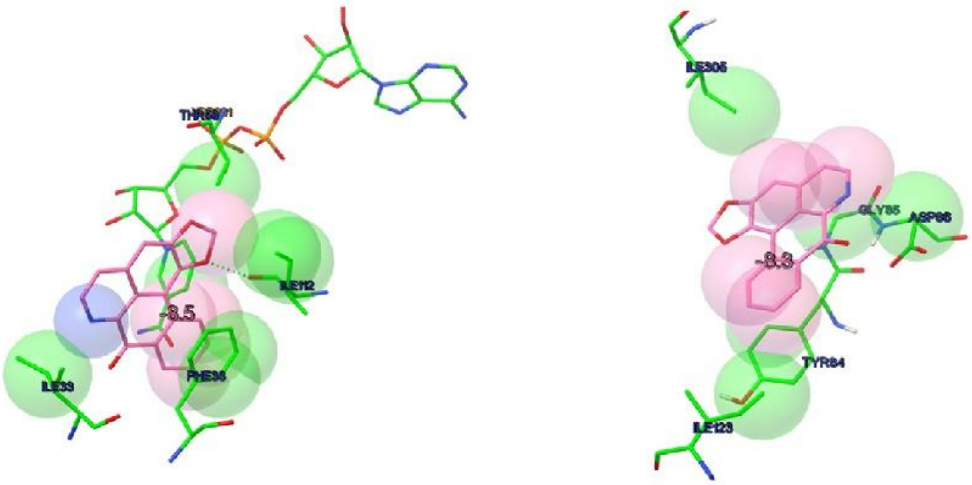

Fig. 8. Ligand–protein interactions of liriodenine-4HOE active site (left) and liriodenine-1ZAP active site (right).

forming C—H—O and C—H—N hydrogen bonds. The comparative IR studies revealed that the interactions of the liriodenine dimer influences the theoretical infrared spectrum by decreasing the stretching frequency oscillator of the groups involved in hydrogen bonds and shown several characteristic vibrations that may be used as a diagnostic tool for other aporphine alkaloids, simplifying their identification and structural characterization. The calculated hyperpolarizability of the title compound is 78 times that of the standard NLO material urea showing liriodenine and its derivatives are an attractive object for future studies of nonlinear optical properties. The molecular docking results reveals good interactions of liriodenine with *Candida albicans* dihydrofolate reductase (DHFR) and *Candida* secreted aspact protease (Sap) active sites and can explain in part its good in vitro activity against *Candida albicans* related on literature.

Acknowledgments

The authors thank Dr. Elaine H.T. Oliveira of Federal University of Amazonas/IComp and Leigh Ann Sample/ITB for the spelling support, Capes and FINEP for the financial support.

Appendix A. Supplementary data

Supplementary data to this article can be found online at http://dx.doi.org/10.1016/j.saa.2016.11.018.

References

[1] M.A. Buchanan, E.E. Dickey, J. Org. Chem. 25 (8) (1960) 1389–1391.
[2] E. Costa, F.D. Marques, M.L. Pinheiro, R.M. Braga, C. Delarmelina, M.C. Duarte, B. H.Maia, J. Braz. Chem. Soc. 22 (2011) 1111–1117.
[3] M.L.B. Pinheiro, C.M. Xavier, A.D.L. Souza, D.M. Rabelo, C.L. Batista, R.L. Batista, E.V. Costa, F.R. Campos, A. Barison, R.H. Valdez, T. Ueda-Nakamura, C.V. Nakamura, J. Braz. Chem. Soc. 20 (2009) 1095–1102.
[4] K.W. Bentley, Nat. Prod. Rep. 2 (2001) 148–170.
[5] N. Nordin, N.A. Majid, N.M. Hashim, Z. Hassan, H.M. Ali, Drug Des. Devel. Ther. (2015) 1437–1447.
[6] A. Nematollahi, N. Aminimoghadamfarouj, C. Wiart, Int. J. Chem. Tech. Res. 3 (2011) 1623–1627.
[7] T.J. Hsieh, T.Z. Liu, C.L. Chern, D.A. Tsao, F.J. Lu, Y.H. Syu, C.H. Chen, Food Chem. Toxicol 7 (2005) 1117–1126.
[8] C.D. Hufford, M.J. Funderburk, J.M. Morgan, L.W. Robertson, J. Pharm. Sci. 5 (1975) 789–792.
[9] C.D. Hufford, A.S. Sharma, B.O.·Oguntimein, J. Pharm. Sci. 10 (1980) 1180–1183.
[10] K.C. Chang, M.J. Su, Y.I. Peng, C.C. Shao, Y.C. Wu, Y.Z. Br, J. Pharmacol. 1 (2001) 29–36.
[11] C.C. Wu, C.L. Wu, S.L. Wang, H.T. Chang, Wood Sci. Technol. 46 (2012) 737–747.
[12] W.L. Chang, C.H. Chung, Y.C. Wu, M.J. Su, Nitric Oxide-Biol. Chem. 47 (2004) 307–315.
[13] C.H. Ling, G.J. Chang, M.J. Su, Y.C. Wu, C.M. Teng, F.N. Ko, Br. J. Pharmacol 1 (1995) 275–281.
[14] S.M. Mohamed, E.M. Hassan, N.A. Ibrahim, Nat. Prod. Res. 15 (2010) 1395–1402.
[15] C.Y. Chen, H.M. Wu, W.Y. Chao, C.H. Lee, Afr. J. Pharm. Pharmacol. (2013) 1067–1070.
[16] D.B. Silva, M.F.C. Matos, S.T. Nakashita, C.K. Misu, N.C. Yoshida, C.A. Carollo, J.R. Fabri, H. Miglio, J.M. Siqueira, Quim. Nova 30 (2007).
[17] R.A. Costa, M.L.B. Pinheiro, K.M.T. Oliveira, A. Barison, K.S. Salomé, J.R. Iank, N.G. Silva, T.S. Cabral, E.V. Costa, J. Chem. (2016), http://dx.doi.org/10.1155/2016/1752429.
[18] M. Whitlow, A.J. Howard, D. Stewart, D. Hardman, L.F. Kuyper, D.P. Baccanari, M.E. Fling, R.L. Tansik, J. Bio. Chem 48 (1997) 30289–30298.
[19] M. Monod, M.B. Zepelin, Biol. Chem. 383 (2005) 1087–1093, http://dx.doi.org/10.1515/BC.2002.117.
[20] C. Abad-Zapatero, R. Goldman, S.W. Muchmore, C. Hutchins, K. Stewart, J. Navaza, C.D. Payne, T.L. Ray, Protein Sci. 5 (1996) 640–652.
[21] M.J. Frisch, G.W. Trucks, H.B. Schlegel, G.E. Scuseriaet, Gaussian 03 Revision B.05, Gaussian, Inc., Pittsburgh, PA, 2003.
[22] R. Dennington, T. Keith, J. Millam, Gaussian Version 5, Semichem. Inc., Shawnee Missions KS, 2009.
[23] M. Jamroz, Vibrational energy distribution analysis, VEDA 4 Computer Program. Poland, 2004.
[24] J.A. Takahashi, M.B. Floreano, M.S. Oliveira, T.S. Oliveira, J.N. Tabudravu, J.L. Wardell, S.M.S. V.·Wardell, Monatsh. Chem. 146 (2015) 1763–1770.
[25] N. Özdemir, S. Dayan, O. Dayan, M. Dinçer, N. Kalaycıoglu, J. Mol. Phys. 11 (6) (2013) 707–723.
[26] R. Parr, Functional Theory of Atoms and Molecules, Oxford University Press, New York, 1989.
[27] R. Parr, L. Szentpaly, S. Liu, Electrophilicity index, J. Am. Chem. Soc 121 (1999) 1922–1924.
[28] J.F. Janak, Phys. Rev. B 18 (1978) 7165.
[29] J.P. Perdew, R.G. Parr, M. Levy, J.L. Balduz Jr., Phys. Rev. Lett. 49 (1982) 1691.
[30] C.G. Zhan, J.A. Nichols, D.A. Dixon, J. Phys. Chem. A 107 (2003) 4184–4195.
[31] J. Luo, Z.Q. Xue, W.M. Liu, J.L. Wu, Z.Q. Yang, J. Phys. Chem. A 110 (2006) 12005–12009.
[32] A.J. Arduengo, H. Bocks, H. Chen, M. Denk, D.A. Dixon, J.C. Green, W.A. Herrmann, N.L. Jones, W. M. Wagner, J. Am. Chem. Soc. 116 (1994) 6641.
[33] J. Murray, K. Sen, Molecular Electrostatic Potentials Concepts and Applications, Elsevier Science BV, Amsterdam The Netherlands, 1996.
[34] B.C. Carlson, J.M. Keller, Phys. Rev. 105 (1957) 102–103.
[35] F. Weinhold, J.E. Carpenter, J. Mol. Struct. (Theochem) 169 (1988) 41–62.
[36] A.E. Reed, R.B. Weinstock, F. Weinhold, J. Chem. Phys. (1985) 735–739.
[37] E.R. Davidson, Reduced Density Matrices in Quantum Chemistry, Academic Press, New York, 1976.
[38] R.S. Mulliken, J. Chem. Phys. (1955) 1833–1841.
[39] Z.F. Chen, Y.C. Liu, L.M. Liu, H.S. Wang, S.H. Qin, B.L. Wang, H.D. Bian, F. B. Yang, H.G. Liu, H. Liang, C. Orvig, Dal. Trans. 2 (2009) 262–272.
[40] D. Kleinman, J. Phys. Rev. 126 (1962) 1977–1979.
[41] C.L. Geskin, J. Am. Chem. Soc. 15 (2003) 15651–15658.
[42] J. Nocedal, S.J. Wright, Numerical Optimization, Springer Series in Operations Research, Springer Verlag, Berlin, 1999.
[43] O. Trott, A.J. Olson, J. Comput. Chem. 31 (2010) 455–461.
[44] G. Morris, D.S. Goodsell, R.S. Halliday, R. Huey, W.E. Hart, R.K. Belew, J. Comput. Chem. 19 (1998) 1639–1662.
[45] C.Y. Panicker, H.T. Varghese, P.S. Nayak, B. Narayana, B.K. Sarojini, H.K. Fun, J.A. War, S.K. Srivastava, C. Van Alsenoy, Spectrochim. Acta 148 (2015) 18–28.

6.4. Propriedades estruturais, vibracionais e eletrônicas do glucoalcaloide Strictosidina: Um estudo teórico e experimental

No artigo a seguir, uma análise detalhada do comportamento espectroscópico e analise estrutural do alcaloide strictosidina com aporte DFT é reportada usando funcional de troca e correlação B3LYP e funções de base 6-31G(d) e 6-311G (2d,p). Este trabalho consistiu na continuação de um trabalho anterior (mestrado), que resultou no isolamento desta molécula de *Strychnos amazônica* seguido de caracterização espectroscópica por RMN, UV-VIS, IR e ESI-MS. O alcaloide strictosidina é a molécula precursora de todos os alcaloides indolo monoterpênicos existentes, estruturas estas que despertam grande interesse no campo da fitoquímica e da farmacologia vide sua ampla faixa de atividade biológica. Esta crucial molécula, apesar de possuir vasta referência na literatura, até o momento não possuía estudos teóricos DFT aliados a dados experimentais a cerca da sua geometria (apenas um artigo de 1994 abordando apenas dados de RMN, no entanto a ausência de dados de cristalografia de raios-x), orbitais HOMO-LUMO, mapas de potencial eletrostático (e possível formação de dímeros), comportamento vibracional (espectros IV teórico e experimental) e aspectos reacionais. O referente trabalho constatou a estereoquímica dos carbonos nas posições 15, 20 e 21, além de fornecer novas informações à cerca da conformação espacial e dados de distância e ângulos. A proximidade entre as constantes de acoplamento de RMN obtidas teoricamente e experimentalmente tornaram possíveis constatar os ângulos diedros e a conformação mais estável da estrutura em estudo. Mapas de potencial eletrostático calculados mostraram regiões com potenciais opostos que formam pontes de hidrogênio que possivelmente estabilizam a forma dimérica proposta, a qual possivelmente influencia na cristalização e solubilidade da molécula.

Hindawi Publishing Corporation
Journal of Chemistry
Volume 2016, Article ID 1752429, 16 pages
http://dx.doi.org/10.1155/2016/1752429

Research Article

Structural, Vibrational, and Electronic Properties of the Glucoalkaloid Strictosidine: A Combined Experimental and Theoretical Study

Renyer Alves Costa,[1] Maria Lucia Belem Pinheiro,[1] Kelson Mota Teixeira de Oliveira,[1] Andersson Barison,[2] Kahlil Schwanka Salomé,[2] Júlio Rodolfo Iank,[1] Noam Gadelha da Silva,[1] Tiara Souza Cabral,[3] and Emmanoel Vilaça Costa[1]

[1]*Department of Chemistry, Federal University of Amazonas, 69077-000 Manaus, AM, Brazil*
[2]*NMR Laboratory, Department of Chemistry, Federal University of Paraná, 80060-000 Curitiba, PR, Brazil*
[3]*National Research Institute of Amazonas (INPA), 69080-971 Manaus, AM, Brazil*

Correspondence should be addressed to Renyer Alves Costa; renyer.costa@gmail.com

Received 21 October 2015; Accepted 3 January 2016

Academic Editor: Arturo Espinosa Ferao

A detailed structural analysis and spectral behavior of the glucoalkaloid strictosidine, a precursor of all monoterpene indole alkaloids, are discussed. The experimental NMR, FTIR, and UV results were compared to the theoretical DFT spectra calculated by Becke using the three-parameter Lee-Yang-Parr (B3LYP) function with 6-31G(d) and 6-311++G(2d,p) basis sets. The theoretical geometry optimization data were compared with the X-ray data for precursors and similar structures in the associated literature. The similarity between the theoretical and experimental coupling constants values made it possible to affirm the values of dihedral angles and their configuration, reinforcing findings from previous stereochemical studies. Theoretical UV analysis agreed well with the measured experimental data, with bands assigned. Calculated HOMO/LUMO gaps show low excitation energy for strictosidine, justifying its stability and reaction kinetics. The molecular electrostatic potential map shows opposite potentials regions that form hydrogen bonds that stabilize the dimeric form, which were confirmed by excellent agreement of the dimeric form theoretical wavenumbers with the experimental IR spectrum. ESI-MS/MS data revealed patterns for the fragmentation of the protonated strictosidine molecule outlined by an NBO study.

1. Introduction

Indole alkaloids play a very important role in the chemistry of natural products and are especially recognized for their use in clinical medicine as an adjunct to anesthetics. The finding of several clinic uses has driven intense study of this class of substances, and many antiplasmodial [1, 2], cytotoxic [3], antibacterial [4], antifungal [5], spasmodic [6], hypotensive [7], and anti-inflammatory [8] properties have been related to indole alkaloids. Strictosidine (Figure 1) is a key glucomonoterpene indole alkaloid precursor of all indole monoterpene alkaloids. This crucial molecule, which originates from a reaction between tryptamine and the monoterpene glycoside secologanin, is found in several plant species [9–13] and was first isolated from *Rhazya stricta* [14]. Strictosidine has also been obtained in cell suspension cultures and under biomimetic conditions [15, 16].

Studies discussing the structure and stereochemistry of strictosidine [16–18] have compared its spectral data with those of similar structures, confirming that its C3 atom has the S configuration or 3α [S]. This configuration is identical to that of known monoterpene indole alkaloids, in disagreement with the proposal that vincoside was the precursor of indole alkaloids with 3β [R] configuration, as previously thought. Patthy-Lukáts et al. [19] studied the stereochemistry of strictosidine based on experimental NMR analysis, determining its spatial configuration. However, there are no X-ray studies because this molecule has not been obtained yet in crystalline

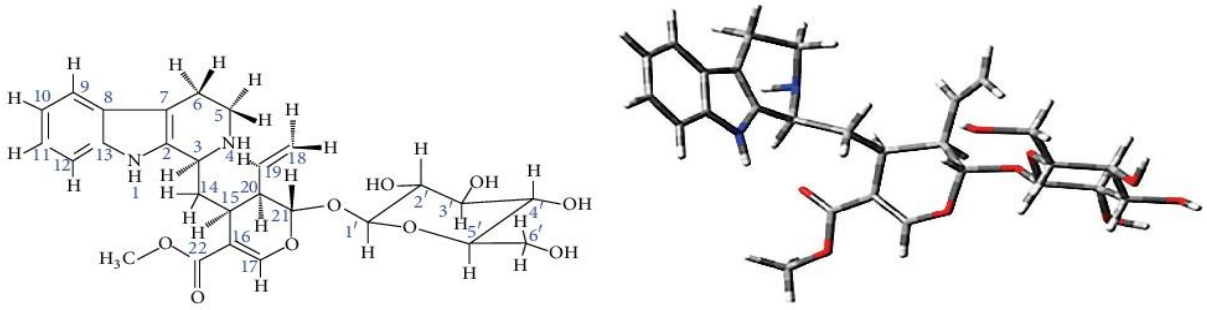

(a) (b)

Figure 1: Structure of strictosidine.

form [19] and no theoretical molecular modeling study that discusses the bond lengths and planar and dihedral angles was previously presented. The determination of the relationship between theoretical vibrational frequencies and experimental IR absorbance bands and between theoretical electronic transitions and experimental UV bands of strictosidine has not been investigated yet. Therefore, a detailed theoretical DFT and experimental investigation of the structure and spectral behavior of this molecule, providing a comprehensive description of strictosidine, have been reported. Initially, the alkaloid has been isolated from *Strychnos amazonica* and the molecule was characterized by NMR (^{1}H, HSQC, and HMBC), MS (ESI-MS/MS), UV, and FTIR. The theoretical data (optimized geometry, UV, IV, MEP, and NBO calculations) were compared with the experimental data to answer questions regarding structure, electronic transitions involved in the UV spectrum, vibrational assignments, and other physical properties of strictosidine.

2. Experimental Section

2.1. General Procedures. Nuclear magnetic resonance (NMR) spectra were recorded on a Bruker 600 AVANCE spectrometer with 12.4-Tesla magnetons at 295 K in deuteriomethanol containing 0.06% TMS as an internal standard. The ESI-MS^n data were recorded on LQC fleet *ion trap* Thermo Scientific spectrometer equipped with an electrospray ionization (ESI) ion source in the positive mode with the following parameters: capillary voltage at 26 V; spray voltage at 5 kV; tube lens offset at 100 V; capillary temperature at 225°C; auxiliary gas at 5%; and sheet gas at 12%. The UV data were recorded in methanol using a PDA Detector plus Finnigan Surveyor (Thermo Scientific). The FTIR data were recorded in KBr pellet technique (solid phase) using an ABB FTLA200.

2.2. Plant Material. The leaves of *Strychnos amazonica* were collected in the Adolpho Ducke Forest Reserve located 25 km from the city of Manaus (2°56′01.0″S, 59°57′45.8″W), Amazonas, Brazil. The species was identified by the DNA barcoding technique, in which the distance matrices, which were calculated for rcbL and rpoC1 and for the concatenated gene sequences (rbcL + rpoC1), showed null values of genetic divergence between the collected specimen and a voucher specimen of *Strychnos amazonica* (INPA 216208) deposited in the herbarium of the National Research Institute of Amazonas (INPA). The rcbL and rpoC1 sequences were deposited in GenBank under accession numbers KJ764797 to KJ764819.

2.3. Isolation of Strictosidine. 30 g of leaf extract in methanol was submitted to a silica-gel column using hexane/ethyl acetate and ethyl acetate/methanol as the mobile phases. Of the 31 fractions obtained, fractions 10 to 16 showed the presence of an alkaloid. These fractions were pooled and submitted to an ESI-TI-MS analysis, which showed an ion peak at *m/z* 531. CID analysis revealed fragments at *m/z* 514, *m/z* 369, and *m/z* 356, which are compatible with strictosidine [20]. This fraction was submitted to a silica-gel column using 100% ethyl acetate, 9 : 1 ethyl acetate/methanol, and 100% methanol in succession, resulting in an amorphous brown solid (20 mg) that appeared to be pure in CCD/Dragendorff and ESI-IT-MS analyses (with only one ion peak at *m/z* 531). Then, it was subjected to NMR (H^1, HMBC, and HSQC), UV, and IR analysis for structural confirmation (see Table S1 and Figures S1, S2, and S3 in the Supplementary Material data available online at http://dx.doi.org/10.1155/2016/1752429).

2.4. Computational Methods. The theoretical quantum chemical calculations were performed using the Gaussian 03 W Program (Revision E.01) on the Debian Linux (5.0 version) platform on an Intel Quadcore™ PC (8 GB RAM) [21]. The DFT approach was used to optimize the geometry using the 6-31G(d) and 6-311G++(2d,p) basis sets and the B3LYP functional. The molecular geometries were fully optimized by the force gradient method using Berny's algorithm, and the potential energy surfaces were characterized using standard analytical harmonic vibrational analysis to confirm that the stationary points corresponded to the minima of the potential energy surfaces (no imaginary frequencies or negative eigenvalues were found). The theoretical $^3J_{HH}$ coupling constants were calculated using the NMR protocols implemented using the DFT B3 LYP

6-31G(d) and 6-311++G(2d,p) basis sets in the Gaussian 03 software. These coupling constants were compared with the measured values that were experimentally obtained, showing RMSD values of 1.45 Hz for DFT B3LYP 6-31G(d) and 1.25 Hz for 6-311++G(2d,p). The UV spectra were calculated using the RTD-B3LYP-FC functional and 6-31G(d) and 6-311G++(2d,p) basis set [22, 23]. The NBO values were obtained with NBO 3.1, as implemented in the Gaussian 03 package using the 6-31G(d) basis set and the B3LYP functional. The harmonic frequencies were calculated at the B3LYP/6-31G(d) level using the optimized structural parameters. The assignments of the calculated wavenumbers were aided by the animation option of the GaussView program, which gives a visual presentation of the vibrational modes [24]. The potential energy distribution (PED) was calculated with the help of the VEDA4 software package [25].

3. Results and Discussion

3.1. Geometry Optimization. Because no crystallographic data for strictosidine are available, the geometry optimization data, which were calculated using the B3LYP/6-31G(d) and B3LYP/6-311++G(2d,p) basis set, were compared with the X-ray data for similar structures [26–29]. Due to the similarity of the data obtained from both basis sets (Table 1), the discussion that follows is based on the B3LYP 6-31G(d) values but should also apply to B3LYP 6-311++G(2d,p).

Initially, the bond lengths indicated a small distortion in the pentacyclic tryptophan ring, showing a greater distance for the C7-C8 (1.44 Å) and C8-C13 (1.42 Å) bonds compared to the N1-C2, C2-C7, and C13-N1 bonds. Significant distortions were observed in the second six-membered ring of the tryptophan portion, which was distinct for all connections. Similar distortions were observed in the dihydropyran ring: 1.52 Å (C15-C16), 1.35 Å (C16-C17), 1.34 Å (C7-O), 1.53 Å (C20-C21), and 1.56 Å (C20-C15). These distortions resulted from the presence of double bonds and heteroatoms, which make these bonds shorter than the C-C bonds.

Concerning the planar angles, the aromatic ring shows no large deformations, which was similar to the experimental data for previously analyzed indole alkaloids [26, 29]. The planar angles were 118.78° (C9-C8-C13), 119.16° (C8-C9-C10), 121.06° (C9-C10-C11), 121.17° (C10-C11-C12), 117.62° (C11-C12-C13), and 122.18° (C8-C12-C13). The pentacyclic ring showed a nonangular uniformity except for the angles between N1-C2-C7 (109.56°) and C13-C2-N1 (109.22°).

^{1}H-^{1}H NMR coupling constants are highly sensitive to the dihedral angles of hydrogen atoms and both the configuration and conformation of a structure can be validated if there is agreement between the experimental and theoretical $^{3}J_{HH}$ values. The calculated initial dihedral angles for the hydrogen atoms in positions 5 and 6 of the third ring of the tryptophan portion were 162.78° (with theoretical $^{T}J_{H5a\text{-}H6b}$ = 11.0 Hz) and 46.76° (theoretical $^{T}J_{H5a\text{-}H6a}$ = 4.2 Hz). These values were consistent with the experimentally measured values for coupling constants, $^{E}J_{H5a\text{-}H6b}$ = 11.9 Hz and $^{E}J_{H6a\text{-}H5a}$ = 4.8 Hz, revealing a pseudoaxial-axial relationship between hydrogen atoms H5a-H6b and an axial-equatorial relationship between H5a and H6a. The obtained dihedral angles for hydrogen atoms of the C3-C14-C15 bridge also showed coupling constants values consistent with the experimental values: 172.28° for H3-H14*proR* with theoretical $^{T}J_{3\text{-}14R}$ = 10.7 (experimental $^{E}J_{3\text{-}14R}$ = 11.4 Hz), −72.41° for H3-H14*proS* with $^{T}J_{14S\text{-}3}$ = 2.8 Hz ($^{E}J_{14S\text{-}3}$ = 3.6 Hz), and −87.53° for H14*proR*-H15 with $^{T}J_{H14R\text{-}H15}$ = 0.6 Hz ($^{E}J_{H14R\text{-}H15}$ = 1.8 Hz). The conformation of the dihedral angles involving H15-H20 (−56.90°), H20-H21 (−178.69°), and H19-H20 (65.23°) is also plausible given the respective experimental hydrogen coupling constants $^{T}J_{H15\text{–}H20}$ = 4.4 Hz (^{E}J = 4.8 Hz), $^{T}J_{H20\text{-}H21}$ = 8.1 (^{E}J = 8.4 Hz), and $^{T}J_{H19\text{-}H20}$ = 3.0 Hz (^{E}J = 3.0 Hz). The similarity between the modeled DFT structure (Figure 2) (with *15S*, *20S*, and *21S* configuration) and the experimental spectroscopic NMR data complements the conformational arrangement study of strictosidine. The *15S*, *20S*, and *21S* configuration was reported in previous experimental X-ray studies of strictosidine precursors [19, 28–30]. Finally, due to the consistency between the geometry calculated using the DFT B3LYP/6-31G(d) and B3LYP/6-31++G(2d,p) methods and the coupling constant values measured from the experimental ^{1}H spectrum, the conformation of the C21-O-C1′ bridge (so far uncertain) was depicted with angles of 81.17° and lengths of 2.65 Å between H21 and H1′ (Figure 2). This depiction is consistent with the NOESY data provided by Patthy-Lukáts et al. [19]. Other interactions between segments found in the NOESY data are justified by the calculated distances between the hydrogen atoms as follows: H3-H5b (3.76 Å), H3-H14S (2.55 Å), H5a-H5b (1.76 Å), H6a-H6b (1.76 Å), H9-H10 (2.48 Å), H10-11 (2.477 Å), H11-H12 (2.488 Å), H14R-H14S (1.75 Å), H14R-H19 (2.83 Å), H14R-H15 (2.66 Å), H14S-H21 (2.59 Å), H15-H20 (2.41 Å), H18Z-H18E (1.85 Å), H18Z-H20 (3.57 Å), H18E-H19 (2.40 Å), and H20-H19 (2.52 Å) (for information about Mulliken charges and natural bond analysis, see Tables S2 and S3 in Supplementary Material data).

3.2. UV Analysis. The electronic spectrum of the molecule in a methanol solution was compared with the calculated spectrum (in the gas phase) at time dependent density functional using the B3LYP 6-31G(d) and B3LYP 6-311G++(2d,p) basis sets, as Figure 3 shows. The bands located at 222 and 272 nm could be experimentally observed and were in agreement with the presence of chromophores. Because strictosidine is an aromatic compound, $\pi \rightarrow \pi^*$ transitions were involved but the presence of conjugations in the pentacyclic ring of the tryptophan portion and in the β-alkoxyacrylate group suggested that $n \rightarrow \pi^*$ transitions also occurred. The theoretical calculations predicted an intense electronic transition of 5.8964 eV, with an oscillator strength f = 0.548 at 210.27 nm for B3LYP 6-31G(d). For B3LYP 6-311++G(2d,p), an electronic transition of 5.62 eV was predicted, with an oscillator strength f = 0.2714 at 220.62 nm. These results showed good agreement with the measured experimental data (222 nm) assigned to the $\pi \rightarrow \pi^*$ and $\pi \rightarrow \sigma^*$ transitions of the indole portion. The calculations also predicted a weaker electronic

Table 1: Calculated geometrical parameters for strictosidine compared with the experimental data.

Parameter	B3LYP 6-31G(d)	B3LYP 6-311++G(2d,p)	Molina et al. [27]	Dupont and Dideberg [26]	Lentz and Rossmann [29]
Bond length					
N1-C2	1.386	1.384	1.363	1.400	
C2-C3	1.507	1.506	—	1.488	
C3-N4	1.479	1.477	—	1.477	
N4-C5	1.472	1.473	—	1.482	
C5-C6	1.543	1.542	—	1.523	
C6-C7	1.501	1.501	—	1.490	
C7-C2	1.375	1.375	1.442	1.429	
C7-C8	1.439	1.439	1.457	1.425	
C8-C9	1.406	1.407	—	1.432	
C8-C13	1.427	1.426	—	1.406	
C9-C10	1.392	1.391	—	1.432	
C10-C11	1.411	1.410	—	1.377	
C11-C12	1.393	1.392	—	1.346	
C12-C13	1.399	1.398		1.409	
C13-N1	1.381	1.381	1.406	1.379	
C14-C3	1.548	1.548	—	1.541	
C14-C15	1.552	1.562	—		1.62
C15-C16	1.515	1.520	—		1.48
C16-C17	1.350	1.350	—		1.60*
C18-C19	1.335	1.334	—		1.51*
C19-C20	1.512	1.513	—		1.60
C20-C21	1.526	1.526	—		1.50
C21-O	1.401	1.403	—		1.43
C22-C16	1.469	1.471	—		1.60
C23-O	1.437	1.441	—		1.49
C1′-O	1.403	1.401	—		1.42
C1′-C2′	1.528	1.526	—		1.52
C2′-C3′	1.528	1.527	—		1.51
C3′-C4′	1.527	1.528	—		1.55
C4′-C5′	1.537	1.537	—		1.52
C5′-C6′	1.523	1.522			1.52
C5′-O	1.438	1.442	—		1.45
Bond angle					
N1-C2-C7	109.570	109.562	108.7	110.5	
C2-C7-C8	107.063	107.071	105.7	107.0	
C7-C8-C13	106.793	106.792	107.5	107.2	
C8-C13-N1	107.347	107.343	—	108.0	
C13-N1-C2	109.221	109.221	—	107.3	
C2-C3-N4	110.742	110.742	—	106.6	
C3-N4-C5	114.580	114.582	—	112.6	
N4-C5-C6	114.370	114.370	—	110.1	
C5-C6-C7	108.976	108.976	—	109.4	
C6-C7-C2	121.873	121.881	128.9	122.1	
C7-C2-C3	125.545	125.546	107.9	126.2	
C13-C8-C9	118.786	118.771	—	119.7	

Table 1: Continued.

Parameter	B3LYP 6-31G(d)	B3LYP 6-311++G(2d,p)	Molina et al. [27]	Dupont and Dideberg [26]	Lentz and Rossmann [29]
C8-C9-C10	119.165	119.172	—	115.3	
C9-C10-C11	121.057	121.052	—	122.7	
C10-C11-C12	121.177	121.181	—	122.2	
C11-C12-C13	117.626	117.625	—	117.6	
C12-C13-C8	122.186	122.186	—	122.4	
C2-C3-C14	111.904	111.903	—	110.8	
N4-C3-C14	110.456	110.456	—	116.9	
C3-C14-C15	113.558	113.562	—	112.7	
C15-C16-C20	112.883	112.883	—	—	
C15-C16-C17	112.915	112.914	—	—	107
C16-C17-O	125.412	125.420	—	—	110
C17-O-C21	119.937	119.941	—	—	121
C18-C19-C20	129.038	129.038	—	—	101
C16-C22-O	113.414	113.415	—	—	111
CH3-O-C22	115.912	115.912	—	—	116
C21-O-C1′	115.516	115.516	—	—	114
O-C1′-C2′	108.278	108.278	—	—	106
C1′-C2′-C3′	109.237	109.237	—	—	106
C2′-C3′-C4′	111.945	111.945			110
C3′-C4′-C5′	109.024	109.024	—	—	105
C4′-C5′-O	108.796	108.795	—	—	106
C5′-O-C1′	114.025	114.027	—	—	108

*Corresponding to single bonds due to the crystallization process of loganin in loganin penta-acetate monomethyl ether bromide.

transition at 265.72 nm (4.66 eV) for B3LYP 6-31G(d) and at 278.26 nm (4.45 eV) for B3LYP 6-311++G(2d,p), which were equivalent to the band at 272 nm in the experimental spectrum. These values were assigned to the sum of the $n \rightarrow \pi^*$ and $\pi \rightarrow \pi^*$ transitions of the indole and β-alkoxyacrylate groups.

The highest occupied molecular orbitals (HOMO) and the lowest-lying unoccupied molecular orbitals (LUMO), also called frontier molecular orbitals (FMOs), play an important role in many properties of a compound as well as in its quantum chemistry and UV-Vis spectra. The energy gap between the HOMO and LUMO energies is the basis for the chemical stability and reactivity of a molecule. The quantum bonding features of strictosidine are depicted by a plot of the HOMO, HOMO−1, LUMO, and LUMO−1 in Figure 4. In the UV-Vis spectrum, the two maximum calculated absorption wavelengths corresponded to the contributions of the electronic transitions from HOMO → LUMO+4 (50.7%) and HOMO−1 → LUMO+1 (23.74%) for 210 nm and HOMO → LUMO+1 (89.8%) for 265 nm in B3LYP 6-31G(d). In B3LYP 6-311G++(2d,p), the wavelengths corresponded to HOMO → LUMO+16 (26%), HOMO → LUMO+19 (14%), and HOMO → LUMO+18 (5.7%) for 220.6 nm and HOMO → LUMO+2 (19%) and HOMO → LUMO+3 (70.81%) for 278.3 nm. It is clear from Figure 5 and Figures S5 and S6 (see Supplementary Information) that the major transitions were restricted to the indolic portion because the HOMO, HOMO−1, and LUMO+1 are located in this region and only the LUMO is located in the β-alkoxyacrylate group. Transitions involving the LUMO contribute minimally to the absorption wavelengths (λ) of strictosidine, showing that the transitions in the β-alkoxyacrylate group have no influence, in disagreement with the ancient proposal that β-alkoxyacrylate group influences strictosidine UV spectrum [14]. This prediction was proven by the similarity of the experimental spectrum of strictosidine to the spectra of several other indole alkaloids that lack alkoxyacrylate groups [31].

3.3. Global and Local Reactive Descriptors. The energy gap between the HOMO and LUMO is very important for determining the electrical properties, kinetic stability, optical polarizability, and chemical reactivity descriptors, such as hardness and softness, of a molecule.

The concept of hardness (η) and softness is related to a compound's reactivity and is a property that measures the extent of chemical reactivity to which the addition of a charge stabilizes the system. The chemical potential (μ) provides a global reactivity index and is related to charge transfer from a system of higher chemical potential to one of lower chemical potential. Electronegativity (χ) is the power to attract electrons and is directly related to all the previously mentioned properties. All these properties are defined as follows [32, 33]:

$$\eta = \frac{1}{2}\left(\frac{\partial_2 E}{\partial N_2}\right)V_{(r)} = \frac{1}{2}\left(\frac{\partial_\mu}{\partial N}\right)V_{(r)},$$
$$\mu = \left(\frac{\partial E}{\partial N}\right)V_{(r)}, \quad (1)$$
$$\chi = -\mu = -\left(\frac{\partial E}{\partial N}\right)V_{(r)},$$

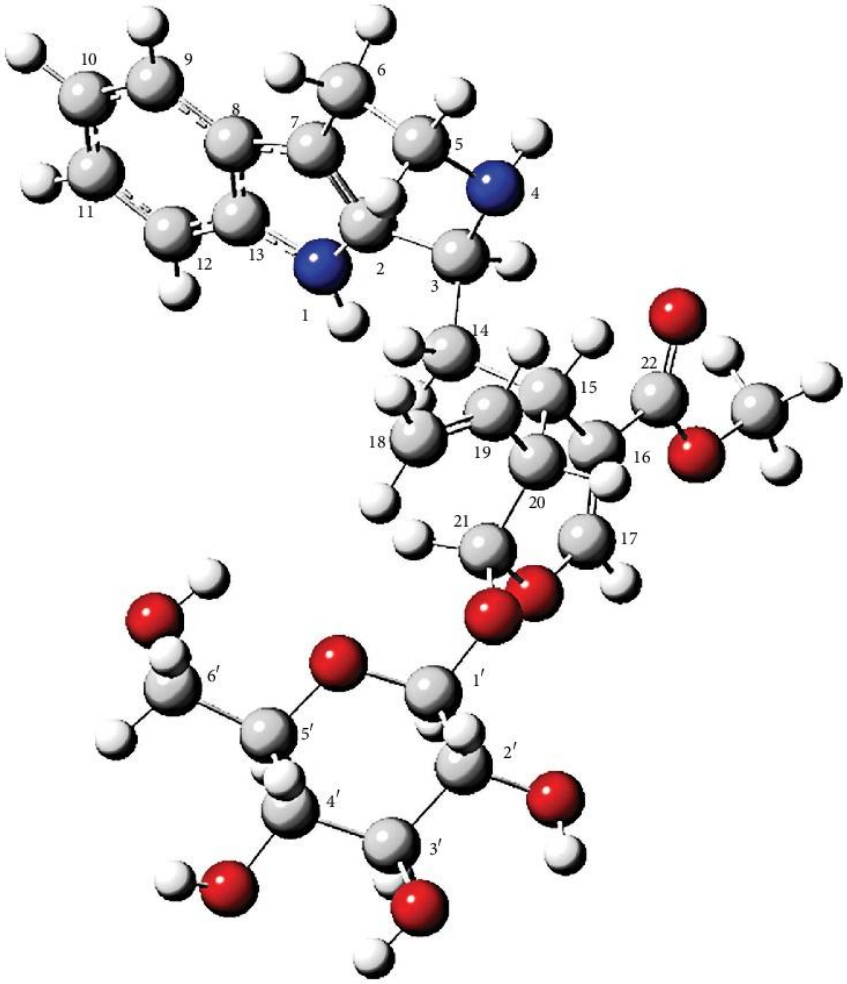

FIGURE 2: The optimized geometry of strictosidine with the scheme of atom numbering.

where E and $V_{(r)}$ are the electronic energy and the external potential of an N-electron, respectively. Based on Koopmans theorem for closed-shell molecules, these global chemical reactivity descriptors can be simplified and defined as follows:

$$\eta = \frac{(I - A)}{2},$$
$$\mu = \frac{-(I + A)}{2}, \quad (2)$$
$$\chi = \frac{(I + A)}{2},$$

where A is the ionization potential and I is the electron affinity of the molecule. The ionization energy and electron affinity are obtained from the HOMO and LUMO energies as $I = -E_{\text{HOMO}}$ and $A = -E_{\text{LUMO}}$. In terms of chemical hardness, a large HOMO-LUMO gap indicates a hard molecule and is related to more stable molecules, whereas a small gap indicates a soft molecule and is related to a more reactive molecule.

Another important descriptor is the electrophilicity index (ω), a global maximum reactivity index that is similar to chemical hardness and chemical potential. The electrophilicity index measures the global electrophilic nature of a molecule and was proposed by Parr et al. [34, 35] as a measure of energy lowering due to charge transfer. The electrophilicity index is defined as follows:

$$\omega = \left(\frac{\mu^2}{2\eta}\right). \quad (3)$$

This scale permits the classification of organic molecules as strong, $\omega > 1.5$ eV, moderate, $0.8 < \omega < 1.5$ eV, and marginal, $\omega < 0.8$ eV, electrophiles. On the other hand, there

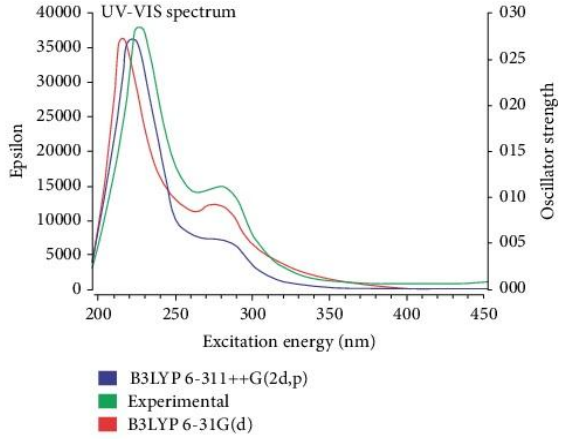

Figure 3: Experimental and theoretical ultraviolet-visible spectra of strictosidine in methanol.

Table 2: Calculated energy values for strictosidine in methanol using B3LYP/6-31G(d) and B3LYP/6-311++G(2d,p).

Basis set	B3LYP/6-31G(d)	B3LYP/6-311++G(2d,p)
Energy (a.u.)	−1835.80	−1836.39
Dipole moment	5.30 Debye	5.50 Debye
E_{HOMO} (eV)	−5.28	−5.60
E_{LUMO} (eV)	−0.83	−1.19
$E_{HOMO\text{-}LUMO}$ (eV)	4.45	4.40
E_{HOMO-1} (eV)	−5.89	−6.20
E_{LUMO+1} (eV)	−0.18	−0.62
$E_{(HOMO-1)\text{-}(LUMO+1)}$ (eV)	5.71	6.80
Hardness (η)	2.22	2.20
Chemical potential (μ)	−3.06	−3.40
Electronegativity (χ)	3.06	3.40
Electrophilicity index (ω)	2.11	2.63
Nucleophilicity index (N)	5.82	5.91

is a good correlation in the inverse of the electrophilicity ($1/\omega$); thus, molecules located at the bottom of the electrophilicity scale are classified as marginal electrophiles, corresponding with good nucleophiles [36]. However, when the molecule bears more than one functional group with opposite electrical charge, its nucleophilic character cannot be straightforwardly associated with the inverse of the electrophilicity. Thus, the nucleophilicity index (N) appears as a different descriptor which gives more information about nucleophilicity and is defined as follows [37]:

$$N = E_{HOMO} - E_{HOMO(TCE)}, \quad (4)$$

where tetracyanoethylene (TCE) is taken as reference. All these properties were calculated using these equations for strictosidine in methanol through B3LYP/6-31G(d) and B3LYP/6-311++G(2d,p) basis sets and their values are shown in Table 2. Both HOMO and LUMO are bonding orbitals, resulting in a low excitation energy for strictosidine. The excitation energies, which were calculated as 4.451 eV for 6-31G(d) and 4.408 eV for 6-311++G(2d,p), reflect the low hardness value (2.22) showing strictosidine as a soft molecule with high polarizability. Electronegativity and electrophilicity values of strictosidine indicate that this molecule has significative attractive electron power acting as an electrophile and in addition to its polarization becomes very reactive since the electrons are farther from the nucleus; however, the nucleophilicity index value indicates that strictosidine is a strong nucleophile too. Such characteristic is justified because strictosidine is a large molecule that has many reactive groups with different potentials which forms small polarized points over its surface (as discussed in Section 3.6), which makes strictosidine a versatile molecule in view of the variety of alkaloids which it forms through intramolecular reactions with groups acting as nucleophiles and others as electrophiles [10]. On the other hand, the calculated chemical potential values, −3.06 for B3LYP/6-31G(d) and −3.40 for B3LYP/6-311++G(2d,p), reveal certain stability, indicating that it does not decompose spontaneously; that is, strictosidine molecule is reactive but does not tend to degrade into the components that formed it.

3.4. Tandem Mass Identification. The tandem mass spectra of protonated strictosidine (Figure S4 in Supplementary Data) of m/z 531 showed major fragment ions of m/z 514, 369, and 352. The ion of m/z 514 [M + H—17 Da] originated by loss of the NH_3 group from the tryptophane portion in a manner that was similar to the fragmentation of aporphine alkaloids (Pathway A) [38]. The ESI-MS^3 of this ion generated fragment ions of m/z 352 [M + H—162 Da] due to the hydrogen rearrangement in the glycoside followed by heterolytic cleavage of the C21-O-C1′ bridge (Pathway C). The fragment ion of m/z 369 [M + H—162 Da] possibly arose directly from the heterolytic breakage of the glycoside portion of strictosidine via the cleavage of the C21-O-C1′ bridge (Pathway B), which occurred through a similar mechanism to Pathway C. No fragment ions were observed in the MS^3 spectrum of the ion of m/z 369. Guided by the ESI-MS^2 and MS^3 data, a fragmentation mechanism is proposed for protonated strictosidine in Figure 5.

3.5. NBO Study. An NBO analysis describes the Lewis-like molecular bonding pattern of electron pairs (or of individual electrons in the open-shell case) in the optimally compact form of the molecule. More precisely, NBOs are orthonormal sets of localized "maximum occupancy" orbitals whose leading $N/2$ members (or N members in the open-shell case) give the most accurate possible Lewis-like description of the total N-electron density. The Lewis-type NBOs determine the localized *natural Lewis structure* (NLS) representation of the wave function, while the remaining "non-Lewis-type" NBOs complete the span of the basis and describe the residual "delocalization effects" (i.e., departures from a single localized Lewis structure). NBOs provide therefore a valence bond-type description of the wave function that is closely linked to classical Lewis structure concepts [39–42].

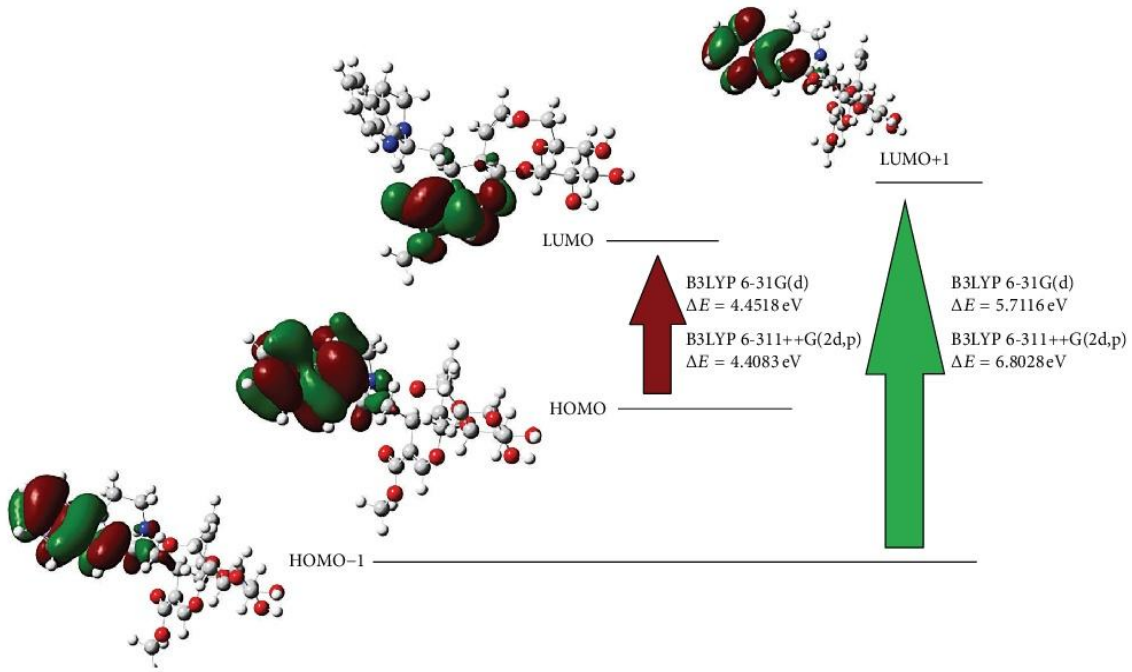

Figure 4: Frontier molecular orbitals of strictosidine.

Table 3: Electron population in Lewis and non-Lewis orbitals for strictosidine.

Orbitals	Electrons	Percentage
Core	75.97	99.96% of 76
Valence Lewis	201.50	97.817% of 202
Total Lewis	277.47	98.39% of 282
Valence non-Lewis	4.02	1.43% of 282
Rydberg non-Lewis	0.50	0.17% of 282
Total non-Lewis	4.53	1.61% of 282

NBO analysis is a helpful tool for understanding the delocalization of the electron density from the occupied Lewis-type (donor) NBOs to properly unoccupied non-Lewis-type (acceptor) NBOs [43–47] within the molecule. This analysis uses the second-order perturbation energies $E^{(2)}$ [donor (i) → acceptor (j)] that involve the most important delocalization instances, which are given as follows:

$$E^{(2)} = \Delta_{ij} = q_i \frac{F_{ij^2}}{\varepsilon_j - \varepsilon_i}. \quad (5)$$

Table 3 shows more-detailed breakdown of the Lewis and non-Lewis occupancies, confirming the quality of the natural Lewis structure description. The total Lewis occupancy was 98.395% and the non-Lewis occupancy was 1.605%. The NBO analysis revealed strong intramolecular interactions formed by the orbital overlaps between C-C bonding and C-C antibonding and by overlaps between the N and O lone pairs (LP) and C-C antibonding. These interactions led to intramolecular electron-density transfer that caused the stabilization of the molecular system (Table 4). The intramolecular hyperconjugative interactions between C2, C7, C8, C9, C10, C11, C12, C13, and N1 revealed strong stabilization of the indolic portion, principally by $\pi \rightarrow \pi^*$ interactions between C11-C10 → C8-C9 (20.07 kcal/mol), C9-C8 → C11-C10 (20.77 kcal/mol), C9-C8 → C13-C12 (20.01 kcal/mol), and C13-C12 → C8-C9 (19 kcal/mol) and electron donation from LP(1) N1 to π^* C2-C7 (36.44 kcal/mol) and π^* C12-C13 (40.91 kcal/mol). Other hyperconjugative interactions, especially the donation of electron density from LP(2) O3 to π^* C16-C17 (37.05 kcal/mol), LP(1) O2 to σ^* C22-O1 (32 kcal/mol), and LP(2) O1 to π^* C22-O2, gave strong stabilization to the dihydropyran ring of strictosidine. In addition, the $\pi^* \rightarrow \pi^*$ interactions of C8-C9 → C7-C2 and C21-O2 → C16-C17 provided enormous stabilization of 191.70 kcal/mol and 62.11 kcal/mol, respectively. Table 4 provides all significant values for the hyperconjugative interactions given by the second-order perturbation theory.

A relationship between the ESI-IT-MS study and the stabilization caused by orbital overlap between bonds in the second-order perturbation theory could be established. The strongest stabilization energies for strictosidine involved hyperconjugative interactions in the indolic portion (aromatic and pentacyclic rings) and in the dihydropyran portion, explaining the small number of cleavages and the absence of breakages in the indolic portion and in the dihydropyran ring. In the fragmentation mechanism proposed in Figure 2, the most stable fragments arose from the heterolytic

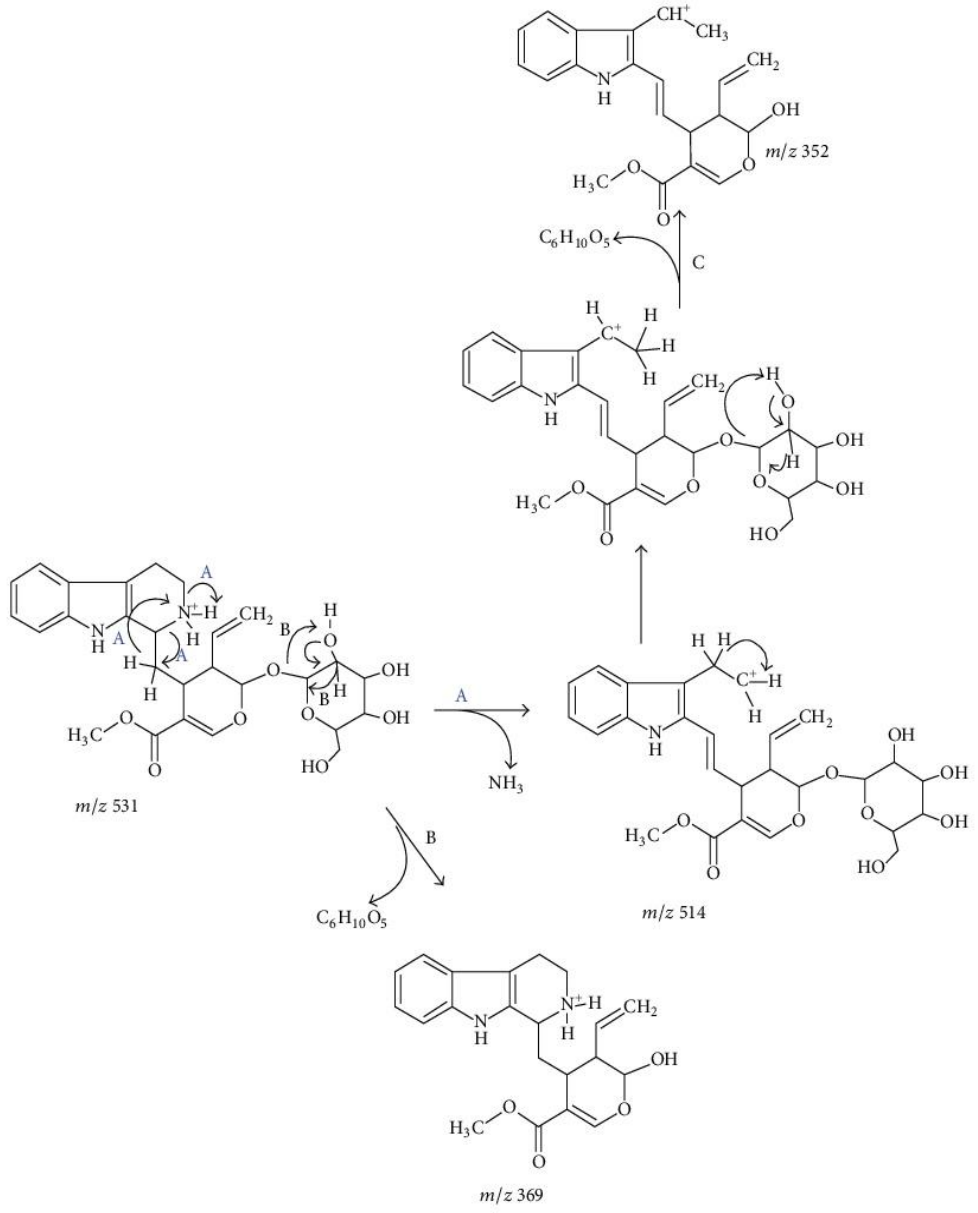

FIGURE 5: Mechanism proposed for the major fragmentation pathways of protonated strictosidine.

breakage of the O4-C1′, N4-C3, and N4-C5 bonds, which have the following weak hyperconjugative interactions: N4-C3 → N2-C3 ($\sigma \rightarrow \sigma^*$, 3.59 kcal/mol), C5-N4 → C3 ($\sigma \rightarrow \sigma^*$, 1.5 kcal/mol), N4-H → C5 ($\sigma \rightarrow \sigma^*$, 1.68 kcal/mol), N4-H → C5-H ($\sigma \rightarrow \sigma^*$, 2.51 kcal/mol), O4-C1′ → C20-C21 ($\sigma \rightarrow \sigma^*$, 1.46 kcal/mol), and O3-C21 → C21-O4 ($\sigma \rightarrow \sigma^*$, 0.51 kcal/mol). These results showed that the NBO study complemented the mass fragmentation study.

3.6. Molecular Electrostatic Potential Surface. Figure 6 illustrates 3D plots of the molecular electrostatic potential (MEP) surface for the strictosidine molecule. An MEP is a plot of the electrostatic potential mapped onto the constant electron density surface and is used primarily for predicting sites and relative reactivities towards electrophilic and nucleophilic attacks. MEPs are used in studies of biological recognition and interactions between the same molecules (e.g., in forming clusters and crystal structures) or other molecules. MEPs also correlate and predict a wide range of macroscopic properties [48, 49]. The color code of these maps ranges from −0.08 a.u. (deepest red) to 0.08 a.u. (deepest blue), where blue indicates a minimal concentration of electrons and red indicates a high density of electrons.

Table 4: Selected second-order perturbation energies for strictosidine.

Donor orbital (i)	Type	Acceptor orbital (j)	Type	$E_{(j)} - E_{(i)}$ a.u.	$E^{(2)}$ (kcal/mol)
C11-C10	π	C9-C8	π^*	0.28	20.07
		C13-C12	π^*	0.27	18.90
C9-C8	π	C11-C10	π^*	0.27	20.77
		C12-C13	π^*	0.27	20.01
		C7-C2	π^*	0.29	14.88
C13-C12	π	C11-C10	π^*	0.28	21.04
		C8-C9	π^*	0.29	16.32
C7-C2	π	C9-C8	π^*	0.29	19.71
C16-C17	π	C22-O1	π^*	0.29	24.34
N1	LP(1)	C13-C12	π^*	0.29	40.91
N1	LP(1)	C2-C7	π^*	0.31	36.44
O3	LP(2)	C16-C17	π^*	0.36	37.05
O4	LP(2)	O3-C21	σ^*	0.56	15.13
O4	LP(2)	C1′-O5	σ^*	0.60	13.48
O2	LP(1)	C22	RY*	1.55	14.52
O2	LP(2)	C16-C22	σ^*	0.72	16.43
O2	LP(2)	C22-O1	π^*	0.63	32.65
O1	LP(2)	C22-O2	π^*	0.32	47.44
C8-C9	π^*	C7-C2	π^*	0.01	191.70
C22-O2	π^*	C16-C17	π^*	0.03	62.11

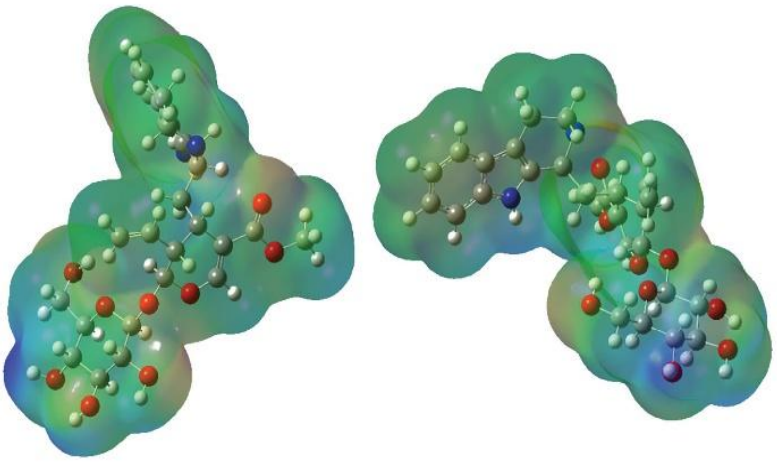

Figure 6: Molecular electrostatic potential maps (from two perspectives) for strictosidine calculated using the B3LYP/6-31G(d) basis set.

The MEPs for strictosidine indicated regions with positive potentials over H1 (0.0627 a.u.) and over the hydrogen atom of the OH group in position 4′ (0.0862 a.u.). Regions with negative potentials were located over the aromatic ring (−0.0429 a.u.), over the carbonyl group O2 (−0.0576 a.u.), between O4 and the OH group of C2′ position (−0.0643 a.u.), over OH on position C6′ (−0.0471 a.u.), and over oxygen atom on C4′ position (−0.0201 a.u.). The predominance of light green color region indicates great charge dispersion. Strictosidine is a large molecule with polarized points scattered over its surface which promotes various possible forms of intramolecular and intermolecular interaction (between strictosidine molecules); in addition, the nonflat shape hinders the chain interactions between strictosidine molecules which facilitate formation of a packed crystal.

3.7. IR Analysis. Figure 7 shows the experimental and theoretical IV spectra. The differences can be attributed to the fact that the theoretical DFT calculations were made for the molecule in the gas phase, whereas intermolecular interactions occur in solution. The assignment of the experimental bands to the normal modes of vibration was made using the optimized structure with the lowest potential energy, considering the potential energy distribution (PED)

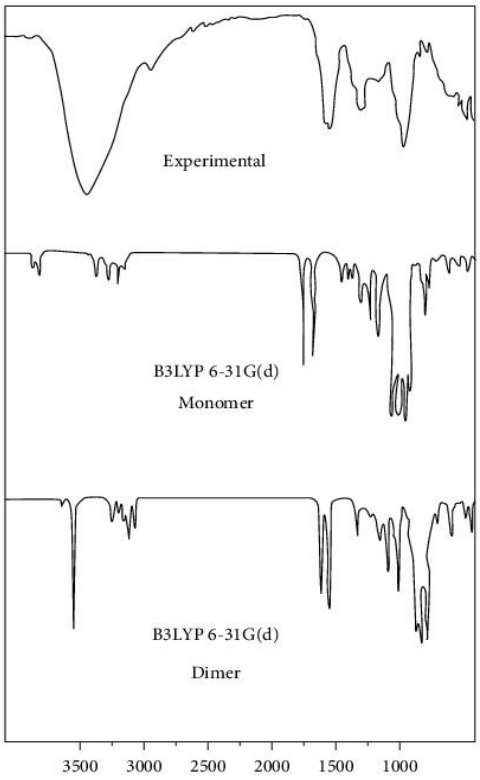

FIGURE 7: Experimental IR spectrum (top), theoretical B3LYP 6-31G(d) strictosidine monomer (middle), and theoretical B3LYP 6-31G(d) (bottom) strictosidine dimer IR spectra, in cm^{-1}.

by using the B3LYP/6-31G(d) level. A total of 210 normal vibration modes were obtained but were compared with the experimental spectrum only between 400 and 4000 cm^{-1} (Table 5).

Modes between 3021 and 3640 cm^{-1} were related to the following vibrations: the strong O-H stretching of the glycoside portion; the H-C stretching of the aromatic ring; the H-C stretching of dihydropyran ring; the N4-H1 and N1-H1 stretching; and the H3-C3, H5-C5, H6-C6, H14-C14, and H15-C15 stretching. The region from 2900 to 3000 cm^{-1} showed a strong band at 2932 cm^{-1} that was assigned to the symmetric CH_2 stretching in C6.

The region between 1060 and 1700 cm^{-1} was related to the following vibrations: the C=O stretching of C22, C=C stretching modes of C16=C17, the H1-N1 bending mode, and the CH_2 scissoring modes (C6′ and C23) in 1400–1690 cm^{-1}; the H-C bending of the glycoside portion and the dihydropyran ring in 1250–1399 cm^{-1}; the O-C stretching of the glycoside portion between 1060 and 1211 cm^{-1}.

The region between 600 and 1030 cm^{-1} was related to the C-C stretching of C10 and C11, the C-O and C-C stretching of the glycosidic moiety, the H-N bending of the N4 position (band at 891 cm^{-1} was noteworthy), the out-of-plane mode of C22 (at 763 cm^{-1}), and the torsion modes of the entire structure.

The large differences from 3500 to 4000 cm^{-1} are related to the H-N1 and O-H stretching, which are indicative that the interactions between strictosidine molecules occur between the tryptophanic and glycosidic regions. These interactions make sense based on the electrostatic potential map (Figure 6), which showed greater polarization of these two regions relative to the entire molecule. The optimized geometry of a strictosidine dimer (Figure 8) showed stabilization due to the existence of intermolecular hydrogen bonds (N1-H1---O-C4′ and C4′-OH---O2=C22) and the values assigned to the stretching of O-H (3556.00 cm^{-1}) and H-N1 (3493.18 cm^{-1}) groups are closer to the experimental ones (3430 and 3390 cm^{-1}). The value assigned to the stretching of carboline group in position C22 (1690 cm^{-1}) shows to be closer to the experimental one in the dimer too (1767 cm^{-1} to the monomer and 1716 cm^{-1} to the dimer form), implying that the interaction between the carbonyl and OH is plausible and decreasing the stretching frequency oscillator related to C=O bond. These interactions directly influenced the infrared spectrum by decreasing the stretching frequency oscillator related to these bonds, causing reduction in the wavelengths (see Figure 8) and in the RMSD values. For the monomer, the RMSD is 84.40 cm^{-1}; for the dimer, the value is 46.41. Applying the empirical scaling factor of 0.9613, the RMSD values feature a visible reduction, 66.33 cm^{-1} for monomer and 30.66 cm^{-1} for dimer.

4. Conclusion

The strictosidine alkaloid, which was isolated from *Strychnos amazonica*, was comprehensively characterized. The interatomic distances and angles proved to be plausible compared to the X-ray data for similar molecules. The similarity between the theoretical and experimental coupling constants values reveals that the theoretical hydrogen dihedral angles of the C14-C15-C20-C21-C19 positions are plausible, showing that the modeled structure justifies the experimental NMR data. The UV analysis was able to explain the similarity between the UV spectra of strictosidine and related indole alkaloids, showing that the transitions involving the indole moiety are energetically more significant and such characteristic can be used as a "fingerprint" for detecting indole alkaloids. The HOMO-LUMO gap is directly related to the reactivity of a compound reflecting the amount of important properties such as chemical hardness, electrophilicity, nucleophilicity index, and electronegativity. Strictosidine theoretically appears to be a nucleophile and electrophile that in addition to its polarizability behaves as a soft molecule. This indicates low charge states and faster reactions, which makes strictosidine a versatile molecule, justifying its high reactivity and its role as a precursor of indole alkaloids. The comparative IR studies revealed that interactions of strictosidine dimers (between the tryptophanic and glycosidic regions) influenced the infrared spectrum by decreasing the stretching frequency oscillator of the groups which forms hydrogen

Table 5: Experimental and calculated wavenumbers* (cm^{-1}) and assignments for strictosidine.

IR solid		B3LYP 6-31G(d)				
		Monomer		Dimer		
Exp.	IR intensity	Calculated	IR intensity	Calculated	IR intensity	Assignment (PED > 5%)
		3767	30	3633	62	Stre. OH (96%)
		3732	30	3602	6	Stre. OH (95%)
3430	42	3731	49	3556	225	Stre. OH (96%)
3411	44	3724	44	3535	64	Stre. OH (97%)
3390	43	3656	44	3493	47	Stre. N1-H1 (88%) + tors. H1-N1-C2-C13 (11%)
3382	58	3488	0.27	3475	2.49	Stre. N4-H4 (88%) + bend H4-N4-C5 (11%)
3320	51	3260	4	3260	5	Stre. C18-H18 (70%) + stre. C19-H19 (26%)
3211	20	3246	3	3239	12	Stre. C17-H17 (99%)
		3205	38	3183	22	Stre. C9-H9 (36%) + stre. C10-H10 (39%) + stre. C12-H12 (10%)
3180	17	3193	39	3190	28	Stre. C9-H9 (21%) + stre. C10-H10 (16%) + stre. C11-H11 (30%) + C12-H12 (23%)
3152	9	3183	3	3173	2	Stre. C9-H9 (12%) + stre. C10-H10 (24%) + stre. C11-H11 (32%) + stre. C12-H12 (13%)
3150	25	3176	19	3139	1	Stre. sim. C23-H23 (22%) + stre. sim. C23-H23 (19%) + stre. ass. C23-H23 (24%) + stre. C23-H23 (19%)
3140	22	3176	2	3152	14	Stre. C9-H9 (12%) + stre. C10-H10 (17%) + stre. C11-H11 (43%)
		3175	14	3140	7	Stre. C19-C18 (41%) + stre. sim. C18-H18 (25%) + stre. C19-H19 (18%)
3129	12	3161	2	3125	17	Stre. C9-H19 (66%) + stre. sim. C18-H18 (26%)
3105	10	3144	23	3122	7	Stre. C23-H23 ass. (92%)
3100	11	3103	35	3104	20	Stre. C6′-H6′ (91%)
		3102	35	3082	8	Stre. C5-H5 (47%) + stre. C14-H14 (33%)
		3093	25	3075	28	Stre. C14-H14 (74%)
		3076	10	3072	27	Stre. C15-H15 (85%) + stre. C3-H3 (11%)
		3071	44	3069	28	Stre. sim. C23-H23 (72%)
		3070	2	3063	44	Stre. C3-H3 (57%) + stre. C15-H15 (12%)
		3061	42.72	3061	1	Stre. C5-H5 (86%)
		3060	44	3052	54	Stre. C21-H21 (60%)
		3052	6	3050	48	Stre. C14-H14 (65%)
		3041	19	3042	14	Stre. ass. C6-H6 (77%)
		3040	110	3033	13	Stre. C1′-H1′ (77%)
3020	15	3032	13	3032	28	Stre. C4′-H4′ (62%)
		3017	6	3011	37	Stre. C20-H20 (94%)
		3016	2	3008	5	Stre. C2-H2 (44%) + stre. C5-H5 (46%)
		3013	12	3007	3	Stre. C2′-H2′ (31%) + stre. C4′-H4′ (20%) + stre. C5′-H5′ (35%)
2931	26	2999	50	2997	4	Stre. C6-H6 ass. (71%)
2929	23	2989	1	2992	8	Stre. C3′-H3′ (63%) + stre. C6′-H6′ sim. (18%)
2920	12	2985	44	2988	46	Stre. C6′-H6′ (72%)

Table 5: Continued.

IR solid		B3LYP 6-31G(d)				
		Monomer		Dimer		
Exp.	IR intensity	Calculated	IR intensity	Calculated	IR intensity	Assignment (PED > 5%)
1690	62	1767	321	1716	308	Stre. C22=O2 (73%)
1628	41	1694	263	1691	272	Stre. C16=C17 (65%) + bend H17-C17-O3 (12%)
1586	7	1619	2	1591	1.5	Stre. (entire indole portion) (33%)
1527	5	1537	3.5	1519	3.6	Stre. C9=C10 (12%) + bend H10-C10 (20%) + bend H1-N1 (11%)
		1531	1.2	1497	4	Bend (scissoring) H6′-C6′ (80%)
		1527	9	1496	7	Bend (scissoring) C23-H23 (63%)
1400	20	1418	32	1415	11	Stre. C15-C16 (16%) + bend H17-C17-O3 (27%)
1399	25	1413	4	1413	4	Bend H-C entire indole portion
1377		1399	6	1395	9	Bend H21-C21 (14%) + bend H5′-C5′ (13%) + tors. H5′-C5′-O5-C1′ (10%) + tors. H4′-C4′-OH (16%)
1365	12	1386	3	1375	8	Tors. H14-C14-C3-N4 (11%) + tors. H15-C15-C14-C3 (11%) + H5-C5-N4-C3 (10%)
1360	10	1381	4	1363	1	Bend H1′-C1′ (16%) + bend H4′-C4′ (15%) + tors. C5′-H5′ (19%)
1350	11	1378	32	1362	19	Bend H3′-C3′ (11%) + bend H21-C21 (16%) + bend H1′-C1′ (14%)
1344	18	1367	47	1345	19	Bend H18-C18-C19 (32%) + bend H2′-C2′ (12%)
1328	13	1348	59	1340	52	Bend H17-C17-O3 (15%) + bend H15-C15 (10%)
		1345	66	1346	29	Bend H17-C17 (12%) + tors. H15-C15-C14-C20 (10%)
1303	30	1342	53	1342	41	Bend H1′-C1′ (22%) + tors. H5′-C5′-O5-C1′ (25%)
		1338	65	1327	9	Bend H20-C20 (15%)
1300	33	1326	22	1320	31	Stre. C13-N1-C2 (29%)
1297	25	1312	7	1301	18	Bend H20-C20 (16%) + bend H3-C3 (10%) + tors. H14-C14-C3-N4 (16%)
1250	22	1267	23	1260	17	Bend H-C entire structure
		1257	40	1243	40	Bend O-H (5′) (18%) + bend H4′-C4′ (10%)
1211	13	1253	117	1252	16	Stre. C17-O3 (22%) + H15-C15 (13%)
		1157	137	1132	41	Stre. O-C2′ (12%) + stre. O-C3′ (22%) + stre. O4-C21 (13%)

Table 5: Continued.

Exp.	IR solid IR intensity	B3LYP 6-31G(d) Monomer Calculated	Monomer IR intensity	Dimer Calculated	Dimer IR intensity	Assignment (PED > 5%)
		1136	191	1136	26	Stre. C2′-O (28%) + stre. C3′-O (19%)
		1130	63	1130	42	Stre. O1-C23 (18%) + O3-C1′ (18%)
		1128	225	1128	152	Stre. C5′-C6′ (12%) + stre. O1-C23 (13%)
		1123	13	1121	67	Stre. C5′-C4′ (20%) + tors. H6-C6-C5-N4 (15%)
		1118	43	1119	53	Stre. C5′-C4′ (50%)
		1109	112	1190	120	Stre. O-C6′ (17%)
		1102	138	1103	18	Stre. O-C6′ (37%)
1073	30	1100	33	1100	66	Stre. C15-C16 (13%)
1069	38	1090	21	1067	294	Stre. O-C4′ (13%)
1060	40	1079	55	1079	99	Stre. O-C6′ (27%)
		1070	230	1046	51	Stre. O5-C1′ (10%)
		1058	33	1042	88	Tors. H19-C19-C18-C20 (53%)
		1046	10	1036	77	Bend H19-C19-C18 (13%)
		1041	12	1030	196	Stre. C10-C11 (15%)
1028	30	1035	33	1027	16	Bend (rocking) H18-C18 (11%)
1020		1028	176	1025	53	Stre. C1′-O5 (32%) + stre. C2′-C3′ (10%) + stre. C5′-C6′ (11%)
		989	14	978	23	Stre. C5-C6 (30%)
960	12	988	5	972	14	Stre. sim. C22-O1-C23 (27%)
		896	29	883	93	Stre. O5-C5′ (13%) + tors. H6′-C6′-C5′-C4′ (18%)
891	7	894	10	893	11	Bend H4-N4 (22%)
		867	10	868	11	Bend H4-N4 (12%)
		856	0.6	856	0.7	Tors. H-C (entire aromatic ring) (59%)
		844	32	843	16	Stre. C3-C14 (13%) + stre. C15-C16 (11%) + tors. H4-N4-C5-C6 (11%)
763	10	764	30	764	4	Out O1-C22-O2-C16 (63%)
720	11	755	38	754	62	Tors. sim. H-C-C (entire aromatic ring) (40%)
700	11	746	14	739	33	Tors. entire indole portion
		619	9	617	5	Tors. entire structure
607	12	606	1.5	606	3	Bend C17-O3-C21 (15%)
		603	12	601	2	Tors. entire structure

*The calculated wavenumbers values in the table are unscaled.

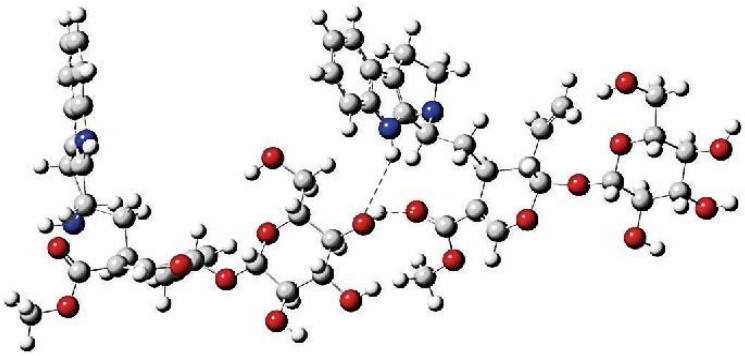

Figure 8: The strictosidine dimer, featuring hydrogen bonds (dashed line) between the tryptophanic and glycosidic moieties.

bonds and revealed several characteristic vibrations that may be used as a diagnostic tool for other indole alkaloids, simplifying their identification and structural characterization. The NBO calculations showed that the strongest stabilization energies for strictosidine involved hyperconjugative interactions in the indolic portion (aromatic and pentacyclic rings) and in the dihydropyran portion, justifying the few fragmentation modes for its protonated molecule observed in the MS^n analysis, and these modes may contribute to the further characterization of strictosidine analogues and derivatives.

Conflict of Interests

The authors declare that there is no conflict of interests regarding the publication of this paper.

Acknowledgments

The authors thank Dr. Doriane Picanço of the Federal University of Amazonas for the support with the botanical identification, Professor Dr. Michel Rossman for the X-ray data for loganin, Dr. Elaine H. T. Oliveira for the spelling support, and Capes and FINEP for the financial support.

References

[1] M. Frederick, M.-P. Hayette, M. Tits, P. De Mol, and L. Angenot, "In vitro activities of *Strychnos* alkaloids and extracts against *Plasmodium falciparum*," *Antimicrobial Agents and Chemotherapy*, vol. 43, no. 9, pp. 2328–2331, 1999.

[2] P. Rasoanaivo, S. Ratsimamanga-Urverg, R. Milijaona et al., "In vitro and in vivo chloroquine-potentiating action of *Strychnos myrtoides* alkaloids against chloroquine-resistant strains of *Plasmodium malaria*," *Planta Medica*, vol. 60, no. 1, pp. 13–16, 1994.

[3] R. Bassleer, M. C. Depauw-Gillet, B. Massart et al., "Effets de trois alcaloïdes extraits du *Strychnos usambarensis* sur des cellules cancéreuses en culture," *Planta Medica*, vol. 45, pp. 123–126, 1982.

[4] C. Caron, M. J. Hoizey, L. Le Men-Olivier et al., "Antimicrobial and antifungal activities of quasi-dimeric and related alkaloids," *Planta Medica*, vol. 54, no. 5, pp. 409–412, 1988.

[5] J. Quetin-Leclercq, A. Favel, G. Balansard, P. Regli, and L. Angenot, "Screening for in vitro antifungal activities of some indole alkaloids," *Planta Medica*, vol. 61, no. 5, pp. 475–477, 1995.

[6] C. L. C. de Medeiros, G. Thomas, and R. Mukherjee, "The source of Ca^{2+} for the spasmolytic actions of longicaudatine, a bisindole alkaloid isolated from Strychnos trinervis (Vell.) Mart. (Loganiaceae)," *Phytotherapy Research*, vol. 5, no. 1, pp. 24–28, 1991.

[7] V. K. Kapoor, S. K. Sharma, K. K. Chagti, and M. Singh, "Synthesis and hypotensive activity of diaboline," *Indian Journal of Chemistry B: Organic Chemistry Included Medicinal. Chemistry*, vol. 27, pp. 641–644, 1988.

[8] M. Tits, J. Damas, J. Quetin-Leclercq, and L. Angenot, "From ethnobotanical uses of *Strychnos henningsii* to antiinflammatories, analgesics and antispasmodics," *Journal of Ethnopharmacology*, vol. 34, no. 2-3, pp. 261–267, 1991.

[9] C. L. Cardoso, D. H. S. Silva, M. C. M. Young, I. Castro-Gamboa, and V. S. Bolzani, "Indole monoterpene alkaloids from *Chimarrhis turbinata* DC Prodr.: a contribution to the chemotaxonomic studies of the Rubiaceae family," *Revista Brasileira de Farmacognosia*, vol. 18, no. 1, pp. 26–29, 2008.

[10] L. F. Szabó, "Rigorous biogenetic network for a group of indole alkaloids derived from strictosidine," *Molecules*, vol. 13, no. 8, pp. 1875–1896, 2008.

[11] X. Huang, Y. Li, Y. Su, X. Chai, and S. Yan, "Monoterpene indole alkaloids and monoterpene diglycosides from the roots of *Triosteum pinnatifidum*," *Phytochemistry Letters*, vol. 7, no. 1, pp. 30–34, 2014.

[12] Y.-J. Xu, K. Foubert, L. Dhooghe et al., "Chromatographic profiling and identification of two new iridoid-indole alkaloids by UPLC-MS and HPLC-SPE-NMR analysis of an antimalarial extract from *Nauclea pobeguinii*," *Phytochemistry Letters*, vol. 5, no. 2, pp. 316–319, 2012.

[13] M. Tits, V. Brandt, J.-N. Wauters, C. Delaude, G. Llabres, and L. Angenot, "Glucoindole alkaloids from stem bark of *Strychnos mellodora*," *Planta Medica*, vol. 62, no. 1, pp. 73–74, 1996.

[14] G. N. Smith, "Strictosidine: a key intermediate in the biogenesis of indole alkaloids," *Chemical Communications*, no. 15, pp. 912–914, 1968.

[15] R. Verpoorte, R. van der Heijden, and P. R. H. Moreno, *The Alkaloids*, vol. 49, Academic Press, San Diego, Calif, USA, 1997.

[16] T. M. Kutchan, "Strictosidine: from alkaloid to enzyme to gene," *Phytochemistry*, vol. 32, no. 3, pp. 493–506, 1993.

[17] A. R. Battersby, A. R. Burnett, E. S. Hall, and P. G. Parsons, "The rearrangement process in indole alkaloid biosynthesis," *Chemical Communications*, vol. 24, pp. 1582–1583, 1968.

[18] A. R. Battersby, A. R. Burnett, and P. G. Persons, "Alkaloid biosynthesis. Part XV. Partial synthesis and isolation of vincoside and isovincoside: biosynthesis of the three major classes of indole alkaloids from vincoside," *Journal of the Chemical Society C: Organic*, vol. 20, no. 8, pp. 1193–1200, 1969.

[19] Á. Patthy-Lukáts, L. Károlyházy, L. F. Szabó, and B. Podányi, "First direct and detailed stereochemical analysis of strictosidine," *Journal of Natural Products*, vol. 60, no. 2, pp. 69–75, 1997.

[20] Y. Yamazaki, A. Urano, H. Sudo et al., "Metabolite profiling of alkaloids and strictosidine synthase activity in camptothecin producing plants," *Phytochemistry*, vol. 62, no. 3, pp. 461–470, 2003.

[21] M. J. Frisch, G. W. Trucks, H. B. Schlegel, and G. E. Scuseriaet, *Gaussian 03 Revision, B.05*, Gaussian, Pittsburgh, Pa, USA, 2003.

[22] C. Timmons and P. Wipf, "Density functional theory calculation of ^{13}C NMR shifts of diazaphenanthrene alkaloids: reinvestigation of the structure of samoquasine A," *Journal of Organic Chemistry*, vol. 73, no. 22, pp. 9168–9170, 2008.

[23] J. A. Dobado, N. Benkadour, S. Melchor, and D. Portal, "Structure and theoretical NMR chemical shifts of modified cyclodextrins," *Journal of Molecular Structure: THEOCHEM*, vol. 672, no. 1–3, pp. 127–132, 2004.

[24] R. Dennington, T. Keith, and J. Millam, *Gaussview Version 5*, Semichem, Shawnee Missions, Kan, USA, 2009.

[25] M. H. Jamroz, *Vibrational Energy Distribution Analysis, VEDA 4 Computer Program*, Warsaw, Poland, 2004.

[26] L. Dupont and O. Dideberg, "Structure cristalline et moleulaire d'un nouvel alcaloide indolique, l'akagerine," *Acta Crystallographica B*, vol. 31, pp. 2378–2383, 1975.

[27] P. Molina, P. M. Fresneda, M. A. Sanz, C. Foces-Foces, and M. C. R. de Arellano, "Investigative studies on the formation of the imidazo [4′,5′:3,4] pyrido [2,3-b]indole ring: formal synthesis of the alkaloids grossularines-1 and 2. X-Ray crystal structures of 5-indol-3-yl-imidazole and bisimidazocarbazole derivatives," *Tetrahedron*, vol. 54, pp. 9623–9638, 1998.

[28] S. C. Nyburg, P. Y. Siew, G. N. Saunders, J. R. Purdy, and S. McLean, "X-ray crystal structure analysis of a bisepoxide derived from secologanin: the structure and absolute configuration," *Canadian Journal of Chemistry*, vol. 61, no. 2, pp. 282–283, 1983.

[29] P. J. Lentz and M. G. Rossmann, "The crystal structure of loganin penta-acetate monomethyl ether bromide," *Journal of the Chemical Society D: Chemical Communications*, no. 21, p. 1269, 1969.

[30] C. R. Hutchinson, A. H. Heckendorf, J. L. Straugh, P. E. Daddona, and D. E. Cane, "Biosynthesis of camptothecin. 3. Definition of strictosamide as the penultimate biosynthetic precursor assisted by carbon-13 and deuterium NMR spectroscopy," *Journal of the American Chemical Society*, vol. 101, pp. 3358–3369, 1979.

[31] A. W. Sangster and K. L. Stuart, "Ultraviolet spectra of alkaloids," *Chemical Reviews*, vol. 65, no. 1, pp. 69–130, 1965.

[32] N. Özdemir, S. Dayan, O. Dayan, M. Dinçer, and N. Kalaycıoglu, "Experimental and molecular modeling investigation of (*E*)-*N*-{2-[(2-hydroxybenzylidene)amino]phenyl} benzenesulfonamide," *Journal Molecular Physics*, vol. 111, no. 6, pp. 707–723, 2013.

[33] E. I. Paulraj and S. Muthu, "Molecular structure analysis and spectroscopic characterization of 5-ethyl-5-phenyl-1,3-diazinane-4,6-dione with experimental (FT-IR and FT-Raman) techniques and quantum chemical calculations," *Spectrochimica Acta—Part A: Molecular and Biomolecular Spectroscopy*, vol. 106, pp. 310–320, 2013.

[34] R. G. Parr and W. Yang, *Functional Theory of Atoms and Molecules*, Oxford University Press, New York, NY, USA, 1989.

[35] R. G. Parr, L. V. Szentpály, and S. Liu, "Electrophilicity index," *Journal of the American Chemical Society*, vol. 121, no. 9, pp. 1922–1924, 1999.

[36] L. R. Domingo and P. Pérez, "The nucleophilicity N index in organic chemistry," *Organic and Biomolecular Chemistry*, vol. 9, no. 20, pp. 7168–7175, 2011.

[37] L. R. Domingo, P. Perez, and E. Chamorro.

[38] C. Stévigny, J.-L. H. Jiwan, R. Rozenberg, E. De Hoffmann, and J. Quetin-Leclercq, "Key fragmentation patterns of aporphine alkaloids by electrospray ionization with multistage mass spectrometry," *Rapid Communications in Mass Spectrometry*, vol. 18, no. 5, pp. 523–528, 2004.

[39] E. R. Davidson, *Reduced Density Matrices in Quantum Chemistry*, Academic Press, New York, NY, USA, 1976.

[40] J. E. Carpenter and F. Weinhold, "Analysis of the geometry of the hydroxymethyl radical by the 'different hybrids for different spins' natural bond orbital procedure," *Journal of Molecular Structure: THEOCHEM*, vol. 169, pp. 41–62, 1988.

[41] B. C Carlson, J. M. Keller, and B. C Carlson, "Orthogonalization Procedures and the Localization of Wannier Functions," *Physical Reviews*, vol. 105, p. 102, 1957.

[42] A. E. Reed, R. B. Weinstock, and F. Weinhold, "Natural population analysis," *The Journal of Chemical Physics*, vol. 83, no. 2, pp. 735–746, 1985.

[43] R. S. Mulliken, "Electronic population analysis on LCAO-MO molecular wave functions," *Journal of Chemical Physics*, vol. 23, pp. 1833–1841, 1955.

[44] R. S. Mulliken and W. C. Ermler, *Diatomic Molecules: Results of Ab Initio Calculations*, Academic Press, New York, NY, USA, 1977.

[45] J. K. Badenhoop and F. Weinhold, "Natural bond orbital analysis of steric interactions," *Journal of Chemical Physics*, vol. 107, no. 14, pp. 5406–5421, 1997.

[46] J. P. Foster and F. Weinhold, "Natural hybrid orbitals," *Journal of the American Chemical Society*, vol. 102, no. 24, pp. 7211–7218, 1980.

[47] A. E. Reed and F. Weinhold, "Natural bond orbital analysis of near-Hartree-Fock water dimer," *The Journal of Chemical Physics*, vol. 78, no. 6, pp. 4066–4073, 1983.

[48] V. Deval, A. Kumar, V. Gupta et al., "Molecular structure (monomeric and dimeric) and hydrogen bonds in 5-benzyl 2-thiohydantoin studied by FT-IR and FT-Raman spectroscopy and DFT calculations," *Spectrochimica Acta—Part A: Molecular and Biomolecular Spectroscopy*, vol. 132, pp. 15–26, 2014.

[49] J. S. Murray and K. Sen, *Molecular Electrostatic Potentials Concepts and Applications*, Elsevier Science, Amsterdam, The Netherlands, 1996.

7. Considerações finais e trabalhos futuros

O estudo teórico através de uma abordagem DFT de moléculas de valor farmacológico é de suma importância para o entendimento das suas propriedades químicas, físicas e quânticas, ajudando na compreensão da forma de atuação e performance biológica das mesmas. Este trabalho visou o estudo alcaloides strictosidina, stricnobrasilina, 12-hidroxi-10,11-dimetoxiestricnobrasilina, liriodenina, cantinona e 7-metoxi-cantinona, isolados em trabalhos anteriores e possuidores de propriedades biológicas características. As estruturas otimizadas por meio de cálculos DFT-B3LYP 6-311G (2d,p) foram comparadas com dados de cristalografia de raio x de estruturas similares encontradas na literatura mostrando similaridade. Dados teóricos de espectroscopia UV-Vis, FT-IR e RMN das estruturas em diferentes conformações e interações (formas monoméricas e dímeros) foram confrontados com dados obtidos experimentalmente com o intuito de entender o comportamento espectral, entendendo assim as propriedades físico-químicas que podem influenciar nas propriedades reacionais e por consequência nas propriedades farmacológicas. Foi possível constatar a formação de dímeros para algumas das moléculas estudadas, formação de ligações de hidrogênio (intra e intermoleculares) que permitem maior estabilização, além da realização de cálculos de docking molecular, capazes de justificar as atividades biológicas que as moléculas em estudo apresentaram. De uma maneira bem ampla, a química teórica tem se consolidado como uma importante ferramenta para o estudo de moléculas bioativas e de interesse farmacológico. Nesse contexto, os resultados obtidos mostraram que abordagem teórica por DFT e docking molecular são técnicas indispensáveis para obtenção dos objetivos que foram propostos.

Concernente às pesquisas em andamento, convém informar que dois outros artigos, dentro da mesma linha de estudo, acerca dos alcaloides annomontina e *N*-hidroxiannomontina (isolados de *Annona foetida*) e do peltatol 4-nerolidilcatecol (isolado de *Piper peltatum*), em nível DFT, já foram submetidos nos periódicos Journal of Molecular Structure e Structural Chemistry. Ambos os artigos discorrem sobre as propriedades quânticas, espectroscópicas, estruturais e biológicas das estruturas mencionadas acima, usando abordagem teórica DFT–B3LYP 6-311G (2d,p).

Parcerias feitas com pesquisadores da Índia, Tunísia e Argentina acerca de estudos teóricos e cálculos de propriedades estruturais e espectroscópicas de alcaloides obtidos sinteticamente estão em andamento, com prazo para publicação ainda este ano . Semelhantemente, estudos teóricos à cerca de alcaloides indolo monoterpênicos isolados de *Strychnos amazônica* (obtidos no período do mestrado) e de alcaloides aporfínicos isolados de plantas do gênero Annonaceae também estão em andamento, com previsão para submissão para o corrente ano.

8. Bibliografia

Abreu, H.A. Estudos de sistemas químicos aplicando-se a teoria de funcional de densidade. Tese de doutorado, Universidade Federal de Minas Gerais, 2004.

Alcácer, L.; Introdução a química quântica e computacional, IST Press, Portugal, 2007.

Armikia, V., Heirinch, M., Alkaloids as lead drugs-A predictive structural and biodiversity-based analysis, 2014, Phytochemistry Letters, 10, xlviii–liii

Barreiro, E.J. , Produtos naturais bioativos de origem vegetal e o desenvolvimento de fármacos, Quím. Nova, 1990, 13, p. 29-39.

Barreiro, E. Sobre a química dos remédios, fármacos e medicamentos, Cadernos temáticos de química nova na escola", 2001 3, 4-9

Brandão, H.N; David, J.P; Couto R.D; Nascimento, J.A.P; David, J.M. "Química e farmacologia de quimioterápicso antineoplásicos derivados de plantas", Quim. Nova, 2010, Vol. 33, No. 6, 1359-1369

Bennett, A.E., *The* history of the introduction of curare into medicine. 1968 Anesth. Analg. 47, 484–492.

Biocca, E. Pesquisa sobre o método de preparação do curare pelos índios, Revista do Museu Paulista 1954, N.S., 8, 164-226

Bisset, N.G., "War and hunting poisons of the New World.Part 1.Notes on the early history of curare", J. Ethnopharmacol. 1992 36, 1–26.

Caron, C., Hoizey, M.J., Men-Olivier, L., Massiot, G., Zeches, M.,Choisy, C., Le Magrex, E., Verpoorte, R.,. Antimicrobial and antifungal activities of quasi-dimeric and related alkaloids. 1988 Planta Med., 54, 409–412.

Costa R A, Pinheiro M L B, Oliveira K M T, Barison A, Salomé K S, Iank J R, Silva NG, Cabral TS, Costa EV. Structural, vibrational, and electronic properties of the glucoalkaloid strictosidine: a combined experimental and theoretical study. JChem ID 1752429 (2016). https://doi.org/10.1155/2016/1752429

Costa RA, Pitt PO, Pinheiro MLB, Oliveira KMT, Barison A, Salomé KS, Costa EV Spectroscopic investigation, vibrational assignments, HOMO-LUMO, NBO, MEP analysis and molecular docking studies of oxoaporphine alkaloid liriodenine. Spectrochim Acta A, 2017b 174:94–104

Costa, R.A., Oliveira, K.M.T., de Cássia Saraiva Nunomura, R. et al**.** Quantum chemical properties investigation and molecular docking analysis with DNA topoisomerase II of β-carboline indole alkaloids from *Simaba guianensis*: a combined experimental and theoretical DFT study. Struc Chem, 2018, 29: 299:314.

Duarte, H. A.; Carvalho, S.; Paniago, E.B.; De Almeida; W. B.; Interaction of N-hydroxyacetamide with Vanadate. A Density Functional Study J. Inorg. Biochem. 1998,72: 71-77.

Duarte, H. A.; Salahub,D. R.; Haslett, T.; Moskovits, M.; Fe(N2)n (n=1-5): Structure, bonding and Vibrations from Density Functional Theory. Inorg. Chem. 1999,38, 3895.

Duarte, H. Índices de reatividade química a partir da teoria do funcional de densidade formalismo e persoectivas, Quim. Nova, 2001, 24: 501-508

Fattorusso, E; Taglialatela-Scafadi, O., Modern Alkaloids, Structure, Sinthersys and Biology. 2008, Wiley-VHC Verlag GmbH, Germany ISBN: 978-527-31521-5

Frisch MJ, Trucks GW, Schlegel HB, Scuseria GE, Robb MA, Cheeseman JR, Scalmani G, Barone V, Mennucci B, Petersson GA, Nakatsuji H, Caricato M, Li X, Hratchian HP, Izmaylov AF, Bloino J, Zheng G, Sonnenberg JL, Hada M, Ehara M, Toyota K, Fukuda R, Hasegawa J, Ishida M, Nakajima T, Honda Y, Kitao O, Nakai H, Vreven T, Montgomery Jr JA, Peralta JE, Ogliaro F, Bearpark M, Heyd JJ, Brothers E, Kudin KN, Staroverov VN, Kobayashi R, Normand J, Raghavachari K, Rendell A,

Burant JC, Iyengar SS, Tomasi J, Cossi M, Rega N, Millam JM, Klene M, Knox JE, Cross JB, Bakken V, Adamo C, Jaramillo J, Gomperts R, Stratmann RE, Yazyev O, Austin AJ, Cammi R, Pomelli C, Ochterski JW, Martin RL, Morokuma K, Zakrzewski VG, Voth GA, Salvador P, Dannenberg JJ, Dapprich S, Daniels AD, Farkas Ö, Foresman JB, Ortiz JV, Cioslowski J, Fox DJ (2009) Gaussian 09. Gaussian, Inc., Wallingford.

Haslett, T. L., Fedrigo, S.; Bosnick,K.A.; Bier, K. D.; Moskovits, M.; Duarte, H. A.; Salahub,D.; Binary Iron-Dinitrogen Compounds Synthesized by Co-Deposition of Mass-Selected Fe, Fe2, and Fe3 with N2. J. Am. Chem. Soc. 2000, 122: 6039-6044

Jamroz M (2004) Vibrational energy distribution analysis. VEDA 4 Computer Program, Poland.

Kohn, W.; Sham, L. J. Self-Consistent Equations Including Exchange and Correlation Effects Phys. Rev. 1965, 140, A1133

Kohn, W; Becke, A. D.; Parr, R. G. Density Functional Theory of Electronic Structure. 1996, J. Phys. Chem., 100, 12974

Ladeira, A. C.Q.; Alves, M. C. M.; Duarte, H. A.; Ciminelli, V. S. T.; Mechanism of anion retention from EXAFS and density functional calculations: arsenic (V) adsorbed on gibbsite Geochim. Cosmochim. Acta 2001 65: 1211-1217

Lee, C., Conformation, action, and mechanism of action of neuromuscular blocking muscle relaxants. Pharmacol 2003. Ther. 98,143–169

Lizzarga, E.; Romano, E.; Raschi, A.B.; Leyton, P.; Paipa, C.; Catalán, C.A. N.; Brándan, S.A. A structural and vibrational study of dehydrofukinone combining FTIR, FTRaman, UV–visible and NMR spectroscopies with DFT calculations, (2013) J.Mol. Struc. 1048, 331-338

Meng, X.; Zhang, H,; Mezei, M.; Cui, M. Molecular Docking: A powerful approach for structure-based drug discovery, Curr Comput Aided Drug Des. **2011**; 7(2): 146–157. PMCID:PMC3151162

Morris, G. M.; Lim-Wilby, M. Molecular Docking, Methods Mol Biol. **2008**; 443: 365-382, Springer. 10.1007/978-1-59745-177-2_19

Newman, D. J.; Cragg, G. M.; Snader, K. M. Natural products as sources of new drugs over the period 1981-2002 J. Nat. Prod. 2003 66, 1022-1037

Nocedal J, Wright SJ (1999) Numerical optimization, Springer series in operations research. Springer Verlag, Berlin

Trott, O., and Olson, A.J. AutoDock Vina: improving the speed and accuracy of docking with a new scoring function, efficient optimization, and multithreading. J Comput Chem. 2010 Jan 30;31(2):455-61. 10.1002/jcc.21334

Oliveira, M.A.; Pernaut, J-M.; Duarte, H. A.; De Almeida, W. B.; J.Phys. Chem. A 2000, 104, 8256

Ouhiri, F.C.; Verpoorte, R.; Svendsen, A.B. "*The African Strychnos Species and their Alkaloids: A review*" (1983) Journal of Ethnopharmacology., 167-223

Parr, R.; Yang, W.; Density-Functional Theory of Atoms and Molecules, Oxford University Press, New York, 1989.

Platts, J. A.; Hibbs, D. E.; Hambley, T. W.; Hall, M. D.; Calculation of the Hydrophobicity of Platinum Drugs J. Med. Chem., 2001, 44 (3), pp 472–474

Philippe, G.; Angenot, L.; Tits, M., Frédérich, M. "*About the toxicity of some Strychnos species and their alkaloids"* (2004),Toxicon 44,405–416

Pinto A.C.. "O Brasil dos viajantes e dos exploradores e a química de produtos naturais brasileira" (1995) *Quim Nova 18:* 608-615

Sievänen,E., Toušeka,J., K. J. Lunerovác, D. Marek, M. Jankovskác, R. Dvorskác, Mareka. (2010) J. Mol. Struc.,979 172–179

Szabo, A and Ostlund, N., Modern Quantum Chemistry: Introduction to Advanced Electronic Structure Theory, 1989, Mcgraw-Hill (Texas), ASIN: B01A1MSRNI

9. Anexos

9.1. Anexo 1 - Investigação das propriedades químico-quânticas e análise de docking molecular com DNA topoisomerase II de acaloides β-carbolinicos isolados de *Simaba guianensis:* um estudo experimental e teórico

Supplementary material

Quantum-chemical properties investigation and molecular docking analysis with DNA Topoisomrase II of β-carboline indole alkaloids from *Simaba guianensis*: a combined experimental and theoretical DFT study

Renyer A. Costa[1*], Kelson M.T. Oliveira[1*], Rita de Cássia Saraiva Nunomura[1], Earle Silva A. Junior[2], Maria Lucia B. Pinheiro[1], Emmanoel V. Costa[1], Andersson Barison[3]

[1]Department of Chemistry, Federal University of Amazonas (DQ-UFAM), 69077-000 Manaus, AM, Brazil

[2]Federal Institute of Science and Technology of Amazonas (IFAM), 69020-120 Manaus, AM, Brazil

[3]NMR Laboratory, Department of Chemistry, Federal University of Paraná, 80060-000 Curitiba, PR, Brazi

Parameter	9-methoxycanthin-6-one	7-methoxy-(9H-β-carbolin-1-il)-(Z)-prop-2-enoic acid	Experimental [30]
Bond length			
C1-C2	1.410	1.387	1.401
C2-N2	1.335	1.336	1.343
C4-C3	1.445	1.465	1.436
C4-C5	1.360	1.344	1.359
C5-C6	1.472	1.502	1.489
C6-N1	1.403	-	1.389
N1-C13	1.413	1.383	1.406
N1-C15	1.377	1.382	1.378
C13-C8	1.387	1.395	1.375
C8-C9	1.396	1.391	1.398
C9-C10	1.407	1.413	1.391
C10-C11	1.381	1.376	1.379
C11-C12	1.395	1.401	1.380
C12-C13	1.414	1.411	1.427
C12-C14	1.455	1.440	1.476
C14-C15	1.399	1.418	1.386
C14-C1	1.389	1.392	1.385
C9-O	1.357	1.357	-
O-CH_3	1.424	1.420	-
C6=O1	1.220	1.211	-
C6-O2	-	1.327	-

Bond angle			
C1-C2-N2	125.603	123.661	126.2
C2-N2-C3	117.247	121.091	116.9
N2-C3-C15	119.979	-	119.1
C3-C15-C14	123.859	121.069	124.7
C15-C14-C1	115.485	118.129	116.3
C15-C3-C4	115.717	120.909	117.3
C3-C4-C5	120.001	132.522	118.8
C4-C5-C6	124.262	134.256	124.1
C5-C6-N1	113.492	-	113.6
C15-N1-C13	107.424	109.476	108.3
N1-C13-C8	128.466	128.645	130.3
C13-C8-C9	116.758	117.009	-
C8-C9-C10	121.225	121.205	-
C9-C10-C11	120.899	120.876	121.3
C10-C11-C12	119.405	119.410	118.5
C12-C13-N1	108.411	108.676	108.3
C12-C14-C15	105.535	106.867	106.2

Table S1. Calculate geometrical parameters for the studied molecules

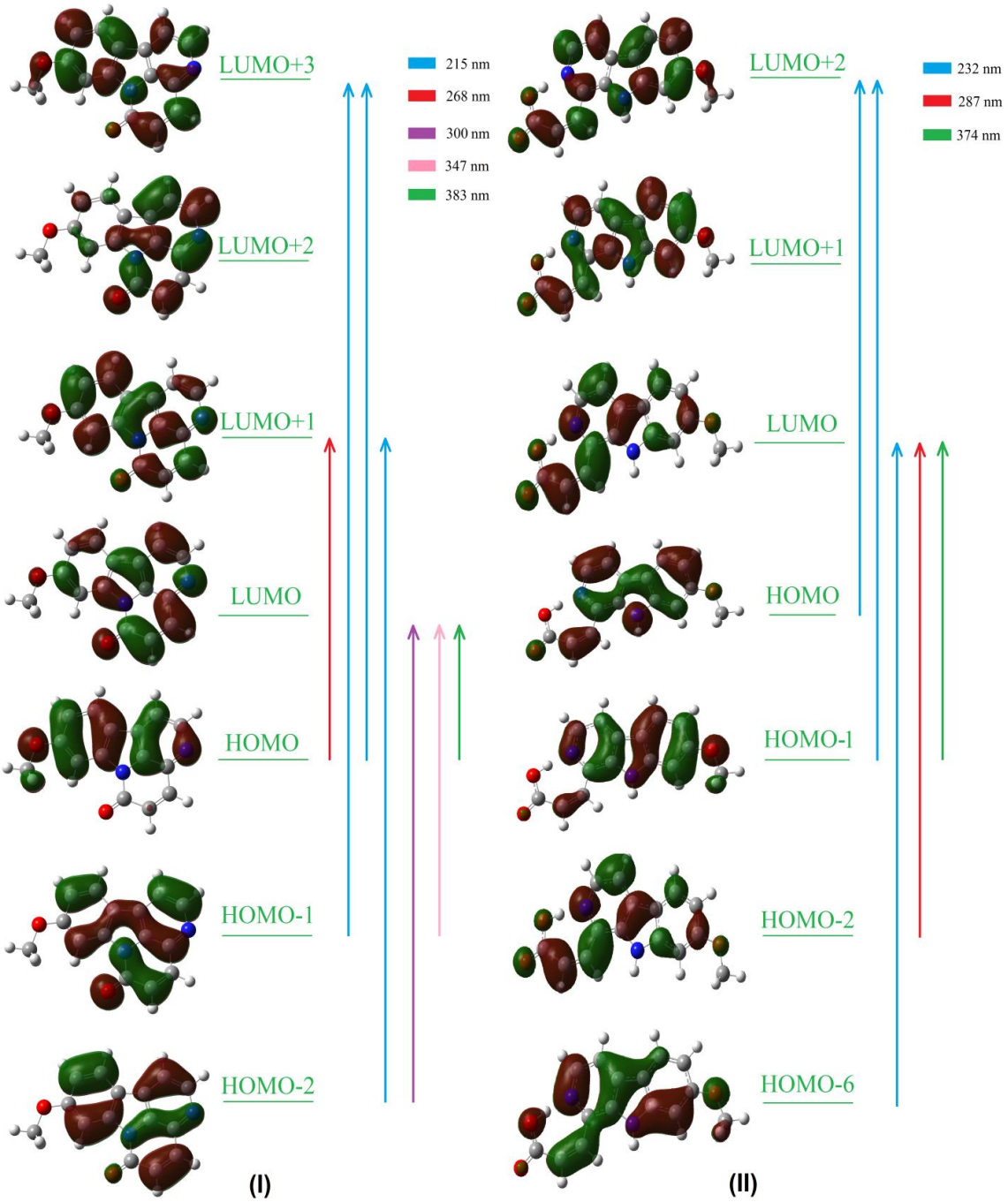

Figure S1. Electronic transitions contributions of calculated absorption wavelengths for structures (I) and (II)

Table S2 Selected second-order perturbation energies of 9-methoxycanthin-6-one.

Donor orbital (i)	Type	Acceptor orbital (j)	Type	$E_{(i)} - E_{(j)}$ a.u.	$E^{(2)}$ (Kcal/mol)
C1-C2	σ	C12-C14	σ*	1.20	6.26
C1-H1	σ	C2-N2	σ*	1.05	4.54
C2-H2	σ	N2-C3	σ*	1.02	5.58
C4-H4	σ	C6-C5	σ*	0.96	5.37
C5-H5	σ	C3-C4	σ*	1.01	5.02
C6-C5	σ	C13-N1	σ*	1.07	4.81
C8-C13	σ	C13-C12	σ*	1.25	5.17
C8-H8	σ	C13-C12	σ*	1.06	4.93
C9-C8	σ	C13-N1	σ*	1.10	6.17
C10-H10	σ	C9-C8	σ*	1.06	4.55
C11-C10	σ	C12-C14	σ*	1.21	5.13
C11-C12	σ	C13-C12	σ*	1.23	4.53
C11-C12	σ	C12-C14	σ*	1.20	4.61
C11-H11	σ	C13-C12	σ*	1.05	4.74
C12-C14	σ	C14-C1	σ*	1.22	4.67
C12-C14	σ	C14-C1	σ*	1.23	4.67
C13-C12	σ	C8-C13	σ*	1.25	4.58
C13-C12	σ	C14-C1	σ*	1.24	5.40
C13-C12	σ	N1-C6	σ*	1.07	4.74
C14-C15	σ	C11-C12	σ*	1.25	5.40
C14-C15	σ	C15-C3	σ*	1.25	5.54
C14-C1	σ	C12-C14	σ*	1.21	5.01
C14-C1	σ	C14-C15	σ*	1.26	4.62
C15-C3	σ	C14-C15	σ*	1.27	5.57
C2-N2	π	C14-C1	π*	0.33	11.86
C2-N2	π	C15-C3	π*	0.33	21.82
C5-C4	π	C15-C3	π*	0.31	11.57
C5-C4	π	C6-O	π*	0.28	22.44
C6-O	π	C5-C4	π*	0.41	4.97
C9-C8	π	C11-C10	π*	0.29	14.97
C9-C8	π	C13-C12	π*	0.28	25.41
C11-C10	π	C9-C8	π*	0.28	22.19
C11-C10	π	C13-C12	π*	0.28	16.66
C13-C12	π	C11-C10	π*	0.29	21.25
C13-C12	π	C9-C8	π*	0.28	16.45
C13-C12	π	C14-C1	π*	0.28	23.12
C14-C1	π	C13-C12	π*	0.28	12.62
C14-C1	π	C15-C3	π*	0.29	20.19
C14-C1	π	C2-N2	π*	0.26	27.21
C15-C3	π	C14-C1	π*	0.30	18.35
C15-C3	π	C2-N2	π*	0.27	16.15
C15-C3	π	C5-C4	π*	0.30	13.34
N1	LP(1)	C13-C12	π*	0.29	31.68
N1	LP(1)	C15-C3	π*	0.30	40.07
N1	LP(1)	C13-C12	π*	0.27	53.00
N2	LP(1)	C15-C3	σ*	0.92	10.32
N2	LP(1)	C1-C2	σ*	0.88	9.90
N2	LP(1)	C2-H2	σ*	0.79	4.57
O1	LP(1)	C6	σ*	1.70	14.90
O1	LP(2)	N1-C6	σ*	0.66	28.09
O1	LP(2)	C6-C5	σ*	0.70	17.30
O2	LP(1)	C9-C8	σ*	1.10	7.41

O2	LP(2)	C9-C8	π*	0.34	32.70
C9-C8	π*	C11-C10	π*	0.01	240.28
C13-C12	π*	C11-C10	π*	0.01	252.47
C2-N3	π*	C14-C1	π*	0.03	121.06
C2-N3	π*	C15-C3	π*	0.03	119.44
C6-O	π*	C5-C4	π*	0.03	53.86

Table S3 Selected second-order perturbation energies of 7-methoxy-(9H-β-carbolin-1-il)-(Z)-prop-2-enoic acid.

Donor orbital (i)	**Type**	**Acceptor orbital (j)**	**Type**	$\mathbf{E_{(i)} - E_{(j)}}$ **a.u.**	$\mathbf{E^{(2)}}$ **(Kcal/mol)**
C10-C11	σ	C12-C14	σ*	1.23	5.02
C4-H4	σ	N2-C3	σ*	1.03	5.13
C4-H4	σ	C5-C6	σ*	0.93	7.21
C5-H5	σ	C3-C4	σ*	0.97	8.54
C9-C8	σ	C13-N1	σ*	1.15	5.60
C8-C13	σ	C9-OCH_3	σ*	1.08	4.60
C8-C13	σ	C13-C12	σ*	1.25	4.92
C13-C12	σ	C14-C1	σ*	1.24	5.47
C12-C11	σ	C14-C1	σ*	1.23	4.56
C11-H11	σ	C13-C12	σ*	1.06	4.55
C14-C15	σ	C12-C11	σ*	1.23	5.38
C12-C11	σ	C12-C14	σ*	1.22	5.17
C14-C1	σ	C12-C14	σ*	1.23	4.90
C1-C2	σ	C12-C14	σ*	1.23	5.62
C2-H2	σ	N2-C3	σ*	1.03	6.06
C10-C11	π	C9-C8	π*	0.28	22.40
C10-C11	π	C13-C12	π*	0.28	14.98
C9-C8	π	C10-C11	π*	0.30	13.48
C9-C8	π	C13-C12	π*	0.29	23.75
C13-C12	π	C10-C11	π*	0.29	21.58
C13-C12	π	C9-C8	π*	0.27	15.13
C13-C12	π	C14-C15	π*	0.27	21.33
C14-C15	π	C13-C12	π*	0.28	16.65
C14-C15	π	C1-C2	π*	0.28	17.65
C14-C15	π	N2-C3	π*	0.25	30.21
C1-C2	π	C14-C15	π*	0.28	20.85
C1-C2	π	N2-C3	π*	0.25	16.99
N2-C3	π	C14-C15	π*	0.33	11.57
N2-C3	π	C1-C2	π*	0.34	23.43
N2-C3	π	C4-C5	π*	0.35	8.67
C4-C5	π	N2-C3	π*	0.27	15.20
C4-C5	π	C6-O2	π*	0.32	13.37
C6-O2	π	C4-C5	π*	0.38	6.90
N1	LP(1)	C13-C12	π*	0.30	36.67
N2	LP(1)	O1-H	σ*	0.50	58.98
N1	LP(1)	C14-C15	π*	0.29	34.78
N2	LP(1)	C15-C13	σ*	0.90	9.63
N2	LP(1)	C1-C2	σ*	0.91	8.52
O1-H	LP(1)	C6	RY	1.79	15.16
O1-H	LP(1)	C9-C8	σ*	1.11	7.35
O1-H	LP(2)	C6-O2	π*	0.32	56.25
O1-H	LP(2)	C5-C6	σ*	0.64	18.97

O1-H	LP(2)	C6-O1	σ*	0.65	30.13
O1-H	LP(2)	C9-C8	π*	0.34	33.25
O1-H	LP(3)	C6-O2	σ*	1.11	6.35
C9-C8	π*	C10-C11	π*	0.02	161.61
C13-C12	π*	C10-C11	π*	0.01	246.33
N2-C3	π*	C14-C15	π*	0.02	203.89
N2-C3	π*	C1-C2	π*	0.03	100.07
N2-C3	π*	C4-C5	π*	0.05	45.30

Table S4. Dipole moment, polarizability and hyperpolarizability data in gas phase for 7-methoxy-(9H-β-carbolin-1-il)-(Z)-prop-2-enoic acid at B3LYP 6-311G(2d,p)

Dipole, *D*	Polarizability, a.u.	Hyperpolarizability, a.u.
$\mu_x = 10.238$	$\alpha_{xx} = 363.6448$	$\beta_{xxx} = -2224.719$
$\mu_y = -1.089$	$\alpha_{xy} = 7.0274$	$\beta_{xxy} = 529.949$
$\mu_z = 0.00130$	$\alpha_{yy} = 207.3078$	$\beta_{xyy} = -12.708$
$\mu_{total} = 10.30$	$\alpha_{xz} = 0.00015$	$\beta_{yyy} = -90.608$
	$\alpha_{yz} = -0.00092$	$\beta_{xxz} = 0.08551$
	$\alpha_{zz} = 84.3149$	$\beta_{xyz} = -0.03195$
	$\alpha_{total} = 3.23208x10^{-23}$ esu	$\beta_{yyz} = 0.009482$
	$\Delta\alpha_{total} = 36.01x10^{-24}$ esu	$\beta_{xzz} = 30.7645$
		$\beta_{yzz} = -41.111$
		$\beta_{zzz} = -0.03464$
		$\beta_{total} = 19.37x10^{-30}$esu

Table S5. Dipole moment, polarizability and hyperpolarizability data in gas phase for 9methoxy-canthin-6-one at B3LYP 6-311G(2d,p)

Dipole, *D*	Polarizability, a.u.	Hyperpolarizability, a.u.
$\mu_x = 1.2472$	$\alpha_{xx} = 282.1595$	$\beta_{xxx} = -1439.91$
$\mu_y = -1.4967$	$\alpha_{xy} = 9.9961$	$\beta_{xxy} = -133.514$
$\mu_z = 0.0013$	$\alpha_{yy} = 224.4506$	$\beta_{xyy} = -66.8909$
$\mu_{total} = 1.9482$	$\alpha_{xz} = 0.00164$	$\beta_{yyy} = 195.9890$
	$\alpha_{yz} = -0.002309$	$\beta_{xxz} = 0.08690$
	$\alpha_{zz} = 79.4109$	$\beta_{xyz} = -0.023524$
	$\alpha_{total} = 3.2370x10^{-23}$ esu	$\beta_{yyz} = 0.002691$
	$\Delta\alpha_{total} = 26.9004x10^{-24}$ esu	$\beta_{xzz} = 16.8806$
		$\beta_{yzz} = 27.8745$
		$\beta_{zzz} = 0.044755$
		$\beta_{total} = 12.79x10^{-30}$esu

9.2 ANEXO 2 - Investigação das propriedades espectroscópicas, assinalamento vibracional, análises HOMO-LUMO, NBO, MEP e estudos de docking molecular do alcaloide oxoaporfínico liriodenina

Material supporting to

Spectroscopic investigation, vibrational assignments, HOMO-LUMO, NBO, MEP analysis and molecular docking studies of oxaporphine alkaloid liriodenine

Renyer A. Costa[1]*, Priscila Olliver Pitt[*], Maria Lucia B. Pinheiro[1], Kelson M.T. Oliveira[1], Andersson Barison[2], Emmanoel Vilaça Costa[1]

1-*Department of Chemistry - Federal University of Amazonas, Manaus, Amazonas, Brazil*

*+55 092 993776434 *E-mail: kelsonmota@ufam.edu.br*

2-*NMR Laboratory - Department of Chemistry - Federal University of Paraná, Paraná, Curitiba, Brazil*

Table S1. NMR data for Liriodenine

Position	^{13}C (δ)	^{1}H δ (mult., J in Hz)
1	147,9	
1a	130,2	
2	151,7	
3	103,29	7,24 (s)
3a	135,7	
3b	123,2	
4	124,21	7,82 (d, 5,3)
5	144,76	8,93 (d, 5,05)
6a	145,2	
7	182,3	
7a	131,2	
8	128,83	8,63 (dd, 8 e 1,7)
9	128,59	7,62 (m)
10	133,81	7,79 (m)
11	127,48	8,71 (d, 8)
11a	132,8	
(1-2)-OCH_2O	102,44	6,40 (s)

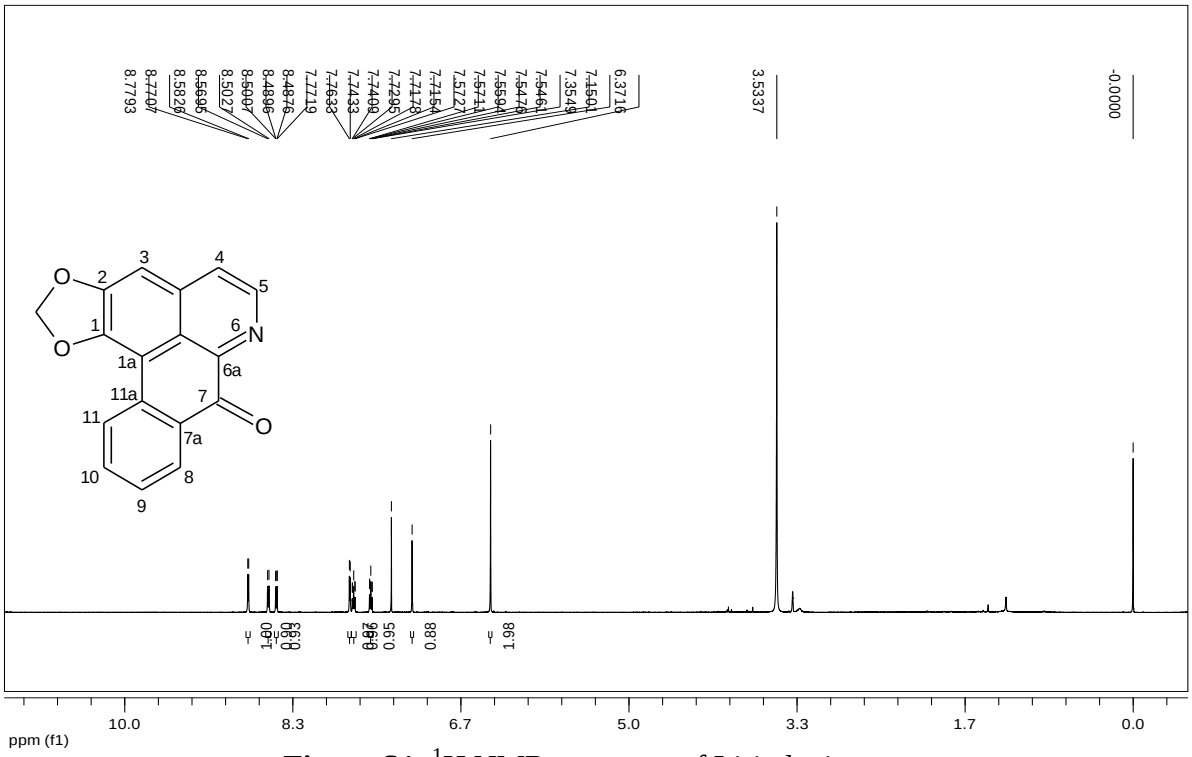

Figure S1. ^{1}H NMR spectrum of Liriodenine

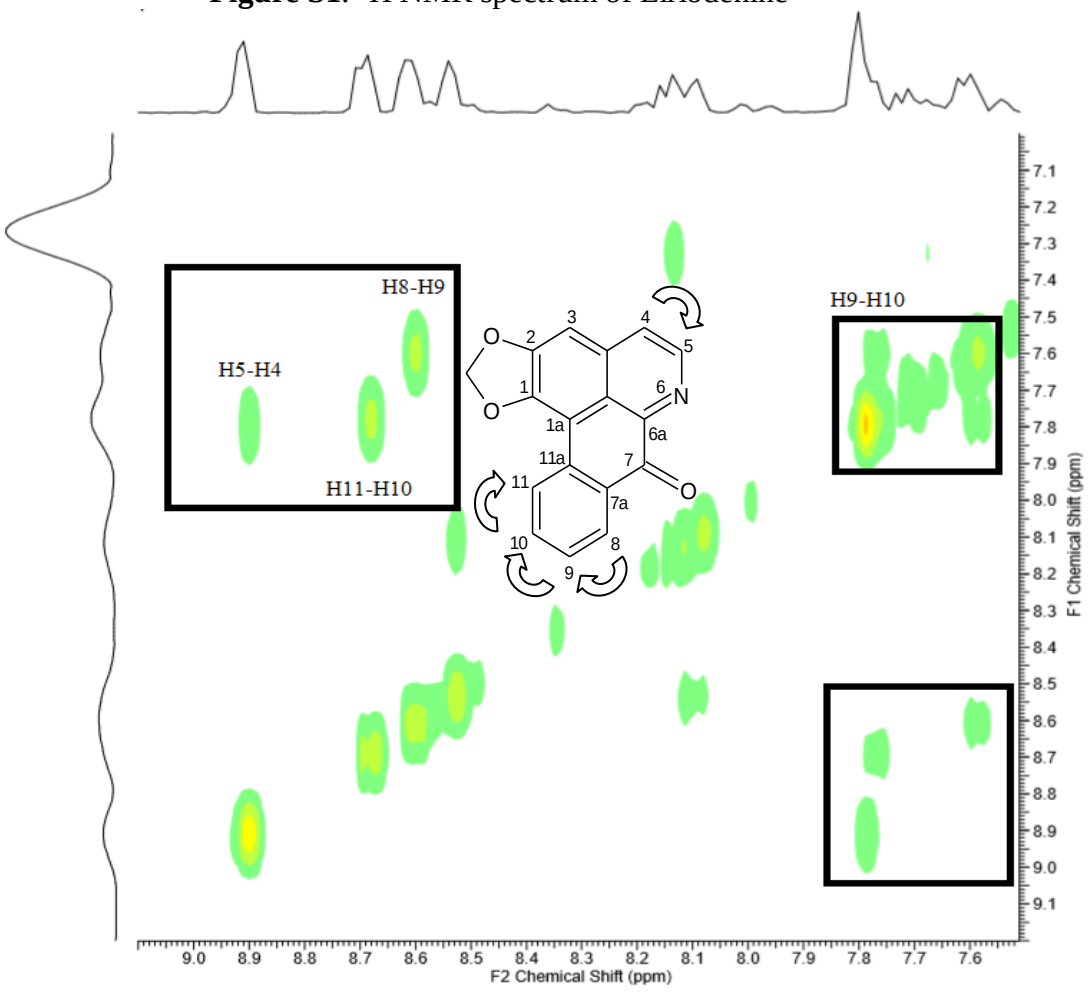

Figure S2. COSY spectrum of Liriodenine

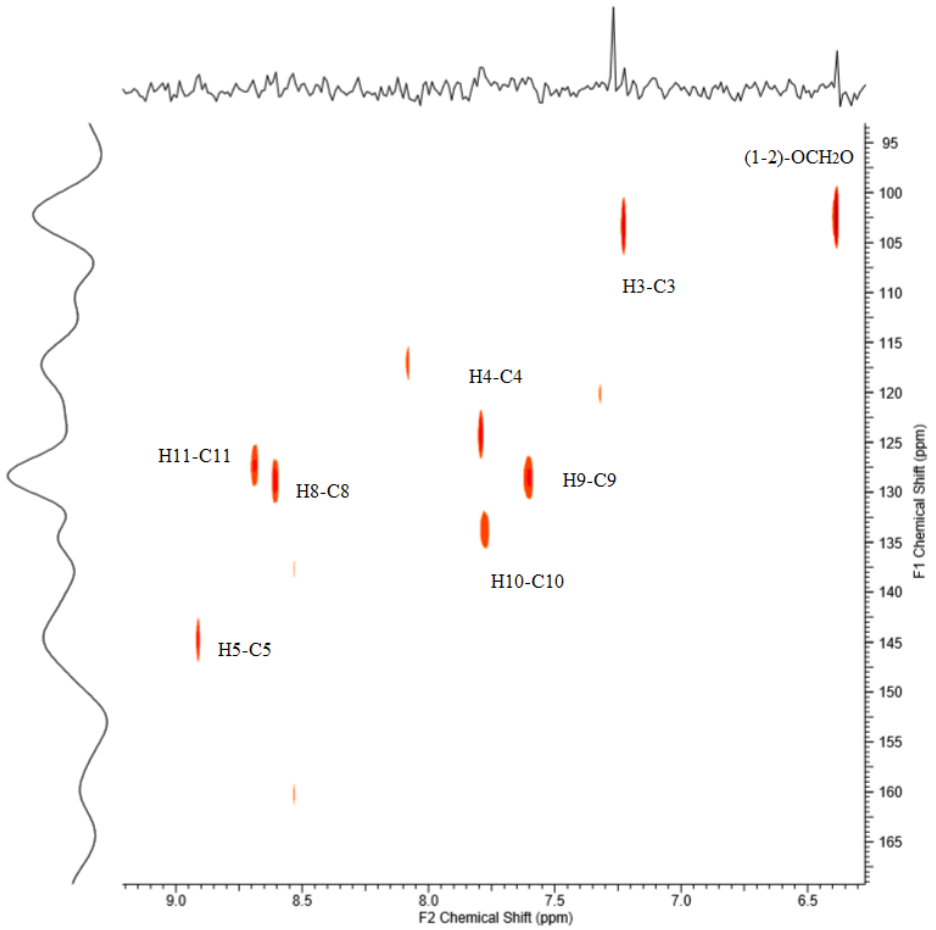

Figure S3. HSQC NMR spectrum of Liriodenine

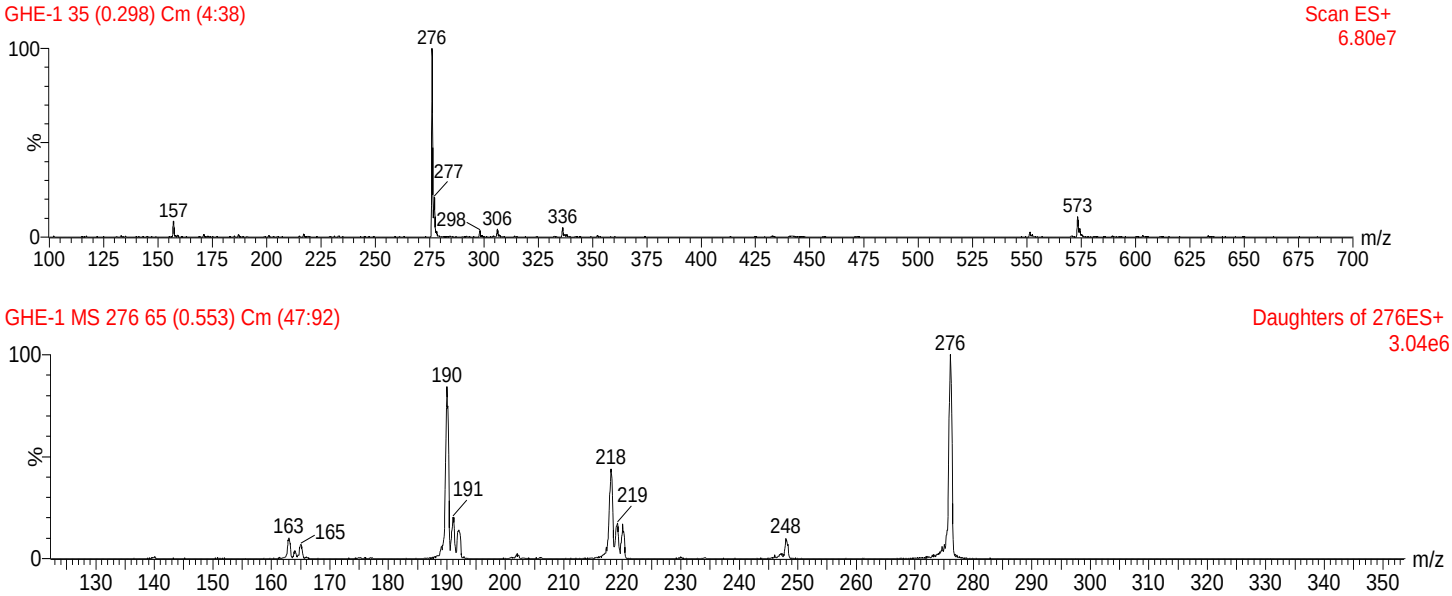

Figure S4. ESI-MS spectra of Liriodenine